Supersymmetry or Universal Extra Dimensions? Utilizing the ATLAS Experiment at CERN

Thomas Joseph Byatt

University College London

A thesis submitted for the degree of Doctor of Philosophy
of the University of London

January 2009

Declaration

I, Thomas Joseph Byatt, confirm that the work presented in this thesis is my own. Where information has been derived from other sources, I confirm that this has been indicated in the thesis.

Thomas Byatt

Er cof am Owain Tudor Stephens, cyfaill mynwesol a adawodd fwlch enfawr ar ei ol ond nad â byth yn angof.

In the memory of Owain Tudor Stephens, a dear friend who is truly missed but shall never be forgotten.

Supersymmetry or Universal Extra Dimensions? Utilizing the ATLAS Experiment at CERN

Thomas Joseph Byatt

Abstract

Supersymmetry and Universal Extra Dimensions are just two of an array of popular and enticing extensions to the Standard Model. The work presented in this thesis evaluates the feasibility of differentiating between these two models by measuring the spins of the new particles, utilising the ATLAS experiment at the Large Hadron Collider at CERN. The method presented depends upon the use of an angular variable, $\cos\theta^*_{ll}$, which is sensitive to the polar angle in the direct slepton pair production process: $q\overline{q} \rightarrow Z^0/\gamma^* \rightarrow \tilde{l^{\pm}}\tilde{l^{\mp}} \rightarrow \tilde{\chi}^0_1 l^{\pm} \tilde{\chi}^0_1 l^{\mp}$. This angular variable is advantageous since it is longitudinally boost invariant along the beam axis. This allows it to be used at the Large Hadron Collider where the initial centre-of-mass frame of reference is unknown and unrecoverable owing to the presence of invisible particles in the event. The work invoked Monte Carlo events, fully simulated in accordance with the mSUGRA Supersymmetry model corresponding to a selected production point in mSUGRA space of the ATLAS detector. It was demonstrated that, using this method and given the Monte Carlo simulation at this test point, the Large Hadron Collider can distinguish between the supersymmetric production angular distribution and that of UED using 30 fb^{-1} of integrated luminosity. A further part of the work involved an investigation into part of the innermost detector system of ATLAS. The work investigated the operational performance of a certain fraction of semiconductor tracker barrel modules utilizing data acquired during cosmic commissioning tests carried out at CERN in 2006. This included measuring the noise occupancy levels and subsequently identifying any problematic modules in the process. Eight

problematic modules were identified, forming three distinct classes, each class pointing toward a different type of problem. Furthermore, an anomaly, the so-called zeroth time bin anomaly, was found and prompted further investigation to its root cause.

Acknowledgements

This is just a short piece to show my gratitude in acknowledging all those poor souls, some of whom I will undoubtedly but certainly not deliberately neglect to mention. As is true of life embarking upon, and more importantly, completing a project of this magnitude requires the mammoth effort of many, and not solely the author, although it is their name that acquires the accolade at the end. However, it is this vital and poignant part of the project that the author is allowed to, but more importantly though, wants to generally show his sincere gratitude to the many people who have expended much time and effort on myself. This thanks extends not just during the Ph.D. but prior to it as well. It is the best I could ad-lib at the time. I hope you enjoy it.

First and foremost, I am deeply grateful to my supervisors: Dr Alan Barr and Dr Nikos Konstantinidis for all their help, unflagging enthusiasm, suggestions and encouragement over the past four years and, of course, for the mandatory painstaking and laborious task in proof reading the thesis. I am particularly indebted to Alan whose original paper and ideas helped motivate this work. Without him, the fascinating topic presented in this thesis could not have been carried out. Also he was far too kind and never uttered a bad thing even in the most frustrating of circumstances. Thank you Alan.

All those Friday morning ATLAS meetings at UCL where I was fortunate to receive invaluable feedback, offered numerous detailed and insightful suggestions and solutions to even the most banal of problems (even if I did feel if though most of the time I was on the stand in court!). I am especially grateful to Professor Jon Butterwoth from whom I received much useful feedback and comments. And not forgetting a special big thanks to Mark Sutton whose presence and opinions

made those Friday meetings that every bit more entertaining and worth while attending.

To Mark Sutton for all those unofficial Friday afternoon hourly chats/discussions plaguing him with annoying and awkward questions over the years. However much you shouted and frustrated you became, I knew you were always trying to make me learn and see the solutions to the problems. Thank you. Oh and Mark, if you do ever read this, please, please, please indulge in purchasing a pad OK. Not least for your sanity.

The work presented in this thesis would not have been possible without the dedicated effort expended by the entire ATLAS collaboration to whom I am very grateful. To those individuals, A Truly Large number of AppreciationS!

Thank you to Switzerland for bestowing the world with the very palatable and delightful Ovomaltine (or Ovaltine for the British), whether it'd be in drink, bar or cereal form! (I know, a terribly sad plug there).

To Professor Mark Lancaster who gave me the chance all those years ago after what could be described as the easiest interview I will ever have the fortune to endure. Furthermore, I would like to thank Mark for his numerous dry humorous jokes in the office which certainly didn't go unnoticed and gave me a smile every time he made one.

A rather sarcastic and regrettable thanks to London Underground for providing me with all those strenuous, tiresome journeys that I had to make twice daily, were frequently delayed and which I (along with millions of other poor despondent, unlucky travelling souls) had to endure and could have really done without! Good luck for the Olympic games!

A richly deserved thank you to the computer support team at UCL who I have, undoubtedly, pestered and troubled over the past four years.

To Robert Thorne for all those intrusive moments to ask him all those vexatious questions that only a theorist could (and dare to!) answer correctly. Much appreciated Robert.

For the SCT work I would like to thank Alan Barr, Bilge Demirkoz, Bruce Gallop, Chris Lester, Peter Phillips, Dave Robinson, Tony Weidberg and Martin White for all their useful and insightful comments.

To STFC (formally PPARC) for allowing me to tap that 'pot' of the required funds. However, as we all know, this pot is really a consequence of the British tax payer, to whom, I am truly grateful to.

To Glen Cowan for his invaluable and, unbeknown to me at the time, thorough lecture course and notes on the world of statistics and C++ programming. A true HEP graduate bible if there was ever one and I know for sure that I am not alone in thinking this. Thank you Glen.

It was my very good fortune to have met and shared the bad times and euphoria of the Ph.D. with five fantastic people in my year at UCL. Those tested souls are: Dan, Jason, Mark, Shiva and Sarah, some of who are already doctors and the rest will very soon be. I would especially like to thank Dr Dorman and Dr Nicholass for all their invaluable and extremely helpful chats and discussions over the years, something I shan't forget. Thanks mates.

And to those hardy individuals who have helped me in some manner, however minor: Claire Gwenlan, Brinick Simmons, Peter Sherwood, Graeme Watt, Simon Bevan, Catrin and Adam (the grid gurus), Alexander Richards, Lizzie, Beryl and Alan, Grahame Blair, Stewart Boogert, Mr JW, The crazy Les Cents Acres crew, Erkcan Ozcan, Ren, Mark and Frank, Ollie Harris, Tegid Jones, Ben C, Roberto and Mariana, Grandma and Sheila, and if there is anyone that I have inadvertently left out please forgive me and you know who you are!

Now two special people at UCL I would like to thank especially. To Janice who, if you should read this, I am much indebted to you for all of your generosity, kindness, patience and continued encouragement that elevated me through the early years of the work and 'holding my hand' in guiding me through the labyrinth of the modern world of computing to which I was truly unaccustomed. All this unsparing effort in the absence of even a single negative remark. You can never know how much I appreciated your help and which I will never forget. I am sincerely thank you for it.

Stathis for all your constant negative remarks and criticism behind all that lied a purpose, a reason for them. I know that you always meant well and I thank you for all your kind persistent help, invaluable guidance and for never giving up on me. Thank you Stathis.

To all my friends back home, especially Cuzzy, Huwy Blue shoes, Samo, Nelly, Azza and Beety who have helped keep my sanity in tact even when they didn't know about it.

When one writes a text, or embarks upon a task of something of this magnitude in life there is always one individual who stands out from the rest. This accolade I would like to bestow upon a certain Dr Simon Dean. An incredibly (too) kind a person, always the optimist who generally offered help and advice, concern and discussion far beyond the call of duty, whilst making 'those' cheese sandwiches, on matters of work and otherwise. This was true to not just me but to any number of people and he always managed to spare time, however short, to people (which to this day, I can never still understand quite how). Thank you Simon.

To my family (Mum, Dad, Holly and Amelia) for their ongoing unconditional love and support prior and during the Ph.D..

For all the support and the forbearance of all my friends and family I am profoundly grateful.

I owe heartfelt thanks to SleepyLili for all her unwavering love and support; and who had to share me with Susy for the past four years. This work could hardly have found expression without her comfort, and in an indispensable sense, this thesis is hers too. Merci beaucoup à SleepyLili.

Finally last, but by no means least, the most important of the acknowledgements go to two special people who I must thank for instilling the scientific curiosity and interest of science into me from a young child. The first will be more familiar to you all. I would like to show my gratitude to a certain Dr. Bruce Banner, who, is more widely and familiarly known by his gargantuan green bodied, angry alter-ego (?). But it is to my father, above all, that recognition is due. I would like to thank him who, eccentric as he is, dispensed his vast knowledge of science and the world around us, into me when I was an inquisitive and curious young boy. For introducing me to the field and doing so much to nurture and captivate my interest in it, all those years ago, with his continued support throughout. I am, and will always be, truly grateful. Thanks Dad.

Tom Byatt, Sunday 14th December, 2008.

Contents

List of Figures

List of Tables

PREFACE

THE Large Hadron Collider (LHC) accelerator complex at Organisation Européen pour la Recherche Nucléaire (CERN) will open up an exciting new energy frontier unmatched by any predecessor. It will be a voyage of discovery into uncharted territories of space-time itself. Awaiting the high-energy physics community there could be an assortment of new, mysterious particle entities, which may or may not exist within extra dimensions of space-time. It will collide two 7 TeV proton beams, rippling the space-time fabric in the process, with the copious amounts of resulting high-energy processes detected and examined by the array of four behemoth experiments that align the LHC ring.

There exists a rich array of popular and enticing extensions to the Standard Model which Man has posited. The resounding theory of Supersymmetry (SUSY) is, by far, since its emergence in the late 1960s and early 1970s, the most studied and most prominent TeV-scale physics model. Another notable and very fashionable class of theories that has emerged in recent time is the realm of extra spatial-dimensional theories. One such theory, Universal Extra Dimensions (UED), forms part of the subject of this thesis. Furthermore, the theories are attractive since each one helps us with solving (albeit, possibly partially) the difficult problem of harmonizing quantum theory and general relativity. In the process, either one of these models could be the Rosetta stone of the TeV energy scale. Therefore, each group eagerly awaits for the compelling experimental evidence (as, so far to date, there has been no experimental confirmation for the existence of either theory) that will exclude all incorrect theories posited and, thus, vindicating their theoretical pre-occupations.

However, to the dismay of the high-energy physics community is the notion that both models could appear to display exceedingly similar collider signatures. The principal objective then, to solve this problem, is to unambiguously differentiate between these two models and decipher which model is false. The work presented in this thesis evaluates the feasibility of differentiating between the two models by measuring the spins of the new particles, utilising the ATLAS experiment, one of the two general purpose detectors, at the LHC.

The introductory material which occupies section I, Chapters 1 to 3, attempts to explain the Standard Model, its successes and its shortcomings. It then con-

tinues describing two of the extensions to the Standard Model that exist, namely SUSY and UED; and finally, the experimental apparatuses that will be utilized to carry out this method: the LHC and the ATLAS detector. Clearly, a vital component in the construction of any experiment is to decipher how it will perform and operate using test data. To this end, the material presented in section II, Chapter 4, details the work carried out which investigates the operational performance of a certain fraction of semiconductor tracker barrel modules. This involved measuring the noise occupancy levels of a subset of barrel modules utilizing data acquired during the cosmic commissioning tests at CERN in 2006, which aided in identifying certain problematic classes of them. The final section, section III, Chapters 5, 6 and 7, focuses on the very essence of the work carried out and presented in thesis; that of making a spin measurment. The notion that both models could appear to display exceedingly similar collider signatures is entertained. The crux of the matter is then, can one measure the spins of the new, hypothetical particle entities posited by each theory, SUSY and UED, using the ATLAS detector and by utilizing an angular variable, $\cos\theta^*_{ll}$. By measuring the spins allows one to, unambiguously, be able to distinguish between these two models. The first chapter of this final section introduces the full and fast simulated Monte Carlo data samples employed in this work. Within the proceeding chapter, Chapter 6, the method will be given, particle definitions detailed, the results and the conclusions drawn. The penultimate chapter discusses the systematic uncertainties incurred during the analysis and the methods by which one hopes to measure them and the means of diminishing them. Finally comes an Epilogue in Chapter 8.

Part I

Introduction

Chapter 1

The Standard Model of Particle Physics

1.1 Introduction

LYING at the heart of particle physics, also referred to as high-energy physics, is physics' most fundamental principle, that of reductionism. That is, all forms of matter in nature are, and can be, reduced to fundamental entities which interact by a small number of forces. This reductionism and the laws of nature are, at this time, described by the Standard Model of elementary particle physics [1–3][a]. Particle physicists are engaged in pursuit of the most elementary constituents of matter and in exploration and elucidation of the laws that govern their behaviour.

The Standard Model is the physics model which has, since its inauguration in the late 1970s, reduced the structure and workings of the Universe to a system of twelve entities or matter particles, each one interacting with each other via the exchange of three out of the four known fundamental forces, the electromagnetic (EM), weak nuclear and strong nuclear. The absence of the fourth force from the theory, the gravitational force, is due to its seeming incompatibility with the

[a]The interested reader is also referred to the following texts on the subject [4–6].

Standard Model framework. Finally, a hypothetical particle which imparts mass to these particles is also included.

It is a relativistic quantum field theory (QFT) which itself is a synthesis of quantum theory (QT), special relativity and field theory. It is this synthesis that forms the mathematical framework in which the regnant theories of the three forces described above are formulated. It has culminated in a highly successful and the most precise scientific theory ever formulated. It is able to support calculations of physical quantities with unparallelled precision. Its overarching structure together with the fundamental laws it encompasses provide a foundation to the domain of particle physics. It is not just restricted to this domain, however, but permeates many branches of science such as condensed matter physics and chemistry.

1.2 The Standard Model

The Standard Model asserts that there exists three types of particle, matter particles called fermions (spin-$\frac{1}{2}$) which interact with each other by forces which are conveyed by the other type of particle, the force particle, which are called gauge bosons (spin-1)[b]. Additionally there is a scalar boson which is reputed to be responsible for imbuing some of the particles (matter and force) with mass. They are both assumed to be geometrically point-like in nature, i.e. have no spatial extension and are, importantly, assumed to have no substructure, that is, they are elementary. Furthermore, for every particle there exists a corresponding antiparticle with exactly the same mass but with opposite quantum numbers.

[b]Bosons are particles with integral spin, i.e. they conform to Bose-Einstein statistics, from which they derive their name. Similarly, fermions are particles with half-integral spin, i.e. they conform to Fermi-Dirac statistics and from which, again, they also derive their name.

The further distinction can be made as to whether or not the fermions interact through the strong nuclear force. These fields that do experience the strong force, in addition to the two other forces, the EM and weak, are referred to as quarks. They form two types of bound states, $q\overline{q}$ and qqq, which are called mesons and baryons respectively. Those which do not experience the strong force are called leptons: charged and neutral (so-called neutrinos). The charged leptons interact through the EM and weak nuclear forces whilst the neutrinos interact through the weak nuclear force only.

The guiding principle of the Standard Model can be attributed to symmetry. Symmetry's ascendancy and its enveloping nature in the domain of particle physics cannot be overstated. It has been, and is, evermore evident that nature poses a high degree of symmetry. At low energies many of these are hidden, whilst at higher and higher energies the symmetries become increasingly manifest. The entities of nature, the matter and force particles of the Standard Model which are described by the Lagrangian density, are intimately related to the symmetries of nature. In formulating the laws of nature the notion of a 'gauge' symmetry[c] has been developed with the fundamental requirement that the Lagrangian remains invariant under such a symmetry or 'gauge' transformation. These symmetries also imply the existence of conserved charges in the theory which is deeply rooted in the eminent German mathematician Emmy Noether's celebrated theorem [7] relating symmetries and conservation laws.

The Standard Model is based upon the gauge group consisting of three symmetries

[c]The pertinent question then arises (and arguably the deepest question of them all), as to why these types of symmetries (gauge) exist in nature.

$$G_{SM} = SU(3)_C \otimes SU(2)_L \otimes U(1)_Y, \tag{1.1}$$

where the subscripts on each group denote the conserved charge type the gauge bosons specific to the gauge group act on in order to interact with the corresponding fermionic sector. The requirement of local gauge invariance implies that there exists, for the $SU(3)_C$ group, an octet of force particles, for the $SU(2)_L$ group, a triplet and finally, for $U(1)_Y$, a singlet. The salient aspects for each symmetry group will now be addressed. It is important to note here that although the Standard Model combines all three forces (and so symmetry groups) into one framework, it is not a truly unified theory. That is, it is not based upon a single representation within which all three gauge groups, $SU(3)_C$, $SU(2)_L$ and $U(1)_Y$, are subgroups and are, furthermore, possibly low energy manifestations of a truly Grand Unified Theory (GUT) governed by one coupling constant. To this end a putative GUT or a Theory Of Everything (TOE) which attempt to truly unify the electroweak (EW) and strong, in the former, and with the addition of gravity in the latter, would seem next on the agenda and the final word on nature.

The first and simplest symmetry group is the $U(1)_Y$ hypercharge symmetry. It is an Abelian symmetry in which there is one gauge boson, the hypercharge boson, (B^μ), which couples to hypercharge (Y) which is conserved in this symmetry. The QFT which describes the way EM charged particles interact with one another is called Quantum ElectroDynamics (QED).

The next symmetry group is the $SU(2)_L$ weak isospin symmetry which is described by the weak theory and in which the gauge fields only couple to left-handed fermions. There are three associated gauge fields which mediate the weak force which are, on the contrary to QED, massive in order for the theory not to violate unitarity. They are the gauge fields $W_1^\mu, W_2^\mu, W_3^\mu$ and the conserved

charge is I_3, the third component of the weak isospin symmetry. The weak force is unique for two reasons. Firstly, it violates parity which is conserved in the EM and strong interactions. Secondly, leptons do not 'feel' the strong force, whilst neutrinos do not interact through either the EM nor strong forces but 'all' leptons and quarks participate in the weak interaction. It also allows for mixing of quark flavours and for this reason, it is sometimes referred to by the rather unorthodox title of Quantum FlavourDynamics (QFD)[d]. Theories which purport to explain that the left-handed and right-handed states are treated differently in nature are referred to as 'chiral' theories. The Standard Model is one such example of a chiral theory.

The otherwise two different, aforementioned forces, the EM and weak, are successfully combined into a single, 'unified' local gauge theory with the gauge group $SU(2)_L \otimes U(1)_Y$ which is called the ElectroWeak theory. Only after ElectroWeak Symmetry Breaking (EWSB) does the residual $U(1)_{EM} \subset SU(2)_L \otimes U(1)_Y$ symmetry group, corresponding to the familiar local gauge symmetry of EM, manifest itself at low energies. The mediator of the EM force is identified as the massless gauge boson, the photon (γ), interacting via the standard EM charge given by $Q = Y + I_3$. The theory is renormalisable as conjectured by S. Weinberg and A. Salam and subsequently proven by G.'t Hooft in 1971. It makes well-defined predictions order by order in perturbation theory.

The third and final symmetry group of the Standard Model is the one which describes the strong nuclear force, $SU(3)_C$. It is also a non-Abelian, local gauge symmetry which has a conserved 'colour' charge associated with it. It is described

[d]Just as quark colour changes at the strong vertex in QCD, flavour is not conserved but can change in weak interactions. However, this only occurs within the quark sector via the charged current (CC) interaction. It is, for this reason, that it is more appropriate for this force to be referred to as simply the weak interaction rather than QFD.

by Quantum ChromoDynamics (QCD). The name was chosen as to deliberately echo that of QED, with the word 'Chromo' used to emphasise the type of charge that the strongly interacting fields couple to. It is a purely whimsical naming convention. A theory for the strong force was proposed in 1934 as the force which binds neutrons and protons together to form atomic nuclei. However, it is actually a vestige of a deeper force operating within the nucleons themselves. The gauge bosons which mediate the strong or 'glue' force are called gluons which form the octet representation, $G^a_\mu, a = 1, ...8$. QCD describes all of the strong interactions as resulting purely from the interactions of spin-$\frac{1}{2}$ quarks and the spin-1 gluons. The fundamental coupling is of the gluon to the quarks, in a completely analogous way to the coupling of a photon to an electron in QED. There are three degrees of freedom associated with the colour charge, 'red' (r), 'green' (g) and 'blue' (b). The non-Abelian (non-commutative) nature of the $SU(3)_C$ gauge group causes gluons themselves to carry colour charge which allows them to interact amongst themselves in trilinear and quadrilinear vertices. This leads to immense ramifications of the dynamics of QCD and results in a much richer structure than in QED. Two pertinent aspects resulting from this are the properties of colour confinement and asymptotic freedom which have been verified experimentally.

The various particle types together with their transformation properties with respect to the $SU(3)_C$, $SU(2)_L$ and $U(1)_Y$ groups are summarised in table 1.1. Furthermore, in table 1.2 is tabulated the complete bosonic particle content of the Standard Model after EWSB, together with some of their unique quantum numbers which each one is furnished with. Also shown in the table is the spin-2 graviton (G), the hypothetical quantum mediator of the gravitational interaction and which possesses its own gravitational charge (energy and momentum) causing

Fermionic Field	$SU(3)_C$	$SU(2)_L$	$U(1)_Y$
q_L	Triplet	Doublet	1/6
l_L	Singlet	Doublet	-1/2
u_R	Triplet	Singlet	-2/3
d_R	Triplet	Singlet	1/3
e_R	Singlet	Singlet	1

Table 1.1: The transformation properties, with respect to the gauge groups, of the Standard Model matter fields. The subscripts, L and R, in the first column denote the left-handed and right-handed chiral components of the fields respectively.

it to interact with itself. It has yet to be correctly incorporated into the Standard Model and is just shown here for completeness.

Boson	Force	Spin	Q(e)	Mass (GeV/c^2)	Range(fm)
γ	Electromagnetic	1	0	$< 6 \times 10^{-23}$	∞
W	Charged Weak	1	± 1	80.425 ± 0.038	$\approx 10^{-3}$
Z	Neutral Weak	1	0	91.1876 ± 0.0021	$\approx 10^{-3}$
g	Strong	1	0	0	< 1
G	Gravity	2	0	0	∞

Table 1.2: The bosonic particle content of the Standard Model, together with the graviton, the hypothetical mediator of the gravitational force which has yet to be correctly incorporated into the Standard Model and, furthermore, observed. Numbers are taken from [8]. The electromagnetic charge (Q) is given in units of the elementary charge $|e| = 1.609 \times 10^{-19}$ C.

1.2.1 Spontaneous Symmetry Breaking and the Higgs mechanism

The unbroken Standard Model discussed so far describes all of the particles as massless entities, which is in contradiction to what is observed in nature from the numerous experiments that have been carried out. Notably, as previously mentioned, experiments demand massive vector bosons. Unfortunately, imbuing the

Standard Model particles with mass by the simple addition of mass terms in the Lagrangian density breaks the gauge invariance and consequently the renormalisability of the theory. Furthermore, as it is the requirement of gauge invariance that gives rise to the gauge bosons in the first place and consequently the interactions, it is evident then that the inclusion of mass terms explicitly in the Lagrangian must be forbidden. This poses an apparent dilemma. To circumvent the problem one resorts to using the putative Higgs mechanism, which is based upon the phenomenon of spontaneous symmetry breaking (SSB), which are the final two cornerstones on which the Standard Model rests upon.

Spontaneous symmetry breaking is the phenomenon that occurs where there is a symmetry preserved by physical laws (the Lagrangian density is invariant) but broken by the actual physical ground state of the system. In the present context this implies that the symmetry of the vacuum is not the same as the symmetry of the Lagrangian density and under the symmetry transformations the latter remains invariant whereas the vacuum does not. To the Standard Model is added, in order to endow particles with masses whilst still maintaining the high energy symmetry in the Lagrangian, a scalar field, the Higgs field. It has, crucially, more than one non-zero vacuum expectation value. It is the acquisition of one of the two possible true, non-zero, physical vacuum states that spoils or 'breaks' the EW gauge symmetry which is referred to as spontaneous symmetry breaking. The collection of 'all' ground states is, of course, symmetric and does share the same symmetry as the Lagrangian. It is also sometimes referred to as 'hidden' since the overall Lagrangian density describing the symmetry remains fundamentally symmetric under a gauge symmetry transformation. The gauge symmetry is still present, it has not disappeared. The vacuum expectation value of the Higgs field is equal to 246 GeV.

1.3 The Shortcomings of The Standard Model

Since the Standard Model's inauguration in the 1970s it has correctly predicted numerous experimental results and for this reason it is very much revered by the contemporaries of modern particle physics. It is, however, still very much incomplete with a plethora of parameters that have to be fed in from experiment. Described below is a list, and by no means a complete one, of the salient omissions of the Standard Model.

1.3.1 Gravity

It is obviously noticeable that the most venerable force of all, the universal attraction between all objects with mass, that is gravity, and which has been known since antiquity, is conspicuously absent from the laws laid down by the Standard Model. With more than seventy years of dedicated research on a quantum theory of gravity (the theory of which is designated 'Quantum GeometroDynamics (QGD)'), it is still proving resistant to being reconciled with quantum theory. There have been attempts for reconciliation, most notably in the mid 1970s before the surge of interest in string theory in this area, where a locally gauged relativistic QFT existed that naturally incorporated gravity. Within its fomulation was a massless bosonic field with spin-2, identified as the graviton. However, this 'Supergravity' theory [9, 10] as it was known, soon fell by the wayside since it was apparent that it suffered from numerous, incurable infinities rendering the theory unrenormalisable. However, from an experimental point of view this dismay is somewhat reduced; the energy scale at which quantum gravity effects manifest themselves are of the order of the Planck mass scale which corresponds to 10^{19} GeV. Until the Standard Model is able to accommodate this force, it will

always be consigned to being an 'effective' theory or model.

1.3.2 The Hierarchy problem: A Problem of Scales

The reason for gravity's downfall in being quantised is its extreme weakness. Furthermore, it is this disparity in the value of the coupling constants of the fundamental forces (which are known to vary or 'run' with energy), the values of which are shown below (at low energies, i.e. for energies E $\ll$ 100 GeV) for illustrative purposes, which introduces a hierarchical structure into the model.

strong	electromagnetic	weak	gravity
1	10^{-2}	10^{-7}	10^{-39}

This is called the 'hierarchy' or 'naturalness' problem to which we now turn. It can be interpreted in one of two ways; in its more pervasive context, that is to why the characteristic energy scale of the Standard Model, the EW scale (10^2 GeV), is so much smaller than the characteristic energy scale of gravity, the Planck scale. This is referred to as the 'gauge' or 'aesthetic' hierarchy problem. It is essentially a problem of dimensional analysis. It should be stressed here that in QFT, the problem alone is not merely one of aesthetics but also one of a serious technical problem which leads one to its second interpretation and the one that is more commonly quoted. That is pertaining to the renormalisation of the Higgs mass which has the tendency to be increased up to very large energy scales such as the GUT (10^{15} GeV) or Planck scales; this is referred to as the 'technical' hierarchy problem. Although both are intrinsically related, they are, in some ways, quite different. In the latter, because it is especially acute for the Higgs boson it is, therefore, worth elaborating somewhat on this last interpretation.

As discussed above, it is purely a QM problem regarding quantum corrections and their contribution to the mass of the Higgs boson; these radiative corrections have the tendency to destroy the hierarchy by increasing this mass up to some large energy scale, Λ. The mass of the Higgs boson (m_h) itself is required to

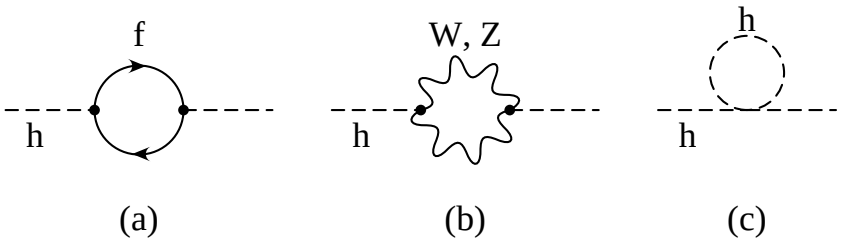

Figure 1.1: 1-loop diagrams contributing to the effective Higgs (mass)^2, from (a) fermion loop; (b) gauge boson loop; (c) scalar loop.

be less than approximately 1 TeV [11]. This stems from its role in the cancellation of high-energy divergences and, thus, unitarising the cross-section for the $W^{\pm}W^{\mp} \rightarrow W^{\pm}W^{\mp}$ elastic scattering process. Without a Higgs boson or any new physics at, or around, the TeV scale this scattering amplitude violates unitarity. A lower bound can also be imposed by virtue of direct searches at past and present colliders. LEP2 carried out direct searches for the Standard Model Higgs boson which resulted in a lower bound of $m_h > 114.4$ GeV at the 95% confidence level [12]. More specifically, divergent loop diagrams contributing to the Higgs mass squared like those shown in fig. 1.1[e], are quadratic in the cut-off Λ, which limits the integral over the loop momenta. The resulting contribution to the Higgs mass squared of a fermion with mass m_f and coupling λ_f takes the form:

$$\delta M^2_{\rm HF} = \frac{|\lambda_f|^2}{16\pi^2}\left[-2\Lambda^2 + 6m_f^2 \ln(\Lambda/m_f) + \cdots\right]. \tag{1.2}$$

There is a similar correction induced by bosons but with the opposite sign for the first term on the right hand side of equation eq. 1.2. This is a very important

[e]For fig. 1.1 I am grateful to Alan Barr from whose PhD thesis [13] it was reproduced with kind permission.

point and one that will be returned to later.

Now, within the context of the Standard Model, in the absence of any interplay of new physics between the EW and Planck scales, Λ, (i.e. under the assumption that the Standard Model is valid all the way up to these large energy scales) these divergences move the EW scale (and so correspondingly, the Standard Model Higgs mass) up to large energy scales such as the GUT or Planck scales. In order to avoid this 'hoarding' of m_h up to large energy scales and preserve the Higgs mass at the EW scale as demanded by the arguments given before, requires that the parameters of the theory be extremely finely tuned. The extremity of the tuning in the theory is needed in order that there exists the cancellation between the quantum corrections to the bare Higgs mass and the bare Higgs mass itself, to, for the case of $\Lambda \sim 10^{15}$ GeV, 1 part in 10^{12} or, for the case of $\Lambda \sim 10^{19}$ GeV, 1 part in 10^{16}. Therein lies the problem; this appears to be wholly unnatural and extremely unlikely that this is truly realised in a theory which aspires to explain Nature's workings at the smallest possible scales.

1.3.3 Other noticeable absentees

Summarised below are some other noticeable omissions from the Standard Model.

- The apparent arbitrariness of the Standard Model which contains some twenty eight unspecified parameters (three gauge couplings, 1 vacuum angle (the weak or Weinberg angle), six quark masses, masses of the three charged leptons, three weak mixing angles, 1 CP-violating CKM phase, 1 $W^{\pm}$ mass, 1 Higgs mass and a further nine in the neutrino sector), all of which, one must concede, must be put in 'by hand'.
- The gauge group which the Standard Model is based upon seems rather *ad hoc* and seemingly complicated. Is it possible for it to be embedded in

some more global gauge symmetry group G, such that:

$$G_{SM} \supset SU(3)_C \otimes SU(2)_L \otimes U(1)_Y, \tag{1.3}$$

where, at just below some high energy scale, would be spontaneously broken into the three, familiar Standard Model gauge groups? Furthermore, as it is known that the EM, weak and strong forces vary with energy (so-called 'run' with energy), could they be extrapolated to some high energy value where there would be one, and only one, universal gauge coupling? The Standard Model, as it stands, suggests otherwise.

- Something which is self-evident of the Standard Model, is the question of why the fermionic sector resides in three families, each one transforming identically under the gauge groups but differing in mass. Furthermore, despite the plethora of apparently 'fundamental' particles the Standard Model accommodates, only the first generation of particles, that is, the up and down type quarks and the electron and electron-type neutrino (there are also the muon- and tau-type neutrinos), make up 'all' the stable, visible matter in the Universe.
- Astronomical observations of rotational velocity profiles within galaxies [14] indicate that a large fraction ($\sim 75\%$) of the energy density (of which only $\sim 30\%$ is matter) in the Universe is non-radiative, the fashionably entitled 'Dark Matter'. What form this matter takes is, as yet, still unanswered.

1.4 Coda

To conclude, it is clear that the Standard Model has its limitations and is incomplete. Its formulation allows for unwieldy quantum effects that need to be tamed.

There is a proliferation of 'new', high-energy completions of the Standard Model. One such one is the possibility of incorporating new types of symmetry; the most promising being the introduction of a novel type, known as 'Supersymmetry' or more prosaically, as SUSY. If its predictions are true and that there does indeed exist a profusion of superpartner particles of the Standard Model ones, then there will be a cornucopia of new species of particles awaiting to be discovered at a forthcoming high-energy experiment. One other, entertaining alternative, is to extend the notion that space-time consists of more than four dimensions. This could also help to ameliorate the Standard Model's shortcomings. Both these ideas will be the subject of the next chapter.

Finally, the veracity of the situation is that any truly fundamental theory of nature must be able to explain each one of the shortcomings, and importantly, without the intervention of Man's empirical hand.

Chapter 2

From the Standard Model to the Super Standard Model and Beyond

2.1 Supersymmetry and Extra Dimensions

PHYSICS in the Twentieth century was founded on the theories of relativity (general and special) and quantum mechanics. The classical theory of general relativity (GR) describes gravitation and shows that space and time are intimately woven together with the gravitational force arising through their curvature. It describes the macroscopic world and has been very successful. Quantum theory (QT) is the framework of physical laws that describe the microscopic world; the molecules, atoms, sub-atomic and sub-nuclear particles. It seems difficult, if not altogether impossible, to construct a consistent theory that is partly quantum and partly classical. It, therefore, seems that both need to be combined in order to formulate a correct quantum theory of gravity.

However, despite the obvious success of quantum theory describing the very small and the general theory of relativity describing gravitation, it has and is still proving to be impossible to combine the two together and, thus, a quantum theory of gravity is proving elusive. It is this problem that lies at the heart of theoretical

and experimental particle physics and remains one of, if not, the greatest challenge facing physicists at the present. Physicists are loath to disposing of QT or GR, as each one has proven capable of extraordinarily accurate predictions at their respective energy scale domains. This hierarchical structure, as we have seen, lies at the very essence of gravity's unruly behaviour within particle physics. This must be reconciled.

There have been many attempts employed in the hope to solve or mitigate the hierarchy problem. Indeed, there are various attempts that are hoped to do much to ameliorate the hierarchy problem but also the numerous other shortcomings that exist within the Standard Model. These include technicolour, introduction of new symmetries, particles or interactions at the EW scale, e.g. SUSY, by far the most studied TeV energy scale physics scenario and the most prevalent in the literature for beyond the Standard Model physics models. This is the subject of the next section. However, a recent alternative put forward has been to exploit the geometry of space-time[a]. Specifically these theories propose the existence of, as yet, undiscovered extra spatial dimensions[b,c]. They express profound ideas on the very nature of the space-time fabric.

[a] Although some aim to solve the hierarchy problem the pertinent question then becomes a dynamical explanation for the size of the radius of stabilisation of the extra dimension, that is why are the extra dimensions of that size and geometry. This then, seemingly just reformulates the problem rather than solves it. However, it is hoped that this new problem, if it should indeed arise, will prove to be more tractable.

[b] It seems difficult, if not altogether impossible, to construct a theory which has more than one temporal dimension. The argument is that these theories would contain tachyons and so would, inevitably, violate the laws of causality. For a fuller treatment consult [15, 16].

[c] Hereafter, when I refer to extra dimensional models I will always be implicitly meaning extra spatial dimensions unless otherwise stated.

2.2 Supersymmetry (SUSY)

As alluded to in the previous chapter, progress in understanding the internal workings of the universe at the elementary level incorporates the notion that one considers the symmetries that nature exhibits. Furthermore, symmetry was the dominant theme in twentieth century physics and its application was heuristically very successful. Supersymmetry, with its seemingly captivating title, is an extension of this notion; a different type of symmetry and one which, since its emergence in the late 1960s has, despite its complexity, allured the minds of those working in not just physics but mathematics as well. Supersymmety, put quite 'simply', posits that there exists an additional, as yet undiscovered symmetry of nature, one that is a generalisation of the space-time symmetry that QFT utilises. The theory posits that there exists a relationship between integer and half odd-integer spin states. The subject has been covered extensively in the literature and the interested reader is referred to references [17–23].

2.2.1 Supersymmetry: The rudiments

Here a first foray into the rudiments of SUSY will be presented. It asserts that for every bosonic degree of freedom (dof) there exists a fermionic degree of freedom[d]. That is, via an operator Q, which, as will become evident shortly, alters the spin of the state by half a unit, transforming particles with integer spin to particles

[d]True this is the most significant implication that SUSY proposes and is, therefore, the argument most often given from a phenomenological perspective. However, in fact, there exists a far more profound and striking notion that SUSY proposes. That is, SUSY invites us to contemplate the possibility of extending our notion of space-time itself to one in which there exists additional fermionic dimensions [23]. The reader should note however that they are quantum dimensions and have no classical analogue. This makes them rather abstruse and difficult to visualise. These additional fermionic degrees of freedom together with the more familiar four dimensions results in an enlargement of space-time to so-called 'superspace'. A SUSY transformation is then identified as a translation in this superspace. This is surely the most radical assertion that the theory makes.

with half odd-integer spins and vice-versa. Furthermore, the operator Q is, in contrast to the bosonic generators of the Poincaré[e] or gauge groups, fermionic[f] and transforms the states such that:

$$Q^N|\text{ Boson }> \;=\; |\text{ Fermion }>,\text{ and}$$
$$Q^{N\dagger}|\text{ Fermion }> \;=\; |\text{ Boson }>,$$

where $Q^{N\dagger}$ is the Hermitian conjugate of Q^N and the superscript, N (=1,.....,N), labels the representation of the internal symmetry group to which the SUSY generators belong. In its simplest incarnation, so-called 'simple' SUSY, there exits only one pair of fermionic SUSY generators Q and its Hermitian conjugate $Q^\dagger$, labelled as N=1, where N counts the number of fermionic generators. This translates as, for every Standard Model particle, there exists one and only one SUSY partner. There does exist however, $N \geq 2$ so-called 'N-Extended SUSY', in which there are more than one SUSY generator and so consequently a larger number of SUSY states which results in the supermultiplets being enlarged. However, these $N > 1$ SUSY theories are automatically 'non-chiral' and so, consequently, discarded (the reader is referred to [17] for a more detailed explanation of this). It appears that these 'simple', N=1, SUSY theories are the best candidates and so the ones of most relevance for the low energy phenomenology to be explored at the current, and foreseeable future, generations of high-energy colliders. No more will be said about extended SUSY. Hereafter, we will be only concerned

[e]Also called the inhomogeneous Lorentz group denoted as ISO(3,1), is the group of isometries of Minkowski space-time and is the semi-direct product of translations and Lorentz transformations.

[f]These generators are different to the usual bosonic ones and so, consequently, they obey anti-commutation relations. To emphasise this new, unique quality that this symmetry exhibits it is prefixed with the word 'super', from which the symmetry derives its fanciful title.

with N=1 SUSY and so, consequently, the superscript N=1 will be suppressed in the relations that follow.

The generators Q and $Q^\dagger$ are two-component (Weyl) spinor operators and must satisfy anticommutation and commutation relations of the form:

$$\{Q_a, Q_{\dot{b}}^\dagger\} = 2(\sigma^\mu)_{a\dot{b}} P_\mu, \quad \{Q_a, Q_b\} = \{Q_{\dot{a}}^\dagger, Q_{\dot{b}}^\dagger\} = 0, \tag{2.1}$$

$$[P^\mu, Q_a] = [P^\mu, Q_{\dot{a}}^\dagger] = 0, \tag{2.2}$$

$$[Q_a, M_{\mu\nu}] = \frac{1}{2}(\sigma_{\mu\nu})_a^b Q_b \ , \quad [Q_{\dot{a}}^\dagger, M_{\mu\nu}] = -\frac{1}{2}(\sigma_{\mu\nu}^\dagger)_{\dot{b}}^{\dot{a}} Q^{\dagger\dot{b}}, \tag{2.3}$$

where $M_{\mu\nu}$ is the Lorentz transformation generator, P_μ is the generator of translations, that is the four momentum operator, $\sigma^\mu = (\mathbf{1}, \vec{\sigma})$, where $\mathbf{1}$ is the 2×2 identity matrix and $\vec{\sigma}$ are the 2×2 Pauli matrices and $\frac{1}{2}$ and 2 are normalisation factors. The subscripts a and b ($a = 1, 2$ and $b = 1, 2$) denote the two non-zero components of each spinor, whilst the undotted and dotted indices refer to the first (upper) and last (lower) components of a Dirac spinor. Since all commutation relations between SUSY generators and the $M^{\mu\nu}$s and P^μs are defined and furthermore, they only involve these quantities, the SUSY algebra is now closed. A theory which is invariant under the group of transformations generated by $M_{\mu\nu}$, P_μ and Q is Supersymmetric. Now, the single particle states of the SUSY theory naturally form irreducible representations of the SUSY algebra, so-called 'supermultiplets'. These are two-component objects which contain both bosonic and fermionic fields, the superpartners of each other, whose spins differ by half a unit and which are related to each other by a SUSY transformation. Importantly,

in all other respects, the two components are identical, in that they must have the same representation as the Standard Model gauge symmetries. An important point to notice here is that by virtue of eq. 2.1 the SUSY generators, Q_a and $Q^\dagger_{\dot{a}}$, are independent to P^μ, the four momentum operator (from eq. 2.2). It is then evident that SUSY is intimately connected to the structure of space-time through eq. 2.1. Furthermore, as the mass-squared operator $m^2 \equiv P^2 \equiv P_\mu P^\mu$, which is a Casimir operator of the Poincaré algebra, it is also, by virtue of eq. 2.2, a Casimir operator of the SUSY algebra, $[P^2, Q_a] = [P^2, Q^\dagger_{\dot{a}}] = 0$. In words this states that SUSY commutes with the operator P^2 and, therefore, if SUSY is an exact symmetry, implies that particles that reside in the same supermultiplet must be mass (or energy) degenerate because they must have the same eigenvalues as the m^2 operator.

So, recapitulating, in an exact supersymmetric theory of nature every particle has, associated with it, a partner which has:

- equal mass;
- the same internal quantum numbers (i.e. same gauge couplings);
- the same number of degrees of freedom (i.e. $n_B = n_F$).

However, with the additional necessity that the spins differ by half a unit. Evidently, the requirement of mass degeneracy is not realised in nature and implies that if SUSY is relevant at all, then one must concede that it is a broken symmetry. This will be discussed in more detail in section 2.2.4.

2.2.2 The Minimal Supersymmetric Standard Model (MSSM)

The Minimal Supersymmetric Standard Model (MSSM) [24–26] is the appellation given to the simplest possible SUSY extension of the Standard Model; it is essentially a supersymmetrisation of the existing Standard Model. It is a low en-

ergy SUSY theory, which is renormalizable, invariant under the Standard Model gauge group, Poincaré group and contains the minimal particle content; with a superpartner, known as 'sparticles', for each and every Standard Model particle and two Higgs doublets. It, thus, approximately doubles the particle content of the Standard Model. It provides a consistent, phenomenologically viable model and is consequently, by far, the most studied SUSY model. The MSSM predominantly forms the basis for experimental studies in searching for the SUSY at current and future accelerators.

Its construction starts with satisfying the condition that for each supermultiplet, of which there exists only two different types, required to accommodate the entire Standard Model states, $n_F = n_B$. Furthermore, each member must have exactly the same gauge quantum numbers as the other. The simplest possibility is one in which a single, massless Weyl fermion ($n_F = 2$, corresponding to the two helicity states) resides together with two scalar particles (for each one $n_B = 1$). The possibility that the bosonic degrees of freedom arise from a single, massless (at least before SSB) spin-1 gauge boson (the latter requirement is for the theory to be renormalisable) is discarded on the grounds that none of the observed gauge bosons have the same quantum numbers as the fermion. Thus, a new set of scalar particles are introduced. This is called the 'chiral' or 'matter' or 'scalar' supermultiplet. Clearly then, this supermultiplet is occupied by the Standard Model Higgs boson. The next simplest supermultiplet, the so-called 'gauge' or 'vector' supermultiplet, is the one in which the spin-1 vector gauge boson of the Standard Model ($n_B = 2$ before EWSB) reside together with a single massless spin-1/2 Weyl fermion (again $n_F = 2$). The possibility of the gauge bosons being paired with a spin-3/2 fermion renders the theory unrenormalisable and so is discarded. Fig. 2.1 conveys the clarity of the possible massless supermultiplets of the MSSM,

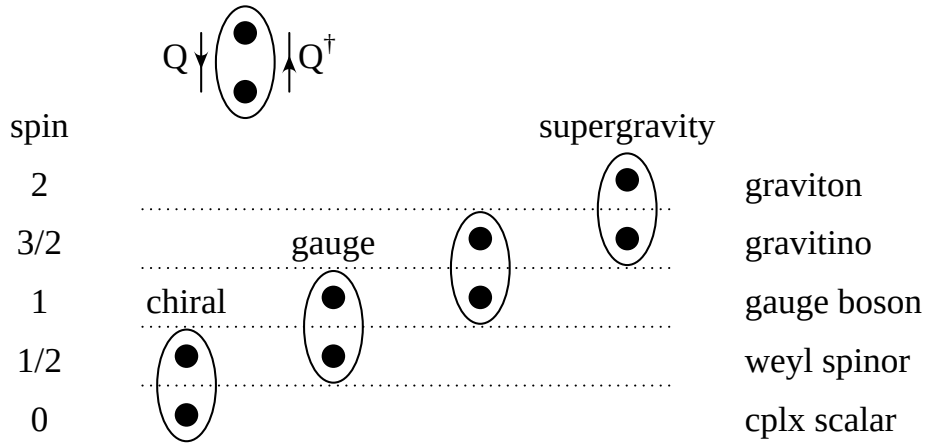

Figure 2.1: The massless N=1 supermultiplets of the MSSM represented by the oval shaped objects. These are two component objects, which contain both bosonic and fermionic fields, the superpartners of each other, whose spins differ by half a unit and which are related to each other by a SUSY transformation, by the application of the generator operators Q_a and $Q^\dagger_{\dot{a}}$. Importantly, in all other respects, the two components are identical, in that they must have the same representation as the Standard Model gauge groups. Note, 'cplx' denotes complex. Figure taken from [13] with the kind permission of the author.

into which the Standard Model particles must reside.

The next point is to decide which supermultiplet the Standard Model fermions reside in since both appear to be able to accommodate them. However, a critical point in answering this, arises from the way that the two types of supermultiplet differ in their treatment of the fermionic fields which inhabit them. The chiral, but crucially, not the gauge, supermultiplets contain fermions whose left-handed and right-handed components transform differently under Lorentz boosts, which is a known property that the fermions of the Standard Model are bestowed with. The Standard Model fermions must, therefore, reside in the chiral supermultiplet.

So, recapitulating, the sparticles of the Standard Model fermions and gauge bosons have spins that are half a unit 'less', whereas the sparticles of the Standard Model scalars have spins half a unit 'greater' than, their Standard Model

Particles		spin 0	spin $\frac{1}{2}$	$SU(3)_C$, $SU(2)_L$, $U(1)_Y$
squarks, quarks	Q	$(\tilde{u}_L\ \tilde{d}_L)$	$(u_L\ d_L)$	$(\mathbf{3}, \mathbf{2}, \frac{1}{6})$
($\times$ 3 families)	$\bar{u}$	$\tilde{u}_R^*$	$u_R^\dagger$	$(\bar{\mathbf{3}}, \mathbf{1}, -\frac{2}{3})$
	$\bar{d}$	$\tilde{d}_R^*$	$d_R^\dagger$	$(\bar{\mathbf{3}}, \mathbf{1}, \frac{1}{3})$
sleptons, leptons	L	$(\tilde{\nu}\ \tilde{e}_L)$	$(\nu\ e_L)$	$(\mathbf{1}, \mathbf{2}, -\frac{1}{2})$
($\times$ 3 families)	$\bar{e}$	$\tilde{e}_R^*$	$e_R^\dagger$	$(\bar{\mathbf{1}}, \mathbf{1}, 1)$
Higgs, Higgsinos	H_u	$(H_u^+\ H_u^0)$	$(\tilde{H}_u^+\ \tilde{H}_u^0)$	$(\mathbf{1}, \mathbf{2}, +\frac{1}{2})$
	H_d	$(H_d^0\ H_d^-)$	$(\tilde{H}_d^+\ \tilde{H}_d^0)$	$(\mathbf{1}, \mathbf{2}, -\frac{1}{2})$

Table 2.1: The 'matter' SUSY eigenstates and two component chiral supermultiplets (scalar and Weyl spinor) of the Minimal Supersymmetric Standard Model, together with the quantum numbers each one is endowed with. The subscripts on the Higgs fields, u and d, denote the quark type they endow with mass.

Particles	spin $\frac{1}{2}$	spin 1	$SU(3)_C$, $SU(2)_L$, $U(1)_Y$
gluino, gluon	$\tilde{g}$	g	$(\mathbf{8}, \mathbf{1}, 0)$
wino, W bosons	$\tilde{W}^\pm$, $\tilde{W}^0$	$W^\pm$, W^0	$(\mathbf{1}, \mathbf{3}, 0)$
bino, B bosons	$\tilde{B}^0$	B^0	$(\mathbf{1}, \mathbf{1}, 0)$

Table 2.2: The 'force' SUSY eigenstates and two component gauge supermultiplets (scalar and Weyl spinor) of the MSSM, together with the quantum numbers each one is endowed with.

counterparts. Table 2.1 lists the full content of the chiral supermultiplets whilst table 2.2 lists the entire content of the gauge supermultiplets, within the MSSM.

2.2.2.1 The SUSY and Mass eigenstates

The nomenclature adopted within SUSY has an often rather whimsical flavour to it. Firstly, the naming convention for all the SUSY spin-0 partners of the Standard Model fermions is simply to prefix an 's' (for scalar and not SUSY) onto the names

of the Standard Model counterparts. Thus, they are generically called sleptons and squarks. For the SUSY fermionic partners of the Standard Model bosons the convention is to suffix 'ino' onto the name of the Standard Model counterparts, replacing 'on' where it exists and consequently are generically called 'gauginos'. Secondly, the SUSY partners are more often than not written with a tilde over the Standard Model particle state symbol to denote it is supersymmetrised. For example, for sleptons and squarks the symbols are $\tilde{l}$ and $\tilde{q}$ for l and q respectively. However, sometimes another convention is adopted and that is to capitalise the symbols to denote the sparticles. Consequently, the MSSM admits a world of sparticles called, for the gauge fermions, gluinos ($\tilde{g}$), winos ($\tilde{W}$) and binos ($\tilde{B}$) before EWSB. The bino and neutral wino mix; the photino ($\tilde{\gamma}$) and zino ($\tilde{Z}$) are the mixed states and associated SUSY partners of the Standard Model photon and Z^0 respectively. Similarly, for the scalar partners of the Standard Model quarks and leptons, generically called 'sfermions', there exists for example, the selectron ($\tilde{e}$), smuon ($\tilde{\mu}$), sneutrino ($\tilde{\nu}$), stop ($\tilde{t}$), sbottom ($\tilde{b}$) and scharm ($\tilde{c}$), and so forth, with l, where l=e, $\nu_e, \mu, \nu_\mu, \tau, \nu_\tau$, and q, where q= u, d, s, c, b, t. Note that left-handed and right-handed scalars are separate states. Furthermore, since they are scalars they, themselves, have no 'handedness'. Instead the label refers only to the helicity of their fermionic counterparts: the SUSY partners of the left-handed electron and right-handed quark are denoted as $\tilde{e}_L^-$ and $\tilde{d}_R^{-1/3}$ respectively.

Now as it transpires, one Higgs doublet is not enough in the MSSM but rather two separate Higgs doublets are required to impart mass to the Standard Model particles (an alternative method is required to endow their SUSY counterparts with mass) through the same manner as in the Standard Model, namely via EWSB. A single Higgs scalar doublet, with Y=+1/2, that exists in the Standard Model is unable to endow the down type quarks and charged leptons in a SUSY

theory with mass. This is due to the formal structure of the SUSY theory whereby any terms like $\phi\phi^*$ are forbidden in the SUSY Lagrangian in order to respect invariance under a SUSY transformation. Therefore, an obligation of the theory is that a second Higgs doublet (H_d, with the other doublet labelled as H_u) is introduced, with opposite hypercharge, in order to impart mass to both up-type and down-type quarks. Intriguingly, without invoking the argument given above, there exists a second, completely independent reason [19] for requiring that there exists two Higgs doublets. This is in order to avoid unwanted triangle gauge anomalies and, thus, avoiding rendering the resulting theory anomalous.

The appearance of a pair of complex Higgs doublets leads to there being eight degrees of freedom. After EWSB, three of these become the longitudinal polarisation states of, again they are 'eaten' by, the Z^0 and $W^{\pm}$ bosons, leaving a surplus of five degrees of freedom. These correspond to five physical, massive Higgs bosons posited by the MSSM. They are a charged scalar Higgs pair $H^{\pm}$, two neutral CP even scalar Higgs bosons h^0 and H^0 and a neutral CP odd pseudoscalar Higgs boson, A^0. After spontaneous breaking of the EW gauge symmetry down to EM ($SU(2)_L \otimes U(1)_Y \rightarrow U(1)_{EM}$) in accord with experiment, results in the interaction (SUSY) eigenstates, that is, the Higgsinos and EW gauginos, to mix with each other forming mass eigenstates. Fields with different $SU(2)_L \otimes U(1)_Y$ quantum numbers are permitted to mix with fields which have the same SU(3) and U(1) quantum numbers. The two neutral Higginos mix with the neutral wino and bino to form four EM neutral states called 'neutralinos' $\tilde{\chi}_i^0$ (i=1,2,3,4), whilst the charged Higginos mix with the charged winos to form two charged fermions called 'charginos' $\tilde{\chi}_i^{\pm}$ (i=1,2). This mixing is shown schematically in table 2.3 and where the subscripts in each case are used to denote the mass ordering of the states, such that $m_{\tilde{\chi}_4} > m_{\tilde{\chi}_3} > m_{\tilde{\chi}_2} > m_{\tilde{\chi}_1}$. Lastly, note that the gluino does not

$$\tilde{B}^0,\, \tilde{W}^0, \tilde{H}^0 \quad \longrightarrow \quad \tilde{\chi}_i^0$$

$$\tilde{W}^{\pm},\, \tilde{H}^{\pm} \quad \longrightarrow \quad \tilde{\chi}_i^{\pm}$$

$$\tilde{g}$$

Table 2.3: The force particle content of the MSSM before, where they exist as interaction eigenstates, and after, where they exist as the physical mass eigenstates, EWSB. Fields with different $SU(2)_L \otimes U(1)_Y$ quantum numbers are permitted to mix with fields which have the same $SU(3)_C$ and $U(1)_Y$ quantum numbers. Whereafter, as in accord with experiment, we demand that the EW gauge symmetry be broken down to $U(1)_{EM}$ ($SU(2)_L \otimes U(1)_Y \rightarrow U(1)_{EM}$).

participate in mixing with the other particle states because it does not have the appropriate quantum numbers to do so.

2.2.2.2 R-parity

In the MSSM, the Lagrangian density ($\mathcal{L}$), or more precisely, the superpotential (V) from which the former is constructed from (since $\mathcal{L} \supset -V$), invites terms that violate baryon-number (B) and lepton-number (L) and $B - L$. These terms in the Lagrangian which are gauge-invariant and renormalisable, and the interactions which they describe, generally give rise to counterfactual predictions such as fast proton decay. To preclude B and L violating terms in the renormalisable superpotential and so circumventing the problem of fast proton decay a discrete symmetry is imposed on the theory. This discrete symmetry is called 'R-parity' (R_P) or equivalently 'matter parity'. It is a discrete, global, multiplicative, conserved and exact symmetry given by:

$$R_P = (-1)^{3B+L+2S}. \tag{2.4}$$

where B, L and S denote baryon-number, lepton-number and the spin of the particle repectively. The quantum number takes the values of $R_P = +1$ for all conventional (Standard Model) matter particles whilst all SUSY particles have $R_P = -1$. SUSY theories where it is an exactly conserved symmetry are called R-parity conserving (RPC). Whereas, the cases where it is not conserved are called R-parity violating (RPV) theories. This leads to there being two quite distinct classes of SUSY theories: RPC and RPV. In RPC theories, only vertices which involve 'pairs' of SUSY particles are permitted. Consequently, they can only be produced in pairs at collider experiments and each one must decay to states which contain an odd number of sparticles with all subsequent SUSY decay chains resulting in the lightest SUSY particle (LSP) remaining stable. These are colourless, EM neutral and interact only weakly with matter and therefore, exhibit a missing-p_T ($\not{p}_T$) signature in a detector. Therefore, the LSP provides a natural candidate for the cold dark matter (DM) of the Universe. This, thus, results in a characteristic signature of RPC SUSY processes which will consist of exactly two LSPs, manifesting as missing E_T, accompanied by a number of Standard Model particles, jets and/or leptons. The entire work carried out in this thesis was only concerned with RPC SUSY type theories and so, therefore, RPV will not be discussed further.

Finally however, despite SUSY precluding fast proton decay by virtue of conservation of R-parity and that, furthermore, predicts a natural candidate for DM, it cannot be overlooked that R-parity is still rather *ad hoc*. It therefore, may be replaced by another discrete symmetry or it may be weakly violated. Without knowing the full, fundamental theory from which, presumably, the MSSM would arise at some lower energy scale, it is apparent that this area in the model is certainly ambiguous and incomplete.

This completes the definition of the MSSM.

2.2.3 Motivations for Supersymmetry

There are many virtues of SUSY, not least that it provides a solution to the hierarchy problem. This problem can be alleviated and, importantly, is natural in the theory, by the introduction of the SUSY particles which have the virtue of taming ultra-violet divergences. This is achieved by the SUSY particles cancelling the divergences arising from the Standard Model particle's contributions in the loop corrections to the Higgs mass. However, in addition to solving or mitigating the hierarchy problem, there are various other motivational arguments for SUSY which have been adduced. They include the following list:

- it can unify the Standard Model gauge couplings of the Standard Model, with all three couplings appearing to meet at a single point at an energy scale of approximately 10^{16} GeV [27, 28]. This arises from the introduction of new particle states at the EW scale which consequently alters the running of the coupling constants. Furthermore, they do not meet convincingly within the Standard Model alone (as illustrated in fig. 2.2). It is, therefore, evident that any other view has to claim that this unification is a coincidence! Also, the unification energy is sufficiently high to avoid current bounds imposed from proton decay. This unification of the gauge couplings at some high energy scale is predicted to occur in GUT or Superstring theories, thereby strongly hinting at each one as possible candidates for higher-energy completions of the Standard Model;
- it can naturally provide, within the context of RPC SUSY models, a cold dark matter candidate in the form of the LSP;

- the important, often quoted and the one that is certainly revered by some contemporary aficionados of particle physics, is the role it plays as a fundamental part amongst formulating a Theory Of Everything (TOE). Thus, in part, touted as a possible quantum theory of gravity. This is in the form of Superstring or, in the deeper, overarching framework, so-called M-theory, which includes Supergravity. It is all based upon the triad of structures: gravity, gauge theory and SUSY. These are, and still remain to this day after over thirty years of work on the subject and whatever ill feeling and unrest they might cause, the 'best' candidate for a consistent theory of gravity. More importantly though, is in accomplishing the unification of all the four fundamental forces. In fact, some would argue, rightly or wrongly, that the reason for SUSY's rise to promience was for this reason; in its part it plays in string/M-theory [29–35];
- a more mathematical motivation and the reason for its birth was that it is the only known possible, non-trivial way of circumventing the restriction known as the Coleman-Madula theorem (actually a set of theorems of which the Coleman-Madula is the most powerful). That is, combining an internal symmetry group with the Poincaré group requires that there exist fermionic charges, i.e. the essential new feature here is that the operators obey anti-commutation relations.

2.2.4 Experimental constraints on SUSY

The main and current constraints on the MSSM model together with the source of each one, are summarised below.

- **Direct collider searches:** The Large Electron Positron (LEP) collider was in operation at CERN from 1989 to 2000 with four detectors each

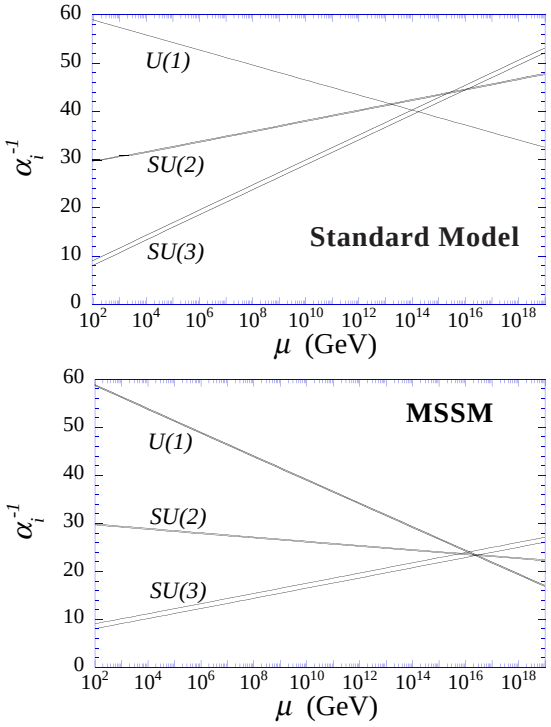

Figure 2.2: The evolution or 'running' of the gauge couplings (EM, weak and strong) constants with energy (μ) as predicted by both the Standard Model (top plot) and SUSY, in the MSSM (bottom plot). The plots are given in the conventional SU(5) normalisation. That is, the U(1) coupling constant is given by $\alpha_1 = \frac{5}{3}\alpha_Y$, where α_Y is the hypercharge coupling. The width of the error bands on the plots are due to the variation of the SU(3) coupling constant $\alpha_3(m_Z)$ between 0.113 and 0.123 whilst the sparticle masses are also varied. Evidently, SUSY allows for possible unification of the three forces at some 'Grand' energy scale, $\sim 10^{16}$ GeV. Figure taken from [27].

collecting a total of approximately 1 fb^{-1} of data. Some of the resulting mass limits at 95 % confidence level were [36]: $m_{\tilde{\chi}_1^0} > 46$ GeV/c^2, $m_{\tilde{e}} > 73$ GeV/c^2 and $m_{\tilde{\mu}} > 73$ GeV/c^2. The other direct searches for SUSY particles were carried out by the Tevatron, a $p\overline{p}$ collider located at Fermilab, U.S.A.. A recent publication [37] excludes masses up to 392 GeV/c^2 at 95 % confidence level in the region where gluino and squark masses are similar, gluino masses up to 280 GeV/c^2 for every squark mass, and gluino masses

up to 423 GeV/c^2 for squark masses below 378 GeV/c^2. Note, all these constraints are for mSUGRA with R-parity conserved and a neutral LSP.

- **Rare decays:** Rare decays of heavy flavour mesons are sensitive to sparticles in loops. The contribution of sparticles to the $b \rightarrow s\gamma$ branching ratio constrains a region in SUSY parameter space. For $10 \leq \tan\beta \leq 20$, where $\tan\beta$ is a specific SUSY parameter that will be explained shortly, sets a lower bound on m_{A^0} where A^0 is the CP-odd Higgs boson of ~ 130 GeV/c^2 [38].
- **Dark matter search:** Within the MSSM there are generally considered to be three main possible viable dark matter candidates responsible for the cold dark matter present in the Universe. One can use cosmological measurements of the dark matter density to constrain supersymmetry models, although the results depend heavily upon the model parameters. The recent data from the WMAP [39] satellite has allowed the matter density of the Universe to be measured with a higher precision and one can infer from these results the density of cold dark matter. The following cosmological constraints on the three MSSM dark matter candidates are: the lightest neutralino ($\tilde{\chi}_1^0$), with $m_{\tilde{\chi}_1^0} \sim 100$ GeV/c^2 [36]; sneutrino ($\tilde{\nu}_R$) with 10 GeV/c^2 $\leq m_{\tilde{\nu}_R} \leq 1$ TeV/c^2 [40]; and the gravitino ($\tilde{G}$) 1 GeV/c^2 $\leq m_{\tilde{G}}$ ≤ 700 GeV/c^2 [41].

2.2.5 Supersymmetry breaking

If SUSY were exact then the world in which humans inhabit would be one of mass degenerate fermions and bosons, existing en masse. Yet despite its aesthetic beauty, its theoretical allure and the plausible solutions it furnishes us with, there has, so far, been no experimental confirmation of SUSY. Thus, the notion that

SUSY is a broken symmetry is adduced and that sparticles (if indeed they do exist) must have masses significantly larger than their corresponding Standard Model counterparts. The issue of SUSY-breaking (which has, to date, had the greatest amount of effort expended on it in an attempt to decipher precisely what viable form this mechanism could take) must therefore be addressed. Numerous models for SUSY-breaking exist, for a review see [19, 42, 43].

There are only two known ways in which to break a symmetry: either through explicit breaking terms in the Lagrangian or by invoking the phenomena of SSB, that is, one that is induced by a non-SUSY vacuum state. This latter method occurs in a manner exactly analogous in the case of the chiral symmetry of QCD and is hypothesised to occur in the EW symmetry of the Standard Model through the Higgs mechanism. Of the two, there are several reasons to disfavour the former. There is no common consensus on how 'best' to spontaneously break SUSY. Whatever the SUSY-breaking mechanism maybe, it is desirable to be able to model it by a choice of parameters.

2.2.5.1 Unification: mSUGRA

One common viewpoint taken on how to construct a phenomenological viable model to break SUSY is that it should occur in a sector, usually referred to as the 'hidden sector'. This hidden sector is weakly coupled to the particles of the MSSM, the so-called 'visible sector'. Although there now exists a rich profusion of these 'hidden sector' subclass of models, there are three main competing ones. Consequently, the phenomenology of each model depends mainly upon the mechanism for communicating the SUSY-breaking rather than on the SUSY-breaking mechanism itself. Historically and the most prevalent in phenomenological stud-

ies of cMSSM[g], is called Minimal Supergravity (mSUGRA) [44–46] and [47–50]. Here, where SUSY is local rather than global, SUSY-breaking is mediated from the hidden sector to the visible sector through non-renormalisable gravity interactions, that is, by interactions of gravitational strength. In mSUGRA models, the 105 degrees of freedom of the MSSM are reduced now to just four real parameters and one sign:

$$m_0, m_{\frac{1}{2}}, A_0, \tan\beta \text{ and } \text{sign}(\mu),$$

where m_0 and $m_{\frac{1}{2}}$ are the universal SUSY-breaking scalar and gaugino mass terms respectively. A_0 is the common SUSY-breaking trilinear Yukawa coupling term. $\tan\beta$ is the ratio of the two Higgs doublets' vacuum expectation values at the weak scale and $\text{sign}(\mu)$ is the sign of the 'μ-term', as it is traditionally called, of the Higgsino mass parameter. It is, therefore, the supersymmetric analogue of the Standard Model's Higgs mass parameter μ. The first three, evaluated at the GUT scale, are responsible for determining the particle spectra from the renormalisation group equations (RGEs) running down to the weak scale. The last two control the degree of mixing in the EW sector, and as such, affect the masses and couplings of the Higgs bosons and other particles through the RGEs.

2.3 Extra Dimensions

The natural question arises as to why there are, or indeed, should be, three spatial dimensions and one temporal dimension, together constituting the familiar four

[g]c here is used to mean constrained: the MSSM SUSY breaking parameters are imposed as boundary conditions (i.e. are constrained) on the running of SUSY breaking masses and couplings at the GUT scale.

dimensional space-time. The class of models that address this question posit that the four dimensional space-time of 'our' universe is supplemented with one or more extra spatial dimensions. Inherent to all these models is the requirement that they do not flatly contradict the observed four space-time dimensions of the observable universe and so, therefore, a way to sequester them is needed. The most plausible way to achieve this is to assume that the reason why one has not observed them is that, in contrast to the familiar four space-times which we know are very large or infinite, these hypothetical extra spatial dimensions are made finite, that is they are 'compactified'[h].

Surprisingly, the ideas of extra dimensional models aren't new. On the contrary, they date back to the beginning of last century when these models were proposed as possible ways to unify the fundamental forces of nature ever since the seminal papers of the Swedish physicist Gunnar Nordstrom [53] (a contemporary of Albert Einstein) and of the Pole Theodor Kaluza and Swede Oskar Klein [54, 55]. In 1919 Kaluza attempted to unify general relativity (and so gravity) with EM by extending GR to five dimensional space-time. Then, in 1926 Klein suggested that the extra dimensions are compactified into an extremely small circle, thus, explaining why they appear hidden from our everyday observations. These original ideas were subsequently found to be untenable and as a result the idea of extra dimensions stagnated somewhat for the next four decades or so, and it wasn't until the 1970s and 1980s that interest was again turned to them. This occured with the advent of supergravity in the former and string theory in the latter, upon the theoretical physics community. In the, then, for-

[h]A feature common to most models is the necessity for the supplemented dimensions to be made small and finite or 'curled up'. This requirement of finiteness is called compactification. However, in other scenarios [51,52] the extra dimensions can be infinite and the extra dimensions are disposed of by other means. It is this compactness of the extra dimensions that ensures that our observable universe appears as 4D, i.e. why they have never been observed in nature.

mulation of supergravity, a relativistic, locally gauged QFT which was combined with GR, thus, seemingly provided a natural framework within which one could construct a unified theory of the four fundamental forces of nature. With the hope that QT and GR could be finally reconciled. Of its many incarnations in various dimensions the most tried and tested version was the one which resided in 11 dimensional space-time. In string theory (superstring theory to be more precise) extra dimensions are a necessity for the theory to work. Within the context of this theory, the ideas were revitalised ([56–60] and references therein).

Building on these ideas but motivated by different means, that was to try and solve the hierarchy problem in its larger and more pervasive context (that is as to why gravity is so weak at the EW scale, the so-called 'aesthetic' hierarchy problem), a novel set of extra dimensional models were proposed. The models posited that, with extra dimensions the fundamental Planck scale, i.e. the scale at which gravity becomes prominent, is not 10^{19} GeV but can be as low as the TeV scale, thus, allowing the trans-Planckian regime to be accessible to present and near future high-energy colliders. The very essence of the these models is that the apparent weakness of the gravitational force is due to the presence of, as yet, unseen extra spatial dimensions.

The first scenario is the so-called 'Large Extra Dimensions' (LED)[i] model [61] [62] of Arkani-Hamed, Dimopoulos, and Dvali (ADD) in 1998. The second, the so-called Randall-Sundrum (RS) model [63], postulates that the fundamental TeV Planck scale can be achieved with the addition of one or more small extra dimensions with a large degree of spatial curvature, so-called 'warped' extra dimensions. The final model, and which is the focus of this thesis, is the so-called

[i]The word *large* here is somewhat of a misnomer but in the context of HEP the size of the extra dimensions is extremely large relative to the fundamental distance/energy scales normally encountered in particle physics.

Universal Extra Dimensions (UED) model [64, 65]. The word *universal* here is used to emphasise the distinction that, in this model, all Standard Model fields are free to propagate through all of the extra dimensions rather than being confined to a brane[j] as in some cases such as those of the LED and RS models. So it is apparent that the nature of each model lies within the detail of how it achieves this TeV scale by exploiting the geometry of space. It is important to make a distinction at this point. Unlike in the cases of the LED and RS models, UED does not allow for a reformulation of the hierarchy problem and was constructed for other motivational purposes [66]. Because of the nature of the work presented in this thesis is concerned with the phenomenology of the UED model, this will be described in more detail in the next section.

Finally, to this end, if any one of these models, which there is a large proliferation of at the time of writing, is realised then one must entertain the reality that space-time is truly more than four dimensional. Clearly the discovery of them would certainly alter Man's view of the universe at the very large, intermediate and very minuscule scales of nature and would be, truly revolutionary.

[j]The recent extra dimensional models are based upon the so called 'Brane-world' picture in which they posit that the three observed spatial dimensions of 'our world' constitute a 3-brane (or wall), where the term brane is derived from the generalisation of a two dimensional membrane or hypersurface. This is then assumed to be embedded in a much larger extra dimension space-time or 'bulk' with the total number of dimensions given by:

$$D = (3 + 1 + \delta) \equiv (4 + \delta), \tag{2.5}$$

where 3 denotes the usual three spatial dimensions, 1 is the sole temporal dimension, together forming the familiar four dimensions of space-time, and δ labels the number of extra dimensions, the 'bulk'. It is important to stress here that is entirely conceivable that some models are constructed such that they are absent of branes. An example of the so-called 'brane-less' theories is UED which was already previously mentioned.

2.3.1 Universal Extra Dimensions (UED)

The model relevant to the work presented in this thesis, is the qualitatively distinct case when *all* Standard Model fields are allowed to propagate in the bulk, the aptly named Universal Extra Dimensions (UED) model. So it is, in a sense, perhaps the most democratic of the TeV scale extra dimensional models. It arose from the TeV^{-1} sized extra dimension models [56] and it is, in part, vaguely reminiscent of, and bears close resemblance to, the original extra dimensional models posited by Kaluza, Klein, Einstein *et al.* at the beginning of the last century. UED does not contain any branes and this is a vital ingredient to the phenomenology of the model.

It is remarkably simple in that it asserts, in its most basic incarnation, that there are one or more extra dimensions with a flat geometry and are compactified to a particular kind of orbifold. The size of the extra dimensions are $R \sim \text{TeV}^{-1}$ which are motivated theoretically and the compactification of them results in a tower of KK states for each and every Standard Model field, which makes for an interesting and distinct TeV scale phenomenological model. It is constructed in such a way as to evade current EW precision constraints. This stems from the conservation of a quantum number called KK-parity. KK-parity can be seen as a 4D remnant of momentum conservation in the extra dimension and is reminiscent of R-parity in SUSY models. Since KK parity is conserved to all orders, it implies that the KK excitations can no longer be produced as s-channel resonances but must be pair produced. Thus, there can be no tree-level diagrams involving UED particles and consequently their contributions to the EW observables can only arise from loops. The end result is that the ability to search and constrain parameter space from precision EW data is diminished and rather weak.

2.3.2 Minimal Universal Extra Dimensions

Concerning ourselves with the Minimal Universal Extra Dimensions (mUED) model, the name given to the 'simplest' and most popular UED extension to the Standard Model. It is defined in five space-time dimensions with the additional extra dimension of size R, compactified on a S^1/Z_2 orbifold[k]. More complicated UED frameworks exist however, defined in a higher dimensional space-time [67,68]. For example, the case of a six dimensional model constructed on the orbifold T^2/Z_2 has some particularly attractive features. There exits a number of reasons for entertaining the idea that the universe consists of one or more extra spatial dimensions and for the proliferation of new particle states that arise from them, as purported by the UED model. The first, and its original intention, was in providing an alternative dynamical mechanism for EWSB [66]. Other additional purposes of the model have since accumulated, which include anomaly cancellation in 6D with the requirement that there exist three generations of fermions [69], increasing the proton decay lifetime above the experimental constraints [65] and, thus, alleviating some of the problems which appear in the other extra dimensional scenarios such as RS and LED. Also there is the Lightest Kaluza-Klein Particle (LKP) constituting a viable DM candidate [70–72] which is stable by virtue of a conserved quantum number which is inherent to the model. For collider phenomenology [73,74] since the KK states within UED are generically light and, therefore, allowing for present and near future collider experiments to confirm or refute their presence. Lastly, a further motivation for UED is that the collider phenomenology it posits gives the popular delusion that it is actually low

[k] An orbifold is a manifold (M) with a discrete symmetry (G) that identifies different points in the manifold. The resulting quotient space $\Gamma \equiv M/G$ defines the orbifold. Here the quotient S^1/Z_2 is obtained from the one dimensional circle by identifying points of S^1 with each other. Z_2 is the symmetry group of parity transformations and is equivalent to the reflection symmetry $y \to -y$.

energy, N=1 SUSY. A method to unambiguously discriminate between SUSY and UED, or 'Bosonic SUSY' as it has also been dubbed, is therefore required.

mUED contains the minimal particle content, in exactly the same way as MSSM does in SUSY models. In concealing the extra dimensions, compactification causes the decomposition of the Standard Model fields (gauge and matter) into a tower of KK states. It replicates the particles for each and every particle of the Standard Model at each level of excitation, with all fields (zero modes and otherwise) traversing the bulk. The full Lagrangian density of the theory contains both bulk and boundary interactions, with the former including a one-to-one correspondence (up to normalisation factors) with the gauge and Yukawa couplings of the Standard Model and the Standard Model Higgs potential. The latter are localised at the orbifold fixed points and, thus, do not respect 5D Lorentz invariance. As with any higher dimensional extra dimension (KK) theory the UED model is assumed to be an effective low energy field theory valid up to some high, ultra-violet cutoff scale Λ, above which, some more fundamental theory is assumed to take over for the high energy completion of the theory. The cutoff scale is typically taken to be $\Lambda \sim 10R^{-1} - 20R^{-1}$. There are only three, free parameters in mUED: R, Λ and m_h, where m_h is the Standard Model Higgs boson mass and, thus, mUED is extremely predictive.

As previously mentioned, there occurs one complication to this otherwise relatively simple model and that is pertaining to the non-chiral structure of the fermionic sector in this 5D model. In the absence of orbifolding a 4D Standard Model chiral theory would not be obtained. To circumvent this problem the extra dimension is orbifolded on a S^1/Z_2 orbifold (see fig. 2.3(a)) and with the inclusion of suitable boundary conditions (BCs) results in the unwanted fermionic degrees of freedom (the vector-like fermions) being removed, culminating in a 5D

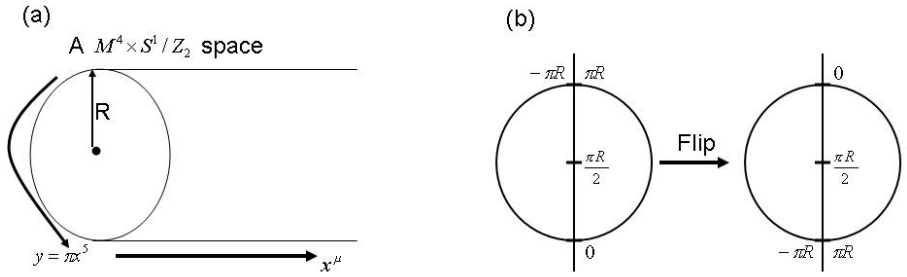

Figure 2.3: Shown in figure (a) is the full space-time structure of the mUED model, with the usual 4Ds (denoted by x^μ) together with the extra dimension (denoted by x^5) which is compactified on an S^1/Z_2 orbifold. Here, M^4 is the Minkowski (1+3)-space and S^1 is identified as a one dimensional circle with discrete symmetries. Whilst in figure (b) KK-parity can be seen as a flip of the line segment about its centre, $x^5 = \frac{\pi R}{2}$, combined with the Z_2 transformation, $x^5 \to -x^5$, which results in changing the sign for all odd fields.

chiral mUED which is what is desired. However, carrying out the orbifolding leads to ramifications regarding symmetry violations. It results in conservation of momentum along the extra dimension being broken and so, hence, the quantum number, KK number, no longer being conserved[1]. Interestingly though, a discrete subgroup of the KK number conservation remains unbroken, resulting in a discrete, conserved quantity called KK Parity ($P = (-1)^n$, where n denotes the nth KK-mode), see fig. 2.3(b). Phenomenologically it leads to several important consequences. One such consequence is that KK parity ensures that the odd-level KK excitations of the Standard Model fields must always be pair produced in collider experiments.

Lastly, and arguably the most interesting aspect of the model and the one that has, by far, triggered the greatest deal of attention, is its assertion that the lightest first level KK excitation, the so-called Lightest Kaluza-Klein Particle (LKP), can constitute a viable candidate for cold dark matter [70, 75, 76] and references

[1]It is conserved at tree-level but is violated at the one loop level.

therein. It posits that the KK partner of the hypercharge gauge boson, B_1, sometimes called the KK-photon (γ_1) [77] is the lightest of all the KK excitations. It is further assumed that it is effectively stable, EM and colour neutral and only interacts weakly with matter. Thus, providing a natural candidate for the cold dark matter of the universe, to date, the particle with one of the strongest arguments for physics beyond the Standard Model. If the LKP is produced in high-energy collisions it will escape detection without interacting with the detector material and so revealing a missing energy signature.

As previously mentioned, after compactification of the extra dimensions, each and every Standard Model field propagating in the bulk decomposes into an infinite[m] set of KK modes, which manifest itself as a tower of KK states. The mass of each n-th level KK mode is given by approximately:

$$m_n^2 = \frac{n^2}{R^2} + m_0^2, \tag{2.6}$$

where R is the radius of the compact extra dimension ($\sim$TeV^{-1}), m_0 is the mass of the ordinary Standard Model field, the zero mode mass, m_n is the mass of the n-th KK excitation of the corresponding Standard Model field and where n is the set of all positive integers and is called KK number. It labels the discrete KK levels of the tower and corresponds to quantised momentum in the extra dimensions and becomes a quantum number under a U(1) symmetry in the 4D description. From equation 2.6, if R^{-1} is considerably larger than the mass of the Standard Model fields then this results in a highly degenerate mass spectrum of KK states at each level, n. However, after inclusion of the effects of radiative corrections, of which there are two contributions, the picture conveyed here is

[m]Strictly speaking, the number of KK excitations, n, depends upon ΛR and so it is, therefore, evident that the tower is not infinite in extent.

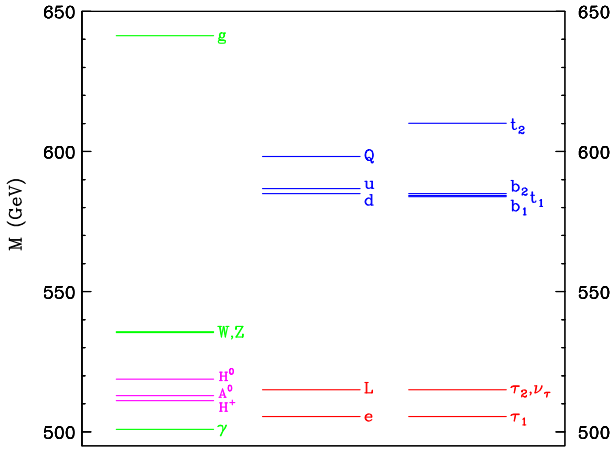

Figure 2.4: The spectrum of the first level Kaluza-Klein states, including the effects of radiative corrections and boundary terms. A compactification radius of $R^{-1} = 500$ GeV, m_h of 120 GeV and cutoff of $\Lambda = 20\,R^{-1}$ are assumed. From [77].

somewhat modified. The result finds typical mass corrections to the strongly interacting states of $\approx$ 20%, whilst a few percent or less for all other remaining first level KK states. Clearly the details of the mass spectrum are very important for understanding the phenomenology of the model and so, therefore, radiative corrections, which are the dominant effect in lifting the mass degeneracy at each level, play a crucial role in dictating which states can decay and which states remain stable. Fig. 2.4 shows a typical mass spectrum for the first level KK excitations of all the Standard Model fields after radiative corrections at the one-loop level, within the context of the mUED. The corresponding parameters for the mass spectrum are assumed to take the values of: $R^{-1} = 500$ GeV, $m_h = 120$ GeV and cutoff $\Lambda = 20\,R^{-1}$. This spectrum conveys the generic mass spectrum that exists at each KK level, n, within mUED.

Regarding possible observations of UED at present and future high-energy colliders, a typical UED event produces a final state that results in large electron or muon yields, a large jet multiplicity and a large missing energy component.

At the LHC the $\not{p}_T$+$(N \geq 2)$ jets signature has the largest cross section and the reach in this channel is $R^{-1} \leq 1.2$ TeV [78].

Existing experimental limits relevant to the phenomenology of UED arise from two primary sources. Firstly direct searches at collider experiments. There are also indirect ways in which UED can manifest itself as experimental signatures. This is via its effect on EW observables, e.g. the new non-zero, virtual KK states would tend to increase the value of the total Z^0 decay width (Γ_Z). Examples are the rare decay: $b \to s\gamma$ and the decay: $Z \to b\overline{b}$. Also the anomalous magnetic moment of the muon. The main, current constraints on the UED model together with the source of each one are summarised below.

- **Direct collider searches:** The most stringent of all the constraints, and which were performed at the Tevatron, are summarised in [79] and set a lower bound on the inverse size extra dimension radius of $R^{-1} \geq 270$ GeV.
- **ElectroWeak precision observables:** The strongest constraints arise from measurements at the Z pole. The current limits on the mass of the KK states depend upon the mass of the Standard Model Higgs boson. For a light Higgs mass, limits as strong as $m_{KK} \geq 700 - 800$ GeV can be obtained. For a heavy Higgs ($m_h \sim 300$ GeV), electroweak precision observables constrain the viable range of R^{-1} from below *and* from above: for instance, at 95% C.L., $400 \leq R^{-1}/\text{GeV} \leq 600$ for $m_h = 500$ GeV, and $300 \leq R^{-1}/\text{GeV} \leq 400$ for $m_h = 800$ GeV [80].
- **Rare decays:** The contribution of UED KK states to the inclusive $B \to X_s\gamma$ decay sets a lower bound on R^{-1} of $R^{-1} \geq 250$ GeV [81]. With the bound from the $Z^0 \to b\overline{b}$ branching ratio the bound becomes $R^{-1} \geq 300$ GeV [82, 83].
- **Dark matter search:** In providing a viable candidate for dark matter

allows one to set a lower bound on R^{-1} of $600 < R^{-1} < 1050$ GeV through direct dark matter searches [75].

2.4 Desperately Seeking SUSY or Bosonic SUSY? Unraveling the Truth

Either SUSY or UED, or indeed both, could be the Rosetta stone of the TeV physics scale. Of course, whilst such models are intellectually stimulating and, furthermore, aesthetically pleasing, to be physically meaningful one must either confirm or refute their claim by the virtue of empirical methods. As alluded to in the previous section, a problem that needs to be addressed is the notion that both models appear to have exceedingly similar collider signatures as professed by the authors of the seminal paper: "Bosonic Supersymmetry? Getting Fooled at the LHC" [84]. In the paper, the notion that UED could bear an uncanny resemblance to low energy, N=1 SUSY was brought to the attention of the particle physics community. The similarities of each model are illustrated in table 2.4.

The principal objective then is to, unambiguously, decipher which model is realised in nature. In forming an unassailable argument one must consider and exploit their differences. Furthermore, it is desirable to have an experimental verification which relies upon a fundamental distinction between the two models. Indeed, in principle, disentangling UED and SUSY appears to be highly non-trivial at hadron colliders [85]. To this end, there are three[n], potentially helpful,

[n] Actually, there is arguably a fourth distinguishing feature; the masses of the UED and SUSY particles. Unfortunately, however, this variable is model-dependent and so, consequently, cannot be used to, unambiguously, differentiate between the two models. Although, as a typically, rather degenerate mass spectrum would be indicative of UED whilst a split spectrum would be suggestive of SUSY, this could, therefore, be used in discriminating between the two models. However, this is not certain and it is, for this reason, that the masses have been included in table 2.4.

	SUSY	UED
Couplings compared with the SM particles	Identical	Identical
Parity conservation	Yes, R-parity. Implies particles are produced in pairs	Yes, KK-parity. Implies odd nth-KK particles produced in pairs
Lightest stable particle	Yes, the LSP. It manifests as $\not{p}_T$.	Yes, the LKP. It manifests as $\not{p}_T$.
Masses of the SM partners	∼TeV, although the mass spectrum depends upon the method of of SUSY breaking.	$\sqrt{(m_0^2 + \frac{n^2}{R^2})}$. $R^{-1} \sim 1$ TeV. Typically rather degenerate mass spectrum.
Generic hadron collider signature	leptons+jets+$\not{p}_T$	leptons+jets+$\not{p}_T$
Dark Matter: WIMP relic density	Acceptable	Acceptable

Table 2.4: The similarities between the SUSY and UED models.

discriminants.

- The first pertains to the Higgs sector. Although the two sectors share exactly the same gauge quantum numbers as each other, the UED Higgs sector carries a different KK parity assignment than the heavy Higgs bosons of MSSM (H^0, A^0, $H^\pm$), therefore, making them more similar to the SUSY Higgsinos, rather than the SUSY Higgs sector;
- SUSY asserts that there exists, for every Standard Model particle, one SUSY particle partner. In contrast, UED posits that there exists a tower of excited KK modes for every Standard Model particle;

- Lastly, the first level KK states in UED have the same spin quantum numbers as their Standard Model counterparts, whilst the SUSY partners differ by half a unit.

And whilst the first two discriminants could prove feasible, the latter appears most suitable in providing a conclusive answer as to whether or not it is SUSY or UED.

The work presented in this thesis attempts to evaluate the feasibility of differentiating between the two models by measuring the spins of the new particles at the LHC. The method presented depends upon the use of an angular variable, $\cos\theta^*_{ll}$, which is sensitive to the polar angle of the final state leptons of either model and which will be introduced in a later chapter, Chapter 6. As a final word, the nature and purpose of this work was never intended to either advocate nor to criticise the UED model as a viable alternative to SUSY, by far, the most studied TeV scale physics model. It was simply to test the feasibility of an angular variable in distinguishing between the models.

2.5 Spin

Our knowledge of the world of microscopic physics: the interactions between particles in nuclear and elementary particle physics, has been obtained by performing quantum scattering experiments. The systematic study of collision processes has elucidated information about the strong, weak and electromagnetic interactions and on this experimental evidence rests the modern picture of matter as being ultimately composed of quarks and leptons. An essential part of these observed phenomena is the spin angular momentum of particles, their quantum mechanical attribute and one that is essential to all elementary particles. The notion

that differential cross-sections depend not only upon the energies but also on the spins states of the participating particles plays an important part in the scattering processes and interactions. Furthermore, fundamental to these scattering experiments is the conservation of spin angular momentum at each interaction vertex. The spin dependence of reactions allows one to probe the underlying theory directly.

The typical way of measuring the spin of a decaying particle is to have an initially polarised colliding beam. Next is to reconstruct its rest frame from the decay products. Finally, the angular distribution in this rest frame contains the full spin information, independent of the boost. Furthermore, each possible spin candidate: 0, $\frac{1}{2}$, 1 and 2 each have different angular distributions about the beam axis, thus, aiding in identification of a particular particle type. Historically, spin has been vital and prevalent in many particle physics experiments aiding in confirming and verifying the Standard Model. Probably none more so than the forward-backward asymmetry ($\mathrm{A_{FB}}$).

The weak neutral current was a critical prediction of the EW part of the Standard Model. After its discovery in 1973 by the Gargamelle experiments at CERN, more and more precision was achieved in $\mathrm{e^+e^-}$ experiments at high energies which allowed one to perform tests of the theory at the level of quantum corrections. Accuracies to the few per-cent level, has been achieved. Two such experiments, which carried out such measurements, were the SLAC Linear Collider (SLC) in the U.S.A. and the LEP collider at CERN. One of the measured precision EW parameters is the forward-backward asymmetry ($\mathrm{A_{FB}}$) in the polar emission angle of final state fermions in the processes: $\mathrm{e^+e^-} \rightarrow f\overline{f}$ where f denotes a lepton (e, μ or τ) or quark. In the Standard Model these annihilations proceed via an intermediate γ at low energies or via a $\mathrm{Z^0}$ boson at and around

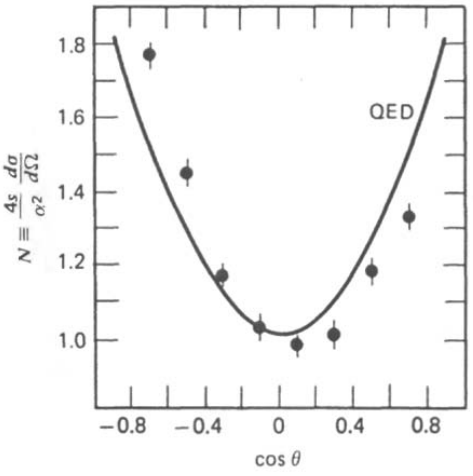

Figure 2.5: The $\cos\theta$ distribution for the process $e^+e^- \rightarrow \mu^+\mu^-$ carried out by the Positron Electron Tandem Ring Accelerator (PETRA) experiment at the Deutches Elektronen SYnchrotron (DESY) laboratory at a centre-of-mass energy ($\sqrt{s}$) of 34 GeV. The plot shows that it does not follow the $1 + \cos^2\theta$ QED prediction and is explained by γ/Z^0 interference. Figure taken from [4].

the Z^0 pole. However, there also exists the possibility for interference between the two matrix elements of the γ and Z^0 boson. Since Z^0 exchange involves both V and A couplings of the quarks and leptons to the Z^0 boson, parity-violating forward-backward asymmetries are expected to occur whereas γ exchange is a pure V coupling. The fact that this angular distribution does not follow exactly the QED prediction (see fig. 2.5) is, thus, explained by interference between Z^0 and γ contributions. This asymmetry can be expressed in terms of the EW parameters, e.g. it explicitly depends upon the EW mixing angle $\sin^2\theta^{\text{lept}}_{\text{eff}}$. Thus, by measuring and evaluating A_{FB} one is then able to scrutinize the validity of the EW part of the Standard Model.

During 1989 to 1995 LEP and its four experiments collected data from more than 15 million Z^0 decays. The differential cross-section for the process: $e^+e^- \rightarrow Z^0 \rightarrow f\overline{f}$, can be written in lowest order as:

$$\frac{d\sigma}{d\cos\theta}(e^+e^- \to f\overline{f}) = \sigma_{tot}\frac{3}{8}(1 + \frac{8}{3}A_{FB}\cos\theta + \cos^2\theta), \tag{2.7}$$

where θ is the scattering angle between the incoming electron and outgoing fermion, $\sigma_{\rm tot}$ is the total cross section for the reaction and $\rm A_{FB}$ is the forward-backward asymmetry. $\rm A_{FB}$ may be defined as:

$$A_{\rm FB} = \frac{N_F - N_B}{N_F + N_B}, \tag{2.8}$$

where $\rm N_F$ is the number scattered into the forward hemisphere $0 \leq \cos\theta \leq 1$ and $\rm N_B$ that into the backward hemisphere $-1 \leq \cos\theta \leq 0$. $\rm A_{FB}$ depends upon the $f\overline{f}$ pair in question and on the centre-of-mass energy. For example, if the fermions were quarks then the parameter, $\rm A_{FB}^{0,q}$, on the $\rm Z^0$ pole, is given by:

$$A_{\rm FB}^{0,q} = \frac{3}{4}A_{\rm e}A_{\rm q}, \tag{2.9}$$

where $\rm A_e$ and $\rm A_q$ are the coupling parameters and measure the strength of the parity violation at the $\rm Z^0ee$ and $\rm Z^0qq$ vertices respectively. The asymmetry, and subsequently the product $\rm A_eA_q$, is then extracted from the angular distribution (i.e. $\cos\theta$) of the final state fermion pairs. Fig. 2.6 shows measurements made by the Apparatus for LEP Physics (ALEPH) experiment of the differential cross-sections for $\rm e^+e^- \to l^+l^-$ for all lepton types combined at different centre-of-mass energies. In the plots the centre-of-mass energy is denoted as $\sqrt{s}$. The curves in fig. 2.6 are the Standard Model predictions and are seen to be in good agreement with the data points. Therefore, by measuring the $\cos\theta$ distribution confirms the following.

- There does indeed exist an asymmetry $\rm A_{FB}$ as predicted by the EW sector of the Standrd Model. For example, the measured size of the forward-

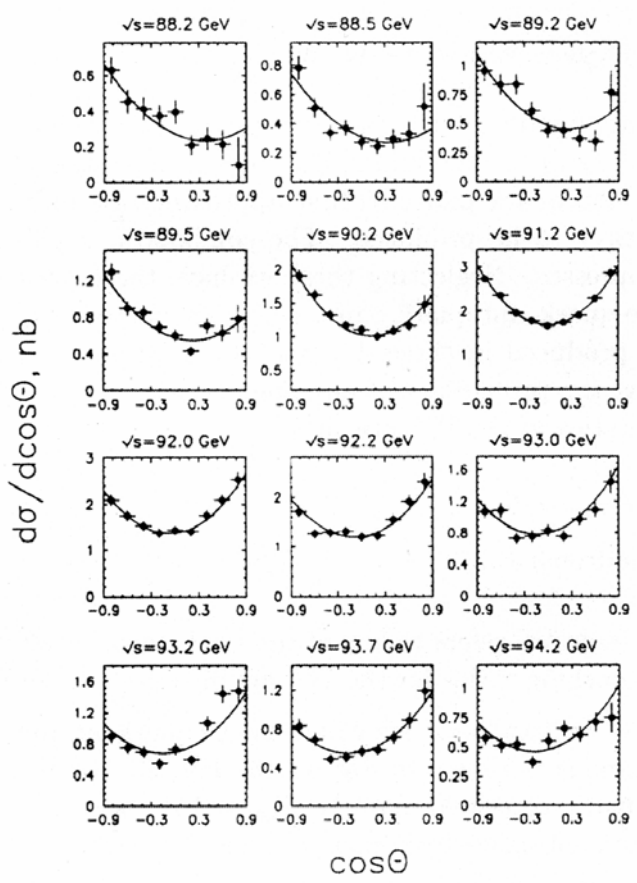

Figure 2.6: Differential cross-sections ($\frac{d\sigma}{d\cos\theta}$) for $e^+e^- \rightarrow l^+l^-$ events for all charged leptons combined for various centre-of-mass energies ($\sqrt{s}$). Figure taken from [86].

backward asymmetries for electrons and b-quarks are: $A_{FB}^{0,e} = 0.0145 \pm 0.0025$ and $A_{FB}^{0,b} = 0.0992 \pm 0.0016$ [87, 88] which when compared to the theoretically predicted values from the Standard Model ($A_{FB}^{0,e} = 0.01627 \pm 0.00023$ and $A_{FB}^{0,b} = 0.1033 \pm 0.0007$ [87, 88]), show excellent agreement;

- The spins of quarks and leptons are a $\frac{1}{2}$. If, for example, we assumed they were spin-0 particles then one would find that $\frac{d\sigma}{d\cos\theta} \propto \sin^2\theta$ rather than $1 + \cos^2\theta$. Moreover, applying simple spin conservation arguments also confirms that the mediators, Z^0 and γ, must both be spin-1 in nature;

- Elucidates the structure of the weak interaction and demonstrates the structure of the weak nuclear interaction: the V-A form of the weak Lagrangian, all predictions of the Standard Model.

So it is clearly apparent that this wealth of information and confirmation that the Standard Model is extremely precise was achieved through the utility of spin measurements.

Two further pertinent examples of the utility of spin measurements was the discovery and subsequent confirmation of the spin of quarks and gluons in high-energy e^+e^- scattering and two-jet events for the former and three-jet events in the latter. Towards the end of the 1960s from studies conducted at SLAC with its three large spectrometers looking at high-energy $e^{\pm}N$ scattering (where N denotes a nucleon) quarks were experimentally observed. Furthermore, from studying the angular distributions of the scattered electrons and matching them to theoretical angular distributions it was found that they were proportional to $1 + \cos^2\theta$ (see fig. 2.7(a)) indicating that quarks have half-integral spin. This would later be confirmed in deep inelastic scattering experiments studying the internal structure of the nucleon using electrons and neutrinos as the probes in the 1970s. A decade later, in the late 1970s, events such as $e^+e^- \rightarrow$ three jets were observed, thus, altering the back-to-back, in the centre-of-mass frame, two-jet events to ones in which there were three jets. These three-jet events are explained by a high energy gluon emitted at a wide angle by a quark or antiquark before fragmentation occurs. As shown in fig. 2.7(b), again although slightly more involved than the two-jet case because it is not obvious which of the jets is due to the gluon, comparing the measured angular distribution with those of theoretical predictions elucidates the spin nature of the gluons (spin-1).

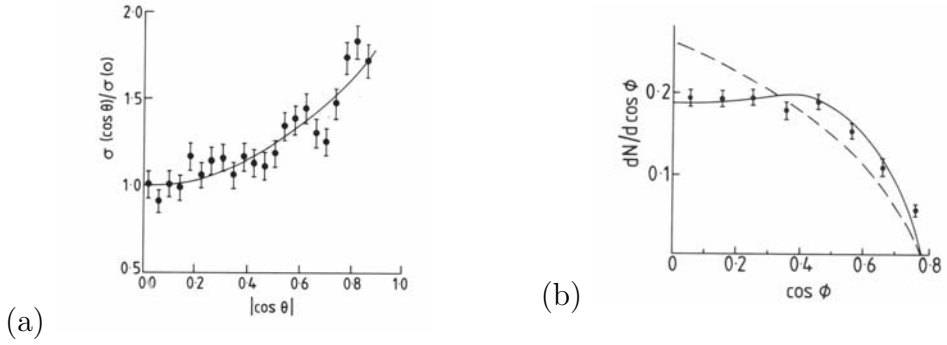

Figure 2.7: Shown in (a) is the angular distribution of two-jet events between the experimentally observed (in an e^+e^- colliding-beam experiment carried out by the CELLO collaboration at DESY) and the predicted behaviour of $1+\cos^2\theta$. Figure taken from [89]. Shown in (b) is the comparison of the angular distributions of three-jet events between events measured by the Two Arm Spectrometer SOlenoid (TASSO) collaboration at DESY and the two theoretically predicted angular distributions for spin-0 (dashed line) and spin-1 (solid line) gluons. The angle ϕ is defined as the angle between the direction of the highest-energy jet and the mutual line-of-flight of the two other jets in three-jet events. Figure taken from [90].

2.5.1 The spin-2 graviton

To complete the discussion on the various spin states of the particles within the Standard Model it is worth mentioning the sole, spin-2 candidate: the graviton. As already mentioned although not yet part of the Standard Model the graviton is reputed to be the conveyer of the gravitational force. Its unique spin-2 characteristic arises from an assortment of arguments based upon gravity within the context of relativistic QFT. In order to obtain a static, attractive force between particles with mass the spin of the mediator is required to be even, i.e. 0, 2 or greater than 2 thus, ruling out the possibility that it is a fermion. Now if it was a scalar particle the theory predicts that gravity would not affect the motion of an EM signal: there would be no bending of light waves by the sun, nor a time delay of a radar echo, both in contradiction with experimental observation.

So, therefore, a spin-0 graviton may be safely ruled out. Finally, if the spin was greater than 2 and was assumed to be massless leads to breaking of the gauge symmetry of the theory. Therefore, one is left to accept that the graviton must be spin-2 in nature. Note however, this is still to be verified experimentally. See for example [91] for a more detailed explanation.

2.5.2 The utility of spin measurements in elucidating the matter of whether it is SUSY or UED at the LHC

The attribute of spin can serve as a very general organizing principle for the many types of physics beyond the Standard Model that have been suggested, including extra dimensions, technicolour and M-theory [92]. The crux of the matter in this work is to see if one is able to differentiate between two theories SUSY and UED, by exploiting the difference in their spins through carrying out a spin measurement at the LHC.

The SUSY process under investigation in this work is that of direct dislepton production via the neutral-current Drell-Yan process: $q\overline{q} \rightarrow Z^0/\gamma^* \rightarrow \tilde{l^{\pm}}\tilde{l^{\mp}} \rightarrow \tilde{\chi}_1^0 l^{\pm}\tilde{\chi}_1^0 l^{\mp}$. So by definition, to identify signal processes each one must contain:

- Number of lightest supersymmetric particles = 2;
- Number of sleptons = 2;
- No other SUSY particles.

The UED equivalent process studied in this work is the decay process: $q\overline{q} \rightarrow Z^0/\gamma^* \rightarrow l_1^{\pm} l_1^{\mp} \rightarrow \gamma_1 l^{\pm} \gamma_1 l^{\mp}$. As the sleptons are scalars and the KK-leptons are fermionic in nature, this then allows the possibility to distinguish between them by studying the resulting, different angular distributions with which they are produced. The two different angular distributions, in the centre-of-mass frame of

reference, are:

$$\left(\frac{d\sigma}{d\cos\theta^*}\right)_{\text{SUSY}} \propto 1 - \cos^2\theta^*, \tag{2.10}$$

for the SUSY dislepton process and:

$$\left(\frac{d\sigma}{d\cos\theta^*}\right)_{\text{UED}} \propto 1 + \left(\frac{E_{l_1}^2 - M_{l_1}^2}{E_{l_1}^2 + M_{l_1}^2}\right)\cos^2\theta^*, \tag{2.11}$$

for the equivalent UED process. E_{l_1} and M_{l_1} are the total energy and mass of the KK-leptons respectively in the centre-of-mass frame and θ^* is the polar angle between the outgoing (KK- or s-) lepton and the incoming quark of one of the protons.

Fig. 2.8 shows the two production angular distributions of SUSY and UED, in addition to a pure phase space (PS) distribution, with which both models can be compared to. The phase space distribution does not correspond to any physical model but simply provides a convenient fiducial distribution with which to compare the other two models against. It has the angular distribution:

$$\left(\frac{d\sigma}{d\cos\theta^*}\right)_{\text{PS}} \propto \text{constant}. \tag{2.12}$$

It should be noted here that as the LHC point 5 for which fig. 2.8 was produced for, is very similar to the SU3 bulk point studied here (i.e. a very similar SUSY mass spectrum) one should therefore not expect the angular disributions for SUSY and UED to change very much. Therefore, one should believe that fig. 2.8 will be sufficient for this SU3 bulk point used in this work. It should also be noted here that the effect of energy, mass and momentum resolutions, the application of kinematic cuts, detector acceptances and initial state radiation will, inevitably,

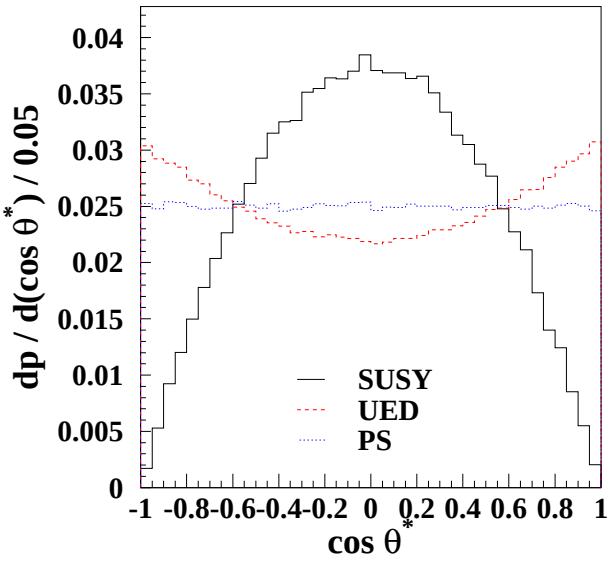

Figure 2.8: The production angular distribution, $\frac{dp}{d\cos\theta^*}$, for spin-0 sleptons (SUSY), spin-1/2 KK-leptons (UED) and pure phase space (PS). The mass spectrum for the UED distribution corresponds to that of the mSUGRA point S5. The five mSUGRA parameters that constitute the LHC point 5 in mSUGRA space take the following values: $m_0 = 100$ GeV/c^2, $m_{\frac{1}{2}} = 300$ GeV/c^2, $A_0 = 300$ GeV, $\tan\beta = 2.1$ and $\text{sign}(\mu) > 0$. Figure taken from [93].

distort the observed angular distributions somewhat from those shown in fig. 2.8. However, as the authors of [94] have professed, even after accounting for all these effects the angular distributions can still be clearly distinguishable. Thus, by directly measuring the spin of the final state leptons from the new, decayed heavy leptons allows the possibility to distinguish between the SUSY and UED models.

2.6 Summary

In this chapter the rudiments of extra dimensions and SUSY has been presented. The notion that a novel type of symmetry exists or that space-time consists of more than four dimensions has been argued as possible extensions to the Standard Model. Furthermore, the two models which will be used later in the analysis work, namely mSUGRA and mUED, have been introduced with all the salient points covered and the ameliorations each one offers to the shortfalls of the Standard Model, motivating them. Also discussed was the notion that both models appear to have similar collider signatures, requiring that one must be able to differentiate between the two at the LHC. This was to be done by exploiting the difference in their spins. It is this issue which has motivated this work. A brief overview of the utility of spin measurements in particle physics and their applicability to elucidate the nature of existing and future theories was also presented.

Finally, whilst such models are intellectually stimulating, there is currently no experimental confirmation that either are realised in nature. Furthermore SUSY or UED have the potential to be the Rosetta stone of the TeV energy scale, thus, allowing each model to be accessible at present and near future high-energy colliders. However if, and so some would argue, when, we do confirm either of these models by empirical methods, then it will surely be a remarkable vindication of theoretical pre-occupations dating back to last century. Specifically for the case of extra dimensions, the turn of last century, whilst for SUSY, the late 1960s and early 1970s.

Chapter 3

Experimental Overview: The LHC and ATLAS

3.1 Introduction

A PARTICLE collider accelerates and collides particles head-on to maximise the energy which then instantly becomes congealed into matter in the form of previously known and unknown particle entities. Furthermore, the exotic nature and rapid decay of some of these particles prevent one from ever observing them directly. Instead, their nature can only be inferred by measuring the mass, energy, momentum and electric charge of their decay products. To assist in their reconstruction and detection, an array of particle detectors are employed. The plentiful supply of new physics events, provided by the high luminosity[a] environment, leads one to studying the resulting statistical distributions in order to gain insight into nature's building blocks. The scale of each of these projects is vast in terms of human endeavour. The LHC and ATLAS are two

[a]The luminosity, $\mathcal{L}$, is defined as:

$$\mathcal{L} = \frac{N_1 N_2 N_B f_0}{4\pi\sigma_x\ \sigma_y}, \tag{3.1}$$

where N_1, N_2 are the number of particles per bunch of each colliding beam, N_B is the number of bunches per beam, f_0 is the beam revolution frequency, σ_x and σ_y are the transverse bunch widths at the interaction point and $4\pi\sigma_x\ \sigma_y$ is the effective cross-sectional area of the colliding beams.

such examples with each one, now, to be addressed in turn.

3.2 The Large Hadron Collider (LHC)

As along ago as December 1994 which saw the nineteen member states of Conseil Européen pour la Recherche Nucléaire (CERN)[b] unanimously approve a resolution for the construction of the 14 TeV LHC, which subsequently allowed the next chapter in high-energy collider physics to be written. After a prolonged delay of the project however, the commencement of its operation began in the Summer of 2008.

Straddling the Franco-Swiss border near to the city of Geneva and buried approximately 100 m beneath the surface, the vast LHC complex resides, which is schematically shown in fig. 3.1. It currently inhabits the existing tunnel that housed CERN's predecessor, LEP, which operated between 1989 and 2000. It will be the world's highest energy and most luminous particle accelerator. It will collide two counter-rotating proton beams, each with energy of 7 TeV, and so with a total centre of mass energy of 14 TeV, at four points around its 27 km circular tunnel. The tunnel is such that the LHC is not completely circular but imparts an eight fold symmetry. Each of the eight straight sections are approximately 538 m in length. Four of the octants are taken up by the array of detectors at the LHC. The remaining octants are where the machine utilities reside. The LHC will recreate the primordial conditions which prevailed in the Universe only 10^{-12} s after the Big Bang. In this way studying matter at the smallest of scales (subatomic particles) has become inextricably linked with research at the largest of scales (the cosmos). In doing so the LHC will allow the field of high-energy

[b]Now called the Organisation Européen pour la Recherche Nucléaire or, in English, the European Organisation for Nuclear Research.

physics (HEP) to traverse the TeV energy scale promising to take us to a deeper understanding of the Universe and could possibly open up new fields of scientific endeavour.

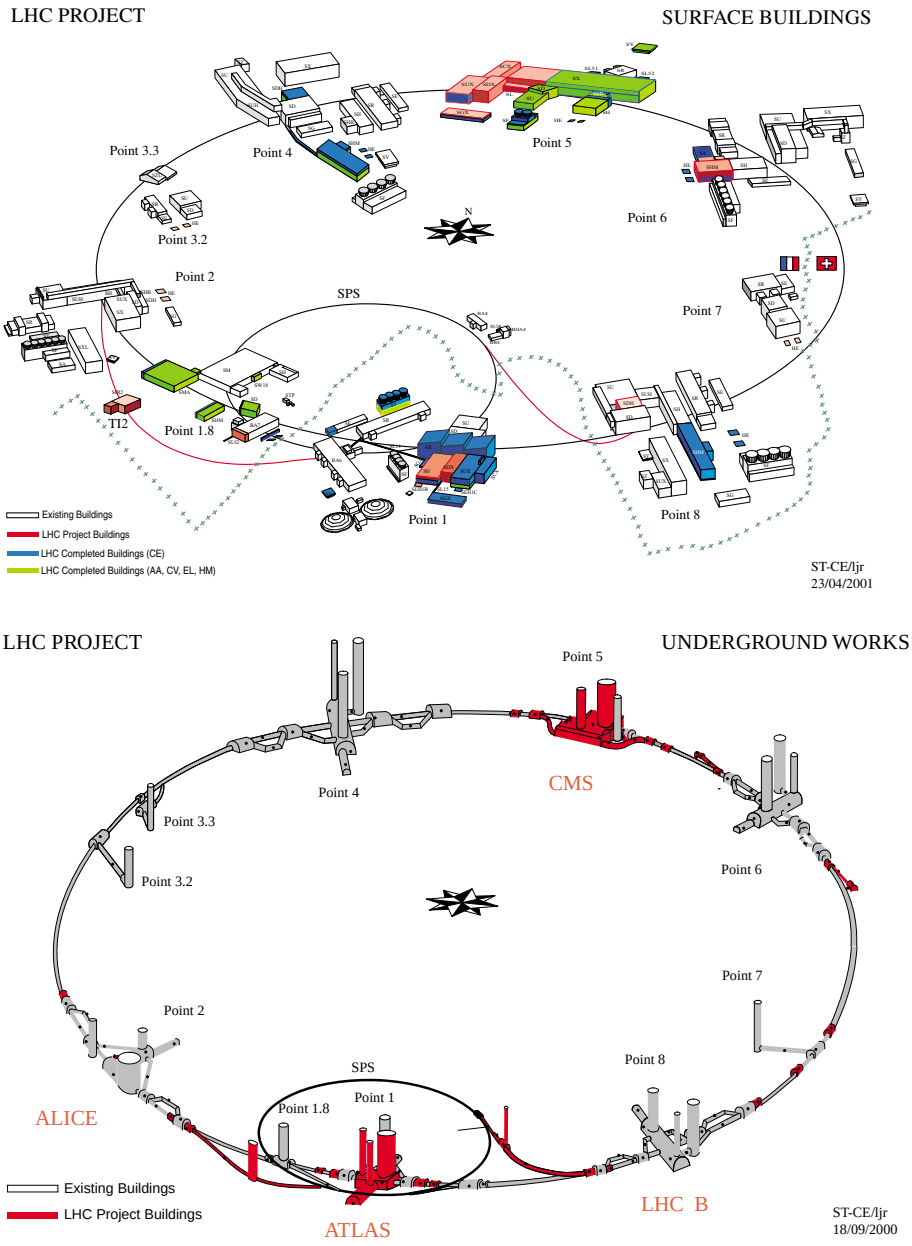

Figure 3.1: A schematic overview of the gargantuan LHC experimental complex which resides both, above (top) and beneath (bottom), ground level [13].

The LHC, in addition to extending the frontiers of particle physics with its unprecedented high energies, will also need to produce a very large number of collisions in order to produce enough of the rare, high energy processes. This necessitates extremely high luminosities in order to furnish one with a plentiful supply of interesting events in a reasonable time period.

Initially it was foreseen that there would be two phases of luminosity delivery for the LHC: initially, for the first three years of running, the luminosity would have been 0.1×10^{34} cm^{-2}s^{-1} (corresponding to 10 fb^{-1} per year), so-called 'low' luminosity. Thereafter, the machine would have reached the design luminosity of 1.0×10^{34} cm^{-2}s^{-1} so-called 'high' luminosity (corresponding to 100 fb^{-1} per year). This has now changed however. The latest schedule (at the time of writing) is that the LHC will enter a 2009 run phase during which it is envisioned that the first collisions will occur at a centre of mass energy of 10 TeV. Thereafter, it is foreseen that the 2010 run will start at the full 14 TeV design energy.

In order to achieve the desirable centre of mass energy in the 27 km tunnel foreseen at the LHC, necessitates a large bending field provided by magnetic fields of up to 8.3 T [95]. To reach these large magnetic fields requires the use of over 1200 superconducting dipole magnets[c] each providing a magnetic field of 8.3 T in strength, operating in superfluid helium at a temperature of 1.9 K. In fact, it is these electromagnets which are among the most challenging pieces of technology used in the LHC. Furthermore, due to space and cost limitations, the engineers used a novel design of a 'two-in-one' magnetic system: that of a single twin-aperture magnet with two superconducting coils incorporated into a single cryostat to accelerate the beams in opposite directions. Finally, this

[c]In contrast, in order to achieve the same centre of mass energy using the conventional, non-superconducting magnets would require a tunnel 120 km in circumference!

Beam energy	7.0 TeV
Time between collisions	24.95 ns
Luminosity	$1.0 \times 10^{34}\text{cm}^{-2}\text{s}^{-1}$
Circumference	26.659 km
Particles per bunch	10^{11}
Bunch length (σ_z)	7.5 cm
Bunch width (σ_x)	15.9 μm
Bunches per beam	2835
Beam current	0.53 A
Magnetic field strength	8.36 T
Dipole magnet temperature	1.9 K

Table 3.1: A summary of the main LHC machine parameters.

environment that the LHC admits, is one of high interaction rates, high radiation levels, large particle multiplicities, large beam currents (0.53A) and high energies. Such 'busy' environments therefore provide a number of challenges for each of the array of four experiments at the LHC have to contend with in making precision measurements. To fully exploit the LHC discovery potential, there are two general purpose experiments: ATLAS and CMS; and two specialised ones: LHC-b and ALICE, the latter being the sole, heavy-ion LHC experiment. One of the two general purpose experiments, ATLAS, is the one used in this work and to which we now turn to.

3.3 ATLAS

The ATLAS (a highly contrived yet humorous acronym which stands for **A** **L**arge **T**oroidal **L**HC **A**pparatu**S**) detector is a multi-purpose experiment designed to

fully exploit the discovery potential of the LHC and is shown in fig. 3.2.

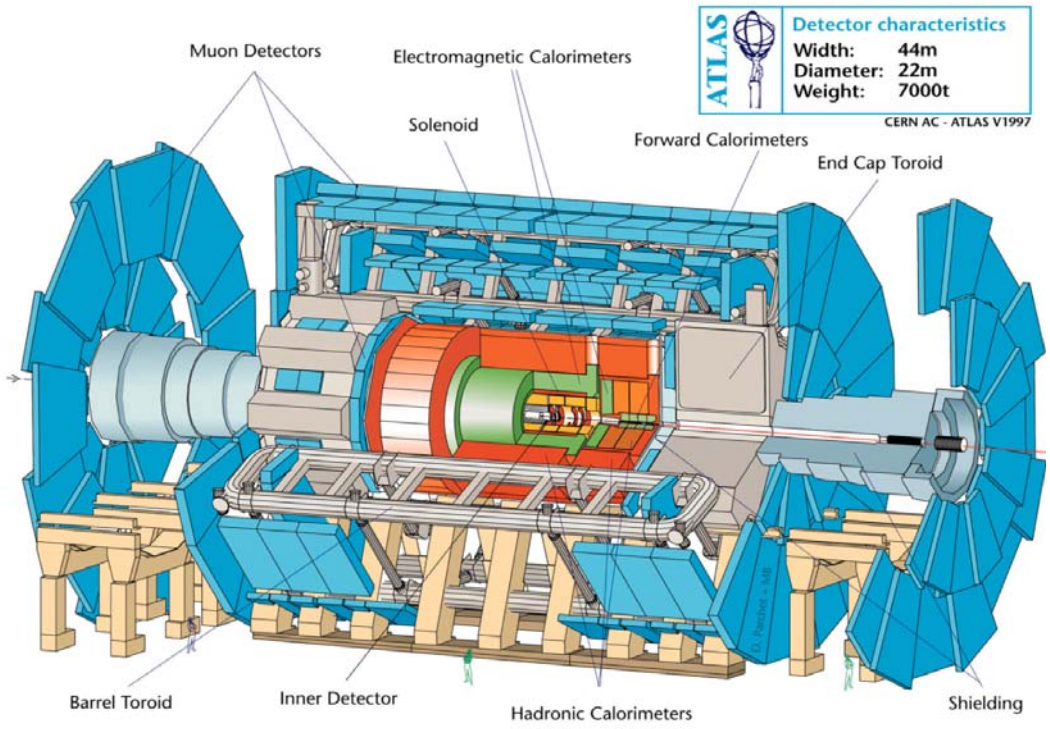

Figure 3.2: A schematic diagram of the ATLAS detector [96].

First devised as early as October 1992 when a letter of intent [97] was submitted to the LHC Committee (LHCC) by the ATLAS collaboration, it has now evolved into a vast collaboration that encompasses over 2700 physicists, 167 institutions and laboratories, in over thirty countries. In terms of dimensions it is the largest of the four detectors at the LHC. This is solely a result of the magnet system employed by ATLAS and, indeed the choice of which, subsequently drove the design of the remaining parts of the detector. The global layout of ATLAS, as with all detectors used in modern day collider experiments, is one which is a multi-layered assemblage of several sub-detectors, each complementing one another, customised to identify the different classes of particles. They

are, from the nominal interaction point (IP) outwards, the inner detector, the electromagnetic and hadronic calorimeters and the muon spectrometer. Each of these principal detector sub-systems will be discussed in turn, in the following subsections. However, beforehand, its primary objectives and familiarity with the detector geometry will be discussed.

3.3.1 Primary Objectives of ATLAS

The LHC offers a large range of physics to be studied and explored, amongst which is the quest for the nature of spontaneous symmetry breaking (SSB) in the ElectroWeak (EW) sector of the SM. In fact, this was the primary motivation proposed in justifying its construction. The primary objectives may be divided into the following four main categories.

- **EW/Higgs:** To search and verify the hypothesised particle thought to be responsible for EWSB of the SM and for endowing particles with mass through the so-called 'Higgs' mechanism, namely the Higgs boson. This forms the main purpose of the LHC and ATLAS. ATLAS can discover the Standard Model Higgs in the full mass range, 100 GeV - 1 TeV, with 30 fb^{-1} [96] of integrated luminosity. Furthermore, precision measurements of the EW sector will be carried out such as searches for anomalous couplings.
- **QCD sector:** ATLAS can make measurements on many QCD parameters such as the strong coupling constant (α_s) and parton density functions (PDFs). Furthermore, this sector is, in addition to it being useful for studying the strong interaction, vital because of the vast array of QCD processes that form important backgrounds to many new physics processes. Evidently therefore, these processes need to be well understood and a task which ATLAS needs to fulfil.

- **Top:** The LHC will produce copious amounts of top quarks and so consequently will be the world's first 'top factory'. ATLAS is expected to make precise measurements of the heaviest quark, such as its mass which is currently measured to be $m_t = 171.2 \pm 2.1$ GeV/c^2 [36] based upon data obtained at the Tevatron. ATLAS will hope to achieve a precision of $\pm 1-2$ GeV/c^2.
- **New Physics beyond the SM:** Finally, searches into the 'unknown' physics regime. This will include SUSY, extra dimenisons (small and large), compositeness of the fundamental fermions and new heavy gauge bosons, to name but a few. ATLAS should be sensitive to a wide variety of physics in the TeV scale range.

All these contributed to, and helped shape the development of, the detector in order to maximise on its all round performance as a general-purpose detector. Clearly the detector should be sensitive to both the wide variety of 'benchmark' SM physics signatures but also to the unexpected 'new' physics that may or may not lurk beyond the SM. To achieve the aforementioned goals, the basic design criteria of ATLAS envisioned are to have excellent EM and hadronic calorimetry for accurate e/γ and jet measurements respectively, over the energy range 3 GeV-1 TeV. Furthermore, it aims to provide excellent missing transverse momentum ($\not{p}_T$) measurements, the $\not{p}_T$ caused by neutrinos or other weakly-interacting particles (such as the Lightest Supersymmetic particle (LSP) in SUSY theories or the Lightest Kaluza-Klein Particle (LKP) in UED models). An inner detector provides efficient tracking of charged particles and accurate high-p_T measurements, which together aid in the identification of electrons, photons, τ-leptons and heavy flavour jets. Complementing the inner detector and calorimeters is the muon-spectrometer, which provides high precision muon measurements and triggering

which are foreseen to operate up to muon momenta scales of approximately 6 TeV. This entire assemblage must also provide a large angular acceptance around the interaction point.

Finally, the ability to trigger on, and make measurements on, particles of low-p_T in order to maintain sufficiently high kinematic efficiencies for most physics processes of interest at the LHC will be carried out.

3.3.2 Detector geometry

In common with all other detectors ATLAS is not completely hermetic, i.e. there is not a complete 4π solid angle coverage around the collision point. There are two coordinate systems adopted by ATLAS: the cylindrical and the Cartesian coordinate systems. The Cartesian (x, y, z) coordinate system is adopted by the ATLAS collaboration to describe positions within the detector. The origin, x=y=z=0, is at the nominal collision point in the geometrical centre of the detector and is referred to as the nominal interaction point (IP). It is defined such that the positive z-axis runs parallel to the beam pipe in the direction toward point 8 (corresponding to the cavern that houses the LHC-b detector), and the positive x-axis points from the nominal IP to the centre of the LHC ring. Finally, the positive y-axis points vertically upwards[d]. The rest frame of reference of the hard collision is generally boosted relative to the laboratory frame of reference along the beam direction. However, to a first approximation, the ATLAS detector is cylindrically symmetric about the mean beam line at the IP. Therefore, the geometry is most frequently described by employing the principal

[d]In fact this is only approximate due to a small and deliberate tilt introduced to the LHC (formally LEP) ring with respect to the horizontal. The reason for the deliberate tilt was to ensure that the LHC tunnel is embedded inside as much solid rock as possible. The result of the tilt means that there exists a small angle between the y-axis and the vertical of 0.704^0.

cylindrical coordinate system r, ϕ, z in which the z-axis and the origin coincide with those of the Cartesian coordinate system. r (or sometimes denoted as ρ) measures the transverse distance from the centre of the beam-pipe, z measures the longitudinal distance along it and the azimuthal angle, ϕ, measures the azimuth about that axis. ϕ is defined such that the planes $\phi = 0^o$ and $\phi = 90^o$ contain the x-axis and the y-axis respectively. Furthermore, where used, x and y measure the positions in the plane perpendicular to the beam pipe and are defined as $x = r\cos\phi$ and $y = r\sin\phi$ ($\phi = \tan^{-1}(p_y/p_x)$). Finally, the polar angle, θ ($\theta = \cos^{-1}(p_z/|\vec{p}|)$, where $|\vec{p}| = \sqrt{p_x^2 + p_y^2 + p_z^2}$), defined with respect to the beam pipe, with $\theta = 0$ corresponding to the positive z-axis. The ATLAS coordinate system is shown in fig. 3.3.

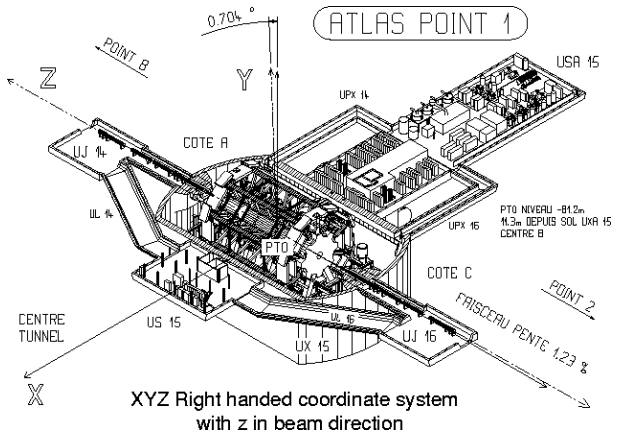

Figure 3.3: The common polar-coordinate system adopted by the ATLAS collaboration.

At hadron colliders the initial z-momentum of the colliding partons is unknown and so, consequently, the resulting longitudinal boost of the centre of mass of the system is also unknown. It is then desirable, in describing the physics of a system, to have a variable which is Lorentz invariant (under boosts). One such coordinate is ϕ. A further, useful one used for describing the longitudinal sepa-

ration of particles is the rapidity y ($y = \frac{1}{2}\ln[(E + p_z)/(E - p_z)]$). Differences in rapidity are Lorentz invariant. In the relativistic limit, however, a further variable, the pseudorapidity η ($\eta = -\ln[\tan(\theta/2)]$) can be applied which is defined in terms of the more directly observed polar angle, θ. Furthermore, cross-sections for inelastic p-p collisions are approximately uniformly distributed in η (from the symmetry under Lorentz boosts). So a more common convention adopted is to describe a particle's three-momentum in terms of three parameters: transverse momentum p_T ($p_T = \sqrt{(p_x)^2 + (p_y)^2}$), pseudorapidity ($\eta$) and azimuth ($\phi$). In addition to describing particle kinematics these angular coordinates η, ϕ are also used for defining the angular separation of the detector through the variable ΔR or R (where $R = \sqrt{\Delta\eta^2 + \Delta\phi^2}$). This is useful for describing the separation between two particles in η, ϕ space within the detector.

3.3.3 Magnet System

The ATLAS magnet system [95, 98], which is shown in fig. 3.4(a), uniquely features a hybrid system of four large superconducting magnets. Indeed, it is this uniqueness, together with the scale, that makes it one of the most challenging engineering feats of the ATLAS experiment. Both magnet systems employ NbTi superconducting material, and are cooled to 4.5 K. The system consists of a central solenoid which provides, on average, a 2 T axial field in the inner detector and a toroid (split into a barrel and two end-caps) providing the magnetic field in the muon-spectrometer. The latter aims to produce an average toroidal magnetic field (the magnetic field map of which is shown in fig. 3.4(b)) of approximately 0.5 T (barrel region) and 1 T (end-cap region) and is produced by a number of superconducting magnets arrayed radially about the beam axis with an eightfold symmetry. It is a light and open structure that provides a strong magnetic field

over a large volume of the muon-spectrometer.

The central solenoid resides outside the inner detector volume and is contained within the barrel cryostat of the electromagnetic calorimeter (ECAL) between the inner detector and ECAL. The hadronic calorimeter acting as the return yoke. The central solenoid is 2.5 m in diameter, 5.8 m in length and only 45 mm thick. It is purposely slender in order to minimise the amount of material introduced in front of the barrel calorimeters so as not to degrade the performance of the ECAL. At the same time however, it must still produce a sufficient magnetic field for the inner detector in order for it to be able to accurately measure momentum of charged particles up to 100 GeV/c.

The purpose of the toroid magnet system is to produce a magnetic field in the azimuthal direction over the region of the muon-spectrometer such that it is perpendicular to the hard (high-p_T) muon tracks. Each of the array of three magnets comprise of eight race-track shaped, air-core superconductor coils, with the barrel toroid being much larger in size to its two end-cap companions, 25.3 m long and an inner diameter of 10 m (in contrast, each of the smaller end-cap magnets have an axial length of 5 m and an inner diameter of 1.7 m). The end-cap coils are rotated in azimuth by an angle of 22.5^o with respect to the barrel toroid coils, for two reasons. Firstly, in order to provide a radial overlap and secondly, to optimise the bending power in the transition region ($1.4 < |\eta| < 1.6$). The peak magnetic fields are, for the central solenoid, 2.6 T and for the toroid, 3.9 T (barrel) and 4.1 T (end-caps).

3.3.4 Inner detector

The inner detector [99] lies at the heart of the ATLAS detector, enveloping a small part (7 m) of the 38 m berylium beam pipe and conforming to the geometry of

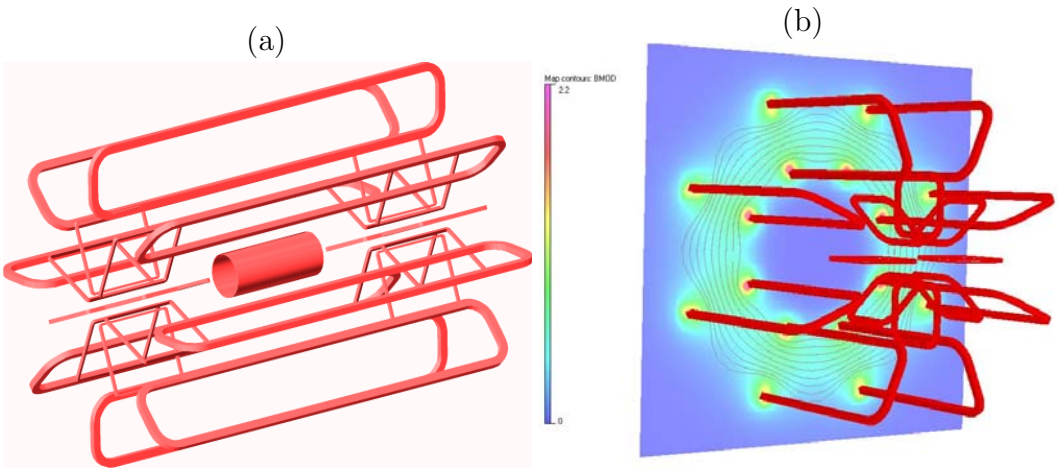

Figure 3.4: An illustration of the conceptual design of the ATLAS magnet system. (a) Shows the full magnet system: the central barrel solenoid and the barrel and two end-caps that comprise the large toroid system. (b) Contours of the toroidal magnetic field that serves the muon-spectrometer are shown in this *x-y projection. Figures taken from [99].*

the overall detector. It is cylindrical with a length of 7 m and radius 1.15 m. It is actually comprised of three independent detector sub-systems nested within each other, an overview of which is displayed in fig. 3.5. They are: the pixel detector, the Semi-Conductor Tracker (SCT) and furthest from the beam pipe, the Transition Radiation Tracker (TRT).

There exists a common (as with all detector systems) detector mechanical layout which is comprised of three distinct, mechanical parts: the barrel and two end-caps. For the central region, which corresponds to low values of $|\eta|$, there exists the barrel part whilst in the more forward regions (that is, those at higher $|\eta|$) there exist the two end-caps. The latter's purpose is to ensure that the detector covers the rest of the cylindrical cavity over the full expected η range, i.e. $|\eta| < 2.5$. The whole assembly is immersed in the solenoidal magnetic field of 2 T.

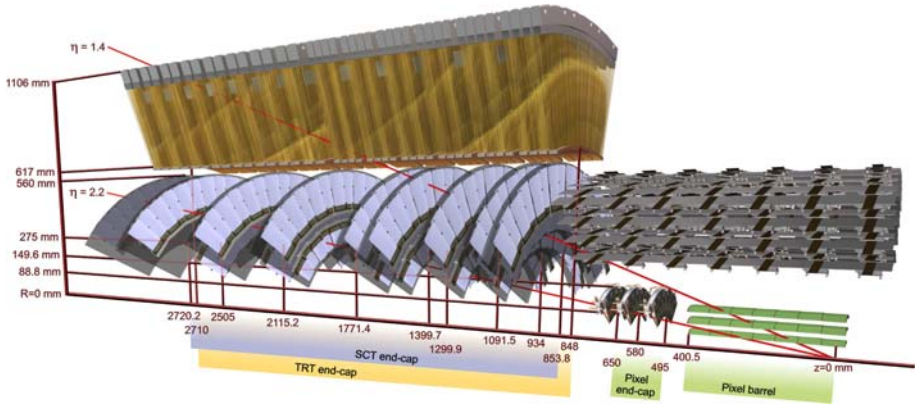

Figure 3.5: The ATLAS inner detector. Diagram displaying a three dimensional representation of the barrel and end-cap regions of the inner detector traversed by two charged tracks (at $\eta = 1.4$ and 2.2), each with p_T of 10 GeV. Shown are each of the three major detector subsystems: Pixel, SCT and TRT, together with the structural elements and their dimensions. Note, the TRT barrel part is not shown. Figure taken from [99].

The purpose of the inner detector is to make, on average, forty three measurements, seven of which are high-precision, of the position of reconstructed charged tracks whilst they traverse, and at the same time, are deflected by the solenoidal magnetic field in the region $|\eta| < 2.5$. A measurement of the charge is also carried out which facilitates with the identification of the particle. Furthermore, secondary-interaction vertices are identified using reconstructed tracks which are important for indicating the presence of short-lived particles such as τ-leptons and b-quarks. All this must be achieved in the hostile LHC environment, with a very high track multiplicity and radiation levels. Due to very large track density and to achieve momentum and vertex resolutions required by benchmark processes, high precision is needed. This requires the sub-detectors to have fine granularity which varies considerably with radius. The inner detector combines high-spatial resolution elements at inner radii which are needed close to the IP (both the pixel and SCT detector technologies offer this performance) with con-

tinuous tracking elements at outer radii (which is the reason for the straw tube technology employed by the TRT) where the track density is much less and so much less material per point is required.

One of the main restrictions in the design of any tracking detector is that it must contain the minimal amount of material possible. This arises largely from physics performance: in order to avoid degrading the inner detector and the calorimeters performance, although budgetary constraints also come into it. A further restriction arises from the readout requirements which requires that the readout electronics are placed within the tracking volume itself. This increases the total amount of material. The combination of silicon and straw tube technology ensures that the relative precision measurements are well matched so that none dominates the momentum resolution.

3.3.4.1 The Pixel Detector

The pixel detector [99] resides nearest to the beam pipe and is therefore located behind the least amount of dead material. Its purpose is to provide three precision (position) measurements of charged particle tracks as close to the IP as possible over the η range ($|\eta| < 2.5$). It plays the most important role in vertex resolutions allowing measurements of impact parameters and secondary vertices. Thus it has the ability to identify short-lived particles such as b-quarks and τ-leptons. The active material is in the form of depleted silicon crystals which are combined to form 1,744 16.4×60.8 mm arrays of detectors or 'pixel modules'. There are 47,232 pixels on each sensor but for reasons of space the total number of readout channels is reduced to 46,080 each of size 50×400 μm^2. In total there are over 80 million readout channels.

The pixel detectors are arranged into three concentric barrels at radii (ρ): 50.5

mm, 88.5 mm and 122.5 mm from the IP. In each end-cap region there are three discs or wheels that are located at z distances: 495 mm, 580 mm and 650 mm. The high radiation environment imposed by the LHC forces stringent conditions upon the design of the inner detector. It is, therefore, envisioned that during the approximately ten year lifetime of the detector the innermost layer is to be removed and replaced approximately every few years at design luminosity.

Each of the three layers of the barrel part is segmented in $\rho\phi - z$ with typically, three pixel layers crossed by each track on traversing the detector sub-system. The intrinsic resolutions are, for both the barrel and end-cap regions, 10 μm in $\rho\phi$ and 115 μm in z (ρ for end-caps). The more accurate measurements in $\rho\phi$ allow for more precise measurements of the sagittas of the particle tracks which are subsequently used in the calculation of a particles momentum. The basic working premise of the pixel detector is to detect electronic charge liberated by a charged particle traversing through the silicon and compare this electrical signal to a threshold to produce a binary output. This is also true for the Semiconductor Tracker, to which we now turn.

3.3.4.2 The Semiconductor Tracker (SCT)

At larger radii resides the Semi-Conductor Tracker (SCT) system [99] which employs the same underlying technology as the pixel detector and whose area is much greater (63 m^2 compared to 2 m^2 for the pixel detector). It is designed to provide eight precision measurements per track (four space-points[e]) in the intermediate range of the position of charged particles, as precisely as possible. Furthermore, high-p$_T$ resolution requires that the measurement of ϕ takes precedence over the

[e]A space-point is a 3D point reconstructed from local ρ and ϕ coordinates on the detector element and the η coordinate.

measurement in η, which strongly influenced its design.

The detector subsystem comprises of four concentric barrel layers in the central region covering $|\eta| < 1.4$ and eighteen end-cap discs (nine on each side) covering $1.4 < |\eta| < 2.5$. The barrel layers have radii of 299 mm, 371 mm, 443 mm and 514 mm from the IP, whilst the five discs in each end-cap lie between $|z|$ of 847.5 mm and 2727 mm. Each individual detector entity, referred to as a 'module', comprises of silicon wafers bonded back-to-back in pairs, aligned approximately along $\pm\eta$, giving an effective length of 123.2 mm. Furthermore, in the barrel and endcap regions the detector deliberately employs a small 40 mrad stereo angle between the front and back planes of the silicon wafers in order to obtain, in addition to the $\rho\phi$ coordinate which is deduced from the hit strip(s), a further, second coordinate of position in η (i.e. along z). The intrinsic resolutions are, for both the barrel and end-cap regions, 17 μm in $\rho\phi$ and 580 μm in z (ρ for end-caps). Again, as is the case for the pixel detector, charge collected in the silicon strip arrays is compared to a threshold value which forms the basis of the binary output from the SCT.

The SCT barrel modules formed the basis of an analysis carried out which is the subject of Section II, Chapter 4 of this thesis, where a more complete overview of the SCT and its modules will be given.

3.3.4.3 The Transition Radiation Tracker (TRT)

The final part of the inner detector system and the one furthest away from the IP is the TRT [99], a drift time detector and the most voluminous of the inner detector subsystems. It is a collection of hundreds of thousands (351,000 in total, with 52,544 in the barrel) of gaseous 'straw' tubes in seventy-three layers (barrel) and 160 (end-caps), interleaved with transition radiation (TR) material. Its purpose

is to provide continuous tracking to enhance pattern recognition and momentum resolution over $|\eta| < 2.0$ and in a region where the track density will be relatively low. Furthermore, the position resolution (for which it has an intrinsic spatial resolution of 130 μm in $\rho\phi$) will be inferior to that of the semiconductor detectors but the cost per point and power dissipation will be greatly reduced. Although the resolution is 130 μm per straw the TRT's overall momentum measurement, when averaged over all straw measurements, is equivalent to a single measurement of resolution 50 μm at the LHC design luminosity.

Each tube is aligned parallel to the beam pipe in the barrel and radially in the end-caps, which has a diameter of 4 mm and a maximum length of 144 cm. It has a central sense, gold plated, tungsten-rhenium (W-Re, in the ratio 99.95% to 0.05%) wire, 31 μm in diameter, at the centre which acts as the anode and from which the signal is read out. The corresponding high-voltage cathode is the Aluminium coated, inside surface of each straw which is surrounded by a gas mixture of $Xe/CO_2/O_2$. A potential difference of 1.5 kV is maintained between the wire and straw inside surface and is used to collect the charge liberated by the passage of charged particles through the gas mixture.

Each channel has two independent thresholds, allowing it to discriminate between hits due to ionisation (lower threshold) and hits due to the transition radiation (high threshold). For the former, with a threshold of typically 250 eV, thirty six position measurements on average, are expected to be made for particles with $p_T \geq 0.5$ GeV/c. In the latter a threshold of approximately 5 keV is designed to detect the transition radiation photons. This arises due to the straws being deliberately embedded in a medium whose permittivity varies abruptly, subsequently causing any ultra-relativistic charged particles, on traversing the boundaries, to emit soft radiation along the track direction. These photons of transition radia-

tion give the detector subsystem its name. Furthermore, the resulting energy of the emitted radiation (which is in the X-ray region) is proportional to the Lorentz factor γ ($E = \gamma mc^2$, where $\gamma = 1/\sqrt{1 - v^2/c^2}$) rather than the particle's velocity (the discharges caused by the TR photons, although of smaller probability, are detected by the surrounding materials which are specifically designed to contain many such transitions. The material employed is polypropylene/polyethylene fibres (barrel) and polypropylene foils (end-caps)).

The lighter the particle (of a given momentum), the more the TR produced, thus, allowing identification of particles. Charged hadrons, for example, produce low threshold hits in the drift tubes whilst electrons produce, in addition to the low threshold ionisation hits, transition radiation X-rays, so giving high threshold hits. This allows for discriminating between electrons and pions and facilitates in electron identification and jet rejection. It is evident then that TR hits measured together with momentum measurements permit the inner detector to, by itself, perform particle identification on the basis of their mass.

3.3.5 Calorimetry

The purpose of calorimetry devices is to provide accurate measurements of the energy of incident neutral and charged particles traversing a material, through absorption, where a fraction of the energy deposited is converted into a measurable quantity (e.g. charge or light). The particle types whose energy are measured include electrons, positrons, photons and, although they are not strictly particles, jets as well. Furthermore, its other important objective is to provide the major contribution (in addition to the muon-spectrometer) to the missing p_T measurement.

The ATLAS calorimeter [99], shown in fig. 3.6, employs only a sampling type

calorimeter, which is to say that the passive medium are layers of dense material interspersed with active layers. The active layers (the cryogenic noble liquid Argon for the electromagnetic calorimeter and scintillator tiles for parts of the hadronic calorimeter) allow ionisation to occur and a signal to be read out. Only a fraction of the total energy deposited is sampled and the resulting intrinsic resolution is determined by sampling fluctuations, leading to fractional resolution which scales as $1/\sqrt{E}$. Thus, the intrinsic resolution improves with energy, making this type of detector system well suited to the high-energy environment expected at the LHC.

The ATLAS calorimetry is in common with most general-purpose high-energy collider detector experiments, an assemblage of three subsystems: the EM calorimeter (ECAL), the hadronic calorimeter (HCAL) and forward calorimeter (FCAL). When combined, the detector systems provides acceptance covering the range of $|\eta| < 4.9$. Furthermore, these subsystems are additionally segmented into barrel and end-cap regions, with a crack[f] occurring at approximately $1.3 < |\eta| < 1.5$. All the inner detector subsystems operate on the principle that the longitudinal and lateral shower profiles are different for the nature of the shower, that is, whether it is electromagnetic or hadronic in origin. This difference in shower profiles allows for enhanced particle identification.

3.3.5.1 The Electromagnetic Calorimeter

The electromagnetic calorimeter (ECAL) is a high granularity, lead-liquid Argon (LAr) sampling calorimeter which is intrinsically radiation-resistant and consists

[f]Strictly speaking it is a poorly instrumented area which is a gap that provides space for cables and services for the innermost detector elements. It is, therefore, not used for precision physics measurements. However, a scintillator slab is inserted in to this region which aims to complement an additional active layer to assist in physics measurements.

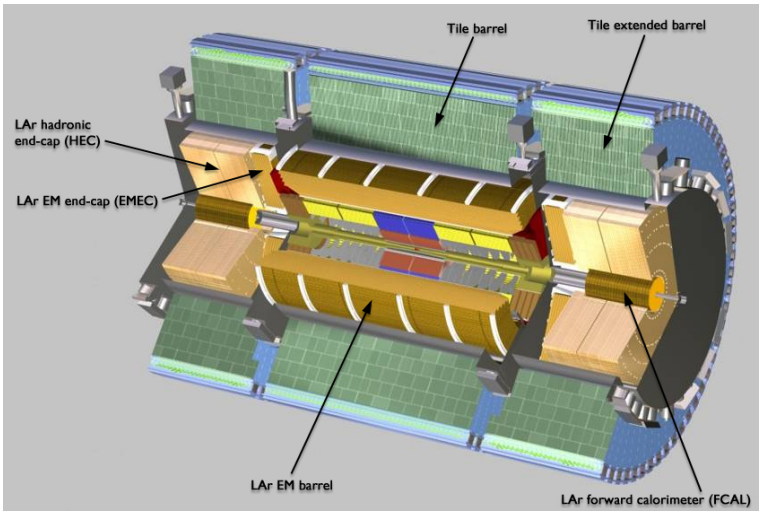

Figure 3.6: The calorimetry system employed by ATLAS [99].

of a barrel and two end-caps [99] covering the region $|\eta| < 2.5$. It is constructed from lead absorber plates and kapton electrodes immersed in LAr which are arranged in the unique accordion geometry, to provide continuous azimuth coverage and minimal density variations. In addition to the aforementioned crack region at approximately $1.3 < |\eta| < 1.5$, there is also a further, smaller one at $\eta = 0$. The ECAL is preceded radially by a 1 cm thick, active layer known as the presampler, located to the rear of the cryostat inner wall. This is designed to correct for energy loss by particles in traversing the intervening material between the IP and the calorimeter (the inner detector, solenoidal coil and cryostat) and assists in measuring the direction of the resulting EM showers.

The region, $|\eta| < 2.5$, is segmented into three longitudinal segments of high granularity samplings, in order to provide good particle identification through varying shower shapes and shower directions. Overall the ECAL has a total thickness of 24 radiation lengths (X_0) in the barrel and 26 X_0 in the end-caps. These are foreseen to be sufficient in thickness in order to prevent high levels of

leakage from high energy showers ($E \geq 500$ GeV) contributing to the error on the missing E_T measurement. The design resolution, for electrons, is $\sigma(E)/E = 10\%/\sqrt{E(\text{GeV})} \bigoplus 0.7\%$ [99].

3.3.5.2 The Hadronic Calorimeter

The hadronic calorimeter (HCAL) [99] utilises a variety of different technologies to cover a large angular range that are suited to the varying requirements brought about by the desired physics processes and large radiation environment. The hadronic calorimetry, which employs a coarser granularity than that of ECAL, covers the pseudorapidity range $|\eta| < 4.9$. The barrel and extended barrel tile calorimeter regions cover $|\eta| < 1.7$ and in the end-cap regions, $1.5 < |\eta| < 3.2$, where LAr, identical to that in the ECAL, is used.

Complementing this and extending the angular region covered by the detector to the very forward region, $3.2 < |\eta| < 4.9$, are the forward calorimeters (FCAL). This LAr assemblage is a particularly challenging subsystem owing to the extreme levels of radiation it has to withstand. It is integrated into the end-cap cryostat and is split into three high density mediums. The first, LAr-Cu, and last two, LAr-Tungsten, each of which consists of concentric rods (cathodes) and tubes (anodes) embedded in a matrix and with LAr, acting as their active medium. It has to be able to contain within its volume, the full extent of the hadronic showers caused by the particles that have traversed the ECAL (excluding the highly penetrating muons which are unique). Furthermore, it is also designed to keep punch-through to the muon-system to a minimum. For these reasons the HCAL is approximately 11 nuclear interaction lengths (λ_0) in thickness.

The hadronic barrel calorimeter is based upon the novel sampling technology of having alternating 14 mm thick Fe absorption plates and 3 mm thick plas-

tic scintillator tiles, from which the barrel detector subsystem derives its name. The tiles are orientated perpendicular to the beam pipe which provides good sampling homogeneity. As previously mentioned, the structural material of the hadronic calorimeter and Fe absorber, together, form the return yoke for the central solenoidal magnet.

Again, as with the ECAL barrel, it is segmented into three layers, with the corresponding granularity being, in $\Delta\eta \times \Delta\phi$, 0.1×0.1 in the first two layers and 0.2×0.1 in the last layer. In contrast, the hadronic end-cap sampling calorimeter is a Cu-LAr composition, exhibiting a parallel-plate geometry and having a granularity of 0.1×0.1 in $\Delta\eta \times \Delta\phi$ in the region $1.5 < |\eta| < 2.5$ and 0.2×0.2 for $2.5 < |\eta| < 3.2$. The expected design energy resolution is, for the HCAL, $\sigma(E)/E = 50\%/\sqrt{E(\mathrm{GeV})} \bigoplus 3.0\%$, and for the FCAL, $\sigma(E)/E = 100\%/\sqrt{E(\mathrm{GeV})} \bigoplus 10\%$, [99].

3.3.6 Muon Spectrometer

Muons, being leptons, have no strong interactions and have a relatively large mass which, therefore, results in a highly penetrating particle. This permits them to transverse matter (the inner detector and calorimetry) relatively unimpeded with minimal energy loss, primarily through ionisation of the medium. Any charged particle that makes it through that amount of material (i.e. the inner detector and calorimetry) is identified as a muon. High momentum final state muons are amongst the most promising and reliable signatures of the rich physics processes expected at the LHC. Most of these processes, e.g. Higgs boson, SUSY particles, new heavy gauge bosons (W′ and Z′) and CP violation in the B sector, imply the presence of muons in final states. It is, therefore, essential to fully exploit this factor by employing a device which can make high resolution muon mea-

surements enhancing the discovery potential of the experiment. This, therefore, necessitates a dedicated detector system to assist in identification and, furthermore, momentum measurement of them. This role is suitably taken up in ATLAS by the muon-spectrometer [99].

Its fundamental working premise is to detect muons deflected by the large toroidal magnetic field produced by the array of three (one barrel and two end-caps) superconducting air-core toroid magnets. Each superconducting magnet is instrumented with an array of several different detector technologies which facilitate high-precision momentum measurements and triggering over a wide fiducial range in p_T, η and ϕ. Furthermore, for the desired momentum resolution at high momenta ($p_T \geq$ 300 GeV/c), a large magnetic field is required to be maintained over a large volume. This necessitates a large scale detector and, thus, explaining the grand scale of the muon-spectrometer, with a span of 26 m in length and 20 m in diameter.

The deflection of particles by the magnetic field can be subdivided into three regions. The first, over $|\eta| < 1.4$, is where the magnetic field is provided by the large barrel toroid. The second, which covers $1.6 < |\eta| < 2.7$, the two end-cap toroids fill this vacancy. The third and final region, the so-called transition region, $1.4 < |\eta| < 1.6$, a combination of them both assists in deflecting the muons.

The overall layout of the detector system (schematically shown in fig. 3.7(a) and (b)) utilises four chambers or 'station' technologies, two of which provide good hermeticity, high precision measurements of muon tracks: the Monitored Drift Tube (MDT) [100] chambers and Cathode Strip Chambers (CSC) [101] (see fig. 3.7(c)). They are positioned such that particles emanating from the IP traverse three layers or stations of the chambers, thus, in the process, providing three position measurements and direction over the full $|\eta|$ range. The MDT,

which consists of three layers in each of the barrel and end-cap regions, covers the angular range $|\eta| < 2.0$. However, in the inner most layer of the inner chambers of the end-caps, a second precision chamber resides, the higher granularity CSC. This is used to assist the MDT in the high $|\eta|$ ($2.0 < |\eta| < 2.7$) region to sustain the demanding and high rate of particle fluxes expected here.

In addition to the precision chambers, a unique feature of the muon-spectrometer is that it is the only subdetector system that ATLAS deploys which incorporates its dedicated triggering hardware. These independent, fast trigger chamber systems, the Resistive Plate Chambers (RPC) [102–104] (used in the barrel region), and Thin Gap Chambers (TGC) [105,106] (used in the end-caps) are intended to complement the high-precision chambers (see fig. 3.7(c)). These trigger chambers are actually there to serve a threefold purpose: to provide bunch-crossing identification which the precision chambers, by themselves, are unable to do; enforce well defined p_T thresholds for triggering; and finally assist with the track fitting and pattern recognition by making a measurement of a second coordinate in a direction orthogonal to that provided by the precision-tracking chambers (typically ϕ).

Tabulated data, which gives an overview of the muon chamber instrumentation, is given in table 3.2 and schematically shown in fig. 3.7(c). Muon p_T can be measured down to a few (~ 4) GeV by utilising the muon-spectrometer alone. When used in this way it is referred to as a 'standalone' measurement. Whereas, when the muon-spectrometer is used in conjunction with the inner detector to make a measurement, this measurement is referred to as one which is 'combined' in nature.

The typical momentum resolutions for muons over the range $|\eta| < 2.7$ (note that there is no coverage at $\eta = 0$ owing to an opening which serves as a pas-

	CSC	MDT	RPC	TGC
Number of chambers	32	1108	544	3588
Number of readouts	31000	339000	359000	318000
Chamber resolution (z/R)	40μm (R)	35μm (z)	10mm (z)	3-12mm (R)
(ϕ)	5mm	-	10mm	8mm

Table 3.2: A summary of some of the parameters of the four subsystems that constitute the muon-spectrometer. Shown are the number of chambers, number of readout channels and their intrinsic resolutions [99].

sage for cables and services which furnish the inner detector, central solenoid and calorimeters), with typical momenta of 20 GeV (1 TeV), is expected to be approximately $\frac{\sigma p_T}{p_T}$ of 2% (10%) [99].

3.3.7 Trigger and Data Acquisition

The formidable LHC luminosity and resulting interaction rates (the total proton-proton inelastic cross-section at the LHC is approximately 80 mb resulting in an interaction rate of $\sim 10^9$ Hz) makes the task for ATLAS triggering and data acquisition (collectively known as TDAQ) extremely challenging. The TDAQ system [99] has the task of selecting interesting events (which have very low cross-sections) from the mass of 'uninteresting', predominantly soft collisions at the LHC. It must reduce the event rate from the initial bunch crossing rate of 40 MHz down to a level suitable for permanent storage, envisioned to be 200 Hz. Simultaneously the TDAQ system must still maintain a high efficiency for retaining the interesting, but rare, new physics processes that ATLAS endeavours to search for. However, even at this rate, where the final event size is expected to be approximately 1.5 MB, ATLAS will still be expected to store approximately 1 petabyte (1 PB) of data annually.

To facilitate with the task of data reduction, ATLAS employs a three-level trigger system (schematically shown in fig. 3.8): the first level trigger (Lvl 1), a hardware based trigger with a latency of approximately 2 μs; the second level trigger (Lvl 2), a purely software based system with an average processing time per event of approximately 1-10 ms; and finally the so-called Event Filter (EF), with an average processing time of the order of 1 s. The latter is also purely software based and, together with Lvl 2, form what is collectively known as the High Level Trigger (HLT) system. Each level refines the decision made at the preceding level and applying additional selection criteria in the process.

Finally, at the EF, the whole event is either accepted or discarded which is also true at Lvl 1 and Lvl 2; depending upon if it satisfies one of the physics signatures given in a trigger menu.

3.3.8 Summary

An overview of the LHC accelerator, ATLAS detector and the physics goals have been given. Furthermore, both have been constructed by the vast numbers of technicians, engineers and physicists and the target for a turn-on in the Summer of 2008 has been met. After much deliberation, research and development and the enormous investment and effort that has been expended in building the LHC and the array of four detectors, it will finally (very soon) lead us into the realm of the TeV energy scale. It will hopefully furnish us with unmatched opportunities for the discovery of new physics beyond the SM. Finally, to this end, ATLAS, as previously described, promises to exploit this potential to the full.

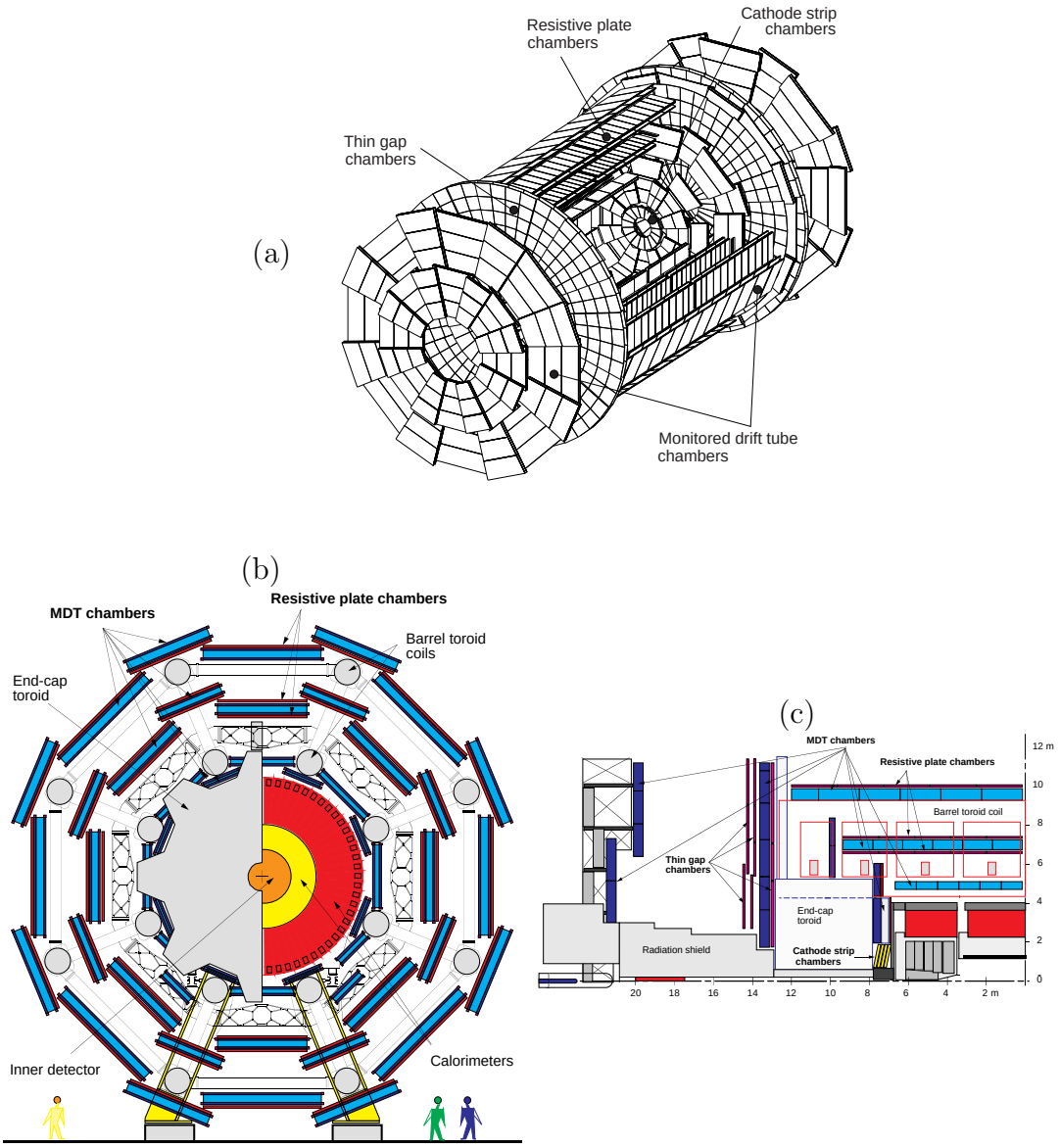

Figure 3.7: The conceptual design layout of the muon-spectrometer. In (a) a three dimensional view and (b) end view. (c) A side view of one quadrant of the muon-spectrometer system, displaying the different chamber technologies employed [99] and [96].

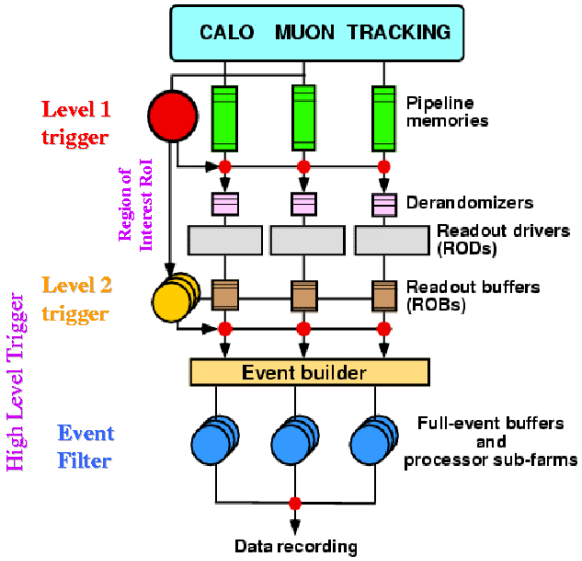

Figure 3.8: A schematic diagram showing the three levels of the ATLAS TDAQ system [96].

Part II

Noise studies of the SCT barrel modules

Chapter 4

Noise studies in the SCT barrel modules of the ATLAS detector

4.1 Introduction

THE ATLAS semiconductor Tracker (SCT) subsystem will soon be exposed to a severe environment; one of extremely high radiation levels, large particle multiplicities and high interaction rates.

Its importance in physics studies, by providing track reconstruction, particle charge identification and vertex tagging must be maintained, in a very challenging environment, over a period of many years. It must meet the resolution requirements set by the benchmark physics processes we intend to study. This hostile environment will be detrimental to the precision tracking carried out by the SCT. The important parameters which the precise tracking depends upon are the efficiency with which the charge particles are detected; the spatial resolution and finally, the occupancy of noise hits. The definitions of each will now be given. A noise hit is when one or more strips[a] registers a hit (that is, when the charge flow exceeds a certain threshold) in the absence of any ionising particles. This last quantity, the noise occupancy, is therefore the average number of noise hits per

[a]A strip, as we will see, is made of silicon and constitutes the fundamental readout channel of the SCT detector.

strip, per event. The efficiency with which the charge particles are detected is explained in the following definition. If n_{hit} and n_{miss} denote the number of hits and no hits[b] respectively then the efficiency with which the particles are detected is given by: $\epsilon = \frac{n_{hit}}{n_{tot}}$, where $n_{tot} = n_{hit} + n_{miss}$. That is, ϵ is the probability of a hit given the passage of a charged particle through the material. The spatial resolution for a silicon hit depends upon the number of strips in a cluster, the spacing of the strips (the so-called pitch) and the length of them.

The noise occupancy is critical in the track reconstruction procedure. Unless sufficiently sparse, these noise hits will interfere with the track reconstruction. The ATLAS requirement is for noise occupancy in the SCT to be less than 5×10^{-4}, both before and after irradiation. It is, therefore, imperative that this quantity is well known before data taking.

This chapter details the work carried out to investigate the noise occupancy levels in a certain fraction of the SCT barrel modules when randomly triggered and identifying any problematic modules and deciphering the root cause(s) in the process. The next section, section 4.2, presents a brief overview of the SCT (as a preliminary description of the SCT has been given in section 3.3.4.2) giving the context within which the components under investigation, the barrel modules, are expected to perform. Following this, a more in-depth overview of the SCT barrel modules and electronic readout are presented, which all serve as the background material for the noise occupancy analysis to be presented in the following sections. Finally, the last two sections, sections 4.3 and 4.4, present the noise occupancy results and the problematic modules identified and thereafter, any conclusions drawn. The work presented in this chapter was published as an ATLAS note [107].

[b] A no hit or 'miss', within the context of the SCT test beam environment, is defined as the case when the residual between the projected reconstructed track position of a cluster (a collection of hit strips) and the observed cluster position was greater than 150 μm.

4.2 The ATLAS SCT barrel modules

The ATLAS SCT [99, 108] is an order of magnitude larger than previous generations of silicon microstrip detectors. By employing the least amount of semiconducting material as possible (so as not to degrade the performance of the SCT or calorimeters) and making as many measurements of the trajectory of the charged particles (in order to obtain precise momentum measurements), together are conducive to highly precise measurements of charged particle tracks being achieved. The barrel forms part of the ATLAS inner detector as shown in fig. 4.1. Consisting of four concentric barrel layers[c] each of length 1.530 m (1.498 m of it being active) and covering radii from 299 mm to 514 mm from the IP. The fundamental detector entity of the detector subsystem, a module [109], is shown in fig. 4.2. A module is the fundamental readout entity (unit) of the SCT. There are, in total, 2112 modules tiling the four coaxial cylindrical barrel layers, covering an area of 34.4 m^2. At least four precision space-point measurements are expected, over the fiducial region $|\eta| < 1.1$. Table 4.1 summarises the barrel SCT detector parameters.

The modules comprise of three main parts: the silicon sensors or wafers; the wrap-around hybrid; and a baseboard. The 285±15 μm thick silicon sensors constitute the active elements of the SCT, registering the charge liberated by charged particles in transit across the silicon layers. Each wafer is implanted with 770 (768 of which are active) readout strips which are 62 mm in length and approximately 22 μm in width, and have a pitch of 80 μm. The single-sided sensors are paired together by daisy-chaining together (thus doubling the strip

[c]The SCT barrels are numbered from three to six. The rationale behind this is that the three barrel layers of the pixel detector are labelled as, in ascending order of distance from the beam pipe, zero, one and two.

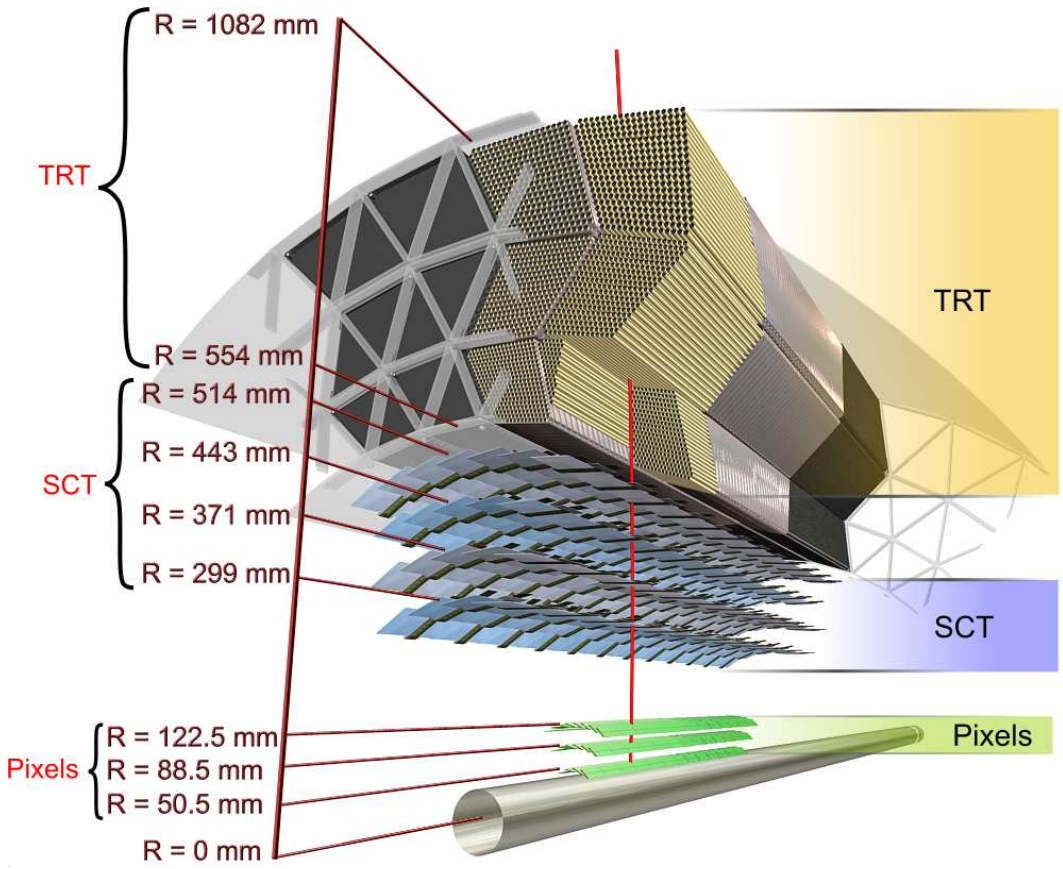

Figure 4.1: The barrel part of the ATLAS inner detector. The diagram displays a 3D representation of the barrel part of the inner detector traversed by a charged track (at $\eta = 0$) with a p_T of 10 GeV. The four barrel layers of the SCT with their individual silicon modules are clearly visible. The hybrids for each module can be seen, represented by the small dark bands. The SCT modules are mounted on the outer barrel layers with a small angle such that neighbouring modules overlap with each other. In addition to the four SCT barrel layers, the three layers of the pixel and TRT detector subsystems are shown together with the structural elements and their dimensions [99].

length) with electrical connecting wire bonds. This creates an inactive region or 'dead-space' of length 2 mm. The active surface of the sensors is 62 mm × 61.6 mm. When situated in the SCT, the strips of the lower wafers are parallel to the beam. The hybrid fulfils the triad of roles: providing mechanical support, cooling through high thermal conductivity and electrical readout, for each module. The

Barrel Cylinder	Radius (mm)	Full Length (mm)	Module tilt angle (degrees)	Number of modules	Number of modules in	
					ϕ	η
3	284(299)	1530(1498)	11.0	384	32	12
4	355(371)	-	11.0	480	40	12
5	427(443)	-	11.25	576	48	12
6	498(514)	-	11.25	672	56	12
Total	-	-	-	2112	176	48

Table 4.1: Details of the SCT barrel cylinder (layer) parameters and number of modules per cylinder. There are a constant number of twelve modules per row (i.e. in η) but a differing number of modules in ϕ. The numbers for radii and length quoted are for the outer barrel surface, with the average active sensor radii and overall length shown in brackets. The tilt angle is with respect to the tangent to the support cylinder [99].

multilayered hybrid bridges the silicon wafers on either side of the module. The upper layer of the hybrid (the so-called stereo layer), together with the silicon sensors, are deliberately misaligned with respect to the lower layer (the so-called $\rho\phi$ layer) by a small stereo angle of ± 40 mrad. The purpose of this is to assist with providing a z-measurement. The beryllium oxide (BeO) baseboard to which the modules are permanently attached to with the application of an adhesive, is used in the support structure of a module due to its mechanical rigidity and high thermal conductivity. Heat dissipated by the front-end electronics, cables and leakage current is conducted away from the silicon detectors to the cooling pipes by the baseboard and beryllium facings.

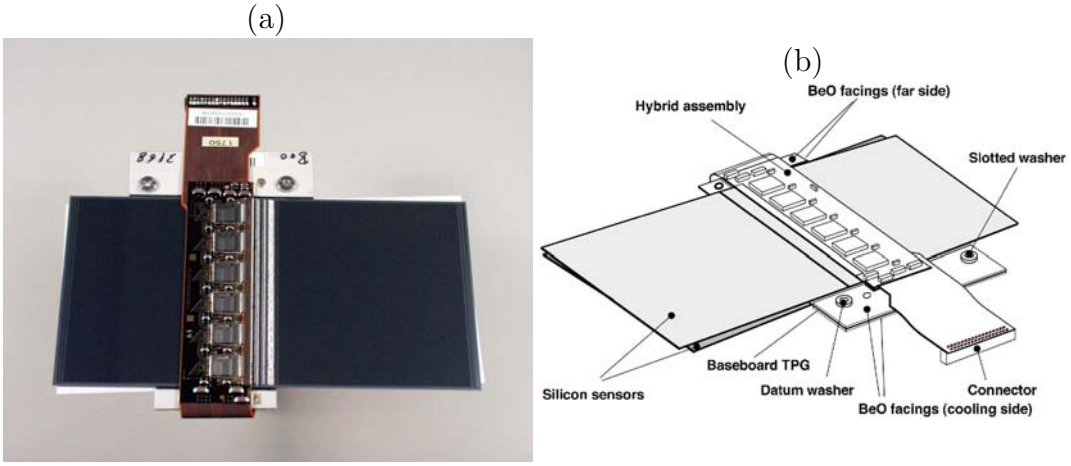

Figure 4.2: A (a) photograph and (b) schematic diagram of an SCT barrel module, showing it components. From [99].

4.2.1 The ATLAS Silicon detectors

The fundamental working premise of the SCT detector is reliant upon semiconductor technology. The Group IV element silicon, used in its crystalline form, is deployed as the active material of the modules. The detectors consist of an n-type silicon substrate with p-type strip implants, thus, forming a p-n junction. To reach thermal equilibrium, a small net flow of electrons from the n-type to the p-type occurs, filling the vacant holes in the p-type. This creates a region either side of the junction almost completely devoid of any free charge carriers, the so-called 'depletion' region. The height of this depletion region can be varied with the application of an applied voltage across the junction. A charged particle traversing the detector ionises the medium creating electron-hole pairs in the depleted bulk. These are separated, and subsequently accelerated by, the electric field of the applied voltage toward the nearest electrodes (for electrons this will be the positively charged anode, whilst for holes this will be the negatively charged cathode) to the particle path where they are collected. The holes are accelerated

towards the strips and electrons toward the back plane. The accumulated charge is shared across more than one strip when a particle is incident at an angle. Aluminium readout strips which are capacitively coupled to the p^+ implants, take the induced signal to the readout electronics. The hole collection times of the silicon detectors are approximately 25 ns. This entire process is schematically shown in fig. 4.3.

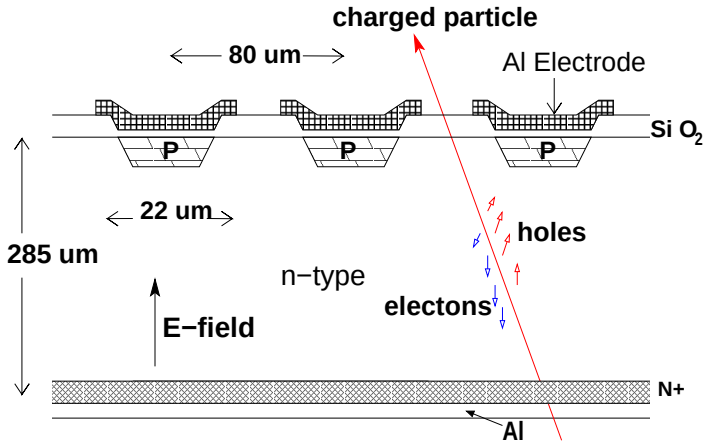

Figure 4.3: A schematic diagram of part of a p-on-n silicon microstrip detector. The three strips extend into the page. The direction of the electric field, E, is also shown. The dimensions given are those of an ATLAS barrel module sensor. Figure taken from [13] with the kind permission of its author.

4.2.2 Electronic Readout

Once the charge is collected through capacitively AC coupling to the Aluminium strips the process next is for it to be electronically readout. Although the readout architecture employed by the inner detector is optimised separately for each of the three detector subsystems, there does exist however, a set of common elements. In the words of [99] these elements are:

- the reception of a 40.08 MHz clock signal synchronous with the LHC bunch-crossings [the beam crossing separation time is 25 ns] used to time-stamp the signal generated in the low noise front-end electronics;
- signal generation in the front-end electronics and storage in binary or digital buffers for approximately $\sim$ 3.2 μs, compatible with the [level 1] Lvl 1 trigger latency of 2.5 μs;
- following a Lvl 1 trigger, the subsequent transfer of the buffer content associated with the bunch-crossing or possibly several bunch-crossings to a readout driver (ROD) off the detector.

Electronic readout of the signals in the SCT modules can be separated into parts or 'sectors'. The SCT 'front-end' or 'on-detector' electronics are physically mounted on the detector modules. The 'back-end' or 'off-detector' electronics are located in Underground Service Area 15 (USA15) outside the cavern where transmission is through electrical and optical links. A brief overview of each one will now be given.

4.2.2.1 SCT front-end electronics

The front-end electronics raison d'être is that it performs the requisite signal processing and storage for the duration of the level 1 (Lvl 1) trigger latency. It is largely specific to each inner detector subsystem. Residing on the wrap-around hybrid of each SCT barrel module are twelve, identical ABCD [110] application specific integrated circuit (ASIC) chips which serve to readout the signal from the modules. There are 6 chips on each side of the module and each one serves 128 silicon detector strips. Thus, 1536 channels are readout per module. The ASIC is fabricated in radiation tolerant bi-CMOS DMILL [111] technology. The initial 128 analogue signals on input to the chip, a simplified block diagram of which is

given in fig. 4.4, are digitised and subsequently read out.

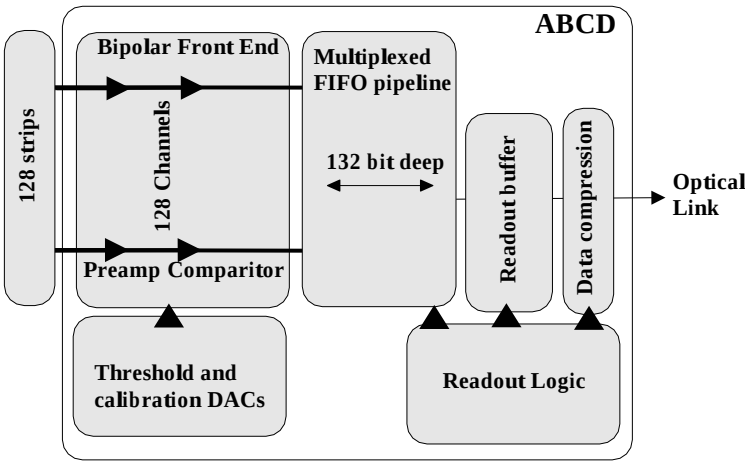

Figure 4.4: Simplified block diagram of the ABCD3TA chip. From [13].

For each channel there exists a pre-amplifier, shaper and tunable discriminator in the front-end part of the chip. This proceeds to amplify, filter the frequencies and carry out charge integration for all 128 channels. Thereafter, the integrated signal is compared to a threshold value (a voltage) set by an internal 8-bit digital-to-analogue converter (DAC), producing a digital 0 or 1. If the signal is below this threshold the value of 0 (or 'no hit') is returned whilst if above, the value of 1 ('hit') is returned. The recorded digital hits are then transferred and stored as single bits in the binary pipeline, the first-in-first-out (FIFO) buffer. It is a 132-bit deep, 12×12 array of dynamic memory cells. Herein, and pending the arrival of a Lvl 1 trigger decision (although the Lvl 1 trigger decision is $\sim 2.5\ \mu s$ the hit information for each channel associated with each beam crossing is stored for $\sim 3.2\ \mu s$), the hit pattern on input is then shifted through the pipeline. Only on receipt of this trigger, after a time equal to the level 1 trigger latency, the last three emerging bins (and so correspondingly 3 bits corresponding to three consecutive bunch crossings centred on the Lvl 1 trigger) are transferred from

the pipeline to the readout buffer. This ensures that the dead-time is negligible for the expected data rates. Thereafter, the data is compressed; only channels which contain a 'hit' are retained (for any given event, the average hit rate is expected to be 1%. Thus, few channels will actually contain interesting data) and subsequently passed to the readout logic for transmission off of the chip to the off-detector electronics, located in the service cavern. The form of the final output is a bit-pattern corresponding to hit information at the 40 MHz clock/bunch-crossing frequency.

4.2.2.2 Data transmission to the off-detector electronics

The main objective of the off-detector (back-end) electronics is the digital transmission of clock, trigger information and control commands to the modules and, furthermore, transfer data from the modules to the off-detector electronics. This is achieved with the aid of optical fibre links [99]. Optical transmissions of signals is preferable to electrical transmission in view of the fact that it can allow for higher nominal data rates of 35.4 Mb/s [d] per module; uses less material and, thus, reduce the material budget; is radiation tolerant; and finally, avoids any of the unwanted problems that would be associated with using electrical signals, e.g. earthing. The readout system is crate based and contains the main modular elements: ROD crate controller (RCC), readout drivers (ROD) [112], back of crate (BOC) card and timing and control system (TTC) information module (TIM) [112]. The RCC, a single computer board, initialises and configures all other electronic hardware and loads the module configuration to the RODs. Once data taking then commences the TIM receives the Lvl 1 trigger and timing

[d] This is based upon the assumption that there is a maximum occupancy of 1% and the maximum Lvl 1 trigger is 100 kHz [99].

information and bunch identification from the central ATLAS trigger, TTC. The TTC distributes this information to the front-end electronics and RODs. These deal with most of the computational tasks: first level data collection upon receipt of a level 1 trigger, error checking, formatting and local event building and calibration. Each ROD contains five OSP processors and over 1 Gb of RAM. Each ROD serves 48 SCT modules and must carry out the task of event building at a rate of 75 kHz (Lvl 1 trigger rate) with minimal dead-time. Upon receipt of this trigger the RODs issue the trigger to the modules via the BOCs. Each BOC is partnered with an ROD. The BOCs handle 48 modules via optical interfaces. Each one contains two types of electrical/optical converter plug-ins: RX-plug-in (of which there are eight) and TX-plug-in (of which there are four per BOC). The initial signal is sent from the TX-plugin and the returning signal corresponding to that trigger from the chips arrives at the RX-plug-ins of the BOCs. These are subsequently transferred to the RODs. The RODs proceed to combine all data received into one single event packet or hit-packet (ATLAS standard event fragment) associated with that Lvl 1 trigger. Thereafter, the packets are sent back to the BOC for subsequent transmission to the Lvl 2 TDAQ system via the ATLAS S-link [113] which is the ATLAS high-speed custom optical data link. A fraction of events are also analysed to monitor performance/data monitoring tasks.

4.3 Analysis Overview

4.3.1 Introduction

On Friday, February 17th 2006, the SCT barrel was inserted into the Transition Radiation Tracker (TRT) barrel at CERN. Thereafter, a series of tests commenced

whose primary purpose was to gauge the feasibility of operating the detector subsystems in a setup similar to that foreseen for data taking in the cavern. These tests were carried out at ground level after the SCT was inserted into the TRT in the SR1 building (and are consequently referred to as the 'SR1' commissioning tests) at CERN and employed a sub-section of the SCT barrel. The tests were so called 'physics' runs in which all modules active in the barrel are triggered simultaneously by either a pulse[e] at a fixed frequency (termed 'noise' runs) or by muons traversing the scintillators (termed 'cosmic' runs). Note that the probability of recording a hit from a muon traversing the scintillators during a noise run is sufficiently small that all hits observed in such a run are assumed to originate from noise. Furthermore, these tests were also intended to investigate the noise resulting from synchronous operation of the SCT system together with the TRT.

The work presented in this report was an investigation into the noise occupancies in the SCT barrel modules for a particular barrel configuration. Also, it should be noted that although there are, in total, 2112 SCT barrel modules, only approximately one quarter (468 modules) were employed for this SR1 cosmic ray test configuration, pertinent to this work. The final setup for the SR1 cosmic tests is shown in fig. 4.5. Readout of the SCT was performed using 12 RODs and with the detector subsystem enclosed in a dry, thermally controlled environment throughout. The SCT data used corresponded to run number 003076 and was taken on the 22/06/2006. The setup was such that a 30 kHz pulsed trigger was employed, with the threshold potential on the chip set at 0.9 fC, with only the SCT active and the TRT was clocked but not triggered. In total 9,150,835 events

[e]This fixed frequency pulse, which was used to imitate the Lvl 1 trigger, was produced by a small pulse unit which would produce pulses at approximately every 50 Hz or so. This was variable however.

were generated for this data run distributed amongst 100 data files. However, for this work only one file was used corresponding to 91,159 events. The analysis of the data was carried out using a private event decoder which then allowed plots to be produced.

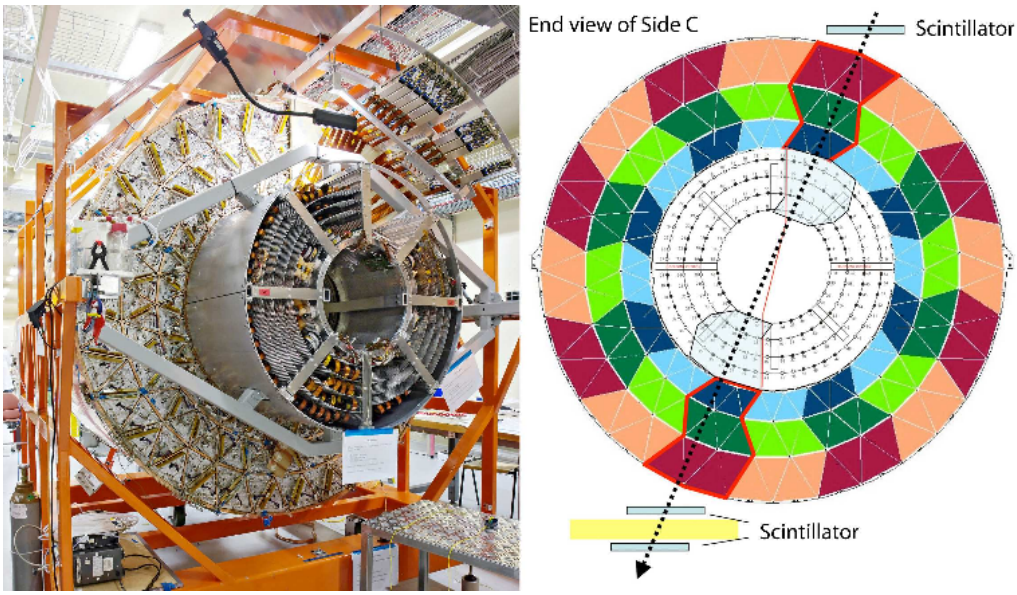

Figure 4.5: In (a) a photograph of the inner detector barrel setup and (b) a diagrammatic representation highlighting the configuration of the regions of modules chosen, for the SR1 cosmic-ray study tests [99].

4.3.2 Method

Two important definitions are now given. Firstly, a time bin is a 25 ns period of time during which data is recorded by the SCT modules. For this work three time bins were read out for (or centred on) each level 1 (Lvl 1) trigger. The duration of each time bin corresponds to one bunch-crossing at the LHC. The data was collected whilst running in expanded mode[f]. The time bins are labelled

[f]This refers to when the ROD uses all information stored within all three time bins in a hit-packet before passing all the information retained in the hit-packet on to the HLT.

−1, 0, +1 with the centre one corresponding to the number 0. Secondly, a bit field or bit word is a value made up of binary digits which indicates that a noise hit has been recorded by the SCT in one, two or all three of the time bins. Each bitfield is labelled as XXX where each X denotes either a hit (1) or miss (0) state in each time bin and the order of the Xs denote the previous, present and future (next) bunch crossing. For example, 010 indicates that a hit has occurred in the central (current) bunch crossing (time bin) and misses in the +1 and -1 time bins. The ABCD data compression logic was configured to run in "any hit" mode which meant that a hit packet was sent off the detector if a hit occurred in any of the three time bins. If no hits are found in any of the three time bins then no information on the hit packet should be sent off the detector. If there were hits found for this bit field value (i.e. 0) then this would indicate a problem. This was indeed observed, the so called 'zeroth time bin anomaly'. Fig. 4.6, which is for all modules, displays this anomaly and for this reason, further investigation was warranted.

The first step was to try and identify those sides of the modules which had recorded noise hits in the zeroth time bin, i.e. those modules found to exhibit this anomaly, "bad module sides". Each side can be uniquely identified by four numbers which locate each side of a module within the SCT coordinate system. The first is on which layer the side resides. There are four layers, 0, 1, 2 and 3, layer 0 being the layer closest to the interaction point[g]. The second is which side of the module one is dealing with, side 0 or the bottom part being the side closest to the interaction point and side 1 the top part. The final two numbers are the η and ϕ values which act as a 2D coordinate system on each layer of modules,

[g]It was stated earlier that the SCT barrels are numbered from three to six. Therefore the mapping is such that here layer 0 corresponds to the SCT barrel layer 3, layer 1 corresponds to the SCT barrel layer 4 and so forth.

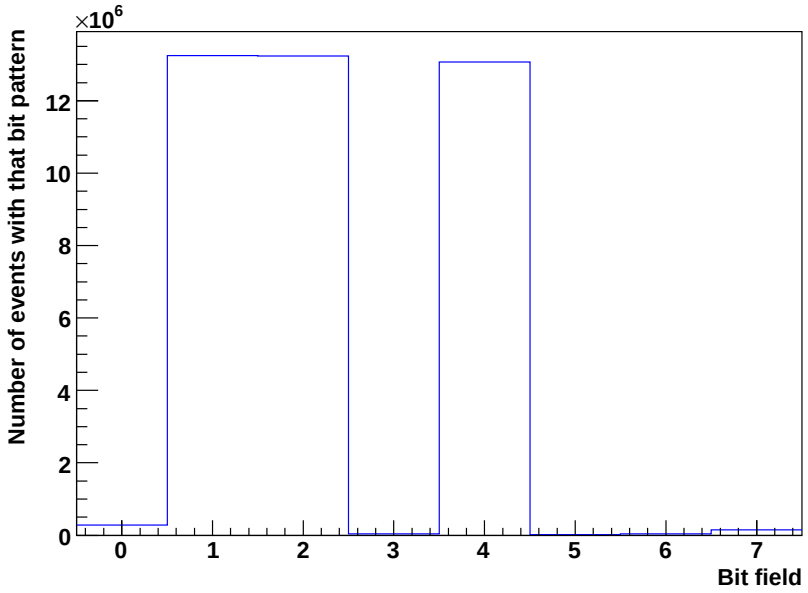

Figure 4.6: Distribution of bit field value versus number of events with that corresponding bit pattern for the sum over all modules and not all modules had 000 hits.

for each side. Twelve modules span the full range in η (+6 to −6), with each module one unit in η. The coordinate ϕ depends upon the barrel layer. The ϕ range for each layer are, for layer 0, 0 to 32; layer 1, 0 to 40; for layer 2, 0 to 48; and finally for layer 3, 0 to 56. In total 14 bad sides (those sides which had exhibited noise hits in the zeroth time bin), out of a total of 468 modules and 936 sides, were identified which were distributed amongst eight modules. However, from closer inspection and from consideration of the noise occupancy values for the cases of when there were noise hits in the zeroth time bin (000) and the central time bin (x1x) and their ratio, it was initially found that there were three different classes of module, denoted by A, B and C, each corresponding to possibly different problems. Table 4.2 shows all 14 bad sides together with their unique location numbers and noise occupancy values.

Class	Layer	Side	η	ϕ	Noise Occupancy(000)	Noise Occupancy(x1x)	Ratio (000/x1x)
A	0	0	-1	8	0.000283854	0.000397005	0.714988
A	0	0	-2	8	0.000202865	0.000260937	0.777448
A	0	0	-3	8	0.000225651	0.000314844	0.716707
A	0	0	-4	8	0.000451953	0.000745964	0.605864
A	0	0	-5	8	0.000134245	0.000198828	0.675182
A	0	0	-6	8	0.000142318	0.000189583	0.75069
A	0	1	-1	8	0.000240625	0.000321354	0.748785
A	0	1	-2	8	0.000214583	0.00029401	0.729849
A	0	1	-3	8	0.000196484	0.000254036	0.773449
A	0	1	-4	8	0.000440625	0.000689323	0.639214
A	0	1	-5	8	0.000142969	0.000178385	0.801463
A	0	1	-6	8	0.0001125	0.000132292	0.850392
B	2	1	-2	6	0.00122266	0.00019375	6.3105
C	3	1	-3	11	$9.11458\text{x}10^{-7}$	0.000292969	0.00311111

Table 4.2: The table displays the three classes which contain the 14 bad sides with their unique identification numbers that were identified in this report along with their corresponding noise occupancy values for both cases of noise hits in the zeroth time bin and the central time bin. Finally the ratio of these two numbers (i.e. noise occupancy(000)/noise occupancy(x1x)) are also given.

The first class contained 6 modules who had recorded hits on both sides of the modules (so 12 sides in total) and very similar values for the ratio of noise occupancy (000) to noise occupancy (x1x). The second and third classes each contained one side of a module, each side from a different layer and only one side of the modules recorded these anomalous hits in the zeroth time bin. In addition to this they also had values for the ratio of noise occupancies that were different

to those of the first class of modules. One side of a module from the first class was selected together with the two sides from the second class and a series of plots were made to try and attempt to ascertain what the cause for the anomaly could be. The three sides selected for investigation were:

- side of the module with layer=0, side=0, η=-1, ϕ=8;
- side of the module with layer=2, side=1, η=-2, ϕ=6;
- side of the module with layer=3, side=1, η=-3, ϕ=11.

The first set of plots (fig. 4.7(a), fig. 4.9(a) and fig. 4.12(a)) were produced to see what value the bit field was for each of the three sides selected. The second set of plots (fig. 4.7(b)(c), fig. 4.9(b)(c) and fig. 4.12(b)(c)) were produced with the intention of seeing how the noise occupancies in the zeroth time bin varied per chip and strip (readout channel) for each side[h]. Fig. 4.7(d)(e), fig. 4.9(d)(e) and fig. 4.12(d)(e) were also produced for the case of when there was at least one hit in the central time bin (x1x) to see if there was any correlation with the case of zeroth time bin hits for each side. Finally the third set of distributions (fig. 4.8, fig. 4.11 and fig. 4.14) was to see if there was any temporal variation (event number) of the noise occupancy for the x1x and 000 hit cases. The results for each side will now be discussed in turn.

4.3.3 Results

4.3.3.1 Side of the module with layer=0, side=0, η=-1, ϕ=8

The set of plots for this side of a module are shown in fig. 4.7 and fig. 4.8. For the first figure, fig. 4.7(a), it would be expected that in almost all events (there is

[h]Note the convention used for the chip and strip numbers for each side was the following. The strip number runs from 0 to 767 per side and the chip number runs from 0 to 5 for side 0 and from 8 to 13 for side 1. Also note that the channel and chip identifications were *online* (hardware) numbers whilst the module identifications were *offline* numbers.

also the possibility, although much smaller, for events to contain two hits rather than one or zero) the only bins occupied should be those corresponding to bit fields 1, 2 and 4 and, furthermore, that each one will contain approximately an equal number of entries. However, it is apparent that there is a large number of these spurious 000 hits for this side. The equivalent figure for the number of hits versus bit field suggests that approximately 19,000 entries have migrated from bin four to bin zero. The second set of plots (fig. 4.7(b) to (e)) appears to suggest that no one strip or chip is problematic in nature. This can be seen from the uniformity of these distributions. Both figures, fig. 4.7(c) and (e) show that there are a number of different strips in each case whose noise occupancy values exceed the threshold of 5×10^{-4}. It appears that the whole side of the module is bad. Finally, fig. 4.8 shows the number of 000 and x1x hits and their variation in time. From the flatness of these distributions one can conclude that there was no visible correlation with time.

4.3.3.2 Side of the module with layer=2, side=1, η=−2, ϕ=6

Displayed in fig. 4.9 are the relevant distributions for this side. Fig. 4.9(a) shows that, again, there are a large number of these spurious 000 hits for this side with the noise occupancy value in bin zero above threshold. Moreover, there appears to have been migration of entries from bins one, two and four to bin zero (this assertion is made on the basis that one would expect, approximately equally populated bins in bins 1, 2 and 4 and this is not observed). However, closer inspection of the corresponding distribution as in fig. 4.9(a) but for the other side of this module suggests that it is not migration but rather there is just a large excess of these spurious 000 values.

As can be seen from fig. 4.9(c) it was apparent that all of the 000 hits oc-

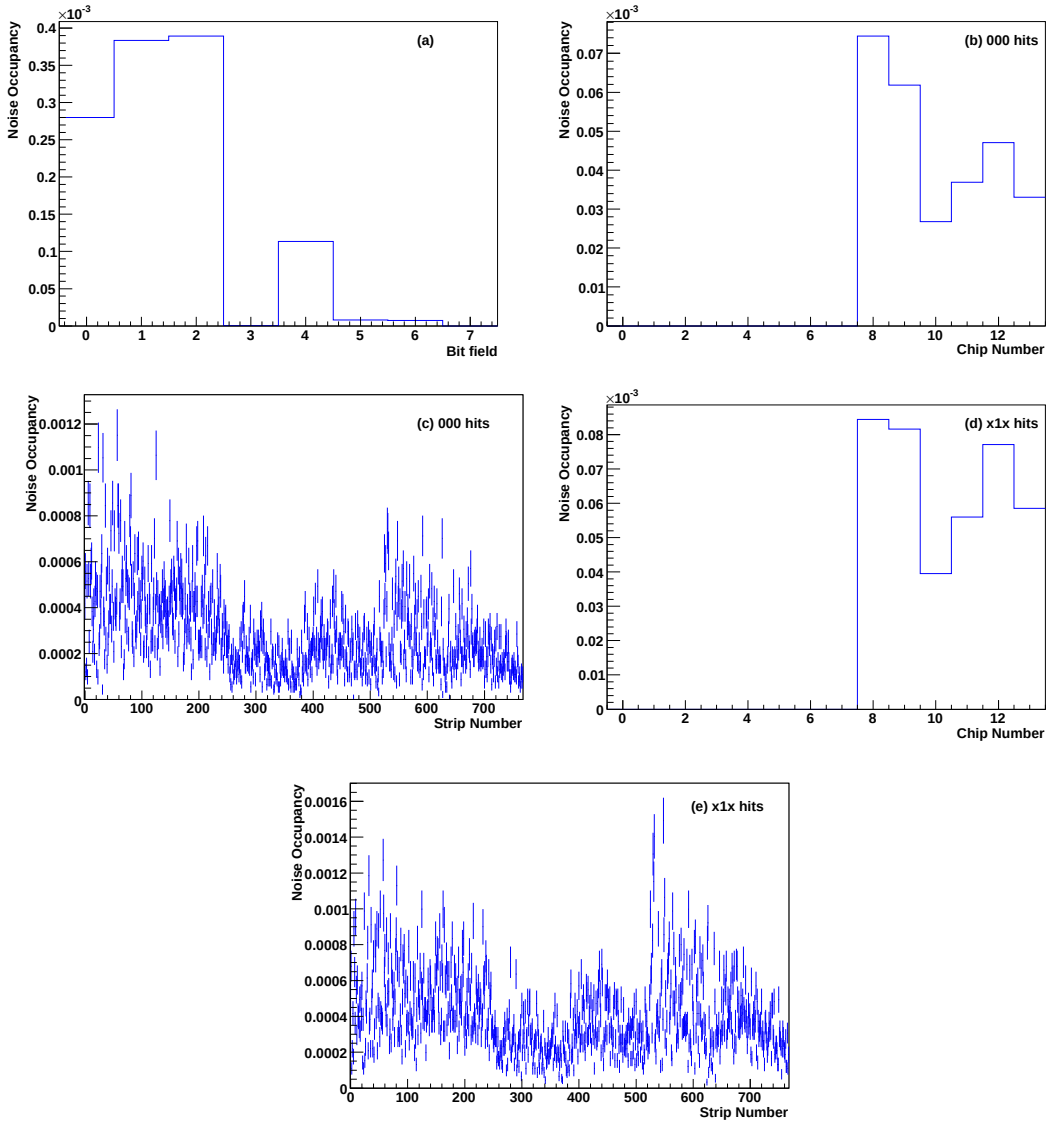

Figure 4.7: The noise occupancy distributions for the cases of hits in the zeroth time bin (000) and central time bin (x1x), for the side of the module with layer=0, side=0, η=-1 and ϕ=-8. The noise occupancy is plotted versus variation in (a) bit field, (b) and (d) chip number and (c) and (e) strip number. Side one also displayed similar behaviour for all cases shown.

curred on one channel, number 623. This channel resides on chip number four (fig. 4.9(b)). It should also be mentioned that there exists a noisy channel for the case of x1x hits (fig. 4.9(e)) but this is a different channel to the one caus-

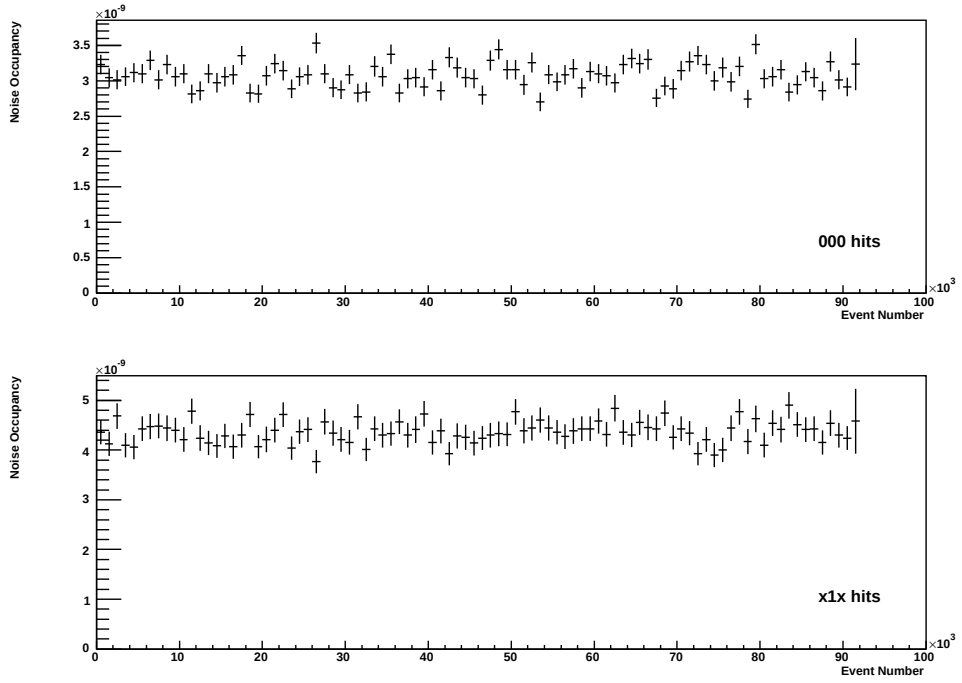

Figure 4.8: The temporal variation of the noise occupancies for the cases of hits in the zeroth time bin (000) and central time bin (x1x), for the side of the module with layer=0, side=0, η=−1 and ϕ=−8.

ing the spurious 000 hits shown in fig. 4.9(c). This then also warranted further investigation. So by plotting the distributions of the number of 1xx and xx1 hits (fig. 4.10) and how these varied per strip (channel) it emerged that there seems to be one (the same one) noisy channel, far above threshold, in each of the three time bins, identified as channel number 599. In scouring the output log file containing information on all hits in channel 599 for this layer for any common, manifestly behaviour, it was evident that there exists a correlation between the bunch crossing identification number (BCID) and the three time bins or any hit mode (1xx, x1x and xx1). Elaborating on this last point, there appeared to be perennial manifestations of the hits on this channel for all hit modes: 1xx, x1x and xx1. It was found that the hits on this channel in a time bin were always

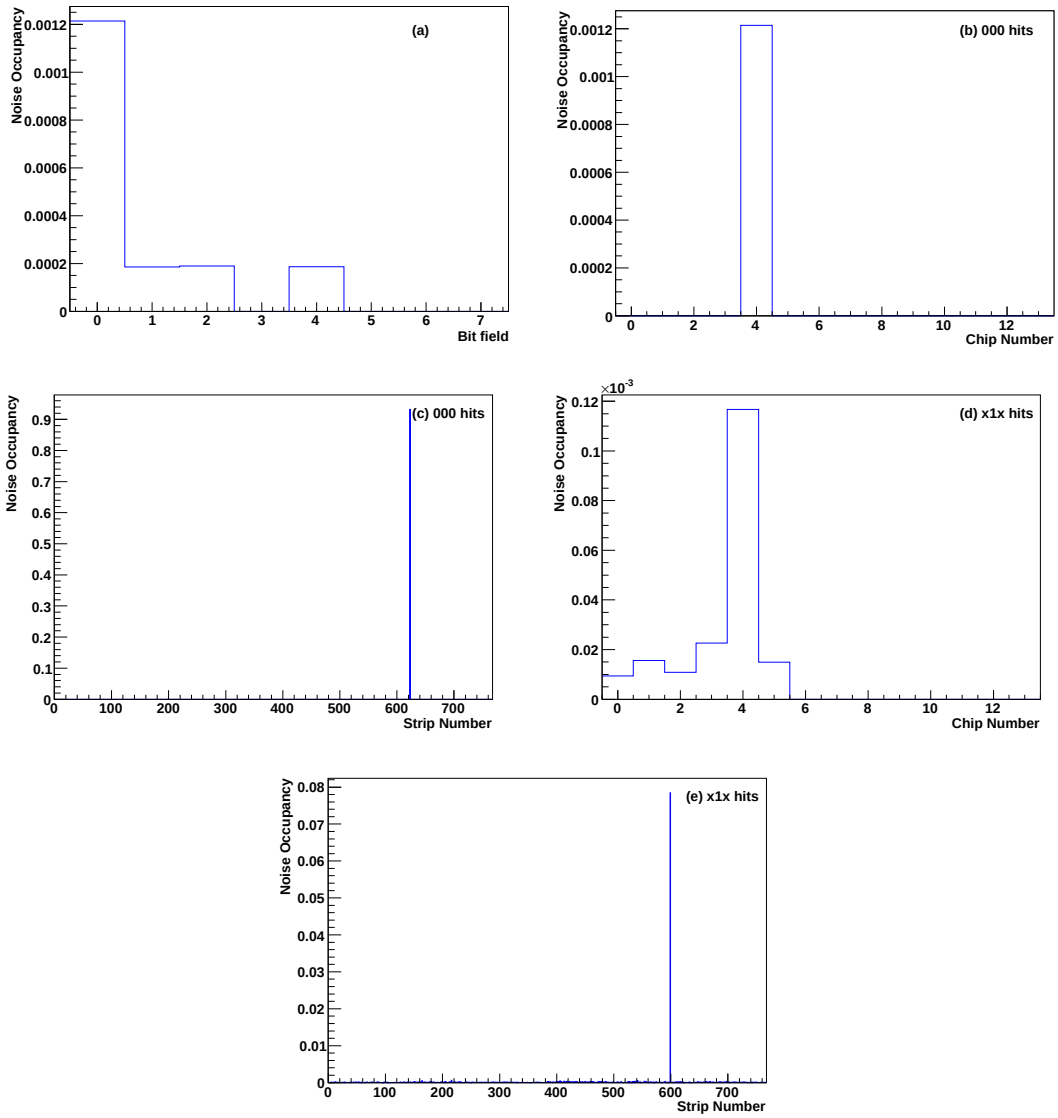

Figure 4.9: The noise occupancy distributions for the cases of hits in the zeroth time bin (000) and central time bin (x1x), for the side of the module with layer=2, side=1, η=−2 and ϕ=6. The noise occupancy is plotted versus variation in (a) bit field, (b) and (d) chip number and (c) and (e) strip number. However, unlike in the earlier case, side one did not exhibit this same behaviour.

separated by an integer number of twelve BCIDs: with BCID%12=5 for time bin −1, BCID%12=6 for time bin 0 and BCID%12=7 for time bin +1. This is consistent with the noise hits being caused by a stuck cell in the chip pipeline block.

This assertion can be supported by the link between the periodicity of the bunch crossing, which was found to be 12, and the 12 non-overlapping clocks in the binary pipeline of the FIFO circuit which controls the array of 12 dynamic memory cells. Each clock has a cycle of 1/12 the bunch crossing frequency (40MHz). Both these channels, 599 and 623, were furthermore masked off for this run. However, the problem still persisted suggesting that there is, indeed, a fault with the chip. Lastly, as was the case for the previous side, there appears to be no variation over long times, in the sense that there was no long-term drift over time, as can be seen in fig. 4.11.

4.3.3.3 Side of the module with layer=3, side=1, η=−3, ϕ=11

The third and final problematic side to exhibit the zeroth time bin anomaly appeared to have a much smaller number of entries in bin 0 compared to the two previous two sides as can be seen in fig. 4.12(a). From looking at the distributions of the noise occupancies and how this varies with chip and strip (fig. 4.12(b) to (e)) it is apparent that although there was a large number of bad channels discovered they were all found to be from the same chip, chip number five. Although, again, as was the case for the previous side, a noisy channel for x1x, channel number 727, is clearly visible in fig. 4.12(e).

This then warranted the distributions of the noise occupancies of 1xx and xx1 hits and how these varied per strip to be plotted which are displayed in fig. 4.13. The results of these plots show that there are no noisy channels in either case (for 1xx and xx1 hits). So for this side it is apparent that it exhibits only one noisy channel, which occurs in only one of the time bins, the central time bin. Again, on examination of the output log file for the case when hits occurred in the central time bin only for this layer, it was apparent that it displayed periodic

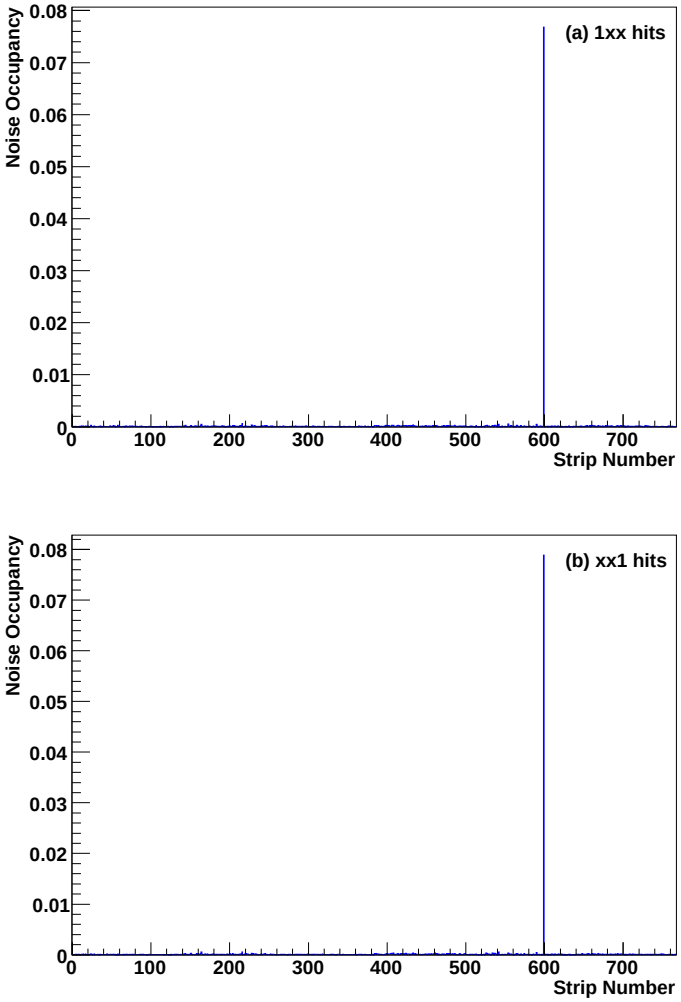

Figure 4.10: Noise occupancy distributions versus strips for the cases of (a) 1xx and (b) xx1 hits, for module with layer=2, side=1, η=−2 and ϕ=6. Clearly apparent is the same, sole noisy channel, identified as channel number 599.

behaviour. More succinctly, it was noted that for this channel, 727, there existed a strong correlation between the Lvl 1 ID of the noise hits on the strip and the trigger number with a periodicity of eight events. It was found that the Lvl 1 ID registered these hits every eight events (or for every eighth trigger). This suggests an error in the ABCD chip readout buffer since the readout buffer has sufficient

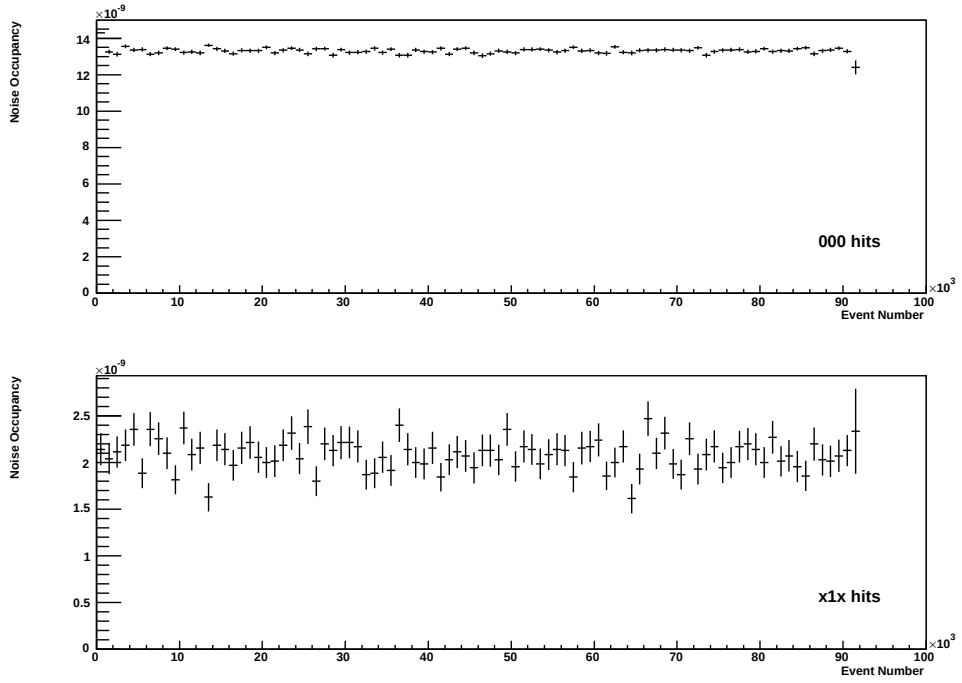

Figure 4.11: The temporal variation of the noise occupancies for the cases of hits in the zeroth time bin (000) and central time bin (x1x), for the side of the module with layer=2, side=1, η=−2 and ϕ=6.

capacity to store in total, at one time, data collected in eight Lvl 1 triggers in storage cells. And finally, fig. 4.14 shows that there was no correlation of the number of hits (000 and x1x) with time for this particular side.

4.4 Conclusion

From the work presented in this report it was apparent that there were three distinct classes of modules (sides), each one corresponding to three different types of problems which had caused this zeroth time bin anomaly. The first class contained twelve sides all of which were identified as being problematic. They were identified as sides (layer=0, side=$\{0, 1\}$, $\eta = -1 \rightarrow -6$, ϕ=8). There was no

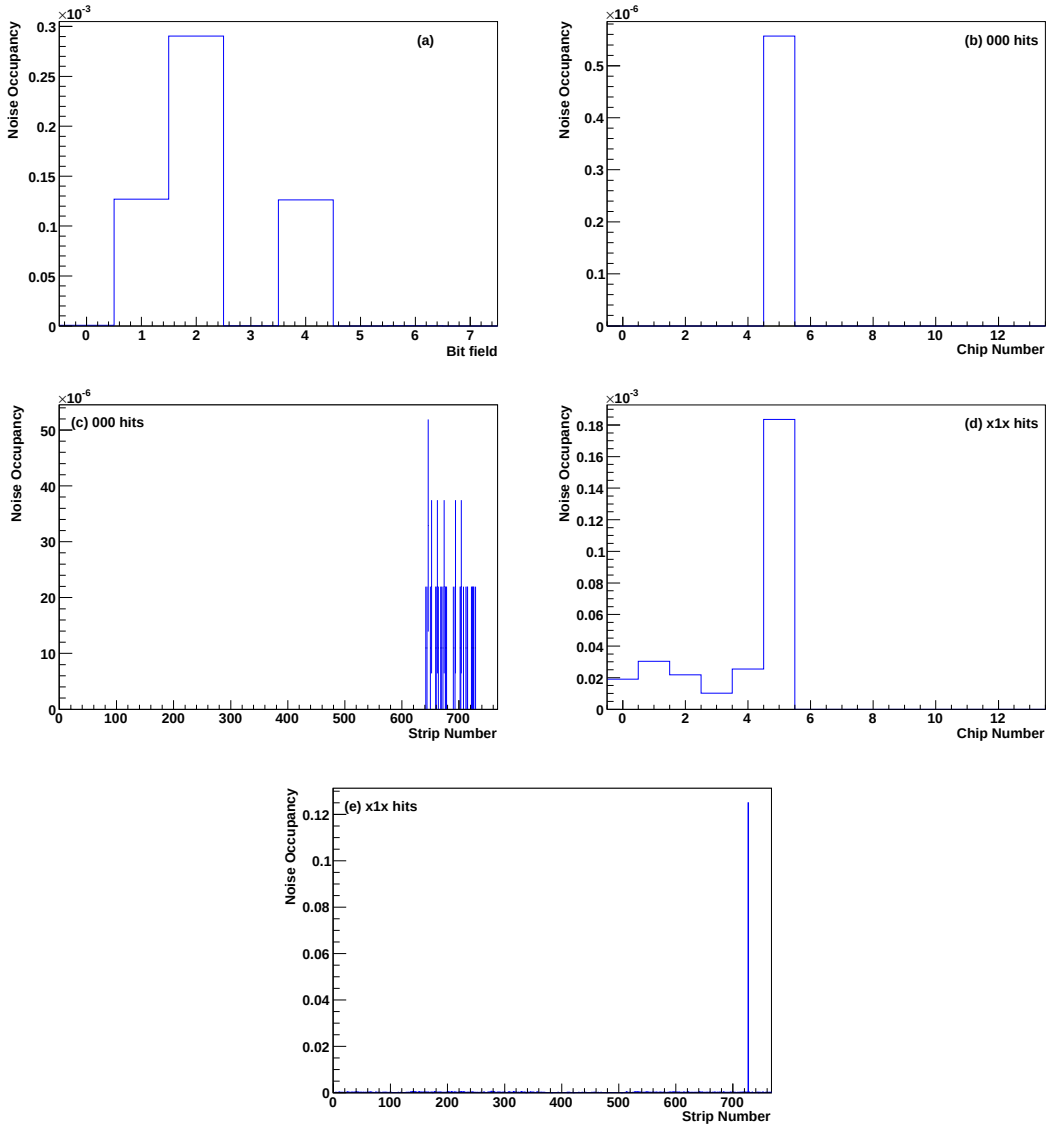

Figure 4.12: The noise occupancy distributions for the cases of hits in the zeroth time bin (000) and central time bin (x1x), for the side of the module with layer=3, side=1, η=−3 and ϕ=11. The noise occupancy is plotted versus variation in (a) bit field, (b) and (d) chip number and (c) and (e) strip number. However, unlike in the earlier case, side one did not exhibit this same behaviour.

channel or chip that was singled out as the cause for the anomaly which affected

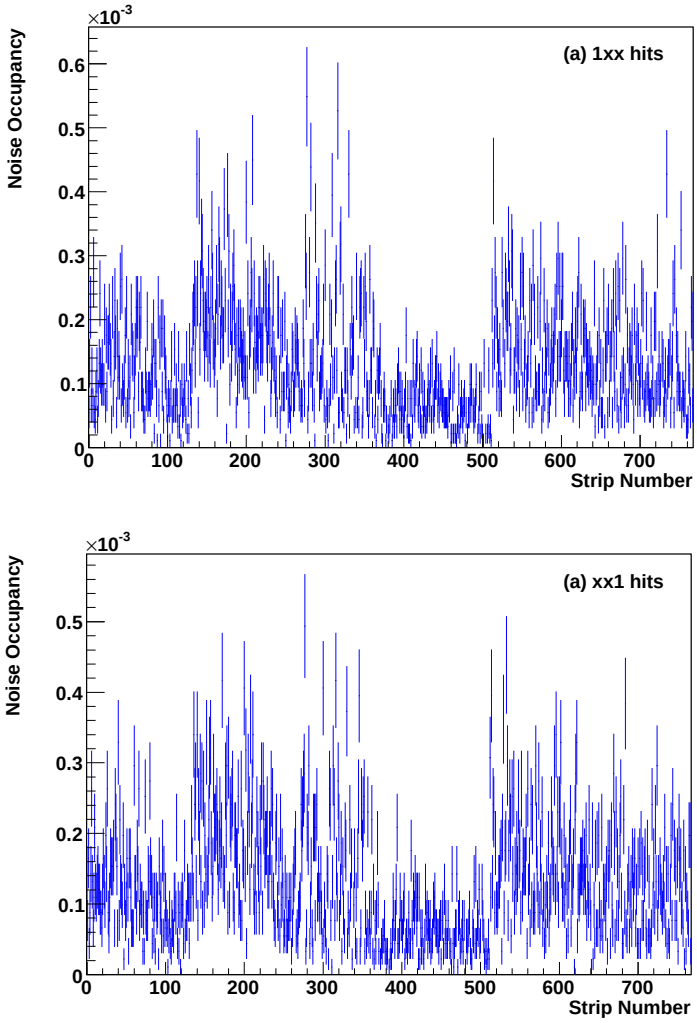

Figure 4.13: Noise occupancy distributions versus strips for the cases of (a)1xx and (b)xx1 hits, for module with layer=3, side=1, η=−3 and ϕ=11. Both these distributions show that no strip exhibits any excessive noise occupancies for the cases of 1xx and xx1 hits.

all six modules and all of which were attached to the same harness[i]. Normally twelve modules are served by the same SCT BOC TX plugin. However, for this data run the other six modules on this TX were not active and so as a result

[i]The service harness provides power to 5-6 modules and also includes two data fibres and one trigger/control fibre for each module.

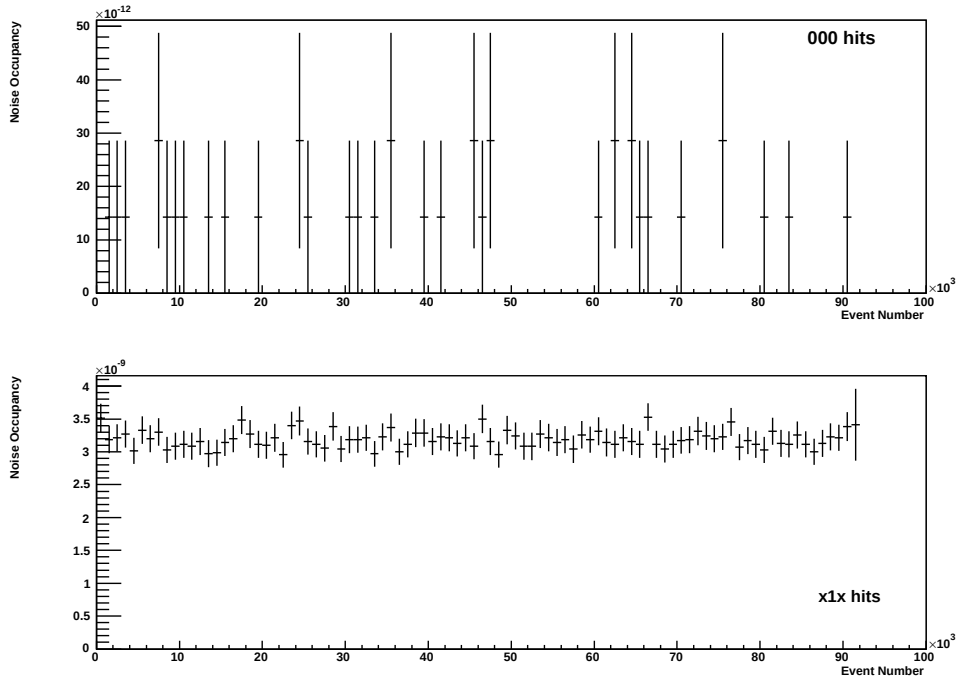

Figure 4.14: The temporal variation of the noise occupancies for the cases of hits in the zeroth time bin (000) and central time bin (x1x), for the side of the module with layer=3, side=1, η=−3 and ϕ=11.

these six modules were the only ones served by both a single RX and TX plugin. Since this TX plugin showed poor mark-space behaviour, it is possible that the problem may be associated with a high-jitter clock. However, this is speculative and alternative explanations might point toward a problem with the RX or the ROD event decoding. However, there remains no clear definitive explanation for the cause.

The next problematic side, side on layer=2, side=1, η=−2, ϕ=6, all the 000 hits occurred on channel number 623. It was further identified that this chip suffered from a stuck pipeline cell, evident from the problem arising every twelve bunch crossings.

The third and final side (layer=3, side=1, η=−3, ϕ=11) had a bad chip (chip

number 5) on which 000 hits occurred. Again this chip had another defect: in this case a defect associated with the ABCD readout buffer.

Finally, it was also apparent from the uniformity of the temporal-hit distributions that there was no drift with time for both cases of 000 and x1x hits, for all three classes of problematic modules.

Part III

SUSY or UED?

Chapter 5

Anatomy of the Analysis Part I: The Monte Carlo data samples

THIS chapter introduces the full and fast simulated Monte Carlo (MC) data samples for the SUSY signal and background processes and the Standard Model background processes used in the analysis. In addition, the 'theoretical' SUSY and UED distributions are also introduced which were simulated using the ATLAS fast simulation package ATLFAST. The Monte Carlo event generator used for each process along with the release of the ATLAS offline software with which the processes were reconstructed are presented. Some example tree-level Feynman diagrams of the SUSY and Standard Model processes are also given. Finally, the entire analysis was carried out within the framework of the mSUGRA model and under the assumption that R-parity is conserved.

5.1 Signal

At hadron colliders such as the LHC, sleptons are pair produced via their EW couplings to the γ , Z^0 and $W^{\pm}$ bosons. The predominant one is via the Drell-Yan process mediated by a virtual Z^0/γ^* in the s-channel. The SUSY process under investigation in this work and so the one that constitutes the 'signal', is given by the decay chain: $q\overline{q} \rightarrow Z^0/\gamma^* \rightarrow \tilde{l^{\pm}}\tilde{l^{\mp}} \rightarrow \tilde{\chi}_1^0 l^{\pm} \tilde{\chi}_1^0 l^{\mp}$, where $\tilde{l^{\pm}}$ and $\tilde{\chi}_1^0$

denote the slepton and the lightest neutralino (the LSP) respectively. The UED equivalent to this process is the decay: $q\overline{q} \rightarrow Z^0/\gamma^* \rightarrow l_1^{\pm} l_1^{\mp} \rightarrow \gamma_1 l^{\pm} \gamma_1 l^{\mp}$, where $l_1^{\pm}$ are identified as the first excited KK-leptons and γ_1 is the first excited KK state of the photon which fills the role as the lightest KK particle (LKP) of the UED model. Both the LSP and LKP are assumed to be stable. Both these particles do not interact in the detector since there is not a sufficient amount of material. Since the longitudinal component of the colliding parton's momentum is unknown, only the transverse component of the LSP or LKP momenta is measured. From momentum conservation, the presence of undetected LSPs or LKPs results in a transverse energy imbalance in the detector which is proportional to the LSP/LKPs momentum and is called missing transverse momentum or $\not{p}_T$.

Now the s-channel, tree-level Feynman diagrams for each theory process are schematically shown in fig. 5.1 where, hereafter, the leptons are understood to mean electrons or muons only. The distinctive signature will, therefore, for either model process, consist of a highly energetic opposite signed charge same flavour (OSSF) lepton pair with associated missing energy and inevitably some hadronic energy creeping in from initial state radiation. It is evident from the final states being exactly the same in either model process that UED can, indeed, masquerade as SUSY. Therefore, a way to unambiguously distinguish between them is required.

The direct pair production of sleptons can also proceed through the production mechanism of vector boson fusion (VBF) via $W^{\pm}W^{\mp}/Z^0Z^0/\gamma\gamma$ and gluon-gluon (gg) fusion. However, the rate for these processes is smaller by an order of magnitude at the LHC and negligible at the Tevatron [114]. For the case of gluon-gluon fusion the two ingoing participating gluons fuse generating a fermionic loop to which is attached a Z^0 or Higgs boson which then proceeds to decay into the

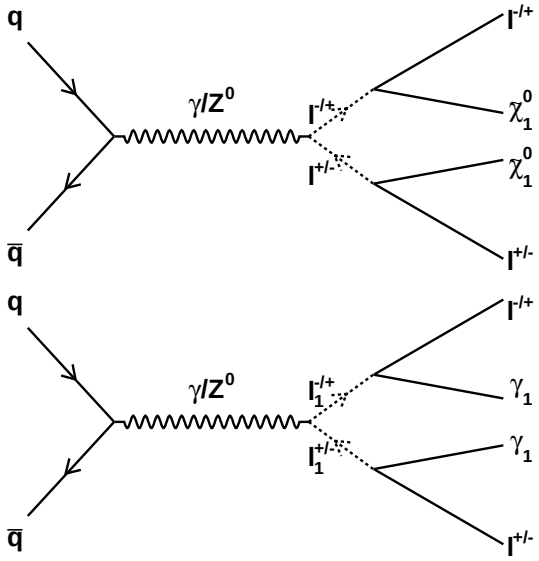

Figure 5.1: The s-channel, tree-level Feynman diagram (top) for the dislepton process that constitutes the 'signal' in the analysis carried out in this work. The equivalent decay process for UED is also shown (bottom).

slepton pair.

The chosen primary test point which constitutes one of the cMSSM benchmark points of the ATLAS full simulation studies, was the SU3 "bulk" region of mSUGRA parameter space which is schematically shown in fig. 5.2. This particular point corresponds to a set of particular values for the five free parameters, defined at the Grand Unified Theory (GUT) scale, which characterise the EW symmetry breaking within the mSUGRA model of SUSY. Furthermore, these benchmark points, first proposed in 2001 [115] act as an aid to the comparative assessments of the prospects for detecting SUSY particles within the context of the cMSSM model, at different accelerator experiments. They are constrained by direct searches for sparticles and Higgs bosons from LEP, the measurement of the $b \rightarrow s\gamma$ branching ratio and the WMAP [39] constraint on the relic density of dark matter. This latter constraint assumes that R-parity is conserved and the

LSP is an ideal candidate for cold dark matter and whose mass is maller than 1 TeV/c^2. The cosmological constraints on the cMSSM are set by requiring that the LSP relic density: $\rho_{\tilde{\chi}_1^0} = \Omega_{\tilde{\chi}_1^0}\rho_{\text{critical}}$ (where $\rho_{\tilde{\chi}_1^0}$ is the LSP density, $\Omega_{\tilde{\chi}_1^0}$ is the closure parameter for the LSP and ρ_{critical} is the cititcal density) falls within the range $0.1 < \Omega_{\tilde{\chi}_1^0}h^2 < 0.3$ where h is the normalised Hubble expansion rate ($h \sim \frac{1}{\sqrt{2}}$ kms^{-1}Mpc^{-1}). The upper limit is quite strict from cosmological arguments. From these constraints there exist generic regions of the MSSM parameter space where the relic density falls within the preferred range. Since the LSP relic density increases with the LSP relic mass this produces an upper limit on the mass of the LSP of $m_{\chi_1^0} < 1$ TeV/c^2. There are, however, various methods by which this upper bound on the $m_{\chi_1^0}$ can be evaded which has resulted in four regions of the five dimensional mSUGRA being identified. They are the following. The relic density may be suppressed by coannihilation [116] which produces a 'tail' extending to large $m_{\chi_1^0}$ and where the next-to-lightest sparticle is the lighter stau, $\tilde{\tau}_1$, and $m_{\tilde{\tau}_1} \sim m_{\chi_1^0}$. The 'funnel' [117] region, extending to large $m_{1/2}$ and m_0 and large $\tan\beta$, results from another mechanism so-called rapid annihilation via a direct-channel pole where $m_{\chi_1^0} \sim \frac{1}{2}m_{\text{Higgs},Z^0}$ [117]. A further region at large m_0 is the 'focus' region [118–120] where the LSP has a sizeable higgsino component, enhancing its annihilation. There is also one final observed central region called the 'bulk' region. The three tails (focus, coannihilation and funnel) extend away from this bulk region. Due to the relatively light scalar and gaugino particles they will be easily within reach by the LHC. Furthermore, it is the 'first place' where SUSY could be discovered at the energy regime probed by the LHC. Table 5.1 shows the typical spectrum of sparticle masses whilst fig. 5.3 shows part of the sparticle spectrum, corresponding to the SU3 point. Regarding fig. 5.2 EWSB is not possible in the top left corner and excludes the region where $\mu^2 < 0$; the LSP

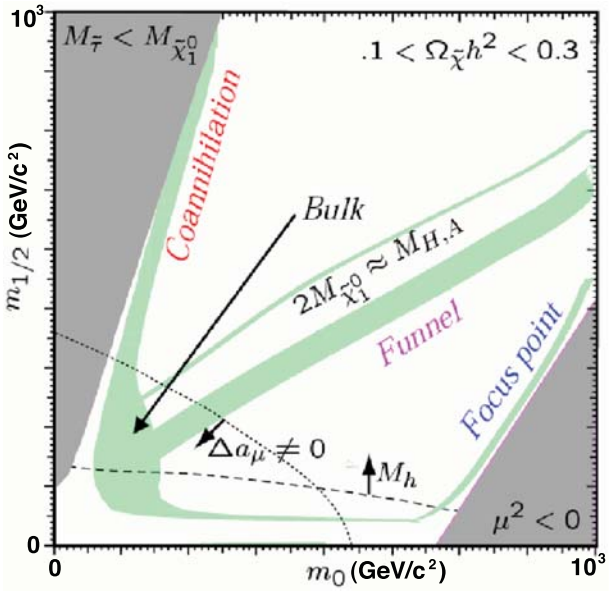

Figure 5.2: Diagram illustrating the region of mSUGRA parameter space for the SU3 point. Shown is the primary test point, entitled the SU3 "bulk" point, which was employed in this analysis and constitutes one of the cMSSM benchmark points of the ATLAS full simulation studies.

would be EM charged in the bottom right region; and the remaining unshaded area to the right is where the relic density is too large and the Universe is over-closed. It should also be pointed out that these regions of cMSSM parameter space are extremely sensitive to the Standard Model input parameters, e.g. m_t or m_b.

The mSUGRA point known as "SU3" is characterised by the following values of the model parameters:

$$m_0 = 100 \text{ GeV/c}^2,\ m_{\frac{1}{2}} = 300 \text{ GeV/c}^2,\ A_0 = -300 \text{ GeV},\ \tan\beta = 6 \text{ and } \text{sign}(\mu) > 0.$$

This point in mSUGRA space was selected in order to exemplify the method of discriminating between SUSY and UED, employed in this work.

Sparticle	$\tilde{\chi}_1^0$	$\tilde{\chi}_2^0$	$\tilde{g}$	$\tilde{u}_R$	$\tilde{u}_L$	$\tilde{d}_R$	$\tilde{d}_L$	$\tilde{e_R}$	$\tilde{e_L}$	h^0
Mass (GeV/c^2)	117.9	218.6	717.5	611.8	631.5	610.7	636.3	155.5	230.5	114.8

Table 5.1: Some example sparticle masses for the SU3 'bulk' point under investigation. This spectrum was calculated using ISAJET-7.71.

ISAJET together with HERWIG were used for the generation of the SUSY samples. ISAJET/ISASUGRA [121, 122] was employed to calculate the sparticle masses, lifetimes and branching ratios within a specified SUSY breaking model. A separate package called ISAWIG [123] is then used to take the output of the ISAJET package and convert it to a readable format by HERWIG [124, 125]. Thereafter, HERWIG is used to simulate the events themselves, i.e. carrying out the leading order matrix element calculation, partonic showering and hadronisation.

In addition HERWIG also, importantly, treats the spin correlations in all $2 \rightarrow 2$ R-parity conserving production processes and all cascade decay processes. The particular versions of the Monte Carlo generators used were: ISAJET-7.71 and HERWIG-6.507. A GEANT04 [126] full simulation of the ATLAS detector was then carried out within the ATLAS offline analysis framework, Athena. Two SUSY samples were used for the expected SUSY signal and background events. Firstly, an inclusive SUSY sample (with a $\sigma_{LO} = 18.5$ pb) was produced corresponding to an equivalent integrated luminosity of 8.17 fb^{-1}. In addition, a sample of direct slepton pair production was also simulated which consisted of all possible $2 \rightarrow 2$, parton to slepton, processes were implemented. This sample had a cross section of 0.27 pb and an equivalent integrated luminosity of 106.75 fb^{-1}. All results were normalised to, and so are quoted for, 30 fb^{-1} which is equivalent

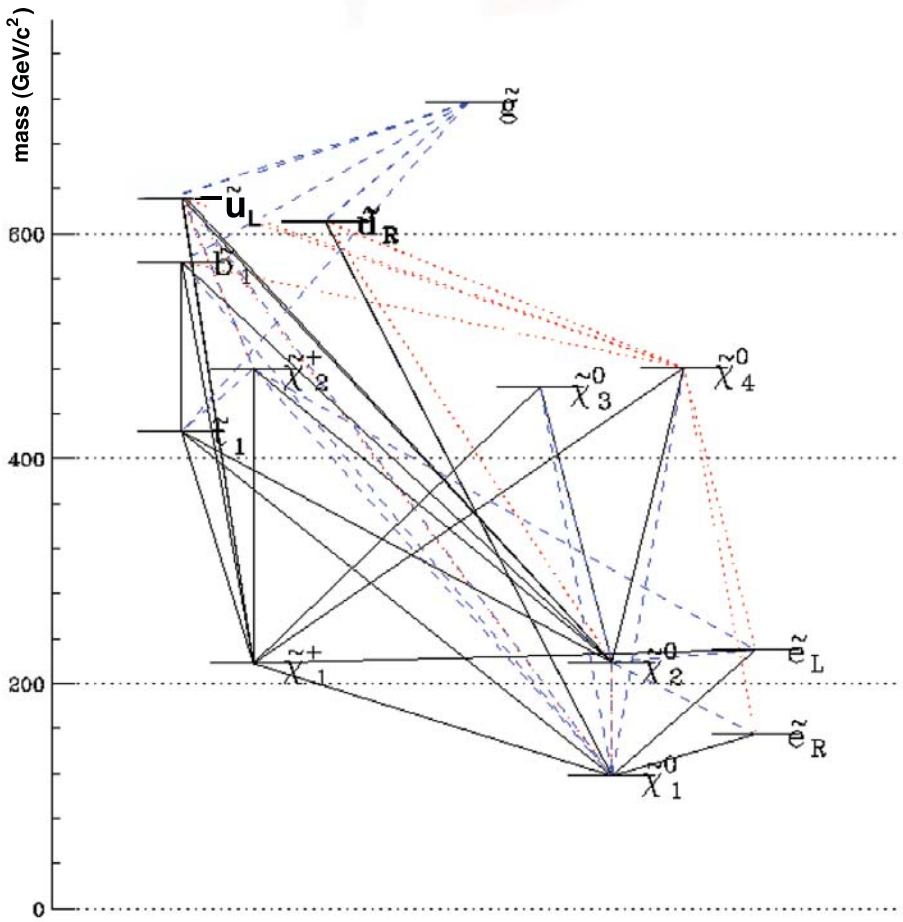

Figure 5.3: Part of the sparticle spectrum for the mSUGRA SU3 bulk point under investigation which has $m_0 = 100$ GeV/c^2, $m_{\frac{1}{2}} = 300$ GeV/c^2 $A_0 = -300$ GeV and $\tan\beta = 6$, $\mu > 0$. The y-axis labels the sparticle masses in GeV/c^2. The horizontal displacement of the sparticles has no meaning other than for clarity. Solid black lines indicate branching ratios (BRs) greater than 10%, dashed blue lines show BRs in the range $1\% \rightarrow 10\%$, while red dotted lines show BRs in the range $0.1 \rightarrow 1\%$.

to 1.0 nominal LHC years of running.

The Analysis Object Data (AOD) analysis stage was carried out using the EventView analysis framework [127]. Tabulated details of the two signal data samples are summarised in table 5.2 presented at the end of the chapter.

Due to the nature of the signal only certain topologies for each background are important. Furthermore, computational resources for the full simulation stage are formidable. So in order to expedite the generation of the background processes a filter was employed. This is a set of parton-level cuts made on a variety of variables including the flavour of lepton, lepton multiplicity and the pseudorapidity and p_T of the lepton. The filter, together with the resulting efficiency, are presented in each subsection (see later) for each background process used in this work.

5.2 Backgrounds

A background process is, by definition, any process that provides a similar detector signature to that of the signal event, which, for the signal process at hand, contains two opposite sign, same flavour (OSSF) leptons, missing transverse momentum and a small amount of hadronic energy. The background processes which provide similar detector signatures to that of the signal process can be achieved through one of two ways. Firstly, processes which are not by definition the signal one of interest, which produce a final state consisting of leptons, $\not{p}_T$ together with a small amount of hadronic energy. The second way is through photons or jets produced in the event which fake the leptons and which are accompanied by $\not{p}_T$ and hadronic energy. There are contributions to the background from Standard Model and SUSY processes.

A vast array of Standard Model and SUSY processes exist which could cause significant backgrounds to this exclusive SUSY channel of interest. Furthermore, the question that needs to be addressed is how detrimental the various background processes are to the signal channel. That is, to what extent is one able to observe a signal above the background distribution. To answer this then, requires resorting

to looking at each background individually to see which ones might be the most harmful. The most prominent Standard Model backgrounds envisioned for this analysis are the direct production of massive vector dibosons $W^{\pm}W^{\mp}$, $W^{\pm}Z^0$ and Z^0Z^0. Also the $t\bar{t}$, $W^{\pm}$+jet and Z^0+b-jet processes may also provide possible sources of background.

Finally, for completeness, the $W^{\pm}+\gamma$ and $Z^0+\gamma$ backgrounds are considered in order to check their influence how observable the signal process is. A brief discussion on each background will now be given by visiting each one in turn.

5.2.1 Direct pair production of vector bosons $W^{\pm}W^{\mp}$, $W^{\pm}Z^0$ and Z^0Z^0

The direct production of massive vector dibosons forms one of the main irreducible backgrounds for the signal process of interest. Some of the leading order (LO) Feynman diagrams are schematically shown in fig. 5.4 for the case of $W^{\pm}W^{\mp}$ where there are three, and fig. 5.5 for $W^{\pm}Z^0$ and Z^0Z^0. $W^{\pm}W^{\mp}$ events can contribute to the background by considering the process $W^+W^- \rightarrow l^+\nu l^-\overline{\nu}$, i.e. two high p_T leptons, $\not{p}_T$ from the undetected neutrinos and hadronic energy arising from the initial state QCD radiation.

For the case of the $W^{\pm}Z^0$ background, it can produce the signature of the signal process in one of two ways. Firstly, when both bosons decay leptonically; where one of the final state leptons is mis-measured and consequently, escapes detection, thus it generates false $\not{p}_T$. In the latter, one boson can decay hadronically and the other leptonically. Here a mis-measurement of a jet can falsify the $\not{p}_T$ signal or a jet could fake a lepton. The former case is the predominantly occurring one. Finally, for the Z^0Z^0 case, one is concerned with the signature $Z^0Z^0 \rightarrow l^+l^-\nu\overline{\nu}$, where again, similar to the $W^{\pm}W^{\mp}$ case, two high p_T leptons

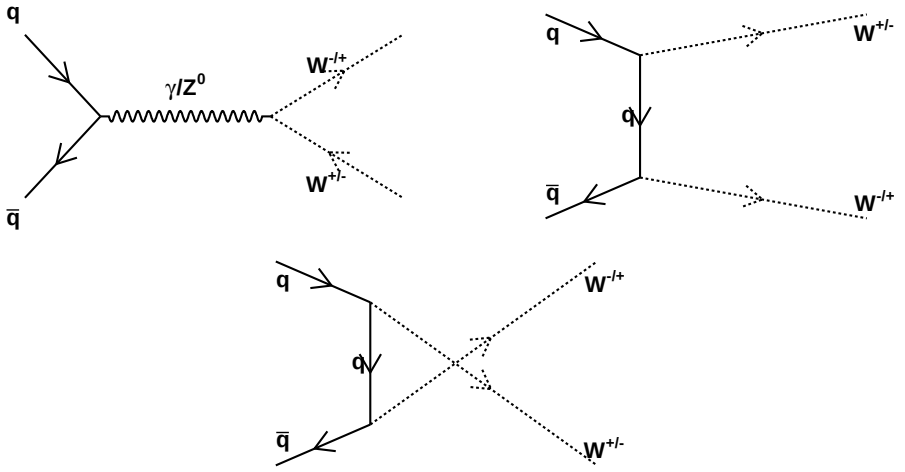

Figure 5.4: The three leading order Feynman diagrams for $W^{\pm}W^{\mp}$ production at the LHC. They are, clockwise from top left, the s-, t- and u-channel diagrams respectively.

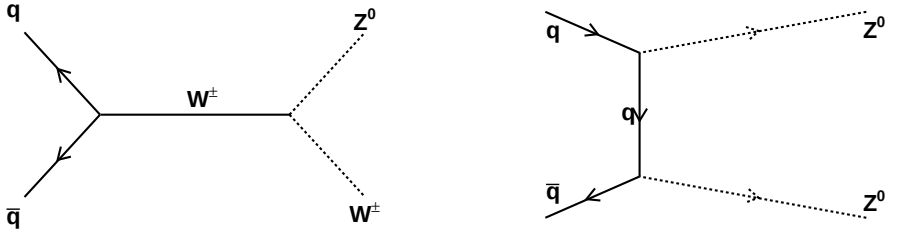

Figure 5.5: Some of the leading order Feynman diagrams for $W^{+}Z^{0}$ and $Z^{0}Z^{0}$ production at the LHC. They are, from left to right, the s-channel and t-channel diagrams respectively.

plus $\not{p}_T$ from the neutrinos mimics the signal process. All Monte Carlo samples employed were inclusive diboson production samples and a leptonic filter was employed, which was:

$$p_T(l = \text{ e or } \mu) > 10 \text{ GeV/c and } |\eta| < 2.8 \text{ (for one lepton only).}$$

The efficiency of the filter was, for case of $W^{\pm}W^{\mp}$ 35%, for $W^{\pm}Z^{0}$ 29% and for

Z^0Z^0 19%.

As for any viable method of studying a signal process of interest, the requirement that the Monte Carlo generation and simulation stage needs to accurately simulate the backgrounds plays a vital aspect of any analysis. Furthermore, for backgrounds to new physics it is desirable to be able to measure the gauge boson pair cross-sections on-mass-shell and then, subsequently, extrapolate them to the off-mass-shell region which forms the irreducible background. These off-shell effects are induced by QCD and/or QED initial state radiation and final state radiation or by intermediate on-shell boson mass states. To do this requires the full Z^0/γ^* interference structure, for the specific case of $W^{\pm}W^{\mp}$ production, which is not implemented in the cases of PYTHIA [128–130] nor MC@NLO [131, 132] nor ISAJET, which all, depending upon the process, implement the narrow width approximation. This interference structure is only provided by HERWIG which is also advantageous since it includes spin correlation effects and accounts for the polarisations in the decays of the bosons which other Monte Carlo generators neglect. For the specific details of the samples the reader is referred to table 5.2.

5.2.2 The $t\bar{t}$ Background

Another background that is foreseen as potentially detrimental is that of $t\bar{t}$ production when one considers the case when the pair decays fully leptonically, i.e. $t\bar{t} \rightarrow W^+bW^-\overline{b} \rightarrow l^+\nu bl^-\overline{\nu}\overline{b}$. This gives rise to two OSSF leptons in the final state, missing p_T from the two undetected neutrinos and hadronic energy. The latter arises from the presence of b-jets and any additional initial state and final state QCD radiation. Another possibility is a mismatch of a final state lepton and an additional, isolated lepton that is identified arising from a b or c decay (i.e. isolated leptons which originate from, but are not associated by the recon-

struction, with those b or c jets). Although suitable cuts are envisioned to remove most of this background it is still, nonetheless, important to consider. This is because despite its small (10^{-2}) branching ratio to leptons, its inclusive production cross-section is large ($\sim$ 590 pb [96]). MC@NLO interfaced with Jimmy [133] was used in the production of this sample. This was because it gives a more accurate calculation of the cross-section than a LO Monte Carlo generator and so consequently of the production of the final state distributions of the irreducible background and thus is more accurate and agreeable with experiment. The sample was produced with a leptonic filter; the requirement that at least one top decayed to a lepton (e, μ or τ). The resulting efficiency of the filter was 54%.

5.2.3 The $W^{\pm}+\gamma$ and $Z^0+\gamma$ Backgrounds

Another potential background are the cases of radiative $W^{\pm}$ or Z^0 production, that is, when a single $W^{\pm}$ or Z^0 is produced in association with a γ which then proceeds to imitate a lepton in the detector. Furthermore, for the $Z^0+\gamma$ background, in addition to the γ faking a lepton the final state lepton escapes detection and then contributes to the $\not{p}_T$. Both Monte Carlo samples were produced using the generator PYTHIA.

5.2.4 The $W^{\pm}$+jet Background

Similar to the case of radiative $W^{\pm}$ production but instead of a γ, a heavy flavour quark jet or gluon jet can provide the extra lepton through their respective decays. Here a $W^{\pm}$ is produced and through one of the b-quarks subsequent decays is where additional jets and/or leptons arise from the parton shower. Although the cross-section for this process is relatively high ($\sim$ 11.3 pb), the expected rate of jets faking electrons is 10^{-4}-10^{-5} [96], which is rather small but was,

nevertheless, still generated for completeness. For this background process the generator, AcerMC [134], was employed together with PYTHIA. A leptonic filter was employed in the generation of this sample, which was:

$$p_T(l = \ e \text{ or } \mu) > 50 \text{ GeV/c and } |\eta| < 2.7 \text{ (for one lepton only).}$$

5.2.5 The Z^0+b-jet Background

A further potential background is that which stems from the associated Drell-Yan and b-quark production which is recognised as an irreducible background to many MSSM processes. There are two ways in which this can mimic the signal process. In the first, predominant case, a b-jet is misidentified for a lepton and one of the leptons emanating from the Z^0 escapes detection. The second case, $Z^0 + b$, the B-hadron has a small but finite probability to decay to a lepton and hadrons. So again, if a lepton, emanating from a Z^0, escapes detection with the additional lepton arising from the semi-leptonic decay of the B-hadron this gives a 'signal'-like signature in the detector. The associated production of a Z^0 boson with a b-jet is problematic in hadron colliders owing to the fact that the b-quark can be produced either in the hard subprocess (order α_s^1) or arise as a remnant from the proton structure functions.

However, the former partially accounts for the higher order process and so it is, therefore, not possible to add these two diagrams directly. The end result incurred is that of double counting. This undesirable end result, therefore, necessitates the use of a specific Monte Carlo generator which takes into account this problem and implements the correct subtraction procedure. For this reason, AcerMC, interfaced with PYTHIA, was employed to carry out the initial state and final state radiation and hadronisations. AcerMC is advantageous since it contains

specific algorithms to do this. It also takes into account spin correlations in the decay of the Z^0 boson and the angular correlations between the resulting leptons and quarks.

5.2.6 The SUSY Background

An important and intriguing facet of the processes that constitute backgrounds to the SUSY signal process of interest is SUSY itself. At the LHC the SUSY background is expected to be dominated by the production of coloured sparticles such as gluinos and squarks because of the large coupling strength of the strong interaction. The generic features will be a plethora of production signatures with a wide variety of many different signatures and interactions with complicated cascade decays of these heavier SUSY particles culminating in a vast array of complex final states, with a large jet multiplicity, $\not{p}_T$ and zero, one, or greater than one, final state leptons. Furthermore, for the case of dileptons the SUSY processes admit the following leptonic combinations: same sign same flavour (SSSF), same sign opposite flavour (SSOF), opposite sign same flavour (OSSF) and opposite sign opposite flavour (OSOF). In addition to direct slepton production mentioned previously (section 5.1), there are three remaining types of LO production mechanisms of SUSY at the LHC:

i) direct pair production of spartons ($\tilde{q}s$ or $\tilde{g}s$) via the hard subprocesses: $gg, q\overline{q} \rightarrow \tilde{g}\tilde{g}$ or $\tilde{q}\tilde{\overline{q}}$, and $qg \rightarrow \tilde{q}\tilde{g}$;

ii) direct pair production of gauginos ($\tilde{\chi}^0_{i=1,2,3,4}$ or $\tilde{\chi}^{\pm}_{i=1,2}$) via the hard subprocesses: $q\overline{q} \rightarrow \tilde{\chi}^{\pm}_i\tilde{\chi}^{\mp}_j$ or $\tilde{\chi}^{\pm}_i\tilde{\chi}^0_j$ or $\tilde{\chi}^0_i\tilde{\chi}^0_j$;

and finally,

iii) associated gaugino production (sparton and gaugino) via the hard subprocesses: $q\overline{q}$ or $g\overline{q} \rightarrow (\tilde{q}$ or $\tilde{g}) + \tilde{\chi}^{\pm}_i$, or, $(\tilde{q}$ or $\tilde{g}) + \tilde{\chi}^0_i$.

The production of uncoloured particles via cascade decays often dominates over direct production. Having explained the production mechanisms for SUSY backgrounds at the LHC the next step is to consider how and why the various processes constitute a background process.

Each of the above mentioned processes can mimic the signal process. For case (i), the cascade decays of the heavy spartons can give rise to two OSSF leptons, $\not{p}_T$ and jets. Although a more indirect way, but nonetheless still possible, is indirect dislepton production (which constitutes a background to our process since this can mimic the dislepton signature) can also arise from these cascade decays. As an example consider the process: $\tilde{g}\tilde{g} \rightarrow \tilde{\chi}_1^- + t + \overline{b} + \tilde{\chi}_1^+ + \overline{t} + b$ which manifests itself in the detector as 2OSSF leptons+ $\not{p}_T$ $+2\tilde{\chi}_1^0 + 2\nu + jets$.

Fortunately, the majority of these events should be accompanied by substantial jet activity which allows for their removal inside the fiducial region of interest. Indirect dislepton pair production can also, in addition to (i), proceed via the production mechanism in (ii) and (iii) and their subsequent cascade decays. These give rise to numerous possibilities for processes which result in OSSF dileptons, $\not{p}_T$ and little hadronic energy, which, therefore, necessitates their removal or measurement. Other example decay channels are: $\tilde{\chi}_2^0\tilde{\chi}_2^+ \rightarrow l^+\tilde{l^-}\tilde{\chi}_1^0 W^+ \rightarrow l^+l^-\tilde{\chi}_1^0\tilde{\chi}_1^0$jet jet or $\tilde{\chi}_1^+\tilde{\chi}_1^- \rightarrow \tilde{\chi}_1^0 W^+\tilde{\chi}_1^0 W^- \rightarrow \tilde{\chi}_1^0 + l^+ + \nu + \tilde{\chi}_1^0 + l^- + \overline{\nu}$, as shown schematically in fig. 5.6.

Again though, as is envisioned for the case of sparton production, the jet energy and multiplicity is expected to be large, allowing one to discriminate between them and the signal channel.

Finally, the direct production of disleptons can also overlap with the final state of the signal in cases where the slepton does not decay directly to an LSP and lepton, examples of which are the processes: $\tilde{l^\pm}\tilde{l^\mp} \rightarrow l^+\tilde{\chi}_2^0 l^-\tilde{\chi}_2^0 \rightarrow l^+\tilde{\chi}_1^0$jetjet

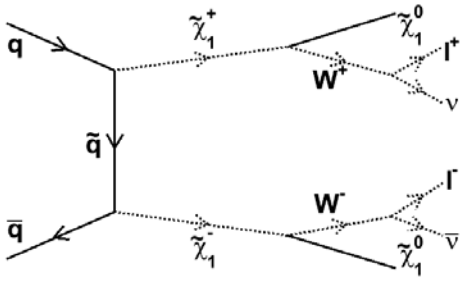

Figure 5.6: The Feynman diagram showing the direct production of gaugino pairs their subsequent cascade decays resulting in a final state of two OSSF leptons, missing p_T and a small amount of hadronic energy. This signature, therefore, overlaps with the final state of the signal process under study.

$l^-\tilde{\chi}_1^0$jetjet. Rather the decay proceeds via the production of two $\tilde{\chi}_2^0 s$, as for the case above, or via the decay of two $\tilde{\tau} s$ in the decay: $\tilde{\tau}_1^+\tilde{\tau}_1^- \rightarrow \tilde{\chi}_1^0\tau^+\tilde{\chi}_1^0\tau^- \rightarrow e^+\nu_e\overline{\nu}_\tau\tilde{\chi}_1^0 e^-\overline{\nu}_e\nu_\tau\tilde{\chi}_1^0$. Other potential backgrounds that are foreseen to be important are the processes: ($q\overline{q}$ or gg or VV) $\rightarrow \tilde{\nu}\tilde{\nu}$ or $\tilde{\tau}_{i=1,2}\tilde{\tau}_{j=1,2}$, where V denotes a vector boson. These are a little more cause for concern since the hadronic energy and jet multiplicities are expected to be low, which is similar to the signal process.

In addition to the two SUSY samples mentioned in the previous section, a third sample was simulated for the evaluation of the SUSY background. This third SUSY sample contained direct pure gaugino pair production processes. This simulated data sample was generated in order to acquire a more accurate knowledge of a background which is foreseen as being important for the signal process under study. This included all chargino and neutralino pair processes and the associated gaugino-sparton production processes. Again, HERWIG interfaced with Jimmy was used in the generation and the sample was reconstructed under release 12.0.6.

5.3 The SUSY and UED 'theoretical' Angular Distributions

In order to compare the Monte Carlo data samples with something, the 'theoretical' production angular distributions for diparent particles corresponding to each model, namely SUSY and UED, were also produced. It was also important to understand their shape and so very large samples were simulated for each model. A large sample of events was generated for each model, 271,000 events for each one. This corresponded to an integrated luminosity of 1000 fb^{-1} of reconstructed Monte Carlo data. HERWIG-6.507 was used in the generation. For the case of UED, no Monte Carlo event generator existed which implemented this model, so HERWIG was modified to generate slepton pairs according to the production angular distribution expected from the UED model, i.e. as if though they were Kaluza Klein (KK-) leptons rather than sleptons. No other process was modified. After the generation stage, the detector effects were simulated with the ATLAS fast simulation package, Atlfast [135,136]. The specific version of Atlfast employed was: AtlfastAlgs-00-02-09, AtlfastEvent-00-06-03 and AtlfastUtils-00-02-00. Again, as was the case for the full simulation data samples, all event generation, fast simulation and AOD analysis, using the EventView AOD analysis package, was performed within the Athena offline software framework [137], under release version 11.0.5.

5.4 Summary

A recapitulation of the signals and background Monte Carlo data samples used in the analysis are:

Process	MC Generator Employed	Cross section after filter (pb)	N_{MC}, sample	Equivalent integrated luminosity ($f\mathrm{b}^{-1}$)
SUSY, inclusive	HERWIG	18.59	158050	8.5
SUSY, slepton pairs	HERWIG	0.27	28850	106
SUSY, gaugino pairs	HERWIG	1.8	29600	16.3
Z^0Z^0	HERWIG	2.1	48550	23.1
$W^{\pm}W^{\mp}$	HERWIG	24.5	50000	2.0
$W^{\pm}Z^0$	HERWIG	7.8	49900	6.4
$t\bar{t}$	MC@NLO	461	410458	0.9
Z^0+b-jet	AcerMC	102	16094	0.2
$W^{\pm}$+jet	AcerMC	111	92756	0.8
$W^{\pm}+\gamma$	PYTHIA	11.3	81550	7.2
$Z^0+\gamma$	PYTHIA	3.8	44050	11.6

Table 5.2: A table that summarises the two SUSY signal reconstructed Monte Carlo data samples corresponding to the SU3 mSUGRA SUSY point, together with all the background reconstructed Monte Carlo data samples used in the analysis presented in this thesis.

- The signal channel under investigation is the direct dislepton process which proceeds via the DY process in the s-channel: $q\overline{q} \rightarrow Z^0/\gamma^* \rightarrow \tilde{l^{\pm}}\tilde{l^{\mp}} \rightarrow \tilde{\chi}_1^0 l^{\pm}\tilde{\chi}_1^0 l^{\mp}$. The UED equivalent to this process is the decay: $q\overline{q} \rightarrow Z^0/\gamma^* \rightarrow l_1^{\pm}l_1^{\mp} \rightarrow \gamma_1 l^{\pm}\gamma_1 l^{\mp}$, where, in both cases, the leptons are assumed to be either electrons or muons. The distinctive signature will therefore, for each model, consist of a highly energetic OSSF lepton pair with associated $\not{p}_T$ and inevitably a small amount of hadronic energy.
- A background process, by definition, is any one that mimics the distinctive signature of the event by its final states overlapping with those of the sig-

nal process in phase space and thereby contributing to the measured cross sections. There are two contributions, arising from Standard Model and SUSY processes. The harmful effects posed by the various types of background have been discussed, with the most detrimental foreseen as those arising from the dibosons ($W^{\pm}W^{\mp}$, $W^{\pm}Z^0$ and Z^0Z^0), $t\bar{t}$, $W^{\pm}$ or $Z^0 + \gamma$, $W^{\pm}$+jet, $Z^0 + b-$jet and SUSY processes, to which, there is a vast array of processes.

- To obtain a detailed as possible simulation of the passage of the generated Monte Carlo event data through the ATLAS detector, the full simulation chain was used for all Monte Carlo data samples.
- Very large samples for the SUSY and UED 'theoretical' angular distributions, to which the fully simulated Monte Carlo samples were compared to, were generated. A fast simulation was then carried out using Atlfast. In total, an integrated luminosity equivalent to 1000 fb^{-1} was simulated for each model.
- Finally, the chosen primary test point of study in mSUGRA parameter space was that which corresponded to the SU3 'bulk' region which is charactersied by the model parameters:

$$m_0 = 100 \text{ GeV/c}^2,\ m_{\frac{1}{2}} = 300 \text{ GeV/c}^2,\ A_0 = -300 \text{ GeV},\ \tan\beta = 6 \text{ and } \text{sign}(\mu) > 0.$$

Chapter 6

Anatomy of the Analysis Part II: Method and Results

6.1 Introduction

AS alluded to in earlier chapters (chapters 1 to 3), one of the main goals of the LHC and, furthermore ATLAS, is to search for new physics beyond the Standard Model in the TeV energy scale. The most prominent, and consequently by far, the most studied TeV-scale model is SUSY. The archetypal signature (and working under the assumption that R-parity and, furthermore, KK-parity are conserved) is one where the SUSY particles must be pair produced and the lightest supersymmetric particle (LSP) is stable. This will manifest itself in the detector as leptons or jets which have large transverse momentum from the cascade decays of heavier sparticles as well as $\not{p}_T$ arising from the undetected LSP.

However, recently the notion that another set of models, namely UED, could appear to have extremely similar collider phenomenology to that of low energy SUSY, thus seemingly masquerading as SUSY, has been recognised. A way to discriminate between the two models is then needed. Various discriminants to help were discussed with spin, or more specifically, the property that their spins differ, appears to be able to provide the most conclusive answer (see section

2.5.2). Thus, the work presented in this chapter investigates the validity of a method whose purpose is to distinguish between two sub-models of SUSY and UED, namely mSUGRA and mUED respectively, and each of which the reader should now have become acquainted with.

The proposed method rests upon measuring the spins of the new, hypothetical particles posited by each model by using an angular variable which is sensitive to the polar angle of the final state leptons. The method discussed is an extension to the one initially proposed by A.J. Barr in the paper "Measuring slepton spin at the LHC" [93]. In fact it should be pointed out here from the outset that the method is completely different to the earlier method suggested by the same author [138] (see also [139]). This different approach invokes the method of measuring the charge asymmetry in lepton-jet invariant mass distributions for particle cascade decays. The method presented here builds upon that proposed in the new paper but extends it to utilizing the ATLAS detector and an up to date full GEANT simulation of it. Furthermore, with the final aim to confirm or confute the assertion that the angular variable, $\cos\theta^*_{ll}$, can indeed, measure the spins of sleptons in direct slepton pair production. Thus, in the process can lend credence to the claim that it is a suitable discriminant in differentiating between the mSUGRA and mUED models. Although the work concentrated solely on using the ATLAS detector, similar arguments for the method should also apply to a general purpose detector such as the CMS detector.

The angular variable, $\cos\theta^*_{ll}$, will be introduced in the next section wherein it will be shown that it is, indeed, sensitive to the production polar angle in slepton pair production. Having already presented the various Monte Carlo event generator and detector simulation samples for both the signal and background processes, the test point in SUSY space and the theoretical angular distributions

for each model under scrutiny in the previous chapter, then allows us to proceed directly to the strategy adopted for the analysis, presented in section 6.3 onwards.

Finally, the final two sections present the results, showing the experimentally-measurable angular distributions and the various background distributions; and conclusion. Importantly, the main systematic uncertainties will be addressed in the next chapter.

6.2 Distinguishing between sleptons and KK-leptons: $\cos\theta^*_{ll}$

As alluded to in Chapter 2 the method here relies upon making a spin measurement to differentiate between SUSY and UED. This spin determination, however, is challenging at hadron colliders. The typical way of measuring the spin of a decayed particle is to, firstly, reconstruct the initial parton-parton centre-of-mass frame of reference which produced it from the decay products. Thereafter, by measuring the angular distributions in this frame of reference furnishes us with the full spin information, independent of the resulting boost. Now this is appropriate for a future lepton linear collider and furthermore, has indeed been proposed. That is, the final state lepton angular distributions could be used to differentiate between the two models using a future high energy e^+e^- collider [76, 140]. However, at a hadron collider the energy and p_z component of the momentum of the incoming partons are unknown thus rendering the initial parton-parton centre-of-mass, of the whole event, unknown. Furthermore, with the production of invisible particles in the event (from the LSP in SUSY or LKP in UED) their momenta are unknown and, consequently, recovery of the initial parton-parton centre-of-mass frame from the final state products is not feasible.

To make a spin measurement at a hadron collider then requires one to consider a distribution that is a function of a relativistic invariant (so not to be reliant upon the need for the centre-of-mass frame which is unrecoverable) constructed out of the decay products of the decayed particle under scrutiny. Importantly, this relativistic invariant variable must be sensitive to the particles spin. One such variable which satisfies this criterion is the difference in pseudorapidities between the final state leptons, $\Delta\eta_{l^+l^-}$. This quantity, $\Delta\eta_{l^+l^-}$, is advantageous since it is longitudinally boost invariant so that by using a function of it we are not constraining ourselves to be reliant upon the need for determining the centre-of-mass along the beam axis. Furthermore, as the leptons are highly relativistic the pseudorapidiy is, to a good approximation, equal to their true rapidities. Also, η is advantageous since it only depends upon θ, which, as seen before, is easy to measure experimentally and has a simple interpretation. Importantly though, the inter-lepton η difference, $\Delta\eta_{l^+l^-}$, is sensitive to the slepton or the KK-lepton production angle, in exactly the same manner that the polar angle of the final state contains information of the parent's production angle (the leptons 'inherit' some knowledge of the polar angle or η of their KK- or s- parents).

Now, concerning ourselves with the production angular distributions of the heavy leptons, eq. 2.10 and eq. 2.11, excited heavy leptons (s- or KK-) which are produced significantly above threshold will have decays that are boosted in the laboratory frame. Furthermore, as long as the mass difference between the heavy lepton (the parent particle) and the LSP or LKP (i.e. $\Delta m = m_{\tilde{l}} - m_{\tilde{\chi}^0_1}$ for SUSY or $\Delta m = m_{l^{(1)}} - m_{B^{(0)}}$ for UED) remains small the final state leptons are well correlated with those of their heavy lepton parents. The implication of this is that a pair of leptons from a slepton pair decay will be, on average, more widely separated in polar angle or less widely separated in η (since larger values

of θ correspond to lower values of η) than the lepton pair emanating from the decays of KK-lepton pairs.

Although perfectly feasible, this discriminant, $\Delta\eta_{l^+l^-}$, and its resulting distribution are rather difficult, by eye, to see the differences between the two models. Therefore, to allow for a more direct comparison to the production angular distribution proposed by the theoretical models the final, Lorentz invariant, discriminating variable proposed is the angular variable:

$$\cos\theta^*_{ll} \equiv \cos\left(2\tan^{-1}\exp(\Delta\eta_{l^\pm l^\mp}/2)\right) \equiv \tanh(\Delta\eta_{l^\pm l^\mp}/2), \tag{6.1}$$

(for more on this variable and the identity please refer to Appendix B). This is the cosine of the polar angle between each lepton and the beam axis in the longitudinally boosted frame, within which, the pseudorapidities of the leptons are equal and opposite. Its simpler, geometrical interpretation and one which adheres to the SUSY and UED production angular distributions, further justify it. It is this angular variable, $\cos\theta^*_{ll}$, that is the final defining variable and the one that is employed in this work to measure the spins of the SUSY particles. Fig. 6.1 shows that $\cos\theta^*_{ll}$ is indeed well correlated with the parent production angle, $\cos\theta^*$. Thus, it is apparent that, on average, the experimental observable, $\cos\theta^*_{ll}$, is smaller for SUSY (fig. 6.1, left-hand plot) than for UED (fig. 6.1, right-hand plot). Again, following along the same arguments as was given for fig. 2.8, although these correlation plots corresponded to the LHC point 5 one should still believe that the same argument will hold and that the degree of correlation still exists for the SU3 bulk point studied in this work. The figure, therefore, attests to the fact that $\cos\theta^*_{ll}$ can indeed be usefully deployed as a spin-sensitive discriminant in slepton/KK-lepton pair production at hadron colliders, just as

$\cos\theta^*$ is often used in spin measurements in cleaner environments.

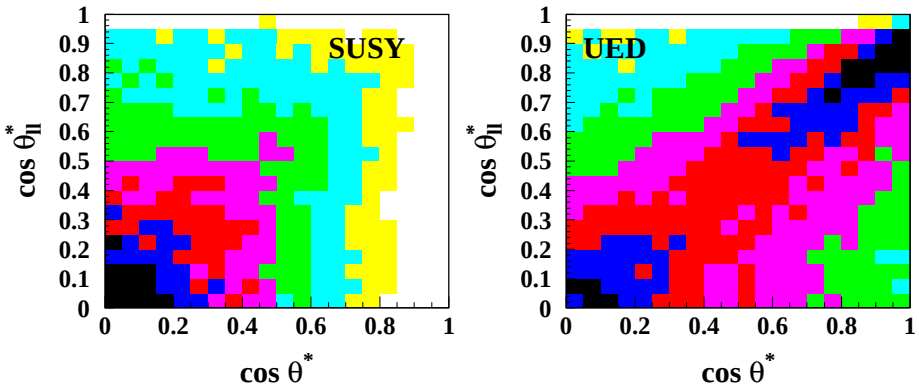

Figure 6.1: Plots showing the high degree of correlation between the dislepton angular variable $\cos\theta^*_{ll}$ (y-axis) and parent production angular variable $\cos\theta^*$ (x-axis) when the parent particles are, in the left-hand plot, sleptons or in the right-hand plot, KK-leptons, in the centre-of-mass frame. Lighter coloured regions correspond to sparsely populated regions. The high degree of correlation attests to the fact that $\cos\theta^*_{ll}$ can be usefully deployed as a spin-sensitive discriminant in slepton, KK-lepton pair production at the LHC. The mass spectrum corresponds to that of the LHC point 5 in mSUGRA space and the normalisation is arbitrary. Figure taken from [93].

6.3 Analysis Strategy

The general approach taken here is one which proceeds along similar lines as those whose purpose it is to discover new physics, e.g. SUSY. Furthermore, any analysis designed to search for new particles has to satisfy a number of competing criteria. Most importantly though, of a good analysis, is one which is maximally sensitive to the signal process of interest and at the same time minimising the background as much as possible. With the additional requirement that, after accounting for

the lepton reconstruction efficiency and fiducial cuts, the signal must be visible and not swamped by the background and, importantly, over the full range of $\cos\theta^*_{ll}$. This is an essential requirement in order to make the spin measurement and, thus, underpins the analysis. After the background subtraction it is most desirable to have any sparsely populated regions in $\cos\theta^*_{ll}$ fiducial space for signal only, absent. Thus, focusing on the final state topology of the signal is paramount in selecting the signal events, to obtain the $\cos\theta^*_{ll}$ distributions which underpin the method.

From considering the topology of the signal process, the signature for the dislepton events gives rise to the presence, in the final state, of two OSSF leptons, missing E_T from the production of two LSPs and a small amount of hadronic energy from the initial state QCD radiation. This is radiated by the initial, incoming, colliding quarks. The presence of two isolated, high p_T leptons in the final state presents a simple signature to trigger on. Thus, to reconstruct these leptonic events in association with missing E_T and initial state radiation in ATLAS, a detailed and thorough understanding of electron, muon and missing E_T reconstruction is required. This requires one to become sufficiently acquainted with:

- lepton (electron and muon) reconstruction efficiencies, purities;
- lepton (electron and muon) residuals and fractional p_T resolutions;
- jet/hadronic energy veto efficiencies;
- missing E_T resolutions and correlations.

Finally, a clear and thorough understanding of what the backgrounds are and to what extent they overlap in phase space with the signal process is required. A suitable set of kinematic cuts are foreseen which serve to avoid the background dominating the signal over the full extent of $\cos\theta^*_{ll}$ region. These are a set of

characteristics that the event must posses and are defined by the values of the cuts. The only means of finding the most favourable set of cut values will involve recourse to some sort of optimisation. This will be discussed in more detail in a later section.

A summary of the method adopted and steps taken for the work in this thesis may be broken down into the following four stages:

- **Preselection cuts**

  Employ a set of basic cuts prior to the main analysis cuts that will be described shortly.

- **Migrations at cut boundaries**

  Apply six cut variables, each set to their default values and which are to be discussed in the next section, to the results of the generated and simulated Monte Carlo data samples. The resulting distributions, for each cut variable, are then examined, in order to gain an insight into those variables which are, and those which are not, sensitive to the region of where the cut is employed. Furthermore, if the distribution of interest displays a strong dependence upon a selection parameter, which are typically poorly known, this can then alter the results by a significant amount and is, consequently, reflected in a large systematic uncertainty. Those distributions which were found to have a significant fraction of events close to the vicinity of where their respective cut was applied were chosen for deployment in the optimisation procedure. For those parameters which were found not to be sensitive to where the cut was made, they took their respective default values and were not involved in the optimisation procedure.

- **Optimisation**

  This forms one of the novel extensions to the original method carried out in the paper [93]. In carrying out a method of optimisation of cuts, a final figure of merit is needed which has the power of discriminating between the SUSY and UED models. This is the purpose of a statistical test where a quantity called a *test statistic* is employed to quantify the significance level or the statistical significance (S).[a] It will depend upon the nature of the scientific investigation under study. For this work a statistical test used in either confirming or refuting a scientific theory is required, thereby acting as a discriminant between the two hypotheses under study. Setting up and carrying out a hypothesis test is an essential part of statistical inference with the ultimate goal, by selecting a particular test statistic to quantify the significance, is to obtain the best possible separation (i.e. achieve maximal separation) between the two hypotheses. The situation at hand pertains to the use where two physical models or hypotheses, SUSY and UED, need to be tested for their validity in light of full reconstructed Monte Carlo event data. This then leads one to attempt to try and quantify the evidence in the reconstructed Monte Carlo data for, for and against the validity of each hypothesis. Now due to the inherent statistical nature of particle physics one uses a *confidence level (CL)* which can be attached to the assertion that the observed data is or is not well described by a given, specified hypothesis. A low CL indicates that the data is not compatible with the hypothesis and so the hypothesis is, therefore, untenable. In addition, it is also a way of describing the spread of a distribution especially in the tails.

[a] In particle physics the statistical significance is usually understood to be the probability to find a value of a test statistic beyond a certain pre-specified critical value.

It is calculated from a test statistic, which itself, is determined from the information yielded by carrying out the test. For the case at hand, the test statistic should be a measure of how 'SUSY-like', that is, how compatible with the SUSY hypothesis the data is. The higher its value, the more SUSY-like the data is. The CL is then given by:

$$CL = \int_{\chi^2_{\text{min}}}^{\chi^2_{\text{measured}}} p(\chi^2) d\chi^2, \tag{6.2}$$

where χ^2_{min} is the minimum possible value of the test statistic and χ^2_{measured} is the actual value from the hypothesis result. For construction of a test statistic we evoke the formal Neyman-Pearson Lemma [141–143] for hypothesis testing. This theorem, despite some limitations such as the fact that it is only valid for simple hypotheses[b], gives considerable discriminating power by allowing the likelihoods of each hypothesis to be related through their ratio which is assigned the letter Q here. It can be defined as:

$$Q = \left(\frac{L_{SUSY}}{L_{UED}} \right) = \left(\frac{P(D|SUSY)}{P(D|UED)} \right), \tag{6.3}$$

where L_{SUSY} and L_{UED} are the likelihoods for the SUSY and UED models respectively. For the work presented here, L_{SUSY} and L_{UED} are computed in the following three steps. Firstly, the Pearson χ^2 statistic is evoked and summed over all bins i in the $\cos\theta^*_{ll}$ variable:

$$\chi^2 = \sum_i \frac{(d_i - t_i)^2}{(\sigma^d_i)^2 + (\sigma^t_i)^2}, \tag{6.4}$$

[b] A simple hypothesis is one which specifies the data distribution completely.

where d_i and t_i are the fraction of events in bin i for the SUSY Monte Carlo reconstructed data and theoretical distribution respectively and the σ^2s are their respective variances. That is, 6.4 is the squared difference between the observed values of the SUSY Monte Carlo reconstructed data and the SUSY or UED theoretical predictions, suitably weighted by the errors of each distribution. Secondly, the p-values are then calculated using the resulting value for the summed χ^2 obtained in the previous step and using seven degrees of freedom. Finally, by taking the natural logarithm of the returned p-value furnishes us with the required log likelihoods for each model respectively. The likelihood is the combined probability, or probability density, that a particular set of data, D, would be produced for a particular value of SUSY or UED. This is the definition given in both the numerator and denominator on the right hand side of equation 6.3. Q is the ratio of the conditional probabilities of a set of actual observations from the reconstructed Monte Carlo data under the SUSY hypothesis to that under the UED one. For this reason it is sometimes called the likelihood ratio. For convenience we use the natural logarithmic form of this ratio, defined as:

$$\ln(Q) = \ln\left(\frac{L_{SUSY}}{L_{UED}}\right), \tag{6.5}$$

and this is our test statistic used for optimising the cuts. What is desirable is that in maximising this quantity corresponds to maximising the separation between the two hypotheses. So the optimal cut values will allow one to differentiate between the two models. It should be noted here that a binned likelihood method was used.

The method invoked relied upon varying a number of parameters, from the

six that will be presented in the next section, in order to constrain the region where the optimum value of this final figure of merit exists. Considering migrations at cut boundaries allows us to acquire some sort of handle on which cuts to vary and which ones not to.

- **Background Subtraction**

  After applying the series of cuts one is left with a distribution in $\cos\theta^*_{ll}$ with N events for Opposite Sign Same Flavour (OSSF) lepton pairs (denoted as OSSF(S+B′)). This will comprise the SUSY signal and both types of backgrounds: the SUSY combinatorial backgrounds and Standard Model backgrounds. We therefore subtract this background producing the residual 'Pure Signal' (OSSF(S)) distribution. An advantageous and consequently, frequently-used method for estimating background rates from data with high accuracy is that of 'background flavour subtraction' [144, 145]. The basic premise is that while the signal process contains an OSSF dilepton pair (due to lepton number conservation), the backgrounds can arise from any number of dilepton pair possibilities, each with equal probability: Same Sign Same Flavour (SSSF, e.g. e^+e^+) pair; Opposite Sign Opposite Flavour (OSOF, e.g. μ^+e^-) pair; or Same Sign Opposite Flavour (SSOF, e.g. $e^+\mu^+$) pair. For slepton pair production the majority of SUSY backgrounds are expected to have similar cross-sections in the OSSF (signal) and the OSOF (background) channels. Furthermore, it has been shown [146] that a simple OSSF-OSOF subtraction can provide a rather clean background subtraction for both the SUSY backgrounds and most of the Standard Model ones. For this reason, the OSOF $\cos\theta^*_{ll}$ event distribution was subtracted from its OSSF counterpart, i.e. for the purposes of this analysis the background

subtraction employed was:

$$\mathrm{N(OSSF(e^{+}e^{-} + \mu^{+}\mu^{-})) - N(OSOF(}e^{\pm}\mu^{\mp})). \tag{6.6}$$

Throughout, care was taken to ensure that the relevant distributions, both the OSSF and OSOF, were suitably normalised. Both an absolute normalisation (equal integrated luminosity) and relative normalisation (equal areas) were employed.

There was found not to be a great difference in efficiency between electrons and muons especially in p_T. Furthermore, although I did not look at trigger efficiencies nor take into account lepton acceptances in this work, one must realise that in real data the lepton detector and trigger acceptances must be included. The difference between the electron and muon efficiencies is expected to be smaller than the results found using the Monte Carlo data in this work. This is owing to a better choice in isolation criteria and an improvement in the reconstruction of lepton objects. However, the overall difference in lepton acceptances found here will not affect the spin measurement.

Lastly, as mentioned in the previous section, the mSUGRA benchmark point chosen in the context of this work and furthermore, one of the WMAP [39] compatible benchmark points considered by ATLAS, was the SU3 'bulk' region point. This SU3 bulk point is characterised by the following values of the model parameters:

$$\mathrm{m_0 = 100\ GeV/c^2},\ \mathrm{m_{\frac{1}{2}} = 300\ GeV/c^2},\ \mathrm{A_0 = -300\ GeV},\ \tan\beta = 6 \text{ and } \mathrm{sign}(\mu) > \ 0.$$

6.4 Physics Object Definitions

Preselection and making sure that no single physics object was reconstructed twice was carried out in this analysis using the EventView set of analysis tools. It creates Athena-Aware NTuples (AANs) from the Analysis Object Data (AODs). The final selection will require an OSSF lepton pair. In this work, electrons are considered first followed by photons, muons, τ-jets and finally particle jets, to ensure that no particles overlap within a cone of size ΔR=0.2.

- **Electrons.** Electron identification and performance is described in detail elsewhere [147]. However, for the purposes of this work the electron candidates must satisfy the 'medium' category of selection cuts. Electrons must satisfy $p_T > 15$ GeV/c and $|\eta| < 2.5$. The algorithm with which they are reconstructed utilises cuts based upon the shower shape properties of the EM calorimeter as well as variables combining inner detector tracks with calorimeter deposits. Furthermore, electron candidates are required to be isolated in the calorimeter to ensure that high p_T jets are not misidentified as electrons. The isolation requirement is that electrons must have less than 15 GeV of E_T in an annulus of radius ΔR= 0.45 about the electron track.
- **Muons.** Again, as with the case of electrons, muon candidates must satisfy the fiducial cuts: $p_T > 15$ GeV/c and $|\eta| < 2.5$ (this corresponds to the fiducial volume covered by the combined muon system). The muon algorithm [147] evoked for the analysis utilises both the muon-spectrometer and inner detector. It takes tracks in the muon system and attempts to match them with inner detector tracks using a χ^2 with five degrees of freedom (dof). For each muon-spectrometer track only the best matched track in the inner detector is taken. Furthermore, to ensure good quality muons in

this work, the requirement of the initial track match to have χ^2/Ndof< 20 was employed. A primary isolation (I) requirement is made and is, furthermore, defined as:

$$I < \frac{E_T^{0.45}}{E_T^{\mu}} \tag{6.7}$$

where the numerator is the E_T in a cone around a muon-track of radius R = 0.45 and the denominator is the total E_T in the calorimeter of the muon candidate. For this work I was set at 0.9, i.e. a muon is considered isolated if I< 0.9.

- **Jets.** Jets are reconstructed based upon ConeTower Particle Jets using a seeded cone algorithm with parameter R = 0.401. The fiducial cuts are $p_T > 15$ GeV/c and $|\eta| < 2.5$. Jets are not considered if they overlap with a reconstructed electron within ΔR< 0.5.
- **Missing $\mathbf{E}_T$.** The missing E_T imbalance in the detector is calculated from all the visible energy deposited in all calorimeter cells and from muons. Furthermore, a correction is applied to take into account the visible energy lost in the cryostat. The negative of the vector returned after the resulting vectorial summation over the energies is the missing E_T. Sources of fake missing E_T from, e.g. dead or noisy parts of calorimeter, fake muons, beam-gas and beam halo events, cosmic rays and electronic noise are not considered here. For a more detailed discussion on the fake missing E_T the reader is referred to [147].

A recapitulation of the main definitions is presented in table 6.1.

	Physics Object		
	Muon	Electron	Jet
p_T cut	$>$ 15 GeV/c	$>$ 15 GeV/c	$>$ 15 GeV/c
η cut	$\|\eta\| < 2.5$	$\|\eta\| < 2.5$	$\|\eta\| < 2.5$
Calorimeter Isolation	$\left\|\frac{E_T^{0.45}}{E_T^{\mu}}\right\| < 0.9$ in $\Delta R = 0.45$	$\|E_T\| < 15$ GeV in $\Delta R = 0.45$	- -

Table 6.1: A summary of the definitions of the physics objects employed in this work.

6.5 Event Selection Criteria

In order to select the SUSY signal process of interest above the expected Standard Model and SUSY backgrounds, the event must pass a set of kinematic cuts. In this work, the cuts employed were applied to leptons (electrons and muons only), jets and missing E_T. Furthermore, except where stated otherwise, cuts are given in the positive sense. That is, for example, a $p_T > 40$ GeV/c is the requirement which an event passing the cut must satisfy. There were six main variables employed in this work to preferentially select signal events. The default values for these cuts were motivated from consideration of the values from the original study [93] and also from consideration of fig. 6.3. They were the following.

- **Missing transverse energy ($\not\!\!E_T$).** The final state of interest consists of, in addition to two OSSF leptons, two invisible particles (the two LSPs). Thus, this manifests in the detector as $\not\!\!E_T$. Furthermore, since in colliders only the transverse component of the total energy can be measured (owing to the detectors imperfect hermeticity), one then only considers the transverse components of the $\not\!\!E_T$. The default cut was $\not\!\!E_T > 100$ GeV.

- **Transverse momentum of the hardest jet ($\mathbf{p}_T(\mathbf{j}_1)$).** As already mentioned, there is expected to be a small number of jets of sizeable p_T in the signal process arising from initial state radiation. The default cut was $p_T(j_1) < 100$ GeV/c motivated by considering the removal of the backgrounds from $t\bar{t}$ production and from cascade decays of heavier KK or SUSY particles.
- **Transverse momentum of the first and second hardest leptons ($\mathbf{p}_T(l_1)$ and $\mathbf{p}_T(l_2)$).** It is foreseen that the final state dileptons in the signal event are relatively hard in nature. The values of these cut variables were therefore taken to be $p_T(l_1) > 40$ GeV/c and $p_T(l_2) > 30$ GeV/c respectively. Furthermore, these values are such that they are sufficiently above the ATLAS dilepton trigger threshold.
- **Final state dilepton invariant mass ($\mathbf{m}_{ll}$).** The invariant mass distribution of the two final state leptons emanating from the decay of the slepton pair. The default cut was $m_{ll} > 150$ GeV/c^2 to remove a large amount of the Standard Model Z^0Z^0 background.
- **Transverse recoil (TransR).** This is defined as:

$$\text{TransR} = |\not{\mathbf{p}}_\mathbf{T} + \mathbf{p_T}(\mathbf{l}^\pm) + \mathbf{p_T}(\mathbf{l}^\mp)|, \tag{6.8}$$

where $\not{p}_T$ indicates the missing transverse momentum ($\not{E}_T$ here), and $p_T(l^\pm)$ ($p_T(l^\mp)$) are the transverse momentum of the first (second) hardest lepton of the OSSF dilepton pair. That is, it is the vector sum of the transverse components of momenta of the two leptons and missing transverse momentum in the event. With the expectation that there will be little jet activity in the event, this variable is then expected to be low. The default cut was

TransR < 100 GeV/c, again motivated for the same arguments as was given for the transverse momenta of the hardest jet default cut.

- **'Stransverse' mass or the Cambridge $\mathbf{m}_{T2}$ variable.** The stransverse mass (from hereafter it shall be referred to as simply the m_{T2} variable) is described in [148, 149] and defined as:

$$m_{T2}^2(m_\nu) \equiv \min_{\not{\mathbf{q}}_T^{(1)}+\not{\mathbf{q}}_T^{(2)}=\not{\mathbf{p}}_T} \Big[\max\left\{m_T^2(\mathbf{p}_T^{l^{(1)}}, \not{\mathbf{q}}_T^{(1)}; m_\nu),\ m_T^2(\mathbf{p}_T^{l^{(2)}}, \not{\mathbf{q}}_T^{(2)}; m_\nu)\right\}\Big] \tag{6.9}$$

where,

$$m_T^2(\mathbf{p}_T^l, \not{\mathbf{p}}_T^\nu; m_\nu) \equiv m_{l^\pm}^2 + m_\nu^2 + 2(E_T^l E_T^\nu - p_T^l \cdot p_T^\nu), \tag{6.10}$$

and

$$E_T^l = \sqrt{(p_T^l)^2 + m_l^2} \quad \text{and} \quad E_T^\nu = \sqrt{(p_T^\nu)^2 + m_\nu^2}. \tag{6.11}$$

It is similar to the more familiar transverse mass, m_T, but is more advantageous in events where two or more same, but unknown, mass particles are simultaneously produced and decay semi-invisibly through production of two or more particles that escape detection. The default cut was set at m_{T2} >100 GeV/c^2 envisioned to help in removal of the Standard Model $W^\pm W^\mp$ pair background.

The cuts are somewhat reminiscent to those employed in studies designed to discover sleptons or mass measurements from Drell-Yan pair production at the LHC [146, 150–153]. Although one notable difference is that there is no requirement for cutting on the principal-valued angle around the detector, that is, the azimuthal angle (ϕ), for leptons or $\not{E}_T$ vector. This variable pervades most pre-

cision SUSY studies. The reason is that it appears to be unnecessary when the m_{T2} variable is employed. One further notable difference from this work to that of previous studies for SUSY analysis is the multiplicity of cut parameters that are deployed in the analysis. This was deliberate so as to minimise the potential of introducing bias into the method and, furthermore, to minimise the degree of correlation between the variables. Whilst, at the same time, still maintaining sufficient power to select signal events from the large SUSY and Standard Model backgrounds.

That concludes the description of all the kinematic variables that were utilised in this analysis. Note that the sequence in which the cuts were introduced above, the so-called 'cut flow', translates to the order in which they were employed in the analysis. However, a set of hard preliminary cuts were initially applied in order to home in on the fiducial region defined by the expected topology of the signal process. The preselection cuts are as follows:

- **Two opposite sign, same family (OSSF) leptons.** The leptons (electrons or muons) with $p_T > 15$ GeV/c and $|\eta| < 2.5$ (this corresponds to the fiducial volume covered by the inner detector).
- **No jets with p_T >150 GeV/c.** This cut is motivated by the topology of the dislepton events, within which, there is expected to be little or no hadronic energy.

6.6 Corrected Fast Simulation

Unfortunately, due to the paucity of Monte Carlo statistics in the diboson background, fully simulated samples: $W^{\pm}W^{\mp}$, $W^{\pm}Z^0$, Z^0Z^0 and the $t\bar{t}$ sample, the analysis was hampered and the subsequent conclusion drawn was inconclusive.

Circumventing the problem involved recourse to utilising the ATLAS fast simulation package, Atlfast. By availing the services of Atlfast an ample sample corresponding to each diboson background and the $t\bar{t}$ background could be simulated. Table 6.2 summarises the samples simulated. However, using Atlfast and its caveat one is required to check the validity of its use as a substitute for full simulation. One normally uses Atlfast, which parameterises one's ignorance of the detector by employing a set of parameterised resolution functions, to imitate, as best it can, the full data simulation in a fraction of the time. It, therefore, trades the accuracy of full simulation for a significant gain in processing speed. This is especially true when considering the reconstruction efficiency distributions for leptons in p_T and η. These residual differences that appear between Atlfast and the full simulation Monte Carlo data sample must, therefore, be accounted for. It is important to note that Atlfast assumes a 100% efficiency for reconstructing leptons (electrons and muons), thus, much higher than the full simulation and, furthermore, what would be expected in the event of real data. A way to veto objects to account for the true efficiency of the detector is therefore required. To tackle this, the following method was employed. The first, involves stochastically rectifying the reconstruction efficiency distribution of leptons, in η, via a 'correction factor'. η was chosen because it was observed that there was a significant η dependence in the lepton efficiency distributions. This is a little more involved since the distributions in η were not flat: lower efficiencies are found in the crack ($1.3 < |\eta| < 1.5$), high η ($|\eta| > 2$) and low η ($|\eta| = 0$) regions which are not accounted for by Atlfast. This is in contrast to the corresponding reconstruction efficiency distributions of leptons in p_T which are flat above $p_T \approx 25$ GeV/c. Therefore, a constant, flat scaling factor should be sufficient to correct for the offset of efficiency between fast and full simulation in p_T. Each of the diboson

and $t\bar{t}$ samples are split, 10% to 90%, into two statistically separate samples so as to avoid introducing a bias. The smaller sample is used for evaluating the correction factor whilst the remaining, larger sample, is used for the analysis proper. A correction factor is constructed from both the efficiencies of the full and fast which are calculated as one dimensional functions of η (i.e. parameterised in bins of η). It is defined as:

$$f_{\mathrm{corr}}(\eta) = \frac{\epsilon_{\mathrm{Full}}(\eta)}{\epsilon_{\mathrm{Fast}}(\eta)}, \tag{6.12}$$

where $\epsilon_{\mathrm{Full}}(\eta)$ and $\epsilon_{\mathrm{Fast}}(\eta)$ are the reconstruction efficiencies of the full simulation and uncorrected Atlfast respectively. Once calculated, the correction factor is then applied to the larger statistics sample along with the aid of a random number generator. The latter is tailored such that once fired it produces random numbers (a) between 0 and 1 for every object (lepton) and discarding the object if a $>$ $f_{\mathrm{corr}}(\eta)$.

Fig. 6.2 displays the results of applying the correction factor to the reconstruction efficiencies for leptons in the diboson samples ($W^{\pm}W^{\mp}$, $W^{\pm}Z^0$ and Z^0Z^0) and the $t\bar{t}$ sample. Shown are the distributions of Full simulation, uncorrected and corrected Atlfast. The results in fig. 6.2 attest to the fact that corrected Atlfast is a suitable replacement for full simulation. After the η-dependant correction was applied it was observed that the lepton reconstruction efficiency in the corrected Atlfast sample was in accord with the corresponding full simulation distribution. Therefore, for this reason, no extra level of correction was carried out for the p_T distrbutions of the final state leptons. Furthermore, the analysis can now proceed with the statistically larger, corrected Atlfast samples for the diboson and $t\bar{t}$ backgrounds rather than the full simulation Monte Carlo diboson and $t\bar{t}$ samples which are deficient in Monte Carlo statistics.

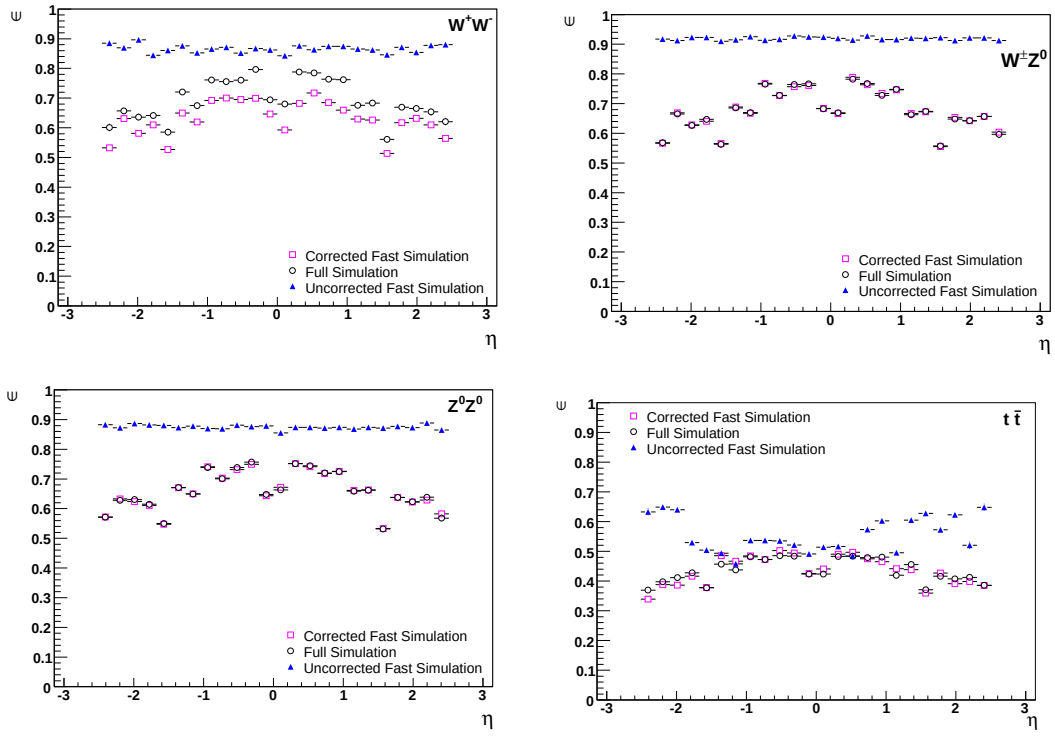

Figure 6.2: Lepton (electron and muon) reconstruction efficiencies as a function of η for the diboson samples: $W^{\pm}W^{\mp}$, $W^{\pm}Z^0$, Z^0Z^0 and $t\bar{t}$ sample. In each plot are the full simulation samples (open circles); uncorrected Atlfast (closed triangles); and corrected Atlfast (open boxes). It is evident that, after the fast simulation correction procedure using the full simulation information, the Atlfast reconstruction efficiency distributions adhere firmly to the full simulation distributions. Thus, this figure clearly shows that the corrected Atlfast samples are an adequate substitute for the full simulation ones.

6.7 Results

Before embarking on examining all the distributions of the full analysis proper it is worth assessing the six distributions for signal and all detrimental backgrounds prior to any deployment of the main analysis cuts. This will furnish us with the typical event characteristics of each signal and background process in each of the six kinematic variables used to cut on. Fig. 6.3 presents the six distributions representing the six kinematic selection variables after only basic cuts have been

Fast Simulation Process	Monte Carlo Generator	Cross section after filter(pb)	N_{MC}, sample	Equivalent integrated luminosity (fb^{-1})
$W^{\pm}W^{\mp}$	HERWIG	24.5	2504318	102.2
$W^{\pm}Z^{0}$	HERWIG	7.8	814985	104.5
$Z^{0}Z^{0}$	HERWIG	2.1	438662	208.9
$t\bar{t}$	HERWIG	461	2215225	4.81

Table 6.2: A table that summarises the various, much larger, fast simulated samples ($W^{\pm}W^{\mp}$, $W^{\pm}Z^{0}$, $Z^{0}Z^{0}$ and $t\bar{t}$) that were used in place of the corresponding full simulated samples which were deficient in Monte Carlo statistics for the purposes of the analysis.

employed ($p_T > 15$ GeV/c for leptons and jets and furthermore for leptons: $|\eta| < 2.5$) for signal and background events. The distributions correspond to 30 fb^{-1} of Monte Carlo simulated data.

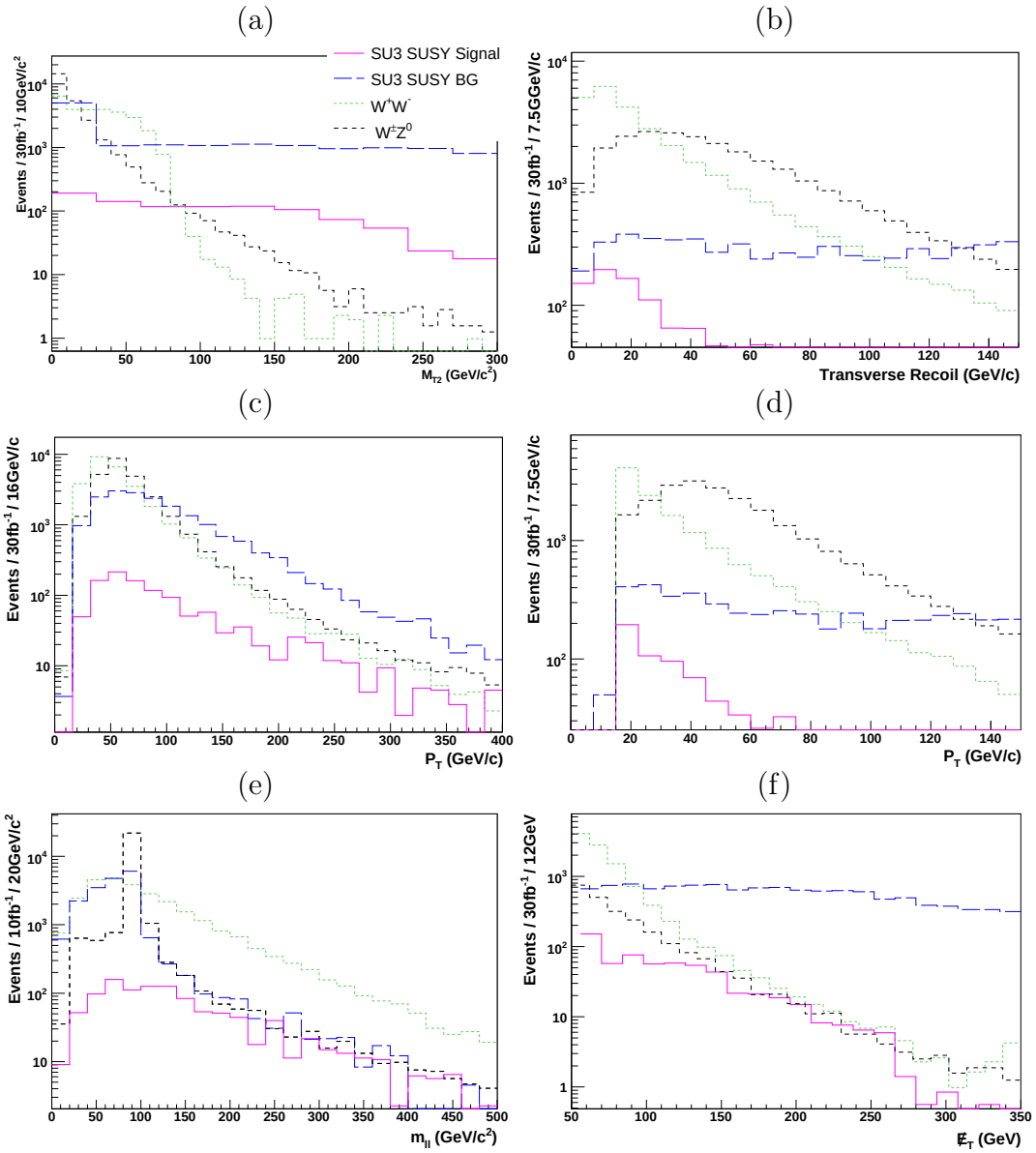

Figure 6.3: The six distributions, for the SU3 SUSY signal and the three most detrimental of the analysis: SUSY and $W^{\pm}W^{\mp}$, $W^{\pm}Z^{0}$ Standard Model backgrounds, representing the six kinematic variables employed in this work after basic cuts ($p_T > 15$ GeV/c and $|\eta| < 2.5$ for leptons). All distributions are normalised to 30 fb^{-1}. Shown are distributions versus (a) m_{T2}; (b) transverse recoil; (c) the p_T of the two hardest leptons in the event; (d) the p_T of the hardest jet in the event; (e) invariant mass of the dilepton final state; and (f) the missing transverse energy.

6.7.1 Kinematic parameter space scan and optimisation

Using the default set of cut values ($\not\!\!E_T > 100$ GeV, $p_T(j_1) < 100$ GeV/c, $p_T(l_1) > 40$ GeV/c and $p_T(l_2) > 30$ GeV/c, $m_{ll} > 150$ GeV/c^2, TransR $<$ 100 GeV/c and m_{T2} >100 GeV/c^2) the final figure of merit (ffm) value, $\ln(Q) = \ln\left(\frac{L_{SUSY}}{L_{UED}}\right)$, was found to be -0.2 (see figure 6.5). This low and negative value indicates that this region of phase space actually favours the UED theoretical distribution rather than the SUSY one. Furthermore, it was found that with 300 fb^{-1} of Monte Carlo data, this ffm value increased to -0.02. It, therefore, demonstrates that some sampling of the allowed parameter space to obtain an optimal ffm value is required.

Having identified which kinematic variables are sensitive to the proximity to where each of the default set of cuts are applied (they were the invariant mass of the lepton pair (m_{ll}), missing transverse energy ($\not\!\!E_T$) and the m_{T2} variable) it is worth sampling the rest of the allowed parameter space to identify the optimal set of cut values. The main purpose is, after having done a tractable global scan of the three dimensional kinematic parameter space, to delineate the region in this parameter space where one can make a spin measurement using the $\cos\theta^*_{ll}$ angular variable. It is hoped that it should enable one to differentiate between SUSY or UED to the 5σ, or better, confidence level. Note that the optimal region of parameter space was identified not as the region where SUSY would be best discovered but rather the region where it lends to one having maximal differentiating power between the SUSY and UED models. The method invoked involved using a grid of points in the 3D kinematic parameter space (m_{ll}, $\not\!\!E_T$ and m_{T2}) and random sampling of it, initially starting with the point corresponding to the default set of cuts. Each step corresponded to 5 GeV/c^2 (5 GeV for $\not\!\!E_T$) in magnitude.

Displayed in fig. 6.4 to fig. 6.6 are the 2D and 3D projections of the tractable global optimisation scan of the final figure of merit and statistical significance values carried out in the 3D kinematic parameter space in order to delineate the optimal region of the parameter space to make such a spin measurement. In each case are displayed (a) the 2D projections of the optimisation of the final figure of merit, $\ln(Q) = \ln\left(\frac{L_{SUSY}}{L_{UED}}\right)$; and (b) the 3D optimisation plane of the statistical significance, $S/\sqrt{(B)}$. In fig. 6.4 the final figure of merit and statistical significance values are plotted versus m_{ll} and m_{T2} for a constant value of $\not{E}_T > 100$ GeV. In fig. 6.5 the final figure of merit and statistical significance values are plotted versus m_{ll} and $\not{E}_T$ for a constant value of $m_{T2} > 120$ GeV/c^2 and fig. 6.6 the final figure of merit and statistical significance values are plotted versus $\not{E}_T$ and m_{T2} for a constant value of $m_{ll} > 140$ GeV/c^2. It is noticeable, from these three figures (fig. 6.4, fig. 6.5 and fig. 6.6), that in all regions of the kinematic parameter phase space there exists a strong degree of positive correlation between $\ln(Q) = \ln\left(\frac{L_{SUSY}}{L_{UED}}\right)$ and $S/\sqrt{(B)}$. That is, a high final figure of merit is also accompanied with a high statistical significance value.

The optimum set of cut values were found to be: $m_{ll} > 113$ GeV/c^2, $\not{E}_T > 100$ GeV and $m_{T2} > 120$ GeV/c^2, with the other cuts taking their default values ($p_T(j1) < 100$ GeV/c, $p_T(l_1, l_2) > 40, 30$ GeV/c^2 and TransR < 100 GeV/c), which corresponded to a final figure of merit of 13.9. Also given for completeness is the statistical significance value, $S/\sqrt{(B)}$, for this point, which was 10.9. The number of events surviving at each stage of the analysis for each signal and background sample can be seen in table 6.3, for the optimised set of cut values. With regard to the values presented in table 6.3, it is evident that the cut of $\not{E}_T > 100$ GeV is the most effectual cut at removing backgrounds as it removes a large proportion of all the backgrounds. However, a large fraction of the signal

is also removed by this cut of $\not\!\!E_T > 100$ GeV.

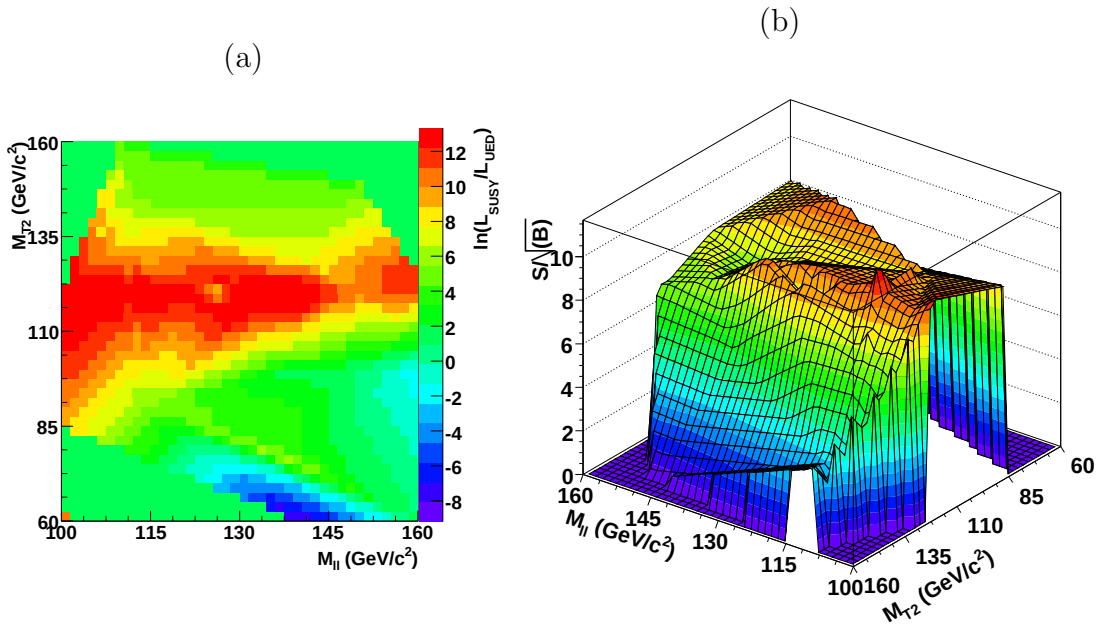

Figure 6.4: The 2D and 3D projections of the optimisation of the final figure of merit and statistical significance values for different values of the kinematic parameters: m_{ll}, m_{T2} and missing transverse energy. Figure (a) illustrates the 2D projection of the optimisation of the test statistic, $\ln(Q) = \ln\left(\frac{L_{SUSY}}{L_{UED}}\right)$, versus two of the three kinematic parameters (m_{ll} and m_{T2} for a constant value of $\not{E}_T > 100$ GeV) varied in the optimisation procedure. Whereas figure (b) illustrates the 3D optimisation plane of the statistical significance, $S/\sqrt{(B)}$, versus the same as in (a).

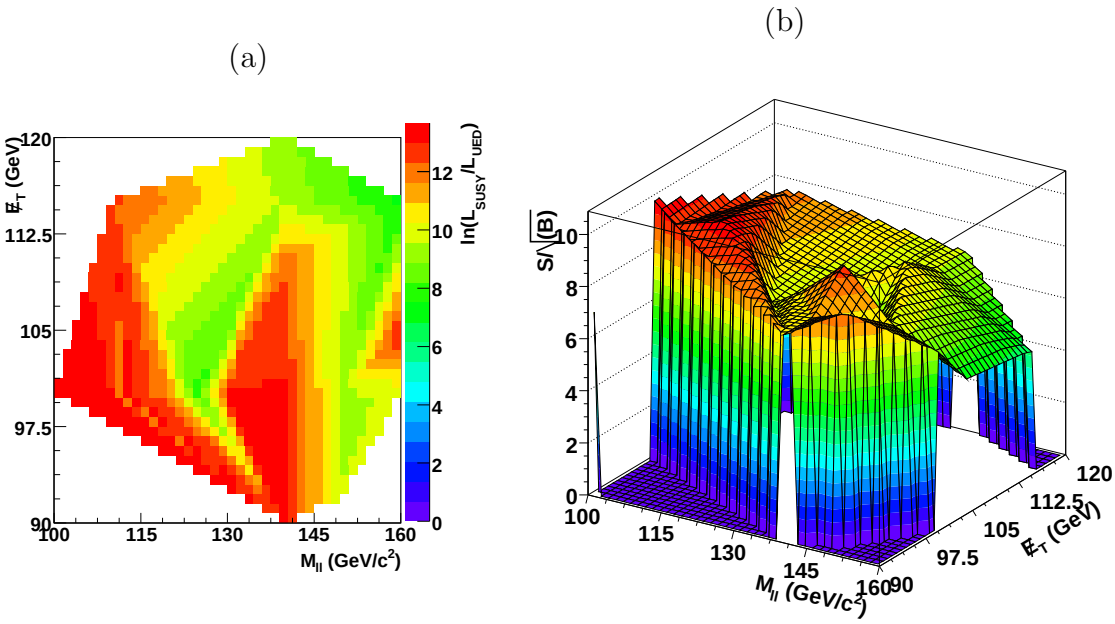

Figure 6.5: As in fig. 6.4 but for m_{ll} and missing transverse energy for a constant value of $m_{T2} > 120$ GeV/c^2.

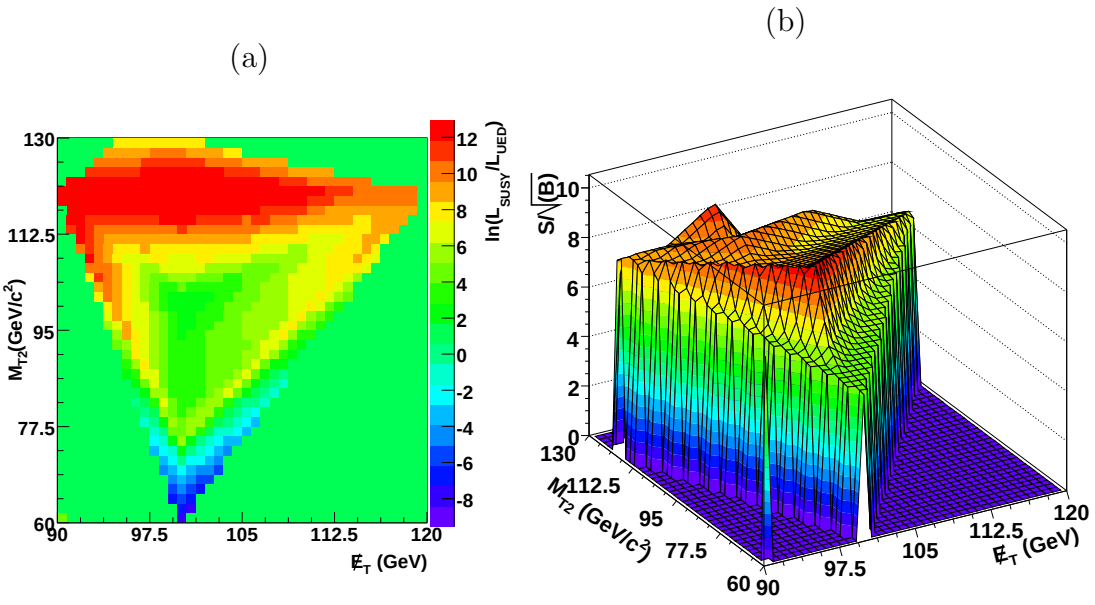

Figure 6.6: As in fig. 6.4 but for $\not\!\!E_T$ and m_{T2} for a constant value of $m_{ll} > 140$ GeV/c^2.

Monte Carlo Data Sample	Kinematic Variable						
	No cut	$\not{E}_T$ > 100 GeV	$p_T(j_1)$ < 100 GeV/c	$p_T(l_{1,2})$ $> 40, 30$ GeV/c	m_{ll} > 113 GeV/c^2	TransR < 100 GeV/c	m_{T2} > 120 GeV/c^2
SUSY Signal	1119	317	249	245	189	167	69
SUSY OSSF BG	18800	14305	818	786	115	71	15
$W^{\pm}W^{\mp}$	27746	1050	697	637	353	306	15
$W^{\pm}Z^0$	26038	588	453	445	45	40	10
Z^0Z^0	22388	871	756	750	0	0	0
$t\bar{t}$	404406	89006	47572	31712	13280	0	0
$W^{\pm}+\gamma$	8	0	0	0	0	0	0
$Z^0+\gamma$	28921	160	111	111	41	10	0
Z^0+b-jet	1209907	461	461	461	0	0	0
$W^{\pm}$+jet	1939	287	36	36	0	0	0

Table 6.3: Number of signal and background events as the optimised event selection is applied for the benchmark point SU3. All results assume an integrated luminosity of 30 fb^{-1}. The normalisation factors used were the following. For the $W^{\pm}W^{\mp}$, $W^{\pm}Z^0$, Z^0Z^0 and $t\bar{t}$ samples normalisation factors were determined from the information displayed in table 6.2. For all other samples table 5.2 and its contents were used.

6.7.2 SUSY and Standard Model backgrounds

Having carried out the optimisation and found the optimal values for the kinematic variables it is then worth considering the size and composition of the SUSY and Standard Model residual backgrounds. Fig. 6.7 shows the six distributions each representing one of the six kinematic parameters employed in the analysis, for signal and the residual background events. After implementing all cuts,

set equal to their optimal values, the dominant background for this particular region of phase space, (38% of the total background) was SUSY OSSF production. Thereafter, in descending order of contribution, the remaining residual backgrounds were $W^{\pm}W^{\mp}$ (37%) and $W^{\pm}Z^{0}$ (25%) respectively.

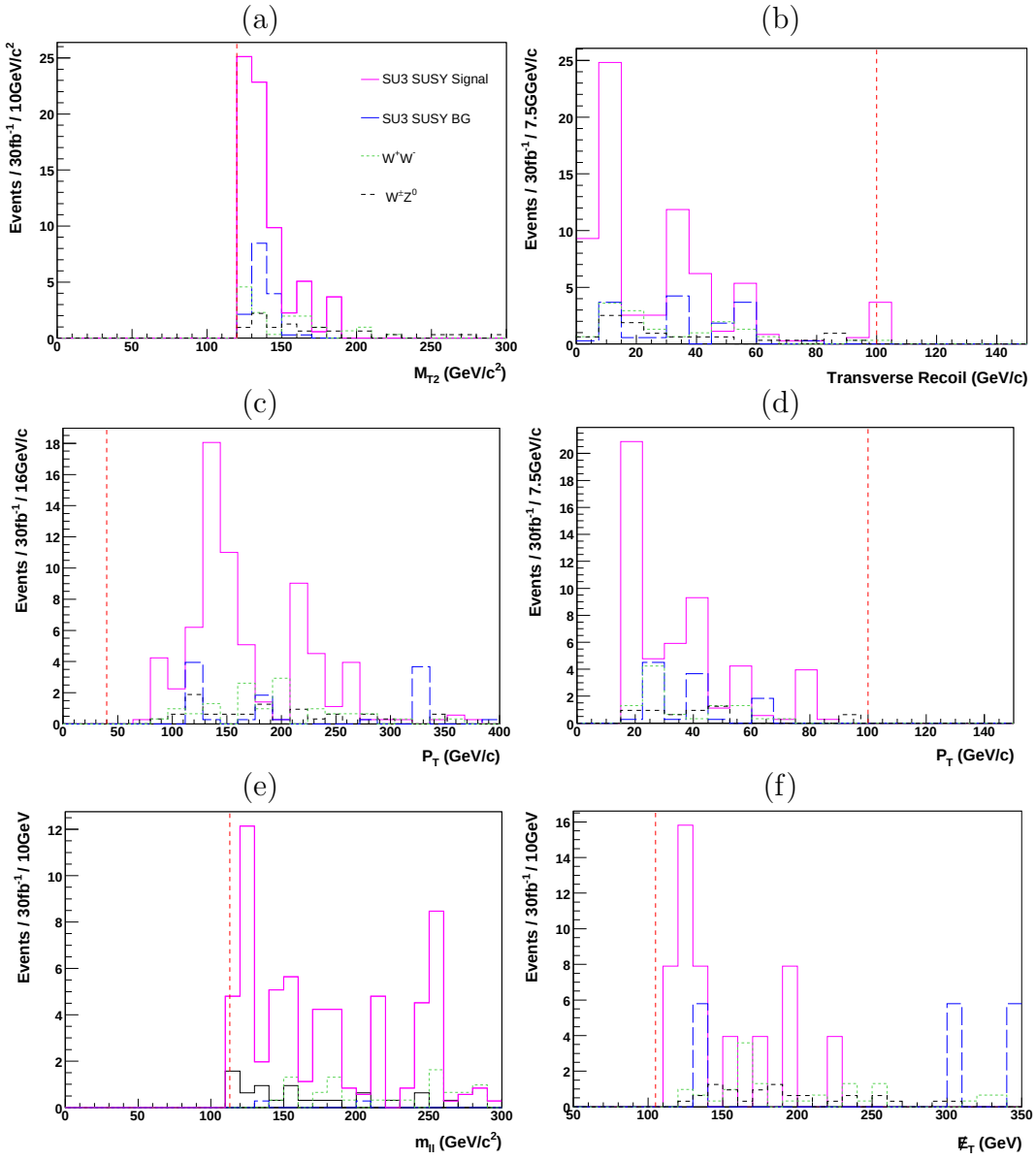

Figure 6.7: The six distributions representing the six kinematic variables, set equal to their optimised values, employed in this work for the signal event selection. The distributions show, in addition to the backgrounds that survive the applied cuts, the number of events in close proximity to each of the various optimised cuts, the position of which, is indicated by the vertical dashed line. All distributions are given for the SU3 signal process and all residual background (SUSY and Standard Model) processes that pass the cuts. Finally, all distributions are normalised to 30 fb^{-1}. Shown are distributions of (a) m_{T2}; (b) transverse recoil; (c) the p_T of the two hardest leptons in the event; (d) the p_T of the hardest jet in the event; (e) invariant mass of the dilepton final state; and (f) the $\not{E}_T$.

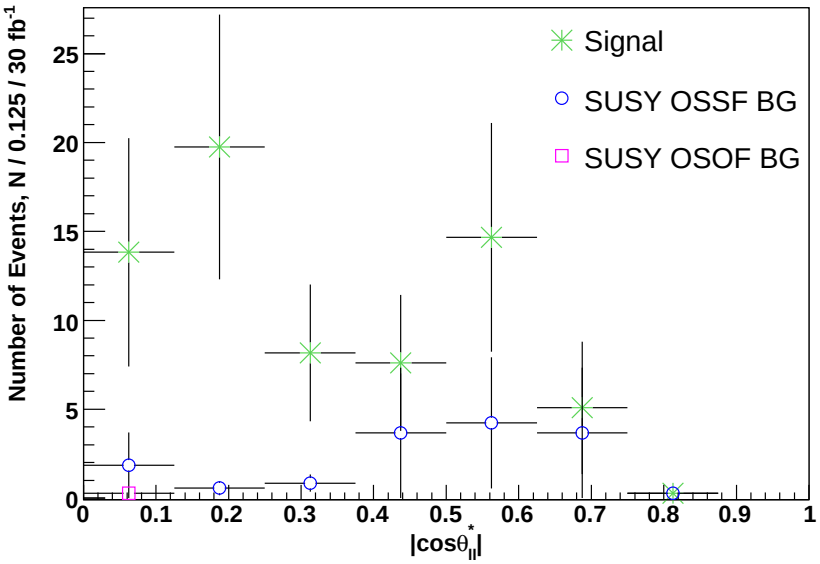

Figure 6.8: The $\cos\theta^*_{ll}$ distribution for signal (green crosses), SUSY OSSF background (blue, open circles) and SUSY OSOF background (magenta, open box) after the optimised event selection corresponding to the SU3 mSUGRA point. All distributions are equivalent to 30 fb^{-1} of integrated luminosity. Note that the right hand most bin, corresponding to the highest values in $\cos\theta^*_{ll}$, is empty for all signal and background distributions.

Fig. 6.8 displays the SUSY signal and combinatorial backgrounds (OSSF and OSOF) in the $\cos\theta^*_{ll}$ angular variable. In the figure the distributions shown are after all six cuts (each set to their optimal value) have been applied. Fig. 6.8 shows that after employing the optimal set of cuts the SUSY backgrounds (OSSF and OSOF) are smaller than the signal although the SUSY OSSF background is certainly not insignificant with respect to the signal distribution. This is especially true at larger values of $|\cos\theta^*_{ll}|$. Furthermore it can also be said that all SUSY backgrounds contribute less than 15 events after all the optimal cuts have been applied. This, together with the sparsity of OSOF events, suggests that the optimised set of cuts do fulfil their role at maximising the separation between

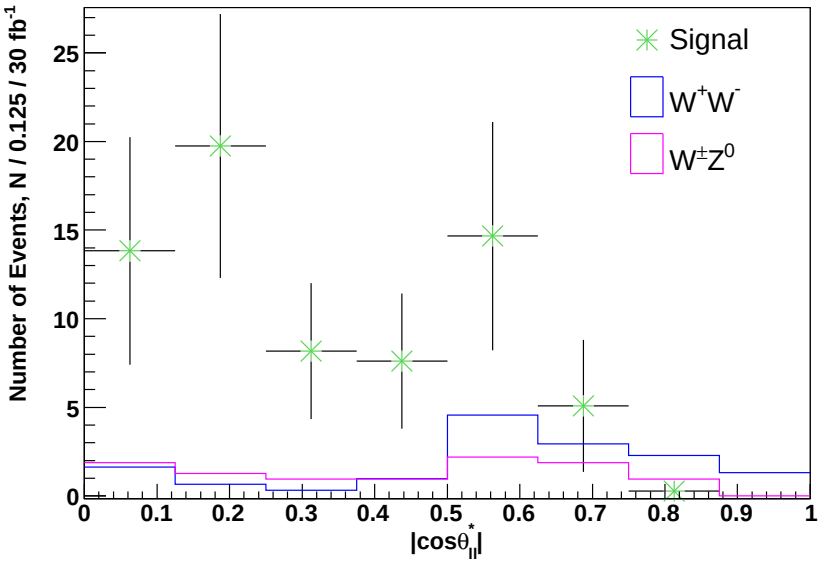

Figure 6.9: The $\cos\theta^*_{ll}$ distribution for the signal and residual Standard Model backgrounds after the optimised event selection. All distributions are equivalent to 30 fb^{-1} of integrated luminosity.

signal and background as much as possible. Similarly, fig. 6.9 shows the Standard Model backgrounds only, in $\cos\theta^*_{ll}$ and again the distributions shown are after all six cuts (each set to their optimal value) have been applied. Fig. 6.9 illustrates that after employing the cuts the Standard Model backgrounds are greatly reduced. However, the residual backgrounds are not insignificant and, again, this is especially true at higher $|\cos\theta^*_{ll}|$. Both figures, fig. 6.8 and fig. 6.9, thus attest to the fact that the backgrounds (Standard Model and SUSY) are greatly reduced. However, due to the low number of signal events the backgrounds are therefore required to be accurately measured if the method of spin measurement, employing the $\cos\theta^*_{ll}$ variable, is to be carried out at the LHC.

6.7.3 Background Subtraction

Before embarking on considering the final distributions we are obliged to consider something that is imperative to the spin measurement presented here. This is the accuracy to which the magnitude of the background is estimated which is then employed in the background flavour subtraction procedure. Moreover we are obliged to consider how effectual the background subtraction procedure is and, furthermore, how true is the assumption of:

$$\text{N(OSSF Background)} = \text{N(OSOF Background)}, \tag{6.13}$$

where here the 'Background' refers to Standard Model and SUSY; or SUSY alone. Fig. 6.10 which shows the total OSSF and OSOF background $\cos\theta^*_{ll}$ distributions after the optimised event selection for 30 fb^{-1} of integrated luminosity and normalised to unit area, demonstrates that this assumption is valid with the statistics available. Tabulated in table 6.4 are the number of OSSF and OSOF background events (SUSY *and* Standard Model, and SUSY *alone*) at each stage of the optimal event selection for an integrated luminosity of 30 fb^{-1}. The results presented in table 6.4 also further consolidate the claim that the total number of OSSF background events (SUSY *and* Standard Model) is approximately equal in size to the total number of OSOF background events from the same background source (after all cuts have been employed the total (Standard Model and SUSY) number of OSSF and OSOF events are 40 $\pm$7 and 23 $\pm$ 3 respectively). The noticeable, sole discrepancy between the total number of OSSF and total number of OSOF events after applying the TransR cut of $<$ 100 GeV/c can be explained by the complete removal of the $t\bar{t}$ OSSF background which does not hold true for the OSOF. Although a large amount of the OSOF $t\bar{t}$ background is removed by this

cut the proceeding m_{T2} cut is required to remove the remaining portion of this background. However, there is an especially pronounced disagreement between the number of OSOF and OSSF events for the case when the source of the background is solely arising from SUSY processes. After all cuts have been employed the total SUSY number of OSSF and OSOF events are 15 $\pm$7 and 0 $\pm$2 respectively. Moreover, from table 6.4 in all but one case regarding the number of OSSF and OSOF events at each stage of the applied selection cuts, the number of OSOF background events is two orders of magnitude smaller than the number of OSSF background events for the case when the background is emanating solely from SUSY processes. Although there exists a discrepancy in the number of OSSF to the number of OSOF background events, equally important and relevant to this work is the shape of the $\cos\theta^*_{ll}$ distribution in each case. Fig. 6.10 attests to the shapes agreeing reasonably well with the statistics available. Still, one cannot ignore the fact that there does indeed exist a clear asymmetry in the total number of OSSF and OSOF background events for the case when the source of the background is solely SUSY. However, a possible explanation and one that is infrequently documented in the literature [145, 154] for the possibility for this asymmetry to exist is the nature of the mother sparticles. For OS dileptons and depending upon the SUSY source of the OS leptons, there exists the possibility of an asymmetry:

$$A_f = \frac{N(OSSF) - N(OSOF)}{N(OSSF) + N(OSOF)}. \tag{6.14}$$

If the OS dileptons emanating from the interaction arise from the decay of:

- neutralinos or sleptons directly, their resulting decays will give predominantly OSSF leptons;
- quarks, squarks or charginos then their respective lengthy and complicated

decays open up a larger number of possible states and this, on average, an equal number OSOF and OSSF final leptons would be expected.

All these results are still based upon the laws of conservation of individual lepton flavour number and lepton universality. Due to the nature (i.e. they contain a high number of sleptons and neutralinos) of two of the three SUSY Monte Carlo data samples employed in this work, namely direct dislepton production and direct gaugino pair production, these samples combined would help to augment the number of OSSF events with respect to the number of OSOF events thus producing a large positive A_f. Moreover, by restricting ourselves to a region of phase space where the signal is (through the use of the applied cuts), removes a large amount of the strongly interacting sparticles and thus, further enhancing this asymmetry between N(OSSF) and N(OSOF). Another factor that contributes to this A_f is the fact that, as I have already mentioned in section 6.3, this work neglected to take into account the difference in lepton detector acceptances between electons and muons. This difference would certainly have to be evaluated in real data.

Therefore, to conclude, from the evidence presented here we are led to believe that, given the statistics available and the fact that the shapes of the $\cos\theta^*_{ll}$ distributions are important, then one should be able to use this background flavour subtraction method, for the case when the background arises from SUSY decays only, as a means of isolating the signal. The results here suggest that the lepton detector acceptances must be carefully taken into account whilst carrying out this background subtraction method. However, from the small difference in lepton detector acceptances found here one should not expect it to be detrimental to the spin method presented in this work.

It should also be remarked that in this work the OSOF background was re-

placed by the true background, the OSSF background, i.e. such that: OSSF(S+B′)−(B′) = (S) so one is left with pure signal. After doing this it was found that the $\cos\theta^*_{ll}$ distribution did not change drastically and the final figure of merit, $\ln(Q) = \ln\left(\frac{L_{SUSY}}{L_{UED}}\right)$, decreased slightly from 13.9 to 9.7. Thus, showing that the spin method is still valid even in the case when the background is not underestimated but rather when all backgrounds (Standard Model and SUSY) are totally removed. Also note that the background flavour subtraction method is also applicable for the case when the source of the background is Standard Model or Standard Model *and* SUSY in nature.

Monte Carlo Data Sample	Kinematic Variable						
	No cut	$\not\!\!E_T$ 100 GeV	$p_T(j_1)$ < 100 GeV/c	$p_T(l_{1,2})$ $> 40, 30$ GeV/c	m_{ll} > 113 GeV/c^2	TransR < 100 GeV/c	m_{T2} > 120 GeV/c^2
Total OSSF Background (SUSY+SM)	1740153	106728	50904	34938	13834	427	40
Total OSOF Background (SUSY+SM)	417154	83993	39779	33649	12839	5746	23
Total OSSF Background (SUSY)	18800	14305	818	786	115	71	15
Total OSOF Background (SUSY)	3453	2776	103	90	47	13	0

Table 6.4: The number of OSSF and OSOF background events passing the optimised event selection for the cases when the backgrounds are SUSY *and* Standard Model; and when it is SUSY *alone*, for the benchmark point SU3. All results assume an integrated luminosity of 30 fb^{-1}. See the caption of table 6.3 for an explanation on the normalisation factors employed.

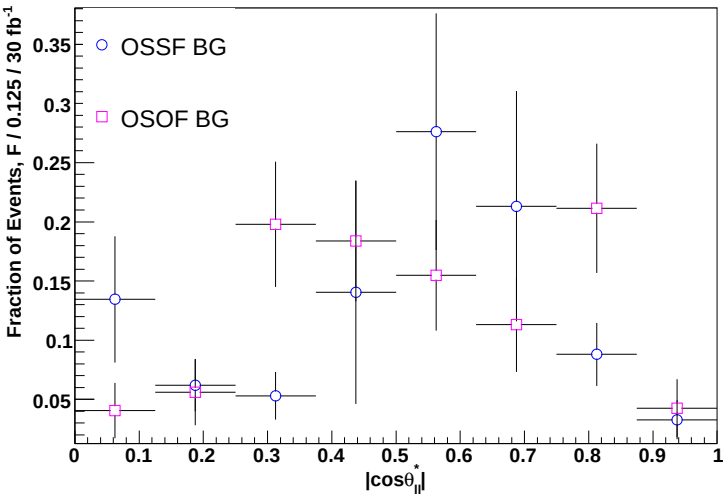

Figure 6.10: The total OSSF and OSOF background $\cos\theta^{*}_{ll}$ distributions after the optimised event selection for 30 fb^{-1} of integrated luminosity. Both are normalised to unit area.

6.8 Conclusion

So, desperately seeking SUSY or Bosonic SUSY? Shown in fig. 6.11 are the final $\cos\theta^*_{ll}$ distributions of the two theoretical motivated models, SUSY and UED, and the one corresponding to the Monte Carlo reconstructed SUSY 'data'. The Monte Carlo reconstructed data is plotted after subtracting the OSOF background and is relatively normalised. The theory distributions are also relatively normalised. Plotted is the fraction of events as a function of the angular variable $\cos\theta^*_{ll}$ with 30 fb^{-1} of accumulated integrated luminosity using the ATLAS detector and based upon the Monte Carlo simulated data available. It is evident from this figure that the SUSY 'data' distribution adheres more closely to the slepton distribution (the theoretical SUSY distribution) rather than to the corresponding UED one. This, therefore, suggests that the $\cos\theta^*_{ll}$ angular variable can measure the spins of the sleptons with 30 fb^{-1} of accumulated luminosity. Furthermore, it also verifies that by using this angular variable one can readily discern and make a distinction between the two theoretical models, SUSY and UED, by measuring the spins of the sleptons for this specific point in mSUGRA parameter space. The method can readily discern the shape of the theoretical SUSY angular distribution over the full range in $\cos\theta^*_{ll}$. This is especially true at low and high values of $\cos\theta^*_{ll}$.

With regard to the test statistic employed in this work, that is, the quantity which quantifies the level of how 'SUSY-like' the Monte Carlo simulated data is (the final figure of merit value defined as: $\ln(Q) = \ln\left(\frac{L_{SUSY}}{L_{UED}}\right)$) for the optimised set of cuts, a final figure of merit value of 13.9 was recorded. One interprets this value as extremely strong evidence that the Monte Carlo data is that of SUSY rather than UED with the statistics available. Thus, this further lends credence to the angular variable, $\cos\theta^*_{ll}$, being capable of spin determination and confounding

our expectations that the Monte Carlo data is UED rather than SUSY.

The results here are similar to those presented in the original paper [93]. One satisfyingly marked difference in the results presented here to those in the original study is that a smaller amount of data is required for a spin determination to be made, thus allowing one to distinguish between SUSY and UED in a shorter period of time. This was due to the more effectual set of optimised cuts and their effect on the fully simulated Monte Carlo data samples.

One further incidental result of the spin analysis that is worth highlighting here is that of the value of the statistical significance, $S/\sqrt{(B)}$. This parameter quantifies the degree of discovery of SUSY for a given set of selection criteria. A value of 10.9[c] certainly suggests that this set of optimised cuts gives rise to an easy discovery reach for the LHC using much less than 30 fb^{-1}.

Fig. 6.12 shows the statistical separation between SUSY and UED expected for the SU3 bulk point as a function of the integrated luminosity together with the statistical and total combined systematic and statistical errors shown denoted by the narrow band around the line. The yellow (lighter) coloured band represents the statistical uncertainty and the outer red (darker) coloured error band represents the total, combined (statistical and systematic) uncertainty. The statistical significance indicated is the Gaussian equivalent significance of the final figure of merit corresponding to a given value of integrated luminosity. The values of integrated luminosity used were: 10, 30, 100, 300 and 350 fb^{-1}. As can be seen from fig. 6.12 for the SU3 bulk point will allow the spin determination to be made in this dislepton channel. In order to achieve a 5σ significance in distinguishing SUSY from UED an integrated luminosity of 50 fb^{-1} (which is equivalent to half

[c]Again, the purpose of this work was never to 'discover' SUSY but rather measure the spins of one type of SUSY particle at this point in mSUGRA space.

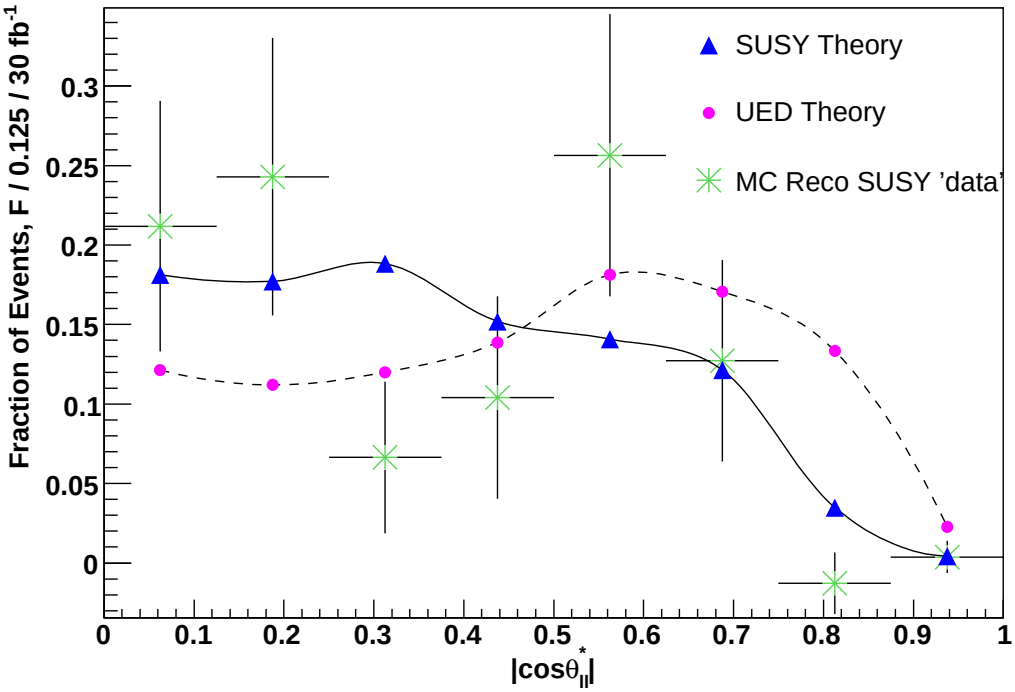

Figure 6.11: The final $\cos\theta^*_{ll}$ distribution, after carrying out a background subtraction and for the optimised event selection, for the SU3 SUSY signal Monte Carlo 'data' sample for an integrated luminosity of 30 fb^{-1}. The lines illustrate the theoretical angular distributions that obey equation 2.10 and equation 2.11, for SUSY (dark line between adjoining blue, closed triangles) and UED (dashed line between adjoining magenta, closed circles) respectively. The error bars on the three distributions are statistical only and all distributions have a relative normalisation employed. Systematic uncertainties in the SUSY signal MC 'data' distribution are not shown here but are discussed in detail in the proceeding chapter.

a year of the LHC operating at design luminosity) was found to be required.

In conclusion, from the work presented in this thesis which substantiates the assertion that the method of spin measurement using $\cos\theta^*_{ll}$ is one which is feasible, we are led to be optimistic about the method in real data. However, only with the advent of real data whence we will seek to either confirm or confute our assertion. We can, nevertheless, be seemingly propitious about differentiating

between SUSY and UED at the LHC.

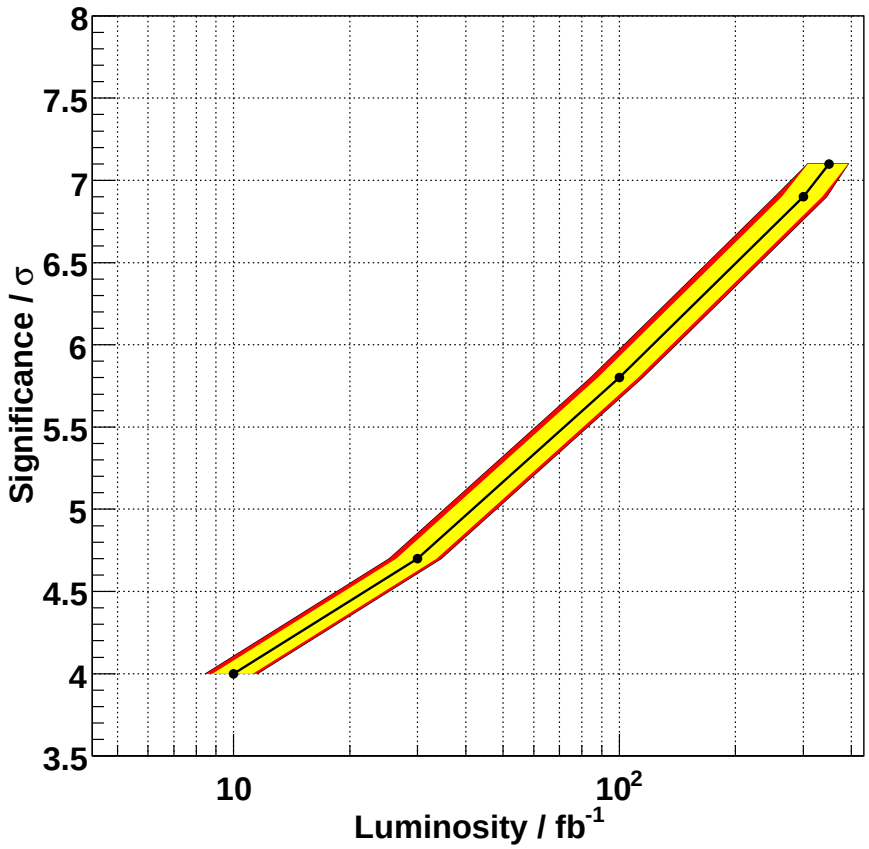

Figure 6.12: The statistical separation between SUSY and UED expected for the SU3 bulk point as a function of the integrated luminosity. Shown are the statistical (the yellow (lighter) coloured band) only and the total combined systematic and statistical (red (darker) coloured error band) errors denoted by the narrow band around the line.

Chapter 7

Anatomy of the Analysis Part III: Addressing the Systematic Uncertainties

7.1 Introduction

JUST as the inherent nature of high-energy physics processes is statistical, leading to an unavoidable source of statistical uncertainty, as experimental practitioners, the inherent nature of using empirical methods also further introduces a source of uncertainty, a systematic uncertainty. As with any experiment the systematic uncertainties are ubiquitous; an occupational hazard; and always the most difficult and time consuming part of the method. They are a quantitative way of describing the measure of the stability of the final result of an analysis with changes in, e.g. the experimental set-up or the analysis selection criteria or the input variables. Furthermore, although modern day high-energy physics experiments are able to employ very sophisticated particle identification they are not infallible. As a result, uncertainties in the identifications owing to the finite detector resolutions, imperfect detector (i.e. non-completely hermetic (no holes/cracks)), finite efficiency arise. The systematics also encompass uncertainties in the theoretical models (unknown masses, radiative corrections). For

the analysis at hand, the array of systematics stems from the reality that this study does not involve real data and detector but rather Monte Carlo data that has been simulated through the detector. So all sources of systematic uncertainty ensue from the accuracy of the Monte Carlo simulation. For the purposes of this analysis the sources of systematic uncertainty looked into were:

- reconstruction efficiencies, purities and resolutions of leptons, jets and $\not\!\!E_T$;
- jet energy scale;
- Standard Model and SUSY background determinations;
- the accumulated integrated luminosity;

with each one, to be addressed in turn in this chapter. Additional smaller sources that are foreseen to be detrimental to the analysis such as the lepton trigger efficiency, fake rates and SUSY mass scale, are further discussed. Also, the reconstruction efficiencies, purities and resolutions of leptons, jets and $\not\!\!E_T$ are given for two different software releases since both were used in this work. The sole reason for this was simply because some Monte Carlo data samples were not available in the earlier software release.

This chapter details some of the largest sources of systematic uncertainties which are foreseen to affect the spin measurement, more succinctly the $\cos\theta^*_{ll}$ variable. Explanations on the methods used to estimate their magnitude and so gauge how detrimental they are are also presented. Moreover, the question of how the various systematic uncertainties will be controlled and diminished will be addressed. Although it is difficult to perform detailed systematic error estimates for analyses utilising the Monte Carlo data used in advance of the construction and operation of the ATLAS detector (or any detector for that matter), it is still worthwhile considering the sources of error which could affect these measurements.

7.2 Efficiencies, Purities and Resolutions

In all analyses it is desirable to maximise the signal events and at the same time, suppress the background events as much as possible. The reconstruction efficiency, purity and resolution are vital quantities that characterise the selection procedure. These quantities account for the detector effects; finite precision of measuring a particle with the detector, so-called instrumental systematic effects. They are important because it is desirable to know how well one can reconstruct a given type or what the likelihood is that the particle will be a fake lepton or how accurate can one expect to measure the p_T of, e.g. a 50 GeV/c electron. A high purity, high reconstruction efficiency and a high degree of resolution are conducive to the quantity in question being measured to a high level of precision which is what the practitioners desire. Furthermore, the quantities most relevant to the physics aspect of the collisions are the p_T and η of the particles, since they characterise the production process. Consequently, all efficiencies, purities and resolutions are presented as functions of p_T and η. The definitions of each quantity employed in this work will now be presented and, following this, how well each particle species fares in being reconstructed will be visited, in turn. The reader should note that the definition of the physics objects to which these quantities apply to were given in section 6.4 of the previous chapter.

The first two quantities, reconstruction efficiency and resolution, purport to infer the true properties of the generated (Monte Carlo truth) particles from the detector response as accurately as possible. They are, therefore, clearly reliant upon the Monte Carlo simulation of the detector employed for modelling the imperfect nature of it. The reconstruction efficiency (ϵ, in what fraction of events when there is a Monte Carlo truth particle, does one reconstruct it) employed in this work and quoted hereafter, is defined as:

$$\epsilon_l = \frac{N_l^{match,Truth}}{N_l^{Truth}}, \tag{7.1}$$

and which has an associated binomial error given by:

$$\Delta\epsilon_l = \sqrt{\frac{(1-\epsilon_l)\epsilon_l}{N_l^{Truth}}}, \tag{7.2}$$

where $N_l^{match,Truth}$ is the number of generator-level leptons matched to a reconstructed candidate and the denominator denotes the total number of generator-level leptons. A geometrical matching (within a cone size of $\Delta R = 0.05$) between the reconstructed candidates which have passed the basic kinematic cuts and object selection criteria according to the definitions given in section 6.4 and the true candidate is required in the evaluation of $N_l^{match,Truth}$. No isolation cut has been applied to these generator-level particles. For this analysis, it is also desirable to know the lepton acceptances (reconstruction efficiencies) well in order to carry out the background flavour subtraction method. This subtraction is reliant upon having a good prior knowledge of what these efficiencies are for each flavour of lepton (i.e. electron or muon for the purposes of this work). Another quantity of interest is the purity ($\mathcal{P}$), i.e. what fraction of leptons that one accepts are true ones. The purity is defined as:

$$\mathcal{P}_l = \frac{N_l^{match,Reco}}{N_l^{Reco}}, \tag{7.3}$$

with the corresponding binomial error is given by:

$$\Delta\mathcal{P}_l = \sqrt{\frac{(1-\mathcal{P}_l)\mathcal{P}_l}{N_l^{Reco}}}, \tag{7.4}$$

where $N_l^{match,Reco}$ is the number of reconstructed leptons which are matched to

a generator-level lepton candidate using exactly the same matching criteria as was given in the definition for reconstruction efficiency and N_l^{Reco} denotes the total number of reconstructed lepton candidates. This quantity is equivalent to 1-fake ratio, where the fake ratio is defined as the ratio of the number of reconstructed leptons not matched to the generator-level leptons (within a ΔR of 0.05) to the total number of reconstructed leptons. Note that this differs from another quantity the fake probability or 'fake rate': the ratio of the number of misidentified reconstructed leptons not matched to generator-level leptons to the total number of generator-level jets. The third and final quantity is the resolution, the degree of precision with which the detector will measure a specific kinematic quantity of a particle. The resolution is defined hereafter (and given here in terms of p_T) as:

$$\mathcal{R} = p_T^{Truth} - p_T^{Reco}, \tag{7.5}$$

i.e. it is the residual in a given kinematic variable where p_T^{Truth} and p_T^{Reco} are the p_T of the generator-level and reconstructed particles respectively. Occasionally it is more instructive to use the fractional resolution, defined as:

$$\mathcal{R}_{frac} = \frac{p_T^{Truth} - p_T^{Reco}}{p_T^{Truth}}. \tag{7.6}$$

Note, both quantities, reconstruction efficiency and purity, are evaluated bin-by-bin in each of p_T and η.

This concludes the definitions of the various instrumental systematic variables. Due to the defiency in statistics in the signal sample, all plots are given for two different SUSY samples. For release 11, Inclusive SUSY and the SUSY signal, both of which correspond to the same SU3 point. For release 12, direct dislepton

pairs and the SUSY signal. These SUSY samples are defined as:

- **Inclusive SUSY:** inclusive sparticle pair production;
- **Signal:** the Drell-Yan direct dislepton pair production process;
- **Direct Dislepton pairs:** all $2 \rightarrow 2$, parton to slepton, direct dislepton pair production processes via the Drell-Yan mechanism.

7.2.1 Leptons: electrons and muons

Pertinent to the analysis is the notion that since the spin sensitive variable, $\cos\theta^*_{ll}$, is a one dimensional function of $\Delta\eta_{ll}$ it is clear that the lepton reconstruction efficiencies must be (i) well known; and (ii) high; across the full range of η.

A notable feature of the $\cos\theta^*_{ll}$ distribution for both SUSY and UED theories and the SUSY reconstructed Monte Carlo data is that there is a down-turn occurring at or near unity. This artefact can be partially ascribed to the fiducial coverage of the detector which only has coverage up to $|\eta| < 2.5$ for all leptons. It is, therefore, important to consider how sensitive the angular variable, $\cos\theta^*_{ll}$, is upon this fiducial cut in η on the final state leptons. So on examination of the η distribution of the selected final state leptons for signal events (fig. 7.1), one can see that, even in the limit of small statistics, only a small number of leptons are expected to appear at or around $|\eta| = 2.5$. Therefore, this suggests that the angular variable is not sensitive to a fiducial cut of $|\eta| = 2.5$ in the reconstruction of the final state leptons.

Figures 7.2 and 7.3 show the lepton and individual flavours of lepton (electron and muon) reconstruction efficiencies as a function p_T and η, for cases of both releases used, namely release 11 and release 12. In addition to the cuts described above, the inclusive sample required the lepton multiplicity to be greater than, or equal to two; and for the signal, the requirement was two OSSF leptons. Both

cases required the leptons (both truth and reconstructed) to have $p_T > 15$ GeV/c and $|\eta| < 2.5$.

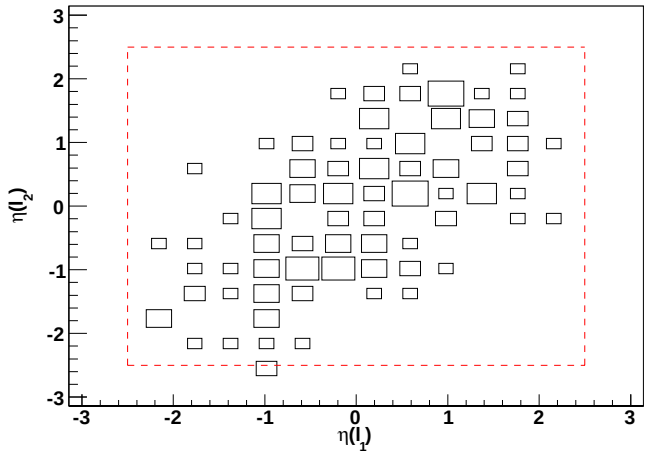

Figure 7.1: Correlation plot between the pseudorapidity of each of the two final state leptons (η_1 and η_2) in signal events. The dashed line denotes the fiducial coverage of the detector ($|\eta| < 2.5$). The distributions are equivalent to an integrated luminosity of 106 fb^{-1}.

Reflecting on fig. 7.3(a) and (b), as would be expected the final state leptons in the signal channel have a higher efficiency than from the inclusive channel owing to the cleaner environment the signal channel admits. The overall, global, average lepton efficiency for each release are, for release 11, 84 % and 63 %; release 12 signal 71 % and for the dislepton sample, 70 %. Note, most of the errors on these efficiency values are negligible. The higher efficiency observed in the SU3 direct dislepton pair processes in release 12 compared to the inclusive release 11 sample can be attributed to the much cleaner, non-hadronic environment the former will bring about. It should also be noted that it is apparent that the release 11 signal sample suffers from a lack of statistics, reflected in the larger error bars making any conclusions drawn from the distributions difficult.

The important 'turn-on' region of p_T between 0-50 GeV/c is shown in fig. 7.2(c) and fig. 7.3(c). This is important because of the applied leptonic p_T cut on the two final state leptons of 40 and 30 GeV/c. In release 12 the efficacy of the hard p_T-cuts on the signal leptons can be clearly seen. At around 20 GeV/c the p_T distribution becomes flat and, therefore, supports the case of employing hard-p_T cuts on the signal leptons of 40 and 30 GeV/c. Furthermore, it is apparent that they are sufficiently above the threshold of the ATLAS trigger such that this channel should not be drastically affected by the lepton trigger cuts. Consideration of how each flavour fares, i.e. on inspection of plots fig. 7.2(d), fig. 7.3(d) and fig. 7.2(e), fig. 7.3(e), it is clearly apparent that muons have a much higher reconstruction and identification efficiencies than electrons. This is no more exemplified than in the distributions of release 11 where the gap between the reconstruction of electrons and muons is striking. This difference is somewhat reduced in release 12. The explanation for these differences lies with the stringent isolation requirement for electrons but not for muons.

Regarding the lepton's efficiency dependency upon p_T there is little dependence on the lepton p_T which is reflected in the rather flat distributions at medium to high p_T values. For the inclusive sample versus p_T, the efficiency increases to a plateau of approximately 73 % starting from p_T approximately above 60 GeV/c and remains reasonably stable thereafter.

It is also apparent that almost all η dependency efficiency plots (fig. 7.2(b) and fig. 7.3(b), and fig. 7.2(d) and fig. 7.3(d)) mirror the geometry of the detector with substantial drops occurring in the crack ($\eta = 0$) and barrel-endcap transition region ($|\eta| \approx 1.4$) with higher efficiencies elsewhere.

Moving to fig. 7.4, it can be seen from all four plots, for p_T and η in both releases, that the signal leptons are extremely pure over the full fiducial range.

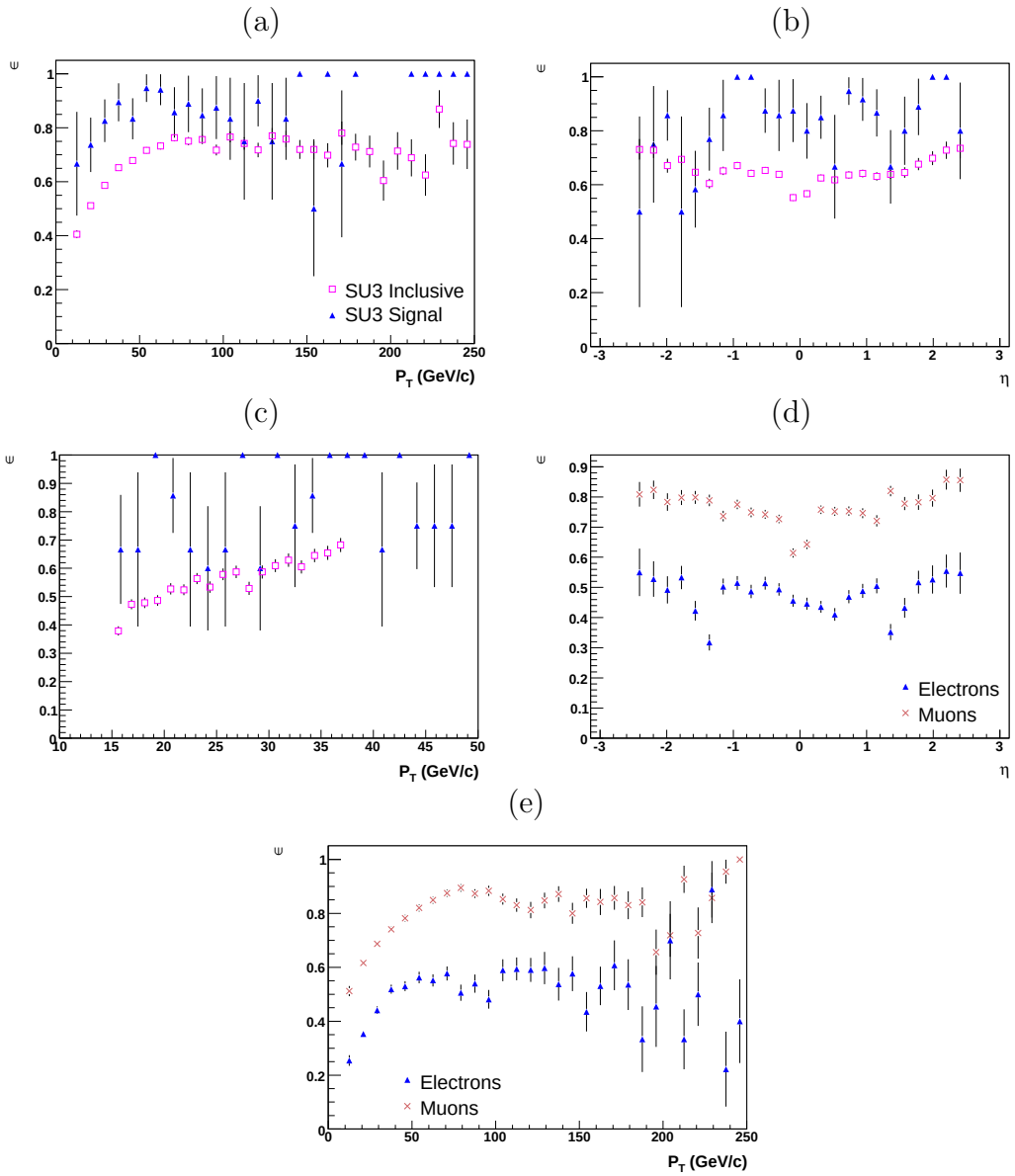

Figure 7.2: The release 11 reconstruction efficiencies as a function of transverse momentum for leptons (a) and (c), muons and electrons (e); and as a function of η, (b) for leptons and (d) for electrons and muons. The lepton, electron and muon object selection criteria are described in the text.

The overall, average purity amounts to 99 % and 95 % for SU3 SUSY signal and inclusive samples respectively for release 11. For release 12, the purities were 99 % for signal and 98 % for disleptons. Again, all errors on these efficiency

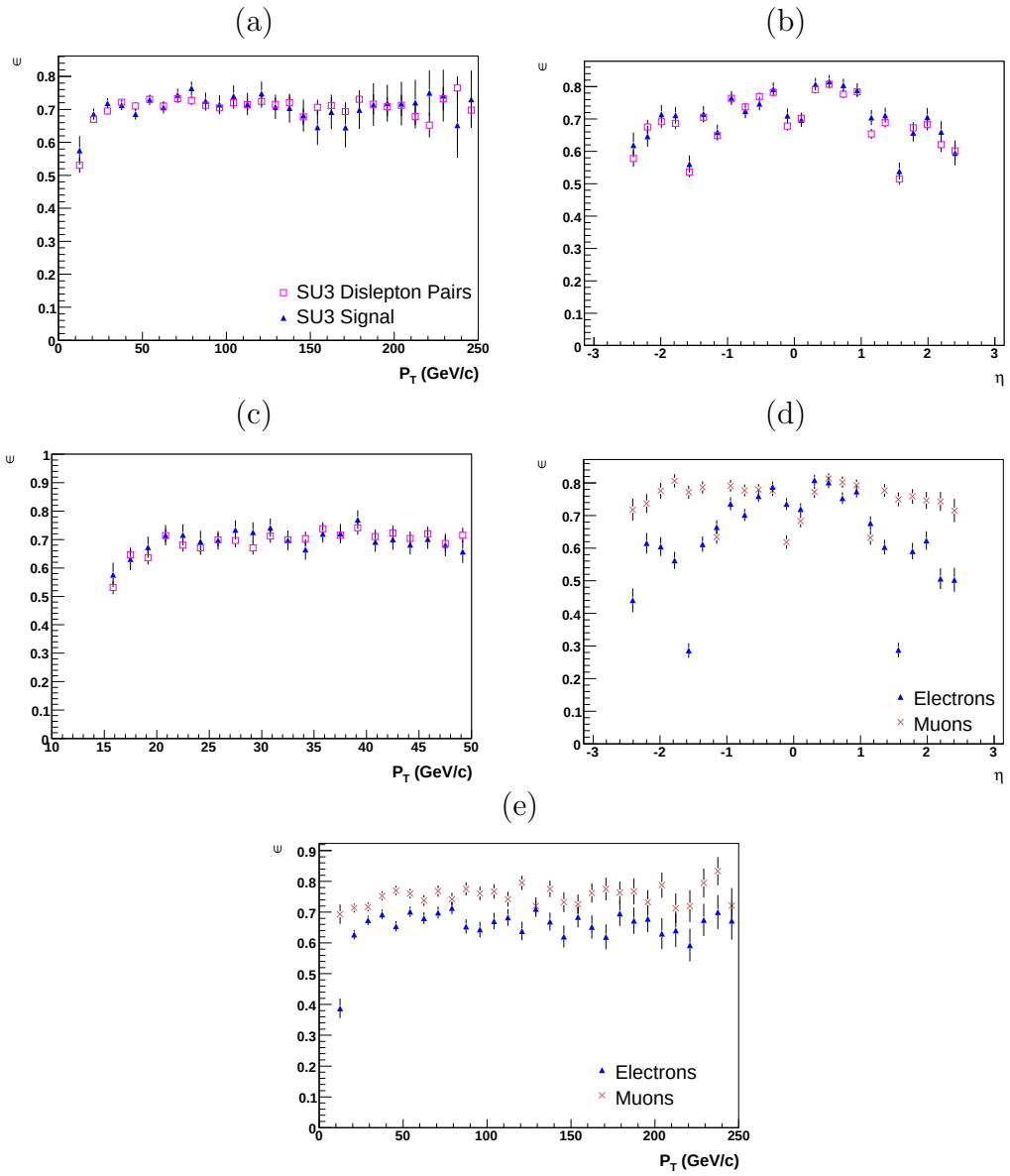

Figure 7.3: The release 12 reconstruction efficiencies as a function of transverse momentum for leptons (a) and (c), muons and electrons (e); and as a function of η, (b) for leptons and (d) for electrons and muons. The lepton, electron and muon object selection criteria are described in the text.

values are negligible. The extremely high purity of the signal samples, in both releases, can be ascribed to both the clean environment of the signal channel; and flavour and multiplicity cuts. However, the paucity of Monte Carlo statistics

also plays a part. This is reflected in the large error bars in fig. 7.2 and fig. 7.3 which are indicative of it being statistically limited. This work could be improved with larger fully simulated samples or, needless to say, when the advent of data arrives. Having said this, one can safely say that with the basic cuts and selection criteria applied one still retains a high purity and the results found were similar to studies found in the CSC notes [147]. Although the SUSY events admit a 'busier' (less clean) environment, a high purity can still be retained mainly due to the harder p_T spectrum of leptons from SUSY events compared to the Standard Model background events. Also noticeable, which is to be expected, is the poor purity in the crack regions and at the very limits of the fiducial volume of the detector ($\eta \approx 2.5$).

The fractional p_T resolution distributions (fig. 7.5(a), (b) and (c)) of the final state leptons in the inclusive, dislepton and signal samples illustrate that the Gaussian fits are good with the mean value in all three distributions consistent with zero. The resulting p_T resolutions are 2.5 % and 2.7 % for releases 11 and 12 respectively. The p_T resolution of the final state signal process is 2.9 %. Comparing this to the resolutions expected and quoted in the ATLAS TDR [96] for 40 GeV/c electrons: $2 - 3$ % (including the constant term) and for muons $\approx 2 - 3\%$ show that the p_T resolutions are in good agreement with the TDR results, for both electrons and muons. Also noted is the fact that there are too few events for statistically meaningful resolution measurements for the signal process and as a result we do not concern ourselves with these.

Finally, the resolutions evaluated in this work each agree well, and to within 1 % of each other. For the purposes of the work presented here the values of the detector systematic uncertainties of lepton reconstruction efficiency and lepton p_T resolutions of 1 % and 4.1 % respectively were chosen in accordance with the

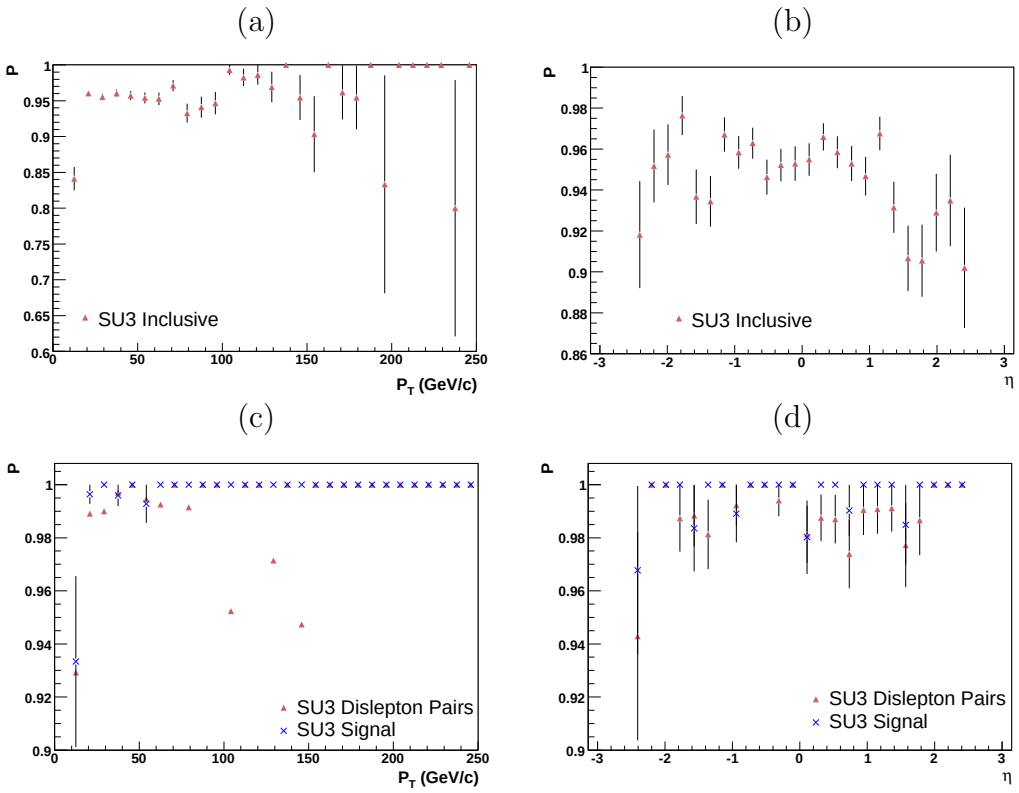

Figure 7.4: The purity as a function of p_T (left hand plots) and η (right hand plots) for (a) and (b) release 11 SU3 Inclusive only and in (c) and (d) release 12 SU3 SUSY signal and direct dislepton processes. Note the signal in both releases are 99 % pure.

results obtained in [147].

7.2.2 Missing transverse energy

As with the majority of SUSY searches the canonical signature is the requirement of a large value of missing E_T. The signal channel under investigation, the direct dislepton pair production process, is no exception with significant missing E_T emanating from the process in the form of a pair of lightest SUSY particles (LSPs) which traverse the detector without interacting in any directly measurable way. Their presence can only be inferred from the energy imbalance in the

hard interaction that had previously occurred. Moreover due to the majority of the total energy (14 TeV) of the proton-proton collisions being carried away by undetected remnants of the underlying event one resorts to measuring the energy in the traverse plane, to measure the missing E_T of the partonic subprocess (hard or soft). It is, therefore, clear that in order to effectuate the method of spin measurement a good missing E_T resolution and optimal missing E_T measurement are vital. The missing E_T quantity is primarily reconstructed from the energy deposits in the calorimeters and reconstructed muon tracks but it is also a convolution of the calorimeter energy resolutions, electronic noise and detector effects such as finite detector hermeticity, cosmic rays, beam-gas and beam-halo events. The resolution of the two components (x and y) of missing E_T in ATLAS is usually parameterised as:

$$\sigma(\not{E}_T(\mathrm{GeV})) = a\sqrt{(|E_T(\mathrm{GeV})|)}, \tag{7.7}$$

where E_T denotes the total scalar sum of E_T over all calorimeter cells and a is a calibration constant and takes the values between 0.53 and 0.57 for values between 20 GeV and 2 TeV [99].

As $\not{E}_T$ is a vector-like quantity in nature a subtraction of vector quantities is carried out in evaluating the $\not{E}_T$ residual. Regarding the missing E_T resolution the means do not agree with zero in release 11 but do in release 12. The missing E_T resolution is 18.2 GeV in release 11 and is an improved value of 10.4 GeV in release 12 and the signal has a resolution 11.0 GeV. In fig. 7.5(d) it can be seen that for the dislepton sample the $\not{E}_T$ resolution is about 10.4 GeV and that the mean of the distribution is only slightly biased with respect to the Monte Carlo reconstructed data and is consistent with zero with the statistics available. Reflecting briefly on the signal distribution (fig. 7.5(e)) shows that due to the

lack of statistics the information in the distribution is not a very good estimate of the mean or σ and their subsequent errors. However, from the offset in the mean one can say that the $\not\!\!E_T$ resolution will not be a large systematic effect. So summarising, as the bias $\sim \frac{1}{20}$ of the resolution (i.e. we can hope to know the $\not\!\!E_T$ scale to the 4 or 5 % level at best) for this particular region of phase space, the size of this resolution is negligible. Other systematic uncertainties are found to be much larger than this and so this is a small systematic effect.

Illustrated in fig. 7.6 are the correlations of $\not\!\!E_T$ distributions in the Monte Carlo truth and reconstructed data. It shows the high degree of correlation between the Monte Carlo reconstructed and truth $\not\!\!E_T$. This plot also serves to illustrate as to why the initial selection cut of $\not\!\!E_T > 100$ GeV is instructive to use in detaching the signal from the large amount of SUSY background processes.

7.2.3 Jets

As the analysis is only concerned with a purely leptonic final state in conjunction with missing transverse momentum we shall not concern ourselves with properties of jets here[a]. However, a jet veto is employed and there is a correlation with $\not\!\!E_T$ so investigating the jet energy scale would be required in any study of real ATLAS data. Therefore, in the next section the jet energy scale will be discussed.

[a]The fake rate was found to be small in this study ($\sim$ 2% for the SU3 sample).

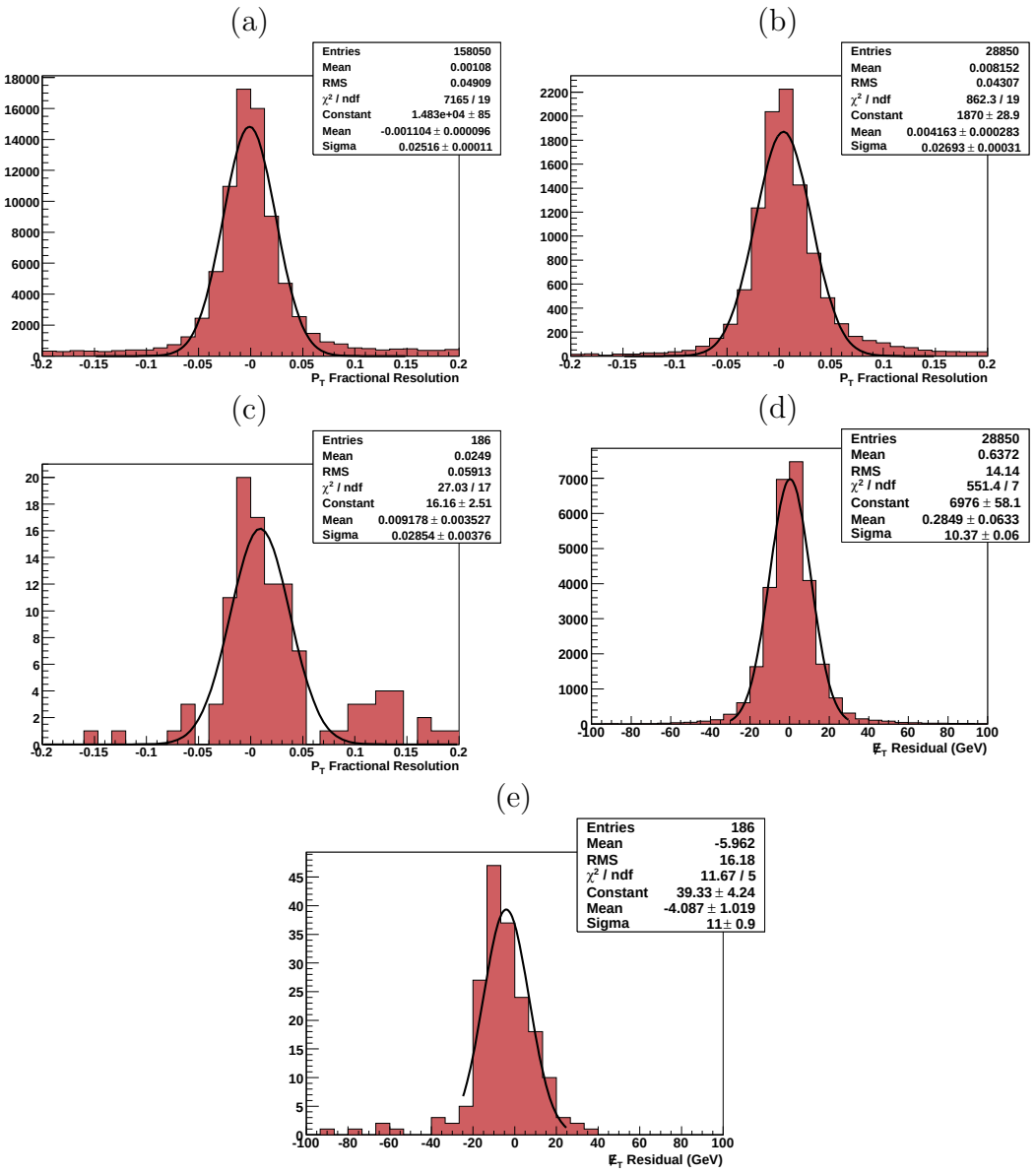

Figure 7.5: The lepton (electron and muon) p_T resolutions and $\not\!\!E_T$ resolutions for release 11, the inclusive SU3 SUSY sample; and release 12, the dislepton and signal SUSY samples. The resolution given for leptons is the fractional resolution ($\mathcal{R}_{frac} = \frac{p_T^{Truth} - p_T^{Reco}}{p_T^{Truth}}$) and for the $\not\!\!E_T$, the residual ($\mathcal{R} = \not\!\!E_T{}^{Truth} - \not\!\!E_T{}^{Reco}$). Shown are the fractional p_T resolutions for leptons in (a) the inclusive release 11 sample, (b) dislepton sample and (c) signal events in release 12. Whereas shown in (d) and (e) are the $\not\!\!E_T$ residuals in the dislepton and signal events in the release 12 sample respectively.

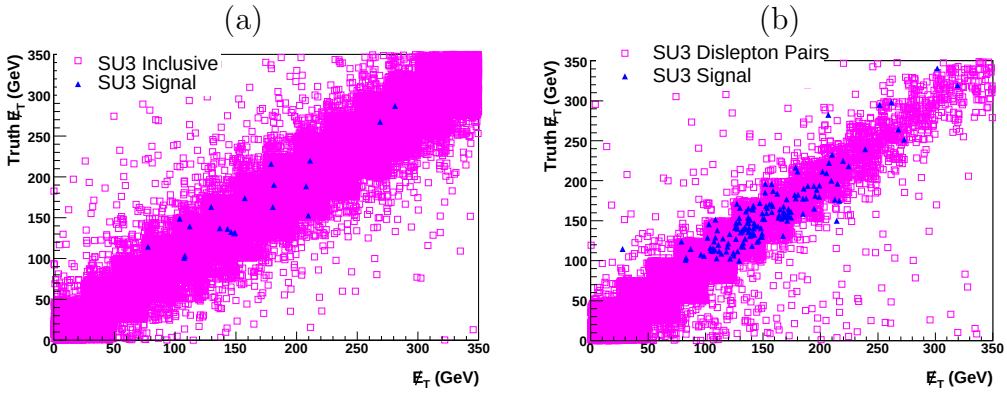

Figure 7.6: $\not\!\!E_T$ correlations between the truth and reconstructed Monte Carlo events in SUSY processes. For release 11, the samples were SU3 Inclusive, signal and background and for release 12, SU3 dislepton pairs, signal and background. The plots correspond to 8.5 fb^{-1} and 106 fb^{-1} for release 11 and 12 respectively.

7.3 Jet energy scale

One of the dominant sources of detector systematic uncertainties is expected to arise from the uncertainty on how well the calorimeters are calibrated to measure energies of jets, the so-called jet energy scale. Badly measured four-momentum of jets can result in a contribution to the spurious $\not\!\!E_T$. Here, a simple estimate of the impact of the jet energy scale uncertainty was performed. It should be pointed out here that, although the jet energy corrections will display a p_T and η dependence, the assumption was that it was a global correction. That is, the jet energy scale uncertainty is independent of the transverse energy and pseudorapidity of the jet. The method involved scaling the four momentum of each jet by a constant factor, corresponding to a $\pm$ 10%, $\pm$ 5% and $\pm$ 1% uncertainty on the jet energy scale. This was performed on an event-by-event basis and, furthermore, the $\not\!\!E_T$ was also scaled by the same constant factor each time.

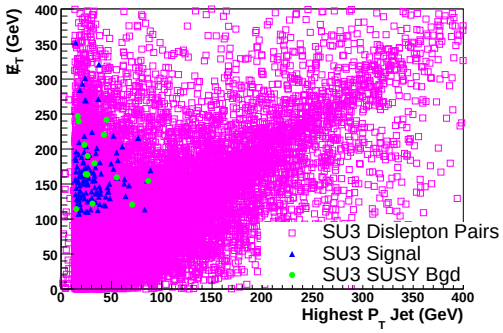

Figure 7.7: Correlation plot of $\not\!\!E_T$ versus highest p_T jet for SUSY events only for release 12 SU3 dislepton pairs, signal and background. The plot corresponds to 106 fb^{-1}. Release 11 also showed similar behaviour.

This correlation between the highest-p_T jet and $\not\!\!E_T$ for release 12 is exemplified in fig. 7.7 where it is clearly evident that the highest p_T-jets in SU3 SUSY events display a strong degree of positive correlation with the $\not\!\!E_T$ in the event.

Release 11 also displayed similar behaviour. Further, fig. 7.8 shows the degree of correlation between the $\not\!\!E_T$ and one other variable used in this work, namely the transverse recoil (TransR = $|\not\!\mathbf{p_T} + \mathbf{p_T}(\mathbf{l}^{\pm}) + \mathbf{p_T}(\mathbf{l}^{\mp})|$). Although a lot less correlated than that which exists between the $\not\!\!E_T$ and highest-p_T jet there is still a degree of correlation. The figure also serves to illustrate as to approximately what values to set each cut variable to in order to separate the signal from the background (transR$<$ 100 GeV/c and $\not\!\!E_T$ $>$ 100 GeV). The latter was, nevertheless, set to an optimised value by an automated procedure. It was for this reason, i.e. a significant degree of correlation between the total $\not\!\!E_T$ and tranverse momentum of the leading jet, that the decision was taken to alter both simultaneously. Tabulated in table 7.1 are the resulting percentage changes to the various test statistic quantities for several jet energy scale uncertainty values: $\pm$10 %, $\pm$5 % and $\pm$ 1 %. For a 10 % value, the uncertainty on the final figure of merit, $\ln\left(\frac{L_{SUSY}}{L_{UED}}\right)$, ranges from -4.5 % to -7.4 %. However, as control of the experiment and an understanding of the calibration mature over time to a level of 5 %, changes this uncertainty to -4.2 % to 1.7 %. This small percentage uncertainty still persists even in the event that the challenging goal of a 1 % jet energy scale is achieved. Moreover, the χ^2_{SUSY} rather than the χ^2_{UED} changes by a larger amount for each change in the jet energy scale and $\not\!\!E_T$. Thus, indicating that the SUSY Monte Carlo data distribution is more sensitive to its proximity to the SUSY theory distribution rather than to the UED one. However, this percentage change is small throughout ($\sim$ 4 %). These small percentage changes also manifest in the changes in the final figure of merit. So it is therefore apparent that the jet energy scale will contribute a small systematic uncertainty toward the spin measurement.

Test Statistic	% change to E_{jet} and $\not\!\!E_T$					
	10 %		5 %		1 %	
	+10	-10	+5	-5	+1	-1
$ln\left(\frac{L_{SUSY}}{L_{UED}}\right)$	-4.54	-7.38	-4.20	1.65	-3.22	-1.11

Table 7.1: The percentage change of the final figure of merit, ln $\left(\frac{L_{SUSY}}{L_{UED}}\right)$, for different percentage changes to the four momenta of the jets and $\not\!\!E_T$. These changes were performed by scaling the four momenta of the jets and $\not\!\!E_T$ by a single factor. Results are shown for several different scale factors of 1.10 and 0.90, 1.05 and 0.95, and 1.01 and 0.99 (corresponding to jet energy scale uncertainty values of ±10 %, ±5 % and ±1 % respectively).

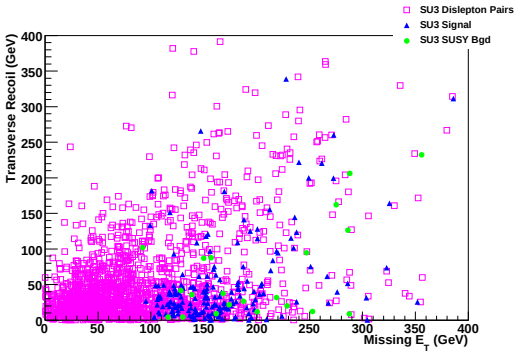

Figure 7.8: Correlation plot of $\not\!\!E_T$ versus the transverse recoil for SUSY events only for release 12. The SUSY events are SU3 dislepton pairs, SU3 signal and SU3 background. The plot corresponds to 106 fb^{-1}. Release 11 also showed similar behaviour.

7.4 Standard Model background determination and extrapolation

Fig. 6.9 demonstrated that although the Standard Model backgrounds do not overwhelm the SUSY signal they are, nevertheless, not insignificant and thus, will need to be accurately determined. Having evaluated the nature of the Standard

Model backgrounds and their magnitudes approximatley from Monte Carlo, one must next address how, and to what accuracy, can we determine them. Then we must associate a systematic error to this method. The final goal of the background determination method is to try and answer, as best we can, with all systematic uncertainties included:

- how well with 30 fb^{-1} of data can we measure the background (i.e. the cross-section);
- what kinematic control region is best for a cross-section measurement for a particular, selected background.

The problematic nature posed by determining, accurately, the Standard Model backgrounds from Monte Carlo arises from an assortment of sources: inaccurate knowledge of the cross-sections, underlying event, parton showers, PDF uncertainties at the 14 TeV energy scale regime the LHC will probe, limited Monte Carlo statistics, uncertainty in the luminosity. All these lead to estimates of the backgrounds in the Monte Carlo simulations alone that are not to the required precision. Note, these also affect the signal Monte Carlo simulation. This poses a major challenge and one is led, therefore, to resorting to accurately measuring the backgrounds from the data itself, once real data-taking commences. The description of the method undertaken of such a data-driven Standard Model background estimation is the subject of this section. However, the author should point out that although there are multiple ways of doing this (and indeed, with the advent of real data-taking employing several methods will probably be better rather than just one) only one was used here. Each method differs in their approach and are characterised by different systematic uncertainties and they also focus on different backgrounds. Even with optimised efficiency selections these can be easily destroyed by uncontrolled systematic uncertainties on the backgrounds.

The general aim adopted by the data-driven method is to be able to accurately estimate the Standard Model backgrounds together with their uncertainties in regions of phase space in which new physics, the SUSY signal process, dominates, the so-called 'signal' region of phase space. This region is defined by the particular array of the six kinematic variables set equal to their optimised values. To do this, the measurement of the cross-sections of the Standard Model backgrounds are carried out in regions of phase space in which each background dominates, so-called 'control samples' or 'background enriched regions' (also phrased as background enhanced regions). The resulting statistical uncertainty in the background measurement in this background enhanced region constitutes a systematic uncertainty in the analysis. It are these control samples from which the predictions of the Standard Model background cross-sections in the signal region are derived through extrapolating from the background enhanced regions of phase space to the signal region of phase space. The control sample regions, therefore, should be as close as possible to the signal region of phase space. Yet, at the same time, the control regions should also fulfil the following criteria:

- largely depleted of SUSY signal and have a sufficient number of background events (abating the statistical uncertainties);
- small theoretical uncertainties;
- admit a low contamination of SUSY and other Standard Model backgrounds (i.e. good control of the composition of the control samples);
- provide an unbiased estimate of the background in the signal region when extrapolating from the control sample.

This section details the method employed that may be used with real data and what the corresponding systematic uncertainty is.

For the purposes of this analysis the idea is to estimate the background from the Monte Carlo data in the $\cos\theta^*_{ll}$ distribution. This, therefore, requires the variable chosen (one of the six) to be uncorrelated with the $\cos\theta^*_{ll}$ variable. One background was selected which was the largest Standard Model contribution, namely $W^{\pm}W^{\mp}$ diboson pairs. The control region (see fig. 7.9) is defined as:

- $m_{T2} < 120$ GeV/c^2, i.e. the m_{T2} cut was *reversed*;
- transverse Recoil < 50 GeV/c, i.e. this cut was relaxed somewhat from 100 GeV/c;
- jet veto: no jets (b or otherwise) with a p_T(jet) > 20 GeV/c within $|\eta| < 3.0$.

These selections result in obtaining a region that is enriched in $W^{\pm}W^{\mp}$ boson pairs. The number of $W^{\pm}W^{\mp}$ events in this background-enhanced region was 163.4 (82 % of the total number of background events in this region. There was zero signal events in this region) and in the signal region for the same background the number was 14.7. Thus, using these numbers this produces a systematic uncertainty in the background rate for this analysis of $\pm 8\%$ (or ± 12.8 events). For completeness the other contributing backgrounds in this background enhanced region of phase space were, in descending order of contribution, SUSY (10 %) and $W^{\pm}Z^0$ (8 %) with all other backgrounds totally removed. This, therefore, illustrates that this region of phase space is ideal to make a cross-section measurement on the $W^{\pm}W^{\mp}$ background due to the low contamination of other backgrounds and the surplus of $W^{\pm}W^{\mp}$ events.

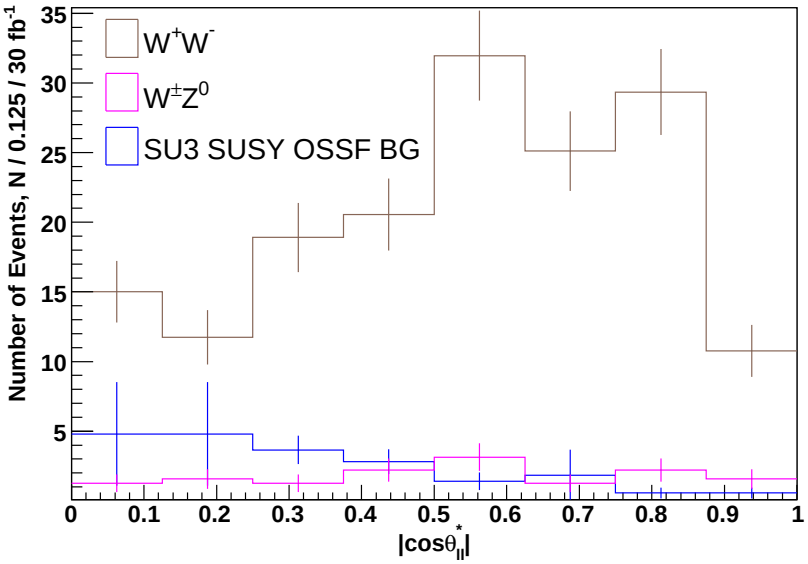

Figure 7.9: The enriched 'control' sample of $W^{\pm}W^{\mp}$ diboson pairs in $\cos\theta^{*}_{ll}$ which was obtained by reversing the m_{T2} kinematic variable, employing a jet veto (no jets (b or otherwise) with a p_T(jet) > 20 GeV/c within $|\eta| < 3.0$) and reducing the value of the Transverse Recoil variable from 100 GeV/c to 50 GeV/c. Error bars shown are statistical only.

7.5 SUSY background determination

As described in previous chapters, in addition to the backgrounds arising from the Standard Model processes there also exists the possibility for various SUSY processes to produce a OSSF lepton pair in the final state. As shown in fig. 6.8 the SUSY backgrounds are generally small, although not insignificant, with respect to the signal. This is especially true at high $\cos\theta^{*}_{ll}$ values. It is, therefore, instructive to attempt to ascertain their magnitude as accurately as possible and try to understand how much of a hindrance they will actually pose. To do this one uses the background flavour subtraction method. This subtraction method is an extremely useful one to determine the SUSY combinatorial background. This argument is also applicable to the Standard Model backgrounds. As documented

in the previous chapter, this method of background flavour subtraction for determining the SUSY backgrounds is applicable here. However, it is recommended that the lepton detector acceptances are taken into account when employing the background subtraction method. Moreover, maybe one may want to employ a different method for measuring the SUSY backgrounds such as using an admixture of the techniques of: using control samples and OSSF-OSOF background subtraction or using a sign subtraction procedure.

7.6 Luminosity systematic uncertainty

A further instrumental systematic uncertainty is the uncertainty on the accumulated integrated luminosity value. Although the method presented is not a counting experiment per se, it is nevertheless, still heavily reliant upon the notion that there must exist a large number of SUSY signal events and at the same time, a minimal number of residual background events from either Standard Model or SUSY or both. Thus, it is then still worth checking and trying to estimate the size of this systematic uncertainty. Unlike the case of cross-sections, the uncertainty on the integrated luminosity is process independent and is completely determined by the uncertainties on the properties of the colliding beams. The method invoked here, to measure the uncertainty on the accumulated integrated luminosity, involved normalising the Monte Carlo data (event numbers and errors) from 30 fb^{-1} to 100 fb^{-1} and recalculating the final figure of merit ($\ln\left(\frac{L_{SUSY}}{L_{UED}}\right)$) thereafter. It was found that by doing this the final figure of merit changed by 0.5 %. One can, therefore, deduce that the uncertainty on the accumulated integrated luminosity value is negligible and it cancels since signal and backgrounds are scaled by the same uncertainty.

As the final figure of merit depends primarily upon the shape of the distributions rather than on the rate (although the latter does play a part in a small way) and together with the statistically limited region found here, then there is no surprise that the percentage change on integrated luminosity value is close to zero.

7.7 Migrations at cut boundaries

A further systematic effect to consider is the magnitude of the migration of events at or in the vicinity of where the cuts are employed. If the kinematic distribution in question has a strong dependence upon a kinematic variable that is poorly known then these together can generate a significant systematic uncertainty. Displayed in fig. 6.7 are the signal and background distributions plotted as a function of each of the six kinematic selection variables: m_{T2}, transverse recoil, the two hardest leptons in the event, the hardest jet in the event, the invariant mass of the dilepton final state and the $\not\!\!E_T$, each set equal to their optimal value. It is apparent that the distributions of transverse recoil, leading lepton p_T and leading jet p_T have very few events at or near to where the cut is employed so migrations arising from the uncertainties in these kinematic variables should not affect the final distribution. Reflecting on the three other kinematic variable distributions however in m_{ll}, m_{T2} and the $\not\!\!E_T$ reveals that these do have a significant fraction of events (especially pronounced for the signal) in the vicinity of their respective cuts. Therefore, it is important that the resolution of these variables is well known and knowledge of what effect they may have on the shape of the $\cos\theta^*_{ll}$ distribution, relevant to this work. Nevertheless, as was found in this work the contribution to the systematic uncertainty from the jet energy scale was small

and should not be detrimental to the spin measurement. Having carried out a complete and thorough, detailed simulation of the ATLAS detector we can still reiterate the point that was made in the original paper on this work [93]. That is, the remark made on the fact that since the signal contains two final state leptons and $\not\!\!E_T$, the former of which will be well measured by the ATLAS detector, the $\not\!\!E_T$ will, thus, also be relatively well measured. Consequently the remark that the m_{ll}, m_{T2} and the $\not\!\!E_T$ distributions will also be well under control, still remains true. Thus we can be confident that the systematic uncertainty arising from migrations at the vicinities of the cut boundaries should be small and under control for this work.

7.8 Further sources of systematic uncertainty

As a final word it is worth mentioning a few other sources of systematic uncertainty that could effectuate the spin work presented here. Among the instrumental systematic uncertainty which were not presented here are the lepton misidentification (i.e. the fake rates of the leptons) and trigger efficiencies. The latter folds into the reconstruction efficiency and moreover, all three (reconstruction efficiency, fake rate and trigger efficiencies) can be determined from using the so-called "tag-and-probe" method in, e.g. the $Z^0 \rightarrow l^{\pm}l^{\mp}$ channel for evaluating the reconstruction efficiency. The best estimates result in values between 1-3 % [147] for both types of leptons at the p_T range we are concerned with in this analysis. Thus, the size should not alter the spin measurement drastically. One other noteworthy source of systematic uncertainty is that which stems from the unknown SUSY mass scale which may lead to uncertainties in the comparative SUSY $\cos\theta^*_{ll}$ distributions employed in this work. However, as noted in [93] this

will not be a significant source of systematic error and we should be confident that this argument still holds at 30 fb^{-1} even if this is at 15 % less integrated luminosity. It will, nevertheless, be important to determine the SUSY mass scale if SUSY is indeed discovered at the LHC.

7.9 Overall combined systematic uncertainty

Incorporating each individual systematic uncertainty in a consistent way so as to form one final total systematic uncertainty is non-trivial owing to the possible correlations between the individual sources of systematic uncertainty without a degree of assumption. This assumption is that each one is assumed to be largely (although not entirely) independent (uncorrelated). By the very virtue of this independence and assuming they are approximately Gaussian can the errors be combined in quadrature form for a total systematic uncertainty, for each Monte Carlo data point, of +9.0% and -9.8 %.

Tabulated in table 7.2 is a recapitulation of all the individual systematic uncertainties that contribute to the overall, final systematic error found in this work. Also shown are the statistical uncertainty and the final, overall, combined statistical and systematic uncertainty.

7.10 Summary of the systematic uncertainties

This section has detailed the various sources of systematic uncertainty on the final figure of merit, $\ln\left(\frac{L_{SUSY}}{L_{UED}}\right)$, and the best current estimates of them which could affect the $\cos\theta^*_{ll}$ variable making a spin measurement at the specific point in mSUGRA space employed in this work. It can be seen that with employing the full optimised event selection and if the supporting measurements can, indeed, be

Source	Uncertainty	
Lepton Efficiency	1 %	1 %
Lepton p_T Resolution	4.1 %	4.1 %
$\not{E}_T$ and Jet Energy Scale	1.7 %	−4.2 %
Luminosity	0.5 %	0.5 %
Standard Model background cross-sections	7.8 %	7.8 %
Total Combined Systematic	9.0 %	−9.8 %
Statistical	12.0 %	12.0 %
Combined Statistical and Systematic	15.0 %	−15.5 %

Table 7.2: Estimates of the dominant systematic uncertainties together with the statistical uncertainty on the final figure of merit, $\ln\left(\frac{L_{SUSY}}{L_{UED}}\right)$, incurred during the spin measurement presented here. The statistical and systematic uncertainties were also combined in quadrature.

made with the precision laid out in this chapter, then the spin measurement utilising the $\cos\theta^*_{ll}$ angular variable will be, ultimately, limited by statistical (12.0%) fluctuations rather than by systematic $(^{+9.0\%}_{-9.8\%})$ sources of uncertainty. However, even if the work studied here is statistically limited it is still worth highlighting the largest source of systematic error, namely that which arises from determining the Standard Model background cross-sections from data. The dominant residual Standard Model backgrounds for this particular region of phase space were $W^{\pm}W^{\mp}$ and $W^{\pm}Z^0$ (fig. 6.9). The sizes of the Standard Model backgrounds are certainly not insignificant and they, therefore, warrant further attention. However, the largest residual background was that arising from SUSY OSSF background events. And although the systematic uncertainty on the size of the SUSY background was not quantified in this work, the method was discussed. Furthermore, the method was shown to be an adequate one for measuring the size of the

SUSY backgrounds in the dislepton process studied here. Although, in doing this it is recommended that one must take into account the difference in reconstruction efficiencies of lepton species. One may want to seek alternative methods for measuring the size of the SUSY backgrounds such as using an admixture of the techniques of: using control samples and OSSF-OSOF background subtraction or using sign subtraction methods.

From fig. 6.12 it can be seen that the systematic uncertainties are not a dominant effect to the spin measurement. Moreover, it can be seen that changes to the sensitivity of the difference between the two models with integrated luminosity will not be drastic. At a value of integrated luminosity of 50 fb^{-1} were one is expected to achieve a 5σ in distinguishing between SUSY and UED, by taking into account the total uncertainty (statistical and systematic) of $\pm$ 15 %, this value of integrated luminosity will be in the range 44 fb^{-1} to 55 fb^{-1}. Thus, the total uncertainty will not have a huge effect on the total amount of accumulated integrated luminosity to achieve a 5σ separation. Looking at higher values of integrated luminosity (where the systematic uncertainty will be much better understood and will, therefore, decrease) at 300 fb^{-1}, again, the total systematic will not alter the final statistical significance drastically. One would, therefore, expect that the significance would vary between 6.6σ and 7σ.

Finally, the investigation and evaluation of the total (systematic and statistical) error ($\sim 15.0\%$) should not impinge upon the slepton spin measurements by too much and thus rendering the method futile. There is, therefore, considerable optimism for carrying out this method using real data at the LHC.

Chapter 8

Epilogue

THE individual chapters of this thesis incorporate their own conclusions so here there only a short, succinct overview will be given.

A rich array of new, high-energy completions of the Standard Model exist which help to ameliorate some of the shortcomings of the Standard Model. Some such theories are also predicted to manifest at the TeV energy scale. In this thesis two different such possibilities have been examined, the theory of Supersymmetry and the theory of Universal Extra Dimensions. Further, the notion that both models could display similar collider has been introduced and thus a way to unambiguously differentiate between them is therefore needed. Whilst, at the same time still remaining impartial to each model which will be important.

To this end, the work presented in this thesis evaluates the feasibility of differentiating between the two models by measuring the spins of the new particles, applicable using the ATLAS experiment, one of the two general purpose detectors, at the LHC. I have shown that by using an angular variable, $\cos\theta^*_{ll}$, to measure the spins in the direct dislepton process: $q\overline{q} \rightarrow Z^0/\gamma^* \rightarrow \tilde{l^{\pm}}\tilde{l^{\mp}} \rightarrow \tilde{\chi}^0_1 l^{\pm} \tilde{\chi}^0_1 l^{\mp}$, based upon Monte Carlo data, fully simulated in accordance with the mSUGRA Supersymmetry framework that, at a specific test point, ATLAS can distinguish between the two models using 30 fb^{-1} of integrated luminosity. Moreover, it was found that a minimum of 50 fb^{-1} of integrated luminosity is sufficient to allow the spin determination to be made in this dislepton channel. This amount of

integrated luminosity provides a sufficient number of events to measure the slepton spin of points in SUSY space which admits left-handed slepton masses in the range 216 to 230 GeV/c^2 and right-handed sleptons in the range 155 to 232 GeV/c^2. I have further investigated the main systematic uncertainties that one might incur if such a spin measurement to the one presented here at the LHC was performed.

Of course whilst such models are intellectually stimulating and however aesthetically pleasing they may be, to have any scientific validity one must either confirm or refute their claim by the virtue of empirical methods. Moreover, the question of how plausible it is that any particular beyond the Standard Model theory is realised in nature is inevitably impossible to answer without the aid of real data. To this end an additional part of the work presented in this thesis investigated the operational performance of one of the ATLAS inner detector subsystems, the SCT. The investigation entailed measuring the noise occupancy levels of a certain fraction of the SCT barrel models, diagnosing eight problematic modules in the process. Furthermore, an anomaly, the so-called zeroth time bin anomaly, was identified which spawned further investigation.

So all eyes will be on the LHC to see if Man's vision of nature will be irrevocably altered once again..... only time will tell.

Appendix A

Abbreviations and Acronyms

ADD	N. Arkani-hamed, S. Dimopoulos and G.R Dvali
AAN	Athena-Aware Ntuples
AOD	Analysis Object Data
ASIC	Application Specific Integrated Circuit
ATLAS	A Large Toroidal LHC ApparatuS
BCID	Bunch Crossing IDentification number
BOC	Back of Crate card
CERN	Conseil Européen pour la Recherche Nucléaire (Obsolete. Now called the Organisation Européen pour la Recherche Nucléaire)
CMS	Compact Muon Solenoid
cMSSM	constrained Minimal Supersymmetric Standard Model
CSC	Cathode Strip Chamber
DAC	Digital to Analogue Converter
DAQ	Data Acquistion
DESY	Deutches Elektronen SYnchrotron laboratory
DM	Dark Matter
ECAL	Electromagnetic Calorimeter
eV	electron Volt $\sim 1.602 \times 10^{-19}$ Joules
EF	Event Filter
EW	ElectroWeak

EWSB	ElectroWeak Symmetry Breaking
FCAL	Forward CALorimeter
FCNC	Flavour Changing Neutral Current
FFM	Final Figure of Merit
FIFO	First-In-First-Out
GR	General Relativity
GUT	Grand Unified Theory
HCAL	Hadronic CALorimeter
HLT	High Level Trigger
HEP	High-Energy Physics
ID	Inner Detector
IP	Interaction Point
KK	Kaluza-Klein
LAr	Liquid Argon
LED	Large Extra Dimensions
LEP	Large Electron-Positron Collider
LHC	Large Hadron Collider
LHCC	Large Hadron Collider Committee
LHCb	Large Hadron Collider beauty experiment
LKP	Lightest Kaluza-Klein Particle
LSP	Lightest Supersymmetric Particle
MDT	Monitored Drift Tube
MSSM	Minimal Supersymmetric Standard Model
mSUGRA	minimal Supergravity
mUED	minimal Universal Extra Dimensions
OSOF	Opposite Sign Opposite Flavour
OSSF	Opposite Sign Same Flavour
PETRA	Positron Electron Tandem Ring Accelerator
QCD	Quantum ChromoDynamics

QED Quantum ElectroDynamics

QFT Quantum Field Theory

QGD Quantum GeometroDynamics

QT Quantum Theory

RCC ROD Crate Controller

RGEs Renormalization Group Equations

ROD ReadOut Driver

RPC Resistive Plate Chamber or R-parity Conserving

RPV R-parity Violating

RS L. Randall and R. Sundrum

SCT Semi-Conductor Tracker

SLAC Stanford Linear Accelerator Center

SLC SLAC Linear Collider

S-Link CERN Serial optical Link

SM Standard Model

SSB Spontaneous Symmetry Breaking

SSOF Same Sign Opposite Flavour

SSSF Sign Same Same Flavour

SUSY Supersymmetry

TASSO Two Arm Spectrometer SOlenoid

TCC Interface between the TIM and the TTC system

TDAQ Triggering and Data Aquisition

TDR Technical Design Report

TGC Thin Gap Chamber

TIM TTC Information Module

TOE Theory Of Everything

TRT Transition Radiation Tracker

TTC Trigger, Timing and Control system

UED Universal Extra Dimenions

USA15 Underground Service Area 15

VBF Vector Boson Fusion

WIMP Weakly Interacting Massive Particle

WMAP Wilkinson Microwave Anisotropy Probe

TDR Technical Design Report

TGC Thin Gap Chamber

TIM TTC Information Module

TOE Theory Of Everything

TRT Transition Radiation Tracker

TTC Trigger, Timing and Control system

UED Universal Extra Dimenions

USA15 Underground Service Area 15

VBF Vector Boson Fusion

WIMP Weakly Interacting Massive Particle

WMAP Wilkinson Microwave Anisotropy Probe

Appendix B

The angular variable $\cos\theta^*_{ll}$

Particle physics utilizes relativistic kinematical, or more succinctly, relativistic invariant variables, in many ways: to relate energies, momenta and here, to measure the scattering angles, in different frames of reference; to deduce the mass of unstable particles from measurements of their decay products. This appendix proceeds to show the relationship between the angular variable, $\cos\theta^*_{ll}$, that underpins the method of measuring spin presented in this thesis and $\Delta\eta_{ll}$ the difference in pseudorapidity between the two final state leptons. Furthermore, it is also shown that it can be written in a more simplified form. The method to show the relationship between $\cos\theta^*_{ll}$ and $\Delta\eta_{ll}$ proceeds in two parts. Part I, initially starting with the variable, $\Delta\eta_{ll}$, proceeds to derive the angular variable, $\cos\theta^*_{ll}$, from it. Within Part II, having derived the angular variable, it is then shown that it can be written in a more simplified form given in terms of the hyperbolic tangent function.

B.1 Part I: $\cos\theta^*_{ll} \equiv \cos\left(2\tan^{-1}\exp(\Delta\eta_{l^\pm l^\mp}/2)\right)$

The angular variable proposed stems from the problematic nature of measuring spin at hadron colliders, in contrast to a leptonic equivalent collider. The relatively simple method for a leptonic collider of making a measurement of the angle of one outgoing lepton relative to the incoming lepton beams in the initial

lepton-lepton centre of mass frame is just not possible for the hadronic equivalent at a hadron collider. The initial partonic momentum is not known and cannot be obtained from the visible final state alone. The information of the momenta of the invisible particles in the event would also be needed and is not available. Thus, as a result, the z-boost which would be required to recover the correct centre of mass frame of the initial colliding partons can not be known. Selecting an angular variable which was a function of $\Delta\eta_{ll}$ only allows one to alleviate this difficulty of observing the differences in the distributions thus allowing one to distinguish between the two models.

Rather than the initial variable $\Delta\eta_{ll}$ (the difference in pseudorapidity between the two final state leptons) which allowed one only faintly discern the shape of the distributions, thus, allowing one to distinguish between the two models, an angular variable was more desirable. It is this beneficent element that makes the angular variable all the more attractive. Moreover, it is Lorentz invariant under z boosts as can be seen below. From the definition of rapidity:

$$y = \frac{1}{2}\ln\frac{[E+p_z]}{[E-p_z]}, \tag{B.1}$$

and using the approximation $E >> m$ (i.e. $E \approx \sqrt{p_T^2+p_z^2}$) allows one to reach the approximation for rapidity through:

$$y \approx \frac{1}{2}\ln\frac{[\sqrt{p_T^2+p_z^2}+p_z]}{[\sqrt{p_T^2+p_z^2}-p_z]}, \tag{B.2}$$

$$y = \frac{1}{2}\ln\frac{[1+p_z/\sqrt{p_T^2+p_z^2}]}{[1-p_z/\sqrt{p_T^2+p_z^2}]}, \tag{B.3}$$

$$y \;=\; \frac{1}{2}\ln[\left[\frac{1+\cos\theta}{1-\cos\theta}\right], \tag{B.4}$$

$$y \;=\; \frac{1}{2}\ln[\left[\frac{2\cos^2\theta/2}{2\sin^2\theta/2}\right], \tag{B.5}$$

$$y \;=\; \frac{1}{2}\ln(\tan\theta/2), \tag{B.6}$$

which is known as the pseudorapidity, η.

As a starting point consider two leptons, 1 and 2, with pseudorapidities η_1 and η_2 respectively. Their difference in pseudorapidity would be:

$$\Delta\eta_{l^\pm l^\mp} = |\eta_1 - \eta_2|. \tag{B.7}$$

Under the application of a Lorentz transformation (boost) from an initial invariant frame of reference S wherein the leptons have ηs η_1 and η_2, to a second frame of reference S$'$, wherein the leptons have ηs now of η'_1 and η'_2. This quantity remains invariant under boosts along the z-axis, from the advantageous property of η (only in the relativistic limit $E >> m$):

$$|\eta'_1 - \eta'_2| = \Delta\eta'_{ll} = \Delta\eta_{ll}. \tag{B.8}$$

From here, we choose to boost along the z-axis such that:

$$\eta'_1 = -\eta'_2 = \frac{1}{2}\Delta\eta'_{ll} = \frac{1}{2}\Delta\eta_{ll}, \tag{B.9}$$

i.e. the reference frame in which the leptons ηs are equal and opposite. This causes the polar angles between each lepton and the beam to also be equal. It is

then apparent that knowledge of $\Delta\eta_{ll}$ gives a handle on this angle θ^*_l, the angle between each lepton and the beam in this frame of reference.

Now from the definition of η:

$$\eta' = \ln\tan(\theta^*_l/2), \tag{B.10}$$

and by using realation B.9 above gives:

$$\Delta\eta/2 = \pm\ln\tan(\theta^*_l/2), \tag{B.11}$$

$$\theta^*_l = 2\tan^{-1}(e^{\pm\Delta\eta/2}), \tag{B.12}$$

where the negative sign infront of $\Delta\eta$ indicates the angular region $0 \leq \theta^*_l \leq \pi$. From taking the cosine of this angle, equation B.12 becomes:

$$\cos\ \theta^*_{ll} = \cos(2\tan^{-1} e^{(\mp\Delta\eta/2)}), \tag{B.13}$$

or equivalently, up to a sign:

$$\cos\ \theta^*_{ll} = \cos(2\tan^{-1} e^{(\Delta\eta/2)}). \tag{B.14}$$

B.2 Part II: $\cos\theta^*_{ll} \equiv \tanh(-\Delta\eta_{l^\pm l^\mp}/2)$

The next part will show how to get from the identity:

$$\cos\theta^*_{ll} = \cos(2\tan^{-1} e^{(\Delta\eta/2)}), \tag{B.15}$$

to

$$\cos\theta^*_{ll} = \tanh(-\Delta\eta/2). \tag{B.16}$$

Starting with:

$$\cos(2\tan^{-1} y) = \cos(2\theta), \tag{B.17}$$

where:

$$y = e^{\Delta\eta/2}, \tag{B.18}$$

$$\Rightarrow \tan^{-1} y = \theta, \tag{B.19}$$

$$\Rightarrow \cos\theta = \frac{1}{\sqrt{1+y^2}}, \tag{B.20}$$

$$\Rightarrow \sin\theta = \frac{y}{\sqrt{1+y^2}}, \tag{B.21}$$

$$\Rightarrow \cos^2\theta = \frac{1}{1+y^2}, \tag{B.22}$$

$$\Rightarrow \sin^2\theta = \frac{y^2}{\sqrt{1+y^2}}. \tag{B.23}$$

Now, using the double angle formulae:

$$\cos 2\theta = \cos^2\theta - \sin^2\theta \tag{B.24}$$

and substituting in for $\cos^2\theta$ and $\sin^2\theta$:

$$\Rightarrow \cos\theta^*_{ll} = \frac{1}{1+y^2} - \frac{y^2}{1+y^2}, \tag{B.25}$$

$$= \frac{1-y^2}{1+y^2}. \tag{B.26}$$

Now,

$$y = e^{(\Delta\eta/2)} \tag{B.27}$$

substituting into b.24 for y^2 and taking $x = -\Delta\eta/2$:

$$\Rightarrow= \frac{e^x - e^{-x}}{e^x + e^{-x}}, \tag{B.28}$$

and using the hyperbolic functions:

$$\sinh(x) = \frac{e^x - e^{-x}}{2} \quad \text{and} \quad \cosh(x) = \frac{e^x + e^{-x}}{2}, \tag{B.29}$$

$$\Rightarrow \cos\theta^*_{ll} = \frac{2\sinh(x)}{2\cosh(x)} = \frac{\sinh(x)}{\cosh(x)} = \tanh(x). \tag{B.30}$$

Finally, substituting $x = -\Delta\eta/2$ back in now gives:

$$\Rightarrow \cos\theta^*_{ll} \equiv \tanh(-\Delta\eta_{l^\pm l^\mp}/2) \equiv \ -\tanh(\Delta\eta_{l^\pm l^\mp}/2), \tag{B.31}$$

as desired.

Bibliography

[1] A. Salam, in *Elementary Particle Theory*, edited by N. Svaratholm, 1968.

[2] S. L. Glashow, *Nucl. Phys.* **20**, 579 (1961).

[3] S. Weinberg, A model of leptons, *Phys. Rev. Lett.* **19**, 1264–1266 (1967).

[4] F. Halzen and A. D. Martin, *Quarks and Leptons: An Introductory Course in Modern Particle Physics*, John Wiley and Sons, 1984.

[5] I.J.R. Aitchison and A.J.G. Hey, *Gauge Theories in Particle Physics: A Practical Introduction*, Adam Hilger, 1989.

[6] L.H. Ryder, *Quantum Field Theory*, Cambridge Univ. Pr., 2 edition, 1996.

[7] E. Noether, Invariant variation problems, (English translation of Invariante Variationsprobleme (2005)), `arXiv:physics/0503066`.

[8] K. Hagiwara et al., Review of Particle Physics, *Physical Review D* **66** (2002),
`http://pdg.lbl.gov`.

[9] Friedemann Brandt, Lectures on supergravity, *Fortsch. Phys.* **50**, 1126–1172 (2002), `hep-th/0204035`.

[10] Dimitrii V. Volkov, Supergravity before 1976, (1994), `hep-th/9410024`.

[11] C. Lee, B.W. Quigg and H.B. Thacker, Strength of weak interactions at very high energies and the higgs boson mass, *Phys. Rev. Lett.* , 883–885 (1977).

[12] R. Barate et al., Search for charged higgs bosons in e+ e- collisions at s**(1/2) = 181-GeV to 184-GeV, (1999), `hep-ex/9902031`.

[13] Alan James Barr, *Studies of supersymmetry models for the ATLAS experiment at the Large Hadron Collider*, PhD thesis, 2002, Cambridge Universty, CERN-THESIS-2004-002.

[14] Zwicky F., On the Masses of Nebulae and of Clusters of Nebulae, *Astrophysical Journal* **86**, 217.

[15] Extra dimensions, 2004, Lecture given by T.G. Rizzo.

[16] G. R. Dvali, Gregory Gabadadze, and Goran Senjanovic, Constraints on extra time dimensions, (1999), `hep-ph/9910207`.

[17] D. Bailin and A. Love, *Supersymmetric gauge field theory and string theory*, Bristol, UK: IOP, 1994.

[18] P.G.O. Freund, *Introduction to Supersymmetry*, Cambridge Univ. Pr., 1986.

[19] Stephen P. Martin, A supersymmetry primer, (1997), `hep-ph/9709356`.

[20] J. Wess and J. Bagger, *Supersymmetry and Supergravity theory*, Princeton, USA: Princeton University Press, 1992.

[21] Manuel Drees, An introduction to supersymmetry, (1996), `hep-ph/9611409`.

[22] Howard E. Haber, Introductory low-energy supersymmetry, (1993), hep-ph/9306207.

[23] John H. Schwarz and Nathan Seiberg, String theory, supersymmetry, unification, and all that, *Rev. Mod. Phys.* **71**, S112–S120 (1999), hep-th/9803179.

[24] P. Fayet, Supersymmetry and Weak, Electromagnetic and Strong Interactions, *Phys. Lett.* **B64**, 159 (1976).

[25] P. Fayet, *Phys. Lett.* **B69**, 489 (1977).

[26] Manuel Drees and Stephen P. Martin, Implications of SUSY model building, (1995), hep-ph/9504324.

[27] Keith R. Dienes, String theory and the path to unification: A review of recent developments, *Phys. Rept.* **287**, 447–525 (1997), hep-th/9602045.

[28] Wim de Boer and Christian Sander, Global electroweak fits and gauge coupling unification, *Phys. Lett.* **B585**, 276–286 (2004), hep-ph/0307049.

[29] B. Zwiebach, *A First Course in String Theory*, Cambridge Univ. Pr., 2004.

[30] J. Polchinski, *String Theory*, volume 1 and 2 of *String Theory*, Cambridge Univ. Pr., 1988.

[31] C. M. Hull and P. K. Townsend, Unity of superstring dualities, *Nucl. Phys.* **B438**, 109–137 (1995), hep-th/9410167.

[32] Joseph Polchinski and Edward Witten, Evidence for Heterotic - Type I String Duality, *Nucl. Phys.* **B460**, 525–540 (1996), hep-th/9510169.

[33] Petr Horava and Edward Witten, Heterotic and type I string dynamics from eleven dimensions, *Nucl. Phys.* **B460**, 506–524 (1996), hep-th/9510209.

[34] Petr Horava and Edward Witten, Eleven-Dimensional Supergravity on a Manifold with Boundary, *Nucl. Phys.* **B475**, 94–114 (1996), hep-th/9603142.

[35] J. Green, M. Schwarz and E. Witten, *Superstring Theory*, Cambridge Univ. Pr., 1987.

[36] C. Amsler et al., Review of Particle Physics, *Physical Letters* **B667** (2008), http://pdg.lbl.gov.

[37] CDF Collaboration, *CDF Note* **9229** (2008).

[38] M.S. Carena, A. Menon, and C.E.M. Wagner, *Phys. Rev.* **D76**, 035004 (2007).

[39] Papers of the five-year wmap observations are available at: http://lambda.gsfc.nasa.gov/product/map/current/map_bibliography.cfm.

[40] C. Arina and N. Fornengo, *JHEP* **0711**, 029 (2007).

[41] F.D. Steffen, *JCAP* **0609**, 001 (2006).

[42] Yael Shadmi and Yuri Shirman, Dynamical supersymmetry breaking, *Rev. Mod. Phys.* **72**, 25–64 (2000), hep-th/9907225.

[43] G. F. Giudice and R. Rattazzi, Theories with gauge-mediated supersymmetry breaking, *Phys. Rept.* **322**, 419–499 (1999), hep-ph/9801271.

[44] Ali H. Chamseddine, Richard L. Arnowitt, and Pran Nath, Locally Supersymmetric Grand Unification, *Phys. Rev. Lett.* **49**, 970 (1982).

[45] S. Barbieri, R. Ferrara and A. Savoy, *Phys. Lett.* **B119**, 343 (1982).

[46] Lawrence J. Hall, J. Lykken, and S. Weinberg, Supergravity as the messenger of supersymmetry breaking, *Phys. Rev.* **D27**, 2359–2378 (1983).

[47] Luis Alvarez-Gaume, J. Polchinski, and Mark B. Wise, Minimal Low-Energy Supergravity, *Nucl. Phys.* **B221**, 495 (1983).

[48] Luis E. Ibanez, Locally Supersymmetric SU(5) Grand Unification, *Phys. Lett.* **B118**, 73 (1982).

[49] John R. Ellis, Dimitri V. Nanopoulos, and K. Tamvakis, Grand Unification in Simple Supergravity, *Phys. Lett.* **B121**, 123 (1983).

[50] Kenzo Inoue, Akira Kakuto, Hiromasa Komatsu, and Seiichiro Takeshita, Aspects of Grand Unified Models with Softly Broken Supersymmetry, *Prog. Theor. Phys.* **68**, 927 (1982).

[51] Lisa Randall and Raman Sundrum, An alternative to compactification, *Phys. Rev. Lett.* **83**, 4690–4693 (1999), `hep-th/9906064`.

[52] Nima Arkani-Hamed, Savas Dimopoulos, G. R. Dvali, and Nemanja Kaloper, Infinitely large new dimensions, *Phys. Rev. Lett.* **84**, 586–589 (2000), `hep-th/9907209`.

[53] G. Nordstrom, *Phys. Zeitschr.1* **504** (1914).

[54] T. Kaluza, *Phys. Math. K.1* **966** (1921).

[55] O. Klein, *Phys. Zeitschr.37* **895** (1926).

[56] Ignatios Antoniadis, A Possible new dimension at a few TeV, *Phys. Lett.* **B246**, 377–384 (1990).

[57] V. A. Rubakov and M. E. Shaposhnikov, Extra Space-Time Dimensions: Towards a Solution to the Cosmological Constant Problem, *Phys. Lett.* **B125**, 139 (1983).

[58] V. A. Rubakov and M. E. Shaposhnikov, *Phys. Lett.* **B125**, 136 (1983).

[59] Matt Visser, An Exotic Class of Kaluza-Klein Models, *Phys. Lett.* **B159**, 22 (1985), `hep-th/9910093`.

[60] Joseph D. Lykken, Weak Scale Superstrings, *Phys. Rev.* **D54**, 3693–3697 (1996), `hep-th/9603133`.

[61] Savas Arkani-Hamed, Nima Dimopoulos and G. R. Dvali, The hierarchy problem and new dimensions at a millimeter, *Phys. Lett.* **B429**, 263–272 (1998), `hep-ph/9803315`.

[62] Nima Arkani-Hamed, Savas Dimopoulos, and G. R. Dvali, Phenomenology, astrophysics and cosmology of theories with sub-millimeter dimensions and TeV scale quantum gravity, *Phys. Rev.* **D59**, 086004 (1999), `hep-ph/9807344`.

[63] Lisa Randall and Raman Sundrum, A large mass hierarchy from a small extra dimension, *Phys. Rev. Lett.* **83**, 3370–3373 (1999), `hep-ph/9905221`.

[64] Thomas Appelquist, Hsin-Chia Cheng, and Bogdan A. Dobrescu, Bounds on universal extra dimensions, *Phys. Rev.* **D64**, 035002 (2001), `hep-ph/0012100`.

[65] Thomas Appelquist, Bogdan A. Dobrescu, Eduardo Ponton, and Ho-Ung Yee, Proton stability in six dimensions, *Phys. Rev. Lett.* **87**, 181802 (2001), `hep-ph/0107056`.

[66] Nima Arkani-Hamed, Hsin-Chia Cheng, Bogdan A. Dobrescu, and Lawrence J. Hall, Self-breaking of the standard model gauge symmetry, *Phys. Rev.* **D62**, 096006 (2000), hep-ph/0006238.

[67] Bogdan A. Dobrescu and Eduardo Ponton, Chiral compactification on a square, *JHEP* **03**, 071 (2004), hep-th/0401032.

[68] Gustavo Burdman, Bogdan A. Dobrescu, and Eduardo Ponton, Six-dimensional gauge theory on the chiral square, *JHEP* **02**, 033 (2006), hep-ph/0506334.

[69] Bogdan A. Dobrescu and Erich Poppitz, Number of fermion generations derived from anomaly cancellation, *Phys. Rev. Lett.* **87**, 031801 (2001), hep-ph/0102010.

[70] Hsin-Chia Cheng, Jonathan L. Feng, and Konstantin T. Matchev, Kaluza-Klein dark matter, *Phys. Rev. Lett.* **89**, 211301 (2002), hep-ph/0207125.

[71] Dan Hooper and Graham D. Kribs, Probing Kaluza-Klein dark matter with neutrino telescopes, *Phys. Rev.* **D67**, 055003 (2003), hep-ph/0208261.

[72] Dan Hooper and Stefano Profumo, Dark matter and collider phenomenology of universal extra dimensions, *Phys. Rept.* **453**, 29–115 (2007), hep-ph/0701197.

[73] Manuel Masip and Alex Pomarol, Effects of SM Kaluza-Klein excitations on electroweak observables, *Phys. Rev.* **D60**, 096005 (1999), hep-ph/9902467.

[74] Thomas G. Rizzo and James D. Wells, Electroweak precision measurements and collider probes of the standard model with large extra dimensions, *Phys. Rev.* **D61**, 016007 (2000), hep-ph/9906234.

[75] Geraldine Servant and Timothy M. P. Tait, Is the lightest Kaluza-Klein particle a viable dark matter candidate?, *Nucl. Phys.* **B650**, 391–419 (2003), hep-ph/0206071.

[76] Marco Battaglia, AseshKrishna Datta, Albert De Roeck, Kyoungchul Kong, and Konstantin T. Matchev, Contrasting supersymmetry and universal extra dimensions at the CLIC multi-TeV e+ e- collider, *JHEP* **07**, 033 (2005), hep-ph/0502041.

[77] Hsin-Chia Cheng, Konstantin T. Matchev, and Martin Schmaltz, Radiative corrections to Kaluza-Klein masses, *Phys. Rev.* **D66**, 036005 (2002), hep-ph/0204342.

[78] S. I. Bityukov and N. V. Krasnikov, Search for SUSY at LHC in jets + E(T)(miss) final states for the case of nonuniversal gaugino masses, *Phys. Lett.* **B469**, 149–154 (1999), hep-ph/9907257.

[79] Chun Lin, *A Search for Universal Extra Dimensions in the Multi-Lepton Channel from Proton-Antiproton Collisions at* $\sqrt{s}$*=1.8 TeV*, PhD thesis, 2005, Yale Universty.

[80] Thomas Flacke, Dan Hooper, and John March-Russell, Improved bounds on universal extra dimensions and consequences for LKP dark matter, *Phys. Rev.* **D73**, 095002 (2006), hep-ph/0509352.

[81] Andrzej J. Buras, Anton Poschenrieder, Michael Spranger, and Andreas Weiler, The impact of universal extra dimensions on B to X/s gamma, B to X/s gluon, B to X/s mu+ mu-, K(L) to pi0 e+ e-, and epsilon'/epsilon, *Nucl. Phys.* **B678**, 455–490 (2004), hep-ph/0306158.

[82] J. F. Oliver, J. Papavassiliou, and Arcadi Santamaria, Universal extra dimensions and Z to b anti-b, *Phys. Rev.* **D67**, 056002 (2003), hep-ph/0212391.

[83] Andrzej J. Buras, Michael Spranger, and Andreas Weiler, The impact of universal extra dimensions on the unitarity triangle and rare K and B decays. ((U)), *Nucl. Phys.* **B660**, 225–268 (2003), hep-ph/0212143.

[84] Hsin-Chia Cheng, Konstantin T. Matchev, and Martin Schmaltz, Bosonic supersymmetry? Getting fooled at the LHC, *Phys. Rev.* **D66**, 056006 (2002), hep-ph/0205314.

[85] AseshKrishna Datta, Kyoungchul Kong, and Konstantin T. Matchev, Discrimination of supersymmetry and universal extra dimensions at hadron colliders, *Phys. Rev.* **D72**, 096006 (2005), hep-ph/0509246.

[86] D. Buskulic et al., ALEPH collaboration, *Zeitschrift für Physik C 59* **215** (1993).

[87] Paul Langacker, Ming-xing Luo, and Alfred K. Mann, High precision electroweak experiments: A Global search for new physics beyond the standard model, *Rev. Mod. Phys.* **64**, 87–192 (1992).

[88] W. M. Yao et al., Review of Particle Physics, *J. Phys.* **G33** (2006).

[89] H.J. Behrend et al., *Physics Letters* **183B**, 400 (1987).

[90] S.-L. Wu, *Physics Reports* **107**, 59 (1984).

[91] M. Blagojević, *Gravitation and Gauge Symmetry*, Bristol, UK: IOP, 2002.

[92] Jens Erler, Spin beyond Standard Model: Theory, (2009), 0901.4763.

[93] A. J. Barr, Measuring slepton spin at the LHC, *JHEP* **02**, 042 (2006), hep-ph/0511115.

[94] Shigeki Matsumoto, Joe Sato, Masato Senami, and Masato Yamanaka, Solving cosmological problem in universal extra dimension models by introducing Dirac neutrino, *Phys. Lett.* **B647**, 466–471 (2007), hep-ph/0607331.

[95] *ATLAS Magnet System TDR*, CERN, 1996, CERN/LHCC 97-18.

[96] *ATLAS Detector and Physics Peformance TDR*, CERN, 1999, CERN/LHCC/99-14, CERN/LHCC/99-15.

[97] *ATLAS Letter of Intent for a General Purpose pp Experiment at the Large hadron Colider*, CERN, 1992, CERN/LHCC 92-4.

[98] *ATLAS Central Solenoid Technical Design Report*, CERN, 1997, CERN/LHCC 97-21.

[99] G. Aad et al The ATLAS Collaboration, The ATLAS Experiment at the CERN Large Hadron Collider, (2008), JINST 3 S08003.

[100] S. Palestini, The muon spectrometer of the ATLAS experiment, *Nucl. Phys.* **125**, 337 (2003).

[101] J. Wotschack, ATLAS muon chamber construction parameters for CSC, MDT and RPC chambers, (2008), ATLAS note, ATL-MUON-PUB-2008-006.

[102] G. Aielli, The RPC first level muon trigger in the barrel of the ATLAS experiment, *Nucl. Phys.* **158**, 11 (2006).

[103] A.et al Aloisio, The trigger chambers of the ATLAS muon spectrometer: production and tests, *Nucl. Instrum. Meth.* **A 535**, 265 (2004).

[104] *ATLAS First-level trigger technical design report*, CERN, 1998, CERN-LHCC-98-014.

[105] G. et al Aielli, Sf-6 quenched gas mixtures for streamer mode operation of RPCs at very low voltages, *Nucl. Instrum. Meth.* **A 493**, 137 (2002).

[106] G. et al Aielli, Electrical conduction properties of phenolic-melaminic laminates, *Nucl. Instrum. Meth.* **A 533**, 86 (2004).

[107] A. J. Barr and T. J. Byatt, Investigation into the zeroth time bin anomaly in the SCT barrel modules in the ATLAS detector, ATLAS internal note, ATL-COM-INDET-2006-013.

[108] *ATLAS Inner Detector TDR*, CERN, 1997, CERN/LHCC/97-16 and CERN/LHCC/97-17.

[109] A. et al. Abdesselam, The barrel modules of the ATLAS semiconductor tracker, *Nucl. Instrum. Meth.* **A568**, 642 (2006).

[110] F. Campabadal et al., Design and performance of the ABCD3TA ASIC for readout of silicon strip detectors in the ATLAS semiconductor tracker, *Nucl. Instrum. Meth.* **A552**, 292–328 (2005).

[111] ATLAS SCT collaboration, ABCD3TA ASIC: Requirements and specification v1.3, 2000, http://edms.cern.ch/file/317413/1/abcd3ta_spec_v1.3.pdf.

[112] A. Abdesselam et al., The Data acquisition and calibration systems for the ATLAS semiconductor tracker, *JINST* **3**, P01003 (2008).

[113] H. McClaren van der Bij, S-LINK, a data link interface specification for the LHC era, *in IEEE Transactions on Nuclear Science* **44**, 398–402 (1997).

[114] Debajyoti Choudhury et al., Slepton production from gauge boson fusion, *Phys. Rev.* **D68**, 075007 (2003), hep-ph/0304192.

[115] Marco Battaglia et al., Proposed post-LEP benchmarks for supersymmetry, *Eur. Phys. J.* **C22**, 535–561 (2001), hep-ph/0106204.

[116] Satoshi Mizuta and Masahiro Yamaguchi, Coannihilation Effects and Relic Abundance of Higgsino- Dominant LSPs, *Phys. Lett.* **B298**, 120–126 (1993), hep-ph/9208251.

[117] John R. Ellis, Toby Falk, Gerardo Ganis, Keith A. Olive, and Mark Srednicki, The CMSSM Parameter Space at Large tan beta, *Phys. Lett.* **B510**, 236–246 (2001), hep-ph/0102098.

[118] Jonathan L. Feng, Konstantin T. Matchev, and Takeo Moroi, Multi-TeV scalars are natural in minimal supergravity, *Phys. Rev. Lett.* **84**, 2322–2325 (2000), hep-ph/9908309.

[119] Jonathan L. Feng, Konstantin T. Matchev, and Takeo Moroi, Focus points and naturalness in supersymmetry, *Phys. Rev.* **D61**, 075005 (2000), hep-ph/9909334.

[120] Jonathan L. Feng, Konstantin T. Matchev, and Frank Wilczek, Neutralino Dark Matter in Focus Point Supersymmetry, *Phys. Lett.* **B482**, 388–399 (2000), hep-ph/0004043.

[121] Howard Baer, Frank E. Paige, Serban D. Protopopescu, and Xerxes Tata, Isajet 7.48: A Monte Carlo event generator for p p, $\bar{p}\,p$, and e^+e^- reactions, (1999), hep-ph/0001086.

[122] Frank E. Paige, Serban D. Protopopescu, Howard Baer, and Xerxes Tata, ISAJET 7.69: A Monte Carlo event generator for p p, anti-p p, and e+ e- reactions, (2003), hep-ph/0312045.

[123] ISAWIG Website: http://www.hep.phy.cam.ac.uk/ richardn/HERWIG/ISAWIG/.

[124] G. Marchesini et al., HERWIG: A Monte Carlo event generator for simulating hadron emission reactions with interfering gluons. version 5.1 - April 1991, *Comput. Phys. Commun.* **67**, 465 (1992).

[125] G. Corcella et al., HERWIG 6: An event generator for hadron emission reactions with interfering gluons (including supersymmetric processes), *JHEP* **01**, 010 (2001), hep-ph/0011363.

[126] S. et al. Agostinelli, GEANT4: A simulation toolkit, *Nucl. Instrum. Meth.* **A506**, 250–303 (2003).

[127] EventView Website: https://twiki.cern.ch/twiki/bin/view/Atlas/EventView.

[128] Torbjorn Sjostrand, High-energy physics event generation with pythia 5.7 and jetset 7.4, *Comput. Phys. Commun.* **82**, 74–90 (1994).

[129] Torbjorn Sjostrand et al., High-energy-physics event generation with PYTHIA 6.1, *Comput. Phys. Commun.* **135**, 238–259 (2001), hep-ph/0010017.

[130] Torbjorn Sjostrand, Stephen Mrenna, and Peter Skands, PYTHIA 6.4 physics and manual, *JHEP* **05**, 026 (2006), hep-ph/0603175.

[131] Stefano Frixione and Bryan R. Webber, Matching NLO QCD computations and parton shower simulations, *JHEP* **06**, 029 (2002), hep-ph/0204244.

[132] Stefano Frixione, Paolo Nason, and Bryan R. Webber, Matching NLO QCD and parton showers in heavy flavour production, *JHEP* **08**, 007 (2003), hep-ph/0305252.

[133] Jimmy Website: http://projects.hepforge.org/jimmy/.

[134] Borut Paul Kersevan and Elzbieta Richter-Was, The Monte Carlo event generator AcerMC version 2.0 with interfaces to PYTHIA 6.2 and HERWIG 6.5, (2004), hep-ph/0405247.

[135] E. Richter-Was, D. Froidevaux, and L. Poggioli, Atlfast 2.0: A fast simulation package for ATLAS, (1998), ATLAS internal note, ATL-PHYS-98-131.

[136] Atlfast validation note: *http://www.hep.ucl.ac.uk/atlas/atlfast/*.

[137] Athena software framework: https://twiki.cern.ch/twiki/bin/view/Atlas/WorkBook.

[138] A. J. Barr, Using lepton charge asymmetry to investigate the spin of supersymmetric particles at the LHC, *Phys. Lett.* **B596**, 205–212 (2004), hep-ph/0405052.

[139] Jennifer M. Smillie and Bryan R. Webber, Distinguishing spins in supersymmetric and universal extra dimension models at the Large Hadron Collider, *JHEP* **10**, 069 (2005), hep-ph/0507170.

[140] Biplob Bhattacherjee and Anirban Kundu, The International Linear Collider as a Kaluza-Klein factory, *Phys. Lett.* **B627**, 137–144 (2005), hep-ph/0508170.

[141] S. Brandt, *Statistical and Computational Methods in Data Analysis*, Springer, New York, 1997.

[142] G. Cowan, *Statistical Data Analysis*, Oxford University Press, 1998.

[143] R. J. Barlow, *Statistics A Guide to the Use of Statistical Methods in the Physical Sciences*, John Wiley and Sons Ltd, 2002.

[144] Toru Goto, Kiyotomo Kawagoe, and Mihoko M. Nojiri, Study of the slepton non-universality at the CERN Large Hadron Collider, *Phys. Rev.* **D70**, 075016 (2004), `hep-ph/0406317`.

[145] Howard Baer, Chih-hao Chen, Frank Paige, and Xerxes Tata, Signals for Minimal Supergravity at the CERN Large Hadron Collider II: Multilepton Channels, *Phys. Rev.* **D53**, 6241–6264 (1996), `hep-ph/9512383`.

[146] E. Lytken, Searches for direct slepton production with ATLAS, *Czech. J. Phys.* **54**, A169–A173 (2004).

[147] G. Aad et al., Expected Performance of the ATLAS Experiment - Detector, Trigger and Physics, (2009), `0901.0512`.

[148] C. G. Lester and D. J. Summers, Measuring masses of semi-invisibly decaying particles pair produced at hadron colliders, *Phys. Lett.* **B463**, 99–103 (1999), `hep-ph/9906349`.

[149] Alan Barr, Christopher Lester, and P. Stephens, m(T2): The truth behind the glamour, *J. Phys.* **G29**, 2343–2363 (2003), `hep-ph/0304226`.

[150] F. del Aguilla and L. Ametller, On the detectability of sleptons at large hadron colliders, *Phys. Lett.* **B261**, 326–333 (1991).

[151] Howard Baer, Chih-hao Chen, Frank Paige, and Xerxes Tata, Detecting sleptons at hadron colliders and supercolliders, *Phys. Rev.* **D49**, 3283–3290 (1994), `hep-ph/9311248`.

[152] Howard Baer, Chih hao Chen, Frank Paige, and Xerxes Tata, Signals for minimal supergravity at the CERN large hadron collider ii: Multilepton channels, *Phys. Rev.* **D53**, 6241–6264 (1996), hep-ph/9512383.

[153] G. Weiglein et al., Physics interplay of the LHC and the ILC, *Phys. Rept.* **426**, 47–358 (2006), hep-ph/0410364.

[154] Howard Baer, Manuel Drees, Chung Kao, Mihoko Nojiri, and Xerxes Tata, Supercollider signatures of supergravity models with yukawa unification, *Phys. Rev.* **D50**, 2148 (1994), hep-ph/9403307.